# Synthesis and applications of hexagonal boron nitride ultrathin films



**PhD Thesis** 

Nilanjan Basu School of Physics University of Hyderabad Hyderabad-500046

**May 2021** 

## Synthesis and applications of hexagonal boron nitride ultrathin films

Thesis submitted to the University of Hyderabad for the award of the degree of

### **DOCTOR OF PHILOSOPHY**

In

**Physics** 

By

Nilanjan Basu (15PHPH17)



### **Supervisor**

Dr. Jayeeta Lahiri Assistant Professor, School of Physics, The University of Hyderabad, Hyderabad-500046, India

### Co. Supervisor

Dr. M Ghanashyam Krishna
Professor, Centre for Advanced Studies in Electronics Science and Technology (CASEST),
School of Physics,
University of Hyderabad,
Hyderabad-500046, India

### Declaration

I Nilanjan Basu in my full sense do hereby declare that this thesis titled "Synthesis and applications of hexagonal boron nitride ultrathin films" is a product of bonafide research and is free of plagiarism and has been carried out by me under the supervision of Dr. Jayceta Lahiri and Prof. M Ghanashyam Krishna. No part of the thesis has been submitted to the University of Hyderabad or any other University/Institution for the award of any degree or diploma.

I hereby give my consent for the lodgement of this thesis to Shodhganga/INFLIBNET.

A plagiarism report about this thesis work endorsed by the Librarian of the University of Hyderabad has been attached at the end of the thesis.

Date 20/5/2021

Place Hyderabad.

Name Nilanjan Bash.

Registration Number -15PHPH17

### **CERTIFICATE**

This is to certify that the thesis titled "Synthesis and applications of hexagonal boron nitride ultrathin films" submitted by Nilanjan Basu (Reg. No. – 15PHPH17), in partial fulfilment for the award of the degree of Doctor of Philosophy in Physics, is a bonafide work carried out by him under the supervision of Dr. Jayeeta Lahiri as the supervisor and Prof. M Ghanashyam Krishna as the co-supervisor.

This thesis is free of plagiarism and no part of it has been submitted to the University of Hyderabad or any other university/institution for the award of any degree or diploma.

Further, the student has passed the following courses towards the fulfilment of coursework required for the commencement of PhD work:

Course Code	Name of the course	Credits	Pass/Fail
PY801	Advanced Quantum Mechanics	4	Pass
PY803	Advanced Statistical Mechanics	4	Pass
PY804	Advanced Electromagnetic Theory	4	Pass
PY821	Research Methodology	4	Pass

Dean

School of Physics University of Hyderabad Hyderabad-500046,India

JAYEETA LAHIRI
Assistant Professor
School of Physics
University of Hydorabad

Dr. Jayeeta Lahiri 00 040. Assistant Professor, School of Physics, The University of Hyderabad, Hyderabad-500046, India Prof. M. GHANASHYAM KRISHNA
Centre for Advanced Studies in
Electronics Science & Technology
School of Physics, University of Hyderabad
HYDERABAD-500 046. Telangana, India.

M. Manashyam

Co. Supervisor Dr. M Ghanashyam Krishna Professor, (CASEST), School of Physics, Hyderabad-500046, India

Place- Hyderabad,

Date-27/5/2021

### **Dedicated**

To

My beloved parents Rintu and Tabul.

### **ACKNOWLEDGEMENT**

With great pleasure and gratification, I would like to convey my gratitude towards the people and institutions that actively supported and helped me to complete this thesis. This message of acknowledgement should and must start by conveying my gratitude towards my supervisor Dr. Jayeeta Lahiri and co-supervisor Prof. M Ghanashyam Krishna. Without the active support of my supervisor and vigilance over my research work, the thesis work would have never been completed. I am in debt for the induction of work ethics and research culture that she inculcated in me. A mere message of acknowledgement would never suffice to truly capture the depth and breadth of guidance that she provided in my PhD work.

I am lucky to get the guidance of Prof. M Ghanashyam Krishna as my co-supervisor. I received unparallel and selfless support from him in the last days of my PhD work. He was always there whenever I reached out to him. I cannot unburden myself by conveying my gratitude towards him.

Apart from the support from my supervisor and co-supervisor, I am fortunate enough to receive active help from my doctoral review committee members comprising, Prof. SVS Nageswara Rao and Prof. S. Srinath. Both of them have provided valuable guidance during my review meetings which were beneficial in correcting the research trajectory.

I would like to convey my gratitude towards Prof. T Som and his group, Institute of Physics, Bhubaneswar, India. He is our collaborator. I have received an immense amount of moral support and practical research inputs from him and also from his group members. He happily overlooked my mistakes in his lab and has always acted as a mentor. Words cannot describe the mentorship that I received from him. Lots of thank you.

My PhD work has been tied with many esteemed collaborators. I am happy to show my respect and gratitude towards all of them. I received invaluable support from Prof. Soma Venugopal Rao and his group, ARCHEM, University of Hyderabad. Without his active support, the paper about the SERS abilities of hBN wouldn't have been published. I express my sheer pleasure for the unconditional gratitude towards him. I would also like to convey my gratitude towards Dr. Avanish Parmar and his group, IIT BHU, India. His help in XPS scans was invaluable. Without his active support, I might not have XPS scans of hBN samples. I am in debt towards Dr. Rajiv Prakash and group, IIT BHU, India and Dr. T.N Narayan and group, TIFR, Hyderabad, India. Both of them provided unconditional support for the fulfilment of the thesis work.

Throughout the whole PhD work, I am fortunate enough to receive assistance from staff and faculty members of the School of Physics and the University of Hyderabad. I am happy to show my acknowledgements towards them.

Apart from the faculty members, I am fortunate to have a conducive environment in our lab, all the credits go to my lab mates Naresh and Nurul. I would like to show my gratitude towards them. They were always there to watch my back. I would also like to show my gratitude to my batch mates of 2015 and seniors, my friends from school and college days and also towards my loved ones and family members.

This acknowledgement message is incomplete without showing my gratitude towards my parents. Who have shown real selfless support for the fulfilment of their son's research work. Their care and love sometimes compel me to think how worthy of it I am. In a true sense feel immensely blessed to have parents like them.

The list of acknowledging is long, I am indebted to numerous unknown people who made a contribution in a way or another. To the lab electrician, to the ac mechanic to the mess cook etc. a true list of acknowledgement is never a complete list. I would like to thank you all. Finally, I would like to show my gratitude towards the Republic of India and its peace-loving people. When I contrast the situation of current India which is a developing nation with other nations in the same bracket like Venezuela or Syria or Iraq I could see the value of peace in research. Without the unconditional, sustainable and homogeneous peace that sprung through my PhD life, the thesis work and the conjunct research would never have been completed. Thank you all.

#### **Publications and Conferences:**

### A. Journal Publications

[1] Large Area Few-Layer Hexagonal Boron Nitride as a Raman Enhancement Material. **N Basu**, Moram Sree Satya Bharathi, Manju Sharma, Kanchan Yadav, Avanish Singh Parmar, Venugopal Rao Soma, Jayeeta Lahiri. Nanomaterials 2021, 11, 622. <a href="https://doi.org/10.3390/nano11030622">https://doi.org/10.3390/nano11030622</a>

[2] Investigating the role of Cu foil orientation in the growth of large BN films synthesized by reactive RF magnetron sputtering.

**N Basu**, A Dutta, R Singh, T Som, J Lahiri. (Submitted) arXiv preprint arXiv:2002.06634

[3] Improved photovoltaic performance of CdTe-based solar cells: Roles of using a hole-blocking layer and nanoscale imaging of barrier height at interfaces.

R Singh, A Dutta, **N Basu**, J Lahiri, T Som - Solar Energy, 2021 <a href="https://doi.org/10.1016/j.solener.2020.12.021">https://doi.org/10.1016/j.solener.2020.12.021</a>

[4] Resistive switching behaviour of amorphous silicon carbide thin films fabricated by a single composite magnetron sputter deposition method.

PC Akshara, N Basu, J Lahiri, G Rajaram, MG Krishna.

Bulletin of Materials Science 43 (1) 2020

https://doi.org/10.1007/s12034-020-02093-8

[5] Electric Field Induced Dissociation of SiC Thin Films Leading to the Formation of Nanocrystalline Graphite.

PC Akshara, MG Krishna, G Rajaram, Y Rajesh, N Basu, J Lahiri

Electronic Materials Letters, 1-8 2020

https://doi.org/10.1007/s13391-020-00204-5

[6] Label-Free Fluorometric Detection of Adulterant Malachite Green Using Carbon Dots Derived from the Medicinal Plant Source *Ocimum tenuiflorum*.

D Shukla, FP Pandey, P Kumari, N Basu, MK Tiwari, J Lahiri, RN Kharwar, ...

ChemistrySelect 4 (17), 4839-4847 2019

https://doi.org/10.1002/slct.201900530

[7] Growth and properties of solvothermally derived CZTSe nanocrystals using elemental precursors.

T Chandel, MB Zaman, N Basu, J Lahiri, R Poolla

Physica B: Condensed Matter 545, 262-267 2018

https://doi.org/10.1016/j.physb.2018.06.031

### **Under preparation**

- [1] Investigation of learning behaviour of CVD grown hBN ultrathin films by using conductive AFM.
- [2] Behaviour of CVD grown hBN as an electrocatalyst in Oxygen reduction reaction.

### B. Conference presentations and oral talks-

- [1] Poster at 2<sup>nd</sup> International Conference on Soft Materials, 2016 Jaipur.
- [2] Poster presentation at" International Conference on Advances in Biological Systems and Material science in Nano world" -2017 at IIT BHU.
- [3] Poster presentation at International Conference on Functional Nanomaterials 22-25 February ,2019, Department of Physics ,IIT (BHU), Varanasi.
- [4] Oral talk at International conference on SMART MATERIALS FOR SUSTAINABLE TECHNOLOGY, 22-25 February 2020, Goa, India.

### **Table of contents**

Chapter 1. Introduction	
Chapter 2. Literature Survey	9
2.1. Introduction to two dimensional materials	9
2.1.1. Hexagonal Boron Nitride and its allotropes	9
2.2. Unique physics about 2D materials	15
2.3. Synthesis techniques of 2D materials	15
2.3.1. Bottom up synthesis techniques	16
Physical Vapor Deposition	
Chemical Vapor Deposition	
Low Pressure CVD	
Atmospheric CVD	
Atomic Layer Deposition	
Molecular Beam Epitaxy 2.3.2. Top down synthesis techniques	18
Solid Phase Exfoliation	16
Liquid Phase Exfoliation	
Unzipping BN nanotubes	
2.3.2 Substrate effect on synthesis of 2D materials	20
2.4. Application of 2D materials and hBN	20
2.4.1. Novel electronic devices	21
2.4.2. Photonic application	21
2.4.3. Memory devices	23
2.4.4. Miscellaneous applications of hBN and other 2D materials.	24
2.5. Heterostructures.	25
2.5.1. Synthesis of heterostructure	25
2.5.2. Fabrication of heterostructure	26
2.5.3. Application of heterostructure	26
2.6. Characterization of hBN and 2D materials	27
2.7. Future scope	28
2.8. Motivation and objective	28
2.9. References	30
Chapter 3. Experimental Methods	37
3.1. Cleaning and electropolishing of copper foil	37
3.2. Synthesis Techniques	38
3.2.1. Exfoliation	39
3.2.2. Radio frequency (r.f) magnetron sputtering	39
3.2.3. Chemical vapour deposition	40
• •	40
3.3. Microscopic Techniques	
3.3.1. Optical microscope	42

3.3.2. Field emission scanning electron microscopy	43
3.3.3. Transmission electron microscopy	45
3.3.4. Atomic force microscopy	46
3.3.5. Scanning Kelvin probe microscopy	48
3.3.6. Conductive atomic force microscopy	48
3.4. Spectroscopic Techniques	50
3.4.1. Energy dispersive X ray spectroscopy	50
3.4.2. X ray photoelectron spectroscopy	50
3.4.3. Raman spectroscopy	52
3.4.4 Fourier transform infrared spectroscopy	54
3.4.5. Ultra violet-visible spectroscopy	54
3.5 Diffraction techniques	55
3.5.1. X ray diffraction	55
3.5.2. Electron backscattered diffraction	57
3.5.3. Selected area electron diffraction	58
3.6 Miscellaneous experiments	58
3.6.1. Transfer process	59
3.7. Materials used	59
3.8. References	61
5.0. References	01
Chapter 4. Hexagonal BN synthesized by RF magnetron sputtering	63
4.1. Deposition by radio frequency sputtering	63
4.1.1. Deposition parameters	64
4.1.2. Single step deposition	66
4.1.3. Multiple step deposition	67
4.2. Results and discussion	67
4.2.1. Film characterization	69
4.2.2. Resistive switching properties	77
4.3. Conclusion.	77
4.4. References.	79
Chapter 5. Hexagonal BN synthesized by CVD	81
5.1. Growth and precursor of hexagonal boron nitride	81
5.1.1. Copper substrate preparation.	81
5.1.2 Atmospheric pressure CVD growth from Ammonia Borane	83
5.2. Results and discussion	86
5.2.1. Film characterization	86
5.2.2. Film thickness and morphology variation	92
5.3. Conclusion	95
5.4. References	96
Chapter 6. Applications of CVD grown hBN and its heterostructures	97
6.1 Resistive switching application of CVD grown hBN.	97
6.2 hBN as an electro catalyst in oxygen reduction reaction (ORR)	101

6.3 Heterostructure and MoS <sub>2</sub> /hBN devices	104
6.4 Surface enhanced Raman spectroscopy by using hBN film	105
6.4.1. SERS experiment	108
6.4.2. Discussion and enhancement factor	108
6.5 Conclusion	117
6.6. References	118
Chapter 7. Conclusion and Outlook	122
7.1 Conclusion	122
7.2 Outlook or perspective	123

### Chapter 1

### Introduction

The progress of human civilization is intricately linked to the development of science and technology. The impact of science and technology can be felt in all spheres of human life, from healthcare, agriculture, food technology, communication, travel, energy, and many more. Civilization has always rallied over the availability of better materials, primarily for their uses in different fields. From the very early days, man has always made materials from natural resources, like ironware, copperware, bronze ware, glass, and other numerous types of materials. Since the dawn of human civilization, from the Stone Age, Bronze Age, Iron Age, and finally Silicon Age, the invention of new materials and new processing techniques has been the corner stone of development. The advent of advanced materials in their own respective ages has far-reaching consequences. It not only stirred up the scientific landscape but many times it also had a decisive effect on the respective regional and global geopolitics. For instance the emergence of "gun powder" in the military field accelerated the expansion of Turko-Arabic dynasties in south Asia. The effect of gun powder in cannons was so phenomenal that empires were built upon their strength and were called gun powder empires. This particular material at that age proved to be decisive in battles which shaped the course of history. The past ages are filled with such examples where the emergence of new materials shaped the world. Different materials throughout the ages played such a pivotal role in shaping them that they were named after them, like Stone age, copper age etc. It shall be little to no exaggeration if were to say that the discovery of new materials with exciting properties not only enrich the scientific community but it also proves to be a strengthening factor for the nation which discovers it. Not only the emergence of new material but also emergence of different synthesis and purification techniques also had their fair share in the development civilization. The development of smelting techniques for metal extraction from minerals led to the bronze and iron age, which ultimately led to the industrial revolution. Advancement in the world of quantum physics led to the discovery of electron and transistors which led to the Silicon revolution. With advancement in fabrication technologies transistors as small as few nanometers were produced that increased the operation speed of computers tremendously. Now with miniaturization hitting its physical limit, the possibility of Silicon Age coming to an end is looking real. Scientists are on the hunt for new materials which will satisfy the ever growing needs of electronics and energy industry, machinery, medicine and other associated fields. In this current context two dimensional materials are emerging to fill the void.

Our current thesis work deals with the aspects of physical science, more precisely about the behaviour of materials, their making processes and their applications. Materials science is the branch of the science which deals with the synthesis, fabrication, application and purification of materials. Unlike astronomy, mathematics etc. whose ancestry dates back to millennia materials science has an early origin. With the advancement of science and technology in the last two centuries material science has made a foot hold in the arena of natural sciences. With the passing age material science itself developed into many branches like metallurgy, polymer science, ceramics engineering etc. The latest and most exciting branch comprises of two dimensional materials. Once thought to be a forbidden material <sup>1</sup>, two dimensional materials

came to existence with the discovery of graphene <sup>2</sup>. As the quest for new metamaterials is stronger than before, fuelled by the expansion in electronics and other associate technology sector, two dimensional (2D) materials have opened a new horizon of the targeted application. As the name suggests 2D materials are materials that exist in two dimensions and have an atomically thin layer. Figure 1.1 shows a brief view of the 2D materials family <sup>3</sup>. Broadly they can be classified into four families namely – graphene, black phosphorous, Group-III –IV and transition metal chalcogenides (TMD) family. The transition metal chalcogenides are atomically thin semiconductors combining a transition metal and a halogen. Altogether these 4 types span the whole range of electronic spectrum from insulating 2D materials like hexagonal boron nitride to metals like titanium sulphide.

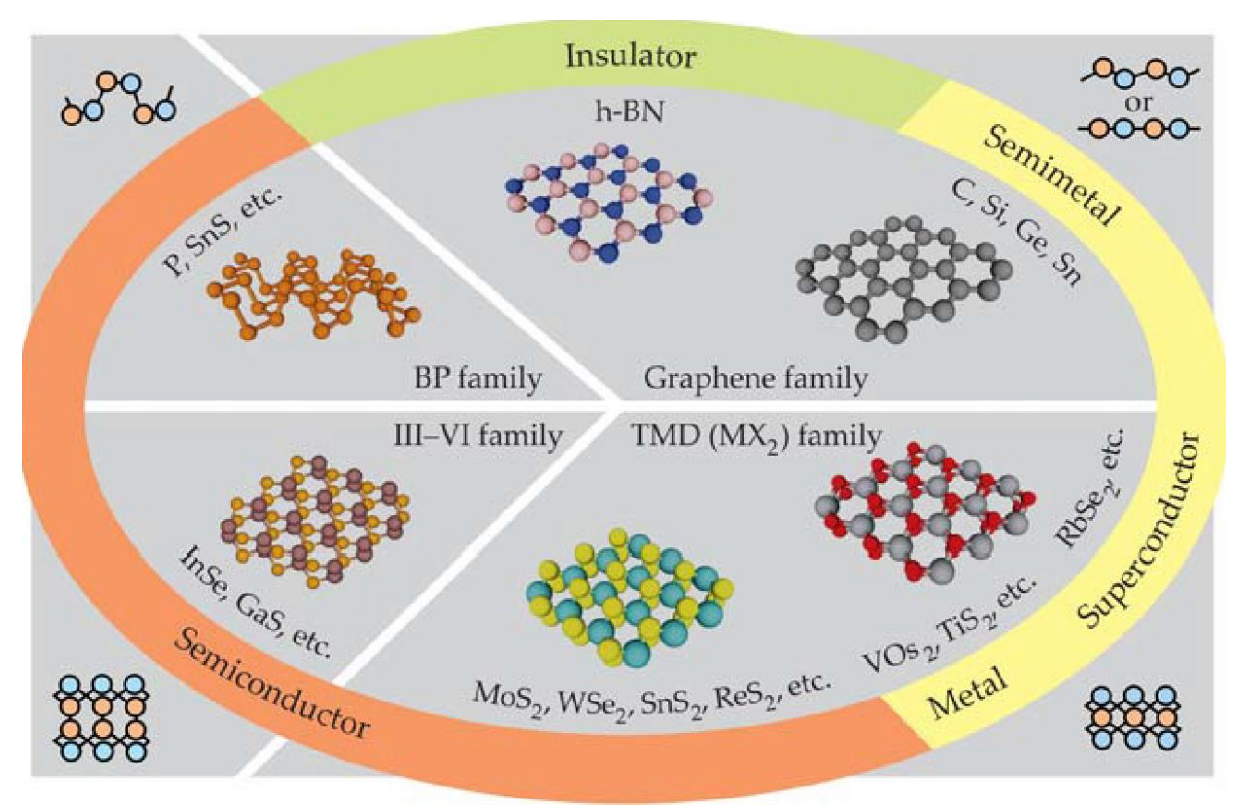


Figure 1.1 Family of two-dimensional materials. Combining all four 2D materials family we get the full range of electronic spectrum <sup>3</sup>.

The interest in two-dimensional materials is not only for their unique properties but also for their unique applicability. Two-dimensional materials have unique properties which are not present in their bulk counterparts, for example, layered dependent nature of band gap; this uniqueness makes them exotic and coveted material to be synthesized. Graphene is the first two-dimensional material to be discovered in 2004 by Geim's group. Pristine monolayer graphene is the strongest material ever tested and conducts electricity 13 times better than copper. The electron mobility of graphene is also 100 times better than silicone. These unique and exciting properties led to its phenomenal popularity; naturally, the majority of research output across a broad spectrum of physics, chemistry and material science is dominated by graphene when compared to other 2D materials. Although the term graphene was coined in 1962 by Boehm and the electronic structure of single-layer graphite has been studied since 1947 but its discovery by isolation of a single layer of graphite through exfoliation is the major

milestone in the research of 2D materials <sup>4</sup>. Figure 1.2 shows the structure of both h BN and graphene <sup>5</sup> at a molecular level.

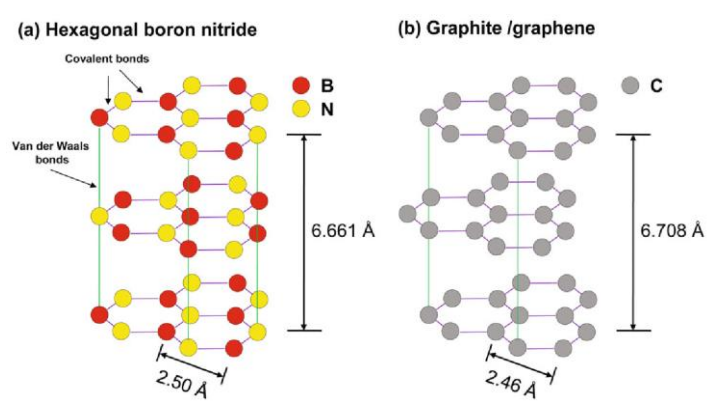


Figure. 1.2 (a) Hexagonal Boron Nitride structure (b) Graphene structure <sup>5</sup>.

This centre stage popularity of graphene didn't overshadow other alike two dimensional materials. Slowly but steadily other 2 dimensional materials like hexagonal boron nitride, phosphene, borophene, silicene, germanene etc. have made their own way to their well-deserved position among the research community. These names are coined to be consistent

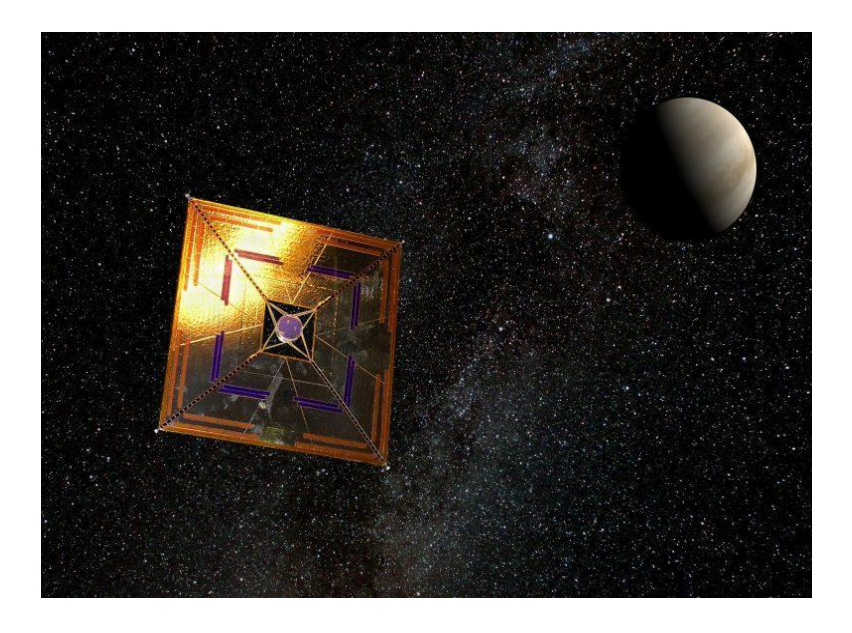


Figure. 1.3 Artists impression of a graphene-based solar sail <sup>7</sup>.

with general nomenclature started with graphene. Silicene is the silicone analogue of graphene and germanene is the germanium analogue of silicene. Graphene and other two dimensional materials like hexagonal boron nitride have the technological potential for a scalable and efficient desalination process <sup>10</sup>. As graphene has very high electron mobility when compared to silicone and also dissipates heat more efficiently it is emerging as a potential candidate to replace silicon in the future electronic industry. Graphene and other two dimensional materials at large have tremendous potential, so much so that this current century might be coined after them. Ideas that didn't have a chance to see light outside paperwork now with the advent of two-dimensional materials have a far better chance to be realized. For example, to achieve

spectacular speed light sail devices were idealized which can travel nearly at 240000 km/hr, about 5 times as high as the speed of any contemporary rockets. But to make the sail no such competent material was available. They are one of the most promising technologies in the field of space propulsion. Figure 1.3 shows one such hypothetical light sail based on graphene, which seems to be possible at least on a small scale in the future <sup>6</sup>. Traditional rocketry requires a heavy amount of fuel for launching, this makes them almost impossible to attain extremely high velocity (fraction of light's speed). Light sail relies on the transfer of momentum when a light photon strikes the sail. As the thinnest material, Graphene is emerging to fill the gap, it has the potential to be the material for a functioning solar sail <sup>7</sup>. Likewise, the application of desalination <sup>8</sup> on large scale is also a major challenge of the current era. Water scarcity around the world is becoming a chronic problem day by day, current desalination processes are too expensive to implement on a wide scale. Apart from these applications 2D materials have a plethora of application, figure 1.4 shows a brief overview of different application of 2D materials like optoelectronics, memory devices, transistors, sensors, LEDs etc <sup>9</sup>.

The major challenge in 2D materials research is to get a scalable synthesis method that can provide us with high-quality materials. The task of getting them from laboratory scale to the large scale market for different purposes is the bottleneck. Every realistic application of any two-dimensional material is totally dependent upon the availability of the material in the market; this, in turn, depends upon the scalable and industrial production of that material. Graphene, hexagonal boron nitride (h BN) and other layered two dimensional materials can be exfoliated from their respective bulk crystal. But exfoliation brings its own challenges like yield is very poor and repeatability is not high. This catered the way to search for other synthesis methods like chemical vapour deposition (CVD), physical vapour deposition (PVD) etc. Most of the graphene or hBN produced for research is through CVD. The trade-off between purity and scalability is the biggest hindrance. If we want to have ultra-pure 2D materials produced by techniques like exfoliation or molecular beam epitaxy then we sacrifice scalability. On the other hand, if we employ considerably large scale production techniques for 2D materials like CVD then evidently we have to sacrifice purity. Finding a most efficient balance between these two is one of the best rewards a researcher can achieve.

This thesis work mostly focuses on hexagonal boron nitride systems. Hexagonal boron nitride is a layered 2D metamaterial that is isoelectronic and isostructural to graphene. Due to its close resemblance with graphene sometimes it is called white graphene. There are four polymorphs namely rhombohedral, wurtzite, cubic and hexagonal boron nitride. The Hexagonal polymorph has a honeycomb lattice with two atoms per unit cell. Owing to its distinct properties like high thermal stability, deep ultraviolet lasing, high thermal conductivity etc. hBN systems has gained quite a lot of attention from the research community. It is an excellent substrate for graphene-based electronics and its high thermal conductivity makes it an ideal candidate for a heat-dissipating layer in nanoelectronic devices. Hexagonal boron nitride has made its way in other diverse fields of application like in desalination of saltwater, resistive switching, SERS, plasmonics study, nuclear detector and many more. Thus the current scenario propels for the hunt for synthesis techniques that are facile and scalable and at the same time provide as much purity as possible.

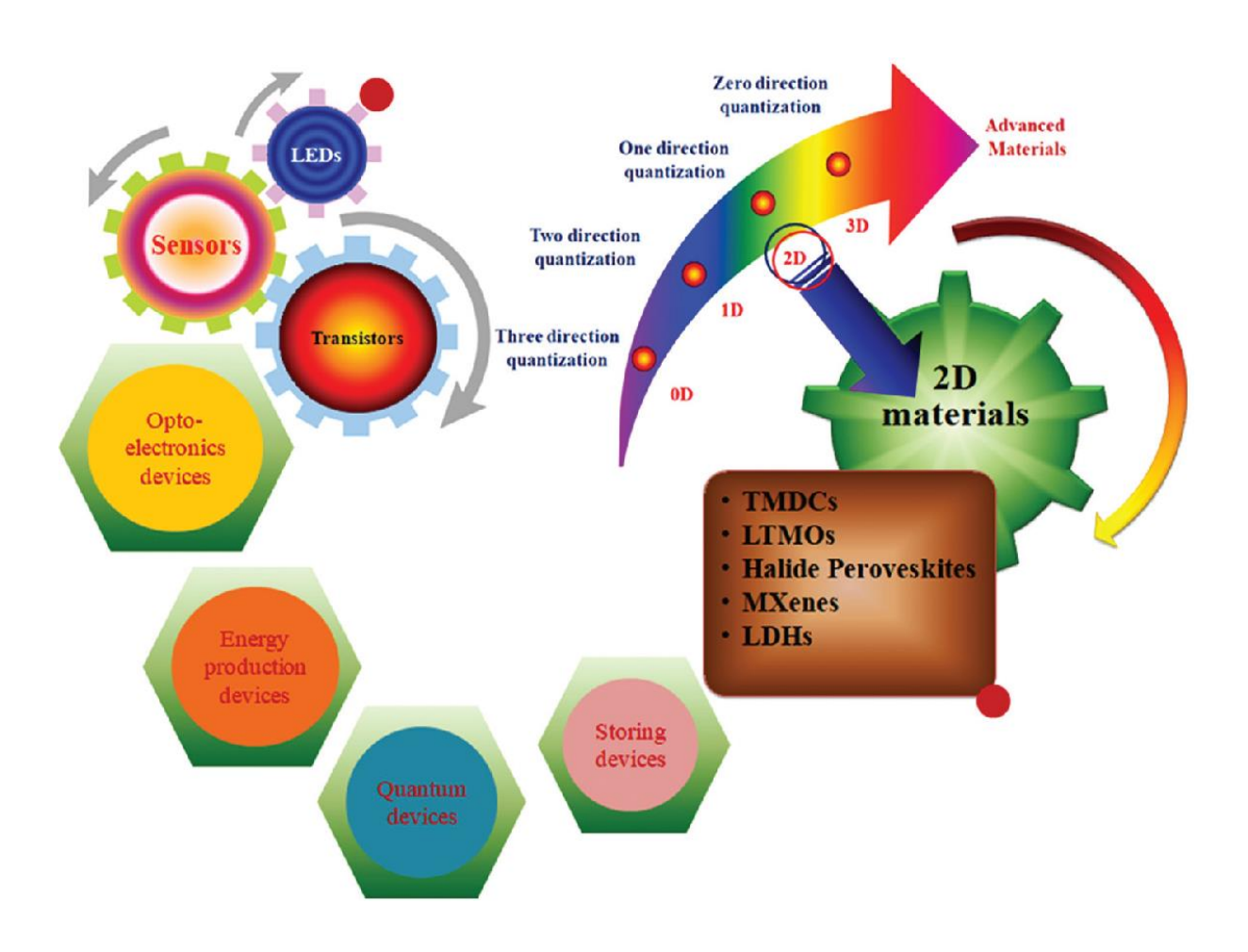


Figure. 1.4 Different applications of two-dimensional materials 9.

CVD is readily used for the synthesis of h BN. PVD methods like magnetron sputtering and pulsed laser deposition have also been applied for their synthesis. Facile synthesis of hBN is still a challenge, although CVD is a scalable technique it provides many challenges like a hazardous precursor, difficulty to control growth parameters and thickness of the film. Sputtering is simpler and easy to control process which is scalable and fits to industry standard. In this work, we have taken the challenge to synthesis hBN by radio frequency magnetron sputtering which is more scalable and easy to control and also by using atmospheric pressure chemical vapour deposition. The motivation of this work is to establish an easy and scalable synthesis method of hBN by sputtering technique and at the same to synthesis hBN by APCVD method for surface-enhanced Raman spectroscopy and other applications. The focus is to elucidate different aspects of both the synthesis techniques with respect to the hBN system. Application of the synthesized film is also a major portion of the thesis work where resistive switching and SRRS occupies major attention. The novelty of the work lies in the application of a few-layer hBN in SERS application for different organic dyes and also in the synthesis of hBN by radio frequency magnetron sputtering over the copper foil. Our motivation for this work is to achieve an easy synthesis route and at the same time exploiting the present synthesis process to harness the various applications of h BN. We have also indulged ourselves in fabricating trilayer of 2D materials by a micromanipulator.

The thesis work is organised into seven chapters. It begins with an introduction followed by an extensive and thorough literature survey and experimental details. Other subsequent chapters

are dedicated to the synthesis, characterization and application of hBN by sputtering and APCVD. The final two chapters are dedicated to the application of hBN and the conclusion of the thesis work. Chapter 2 i.e literature survey extensively deals with the recent development in synthesis techniques of two-dimensional materials at large with h BN in focus. It also elaborates contemporary research over aspects like characterization, application, defects and heterostructure of hBN and other related 2D materials. Chapter 3, which is experimental details talks about the experiments that were undertaken during the synthesis of hBN and as well as during the characterization and application of the film. Each experimental technique has been elaborated by mentioning its working principle accompanied by a suitable diagram, brief working procedure and efficacy regarding the thesis work. We have tried to incorporate handson details of characterization techniques as well as synthesis routes used.

The two middle chapters that are chapter 4 and chapter 5 are dedicated to the experimental results from hBN synthesis by both r.f sputtering and APCVD. The 25-micron thick copper foil has been used as a substrate for the growth of hBN and has been studied extensively and the results are presented in these chapters. Chapter 4 is about the synthesis of h BN by sputtering. Where we studied the role of the surface orientation of the copper foil over the synthesis of h BN by the r.f sputtering method. The surface orientation of the copper foil was investigated by electron backscattered diffraction. A thorough and comprehensive investigation regarding the dependence of the synthesis of a particular phase of BN over the surface orientation of the copper has been the prime motivation. The as-synthesized film by radio frequency magnetron sputtering was transferred to different dielectric substrates to elucidate its different properties. We performed Raman spectroscopy, XPS. SEM and AFM imaging over these samples. Also, other spectroscopic studies like FTIR, UV-Vis have been done. Resistive switching properties of the synthesized film have also been studied by using conductive AFM. The synthesis of h BN by sputtering is heavily dependent upon the substrate preparation process. Annealing of the copper foil after thorough cleaning and electropolishing in a different environment has been done. The thesis work also extensively deals with copper annealing and electropolishing. Annealing in the total inert atmosphere of Argon and in reducing atmosphere in both suspended and non-suspended position has been done. The effect of electropolishing over synthesis has also been recorded.

In chapter 5, we present the results of different thicknesses of hBN grown in CVD. The synthesized film was subjected to an array of characterization techniques. Surface properties, structural properties, and stoichiometric properties have been investigated. Wrinkle formation, wrinkle thickness, and coverage of the film over the copper substrate have been studied by AFM and SEM. Selected area electron diffraction was done to examine the crystallinity of the film. To confirm the stoichiometry, XPS was done.

Surface-enhanced Raman spectroscopy using two-dimensional materials is an emerging field. 2D materials in many respect has a greater edge than conventional materials used for SERS (surface-enhanced Raman spectroscopy). Graphene, nitrogen-doped graphene, hexagonal boron nitride, etc. has proved to be a resilient and effective SERS substrate for an array of probe material. In our thesis work, the synthesized film has been applied to enhance the Raman signal of different organic molecules like Methylene blue, malachite green, crystal violate, etc.

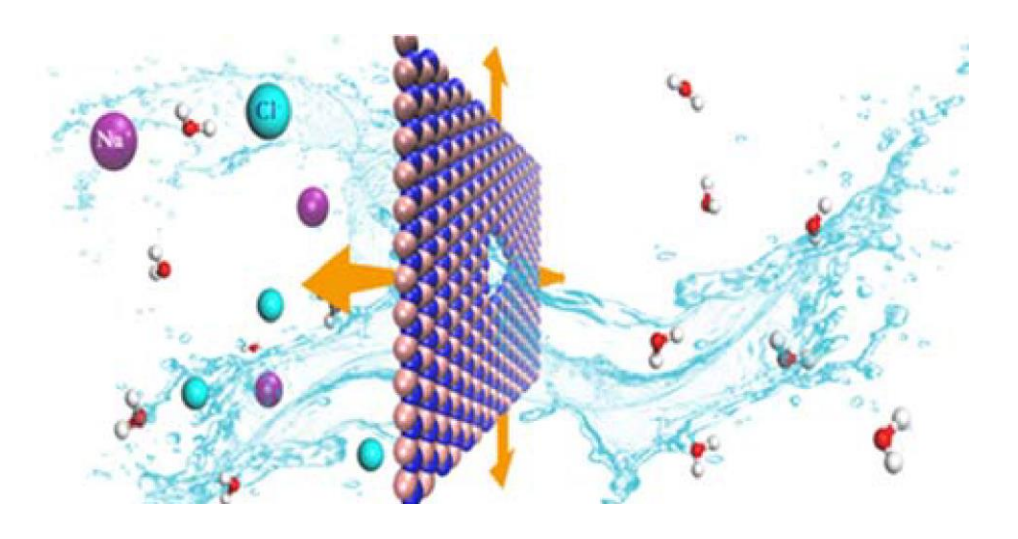


Figure. 1.5. Hexagonal boron nitride membrane as a desalination layer 8.

Film of different thicknesses with and without wrinkles was subjected to SERS experiments to see their effect on the enhancement factor. We wanted to have a comprehensive understanding of the nature of enhancement, its relation with the film morphology, thickness, and grain size. Hexagonal boron nitride is known to exhibit current-voltage hysteresis. To gain an understanding of this aspect of our synthesized film, we examined the resistive switching properties of the film by using conductive atomic microscopy. Chapter 6 describes these applications of the CVD grown hBN film along with studies about the role of hBN in oxygen reduction reaction and hBN heterostructures. The oxygen reduction reaction is important in a fuel cell in which catalyst is used to increase the cathode current. hBN is emerging to be an excellent electrocatalyst that can replace conventional catalysts like platinum. The heterostructure of 2D material has exciting applications in the fields of electronics, photonics and other associated fields. MoS<sub>2</sub>/hBN heterostructure has been fabricated to study the encapsulation properties of hBN in photocurrent generation of MoS<sub>2</sub>. The thesis work concludes with the last chapter, which is the conclusion of the work undertaken in the doctoral program. It also depicts the future scope of the work in various field for different applications.

### **References:**

- 1. Search, S. *et al.* U. Manchester's Andre Geim: Sticking with Graphene For Now. 1–5 (2008).
- 2. Meyer, J. C. *et al.* The structure of suspended graphene sheets. *Nature* **446**, 60–63 (2007).
- 3. Ajayan, P., Kim, P. & Banerjee, K. Two-dimensional van der Waals materials. **38**, (2017).
- 4. Applications, P. TWO-DIMENSIONAL MATERIALS.
- 5. Kim, K. K., Kim, S. M. & Lee, Y. H. A New Horizon for Hexagonal Boron Nitride Film. **64**, (2014).
- 6. Produ, N. One Atom Thick Graphene Light Sail Could Speed Journey to Other Star Systems Clever Trick Allows Precision Measurement of Exoplanet Surprisingly High Density Challenges Planet Formation Theories. (2020).
- 7. Matloff, G. L. Graphene: The Ultimate Interstellar Solar Sail Material? *Jbis* **65**, 378–381 (2012).
- 8. Gao, H., Shi, Q., Rao, D., Zhang, Y. & Su, J. Rational Design and Strain Engineering of Nanoporous Boron Nitride Nanosheet Membranes for Water Desalination. (2017) doi:10.1021/acs.jpcc.7b06480.
- 9. Khan, K. *et al. dimensional materials and their applications*. (Royal Society of Chemistry, 2020). doi:10.1039/c9tc04187g.
- 10. Chen, Y., Gong, X. L. & Gai, J. G. Progress and Challenges in Transfer of Large-Area Graphene Films. *Adv. Sci.* **3**, 1–15 (2016).

### Chapter 2

### Literature survey

### 2.1 Introduction to two dimensional materials.

Two-dimensional materials are crystalline materials that consist of only one layer of atoms, for this reason sometimes they are referred to as single-layer material. After the discovery of graphene in 2004, the list of two dimensional materials has kept on increasing. The earliest discovery of Mxene was reported in 2011<sup>1</sup>. About 700 two-dimensional materials are predicted to be stable in ambient conditions, although most of them are yet to be synthesized <sup>2</sup>. The global market for two materials is booming in recent days and is expected to reach 4000 crore Rs by 2025. Most market activities are based on graphene-based applications or 2D materials aiding graphene research.

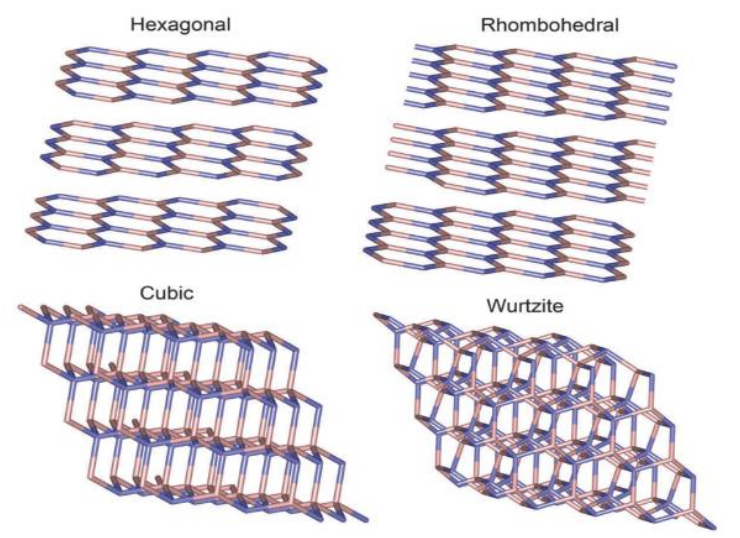


Figure. 2.1 Structures of Hexagonal, rhombohedral, cubic, and wurtzite BN <sup>3</sup>.

### 2.1.1. Hexagonal Boron Nitride and its allotropes-

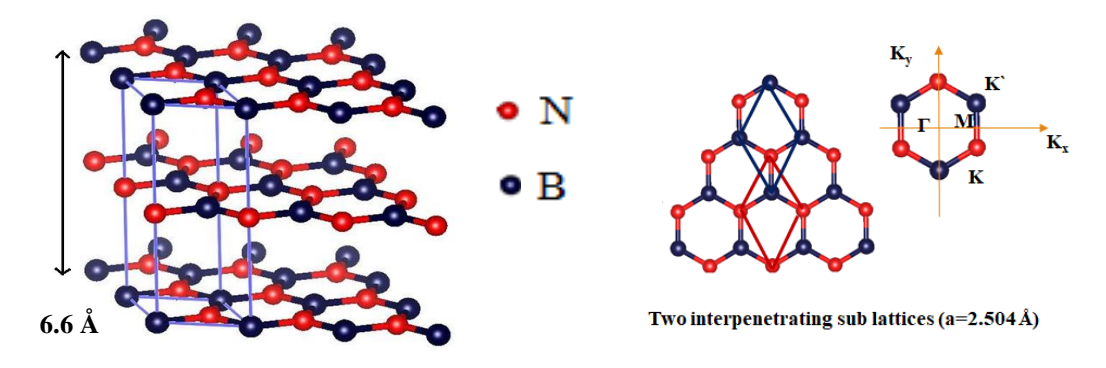


Figure. 2.2 Three layers of h BN and two interpenetration lattices.

Hexagonal boron nitride (hBN) is a 2D material with a high band gap of 5.9 eV it has another three polymorphs, namely wurtzite, cubic and rhombohedral. Cubic boron nitride (cBN) is a dense phase where B and N atoms have sp<sup>3</sup> hybridization. cBN structure is similar to zincblende

structure and sometimes cBN is referred to as zincblende BN. Cubic boron nitride is stable in ambient conditions and also in high-pressure conditions. Wurtzite BN is also sp<sup>3</sup> bonded like cBN but in the ambient condition it is metastable and at high temperature and high pressure it is thermodynamically stable <sup>4</sup>. The other two phases of BN namely rhombohedral and hexagonal boron nitride has sp<sup>2</sup> hybridization. Their structure differs only by the difference in stacking. Naturally occurring graphite has Bernal (AB) stacking, whereas hBN is synthetic and almost all synthesis methods produce AA' stacking. In AA' stacking Nitrogen atom stays directly above the Boron atom and vice versa. Whereas rhombohedral BN or rBN has ABC stacking. Figure 2.1 shows the atomic structures of four polymorphs of BN ranging from hexagonal BN to wurtzite BN.

**hBN structure-** Hexagonal boron nitride is a metamaterial which means that it doesn't occur in nature, only synthesized. hBN exists in all modes like in 2D, 1D, and 0D. Figure 2.2 shows three layers of h BN stacked in AA' configuration, these interlayers are held by weak Vander Waals forces.

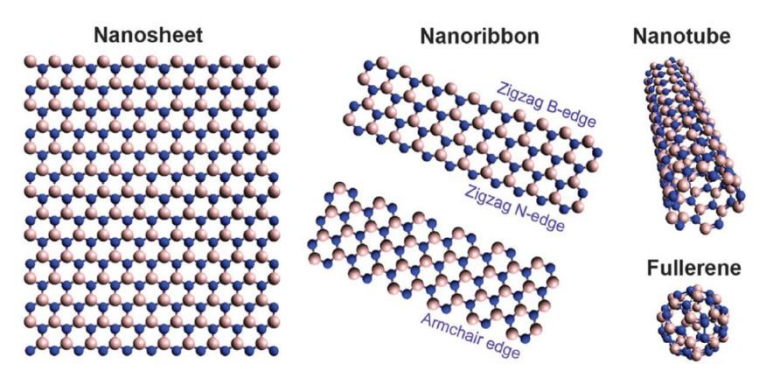


Figure. 2.3 Hexagonal boron nitride in 2D, 1D, and OD modes <sup>3</sup>.

The separation between two consecutive layers is 3.3 Å. The planar structure of hBN is similar to that of graphene, both having hexagonal lattices with 2 atoms per unit cell. Figure 2.3 shows different structures of h BN in different forms<sup>3</sup>. Both armchair and zigzag edges can be seen at the edges of BN nanosheets. The lattice mismatch between graphene and hBN is about 1.8% (lattice constant of hBN-0.250 nm and for graphene 0.246). The B-N bonds have a bond length of 0.144nm (for graphene it is 0.142nm). The AA' stacking in hBN arises to satisfy the polar-polar interaction which also known as lip-lip interaction<sup>5</sup>. In AA' stacking the adjacent layers have alternate B and N atoms. When compared to C-C bonds in graphene the B-N bonds are partially ionic in nature. This makes interlayer interaction more strong in hBN than in graphitic materials. The enhanced interaction between the B-N atoms and also the fact that the B-N bond is more energetically stable creates a metastable energy minimum which reduces the number of dangling bonds.

**hBN properties-** Hexagonal boron nitride is an indirect band gap material, with a band gap of 5.955 eV<sup>6</sup>. Although it is generally accepted as an indirect band gap material but many reports have suggested it has a direct band gap <sup>7,8</sup>. Two photon spectroscopy has revealed photon-assisted transition in multilayer hBN <sup>6</sup>. But monolayer hBN is believed to be a direct band gap material <sup>9</sup>. The current general consensus is that monolayer hBN has a direct band gap and indirect band gap for thicker ones. Figure 2.4 describes the Brillouin zone of multilayer hBN, where the B and N atoms reside at alternate K points <sup>9</sup>. Figure 2.5 shows the evolution of band

structure in hBN from monolayer to bulk, which has been calculated by using the Vienna Abinitio simulation package. The valence band maximum occurs at the K point and the conduction band minimum occurs at the M point. The band gap of 5.955 eV gives rise to an optical absorption peak centered at 203 nm  $^{10}$ . Although the nature of the band gap changes from monolayer to bulk, there is no considerable change in it's value. Owing to this high electronic band gap the room temperature resistivity of multilayer hBN is  $10^{11}\Omega$ cm, the order of resistivity has no significant change for mono layer.

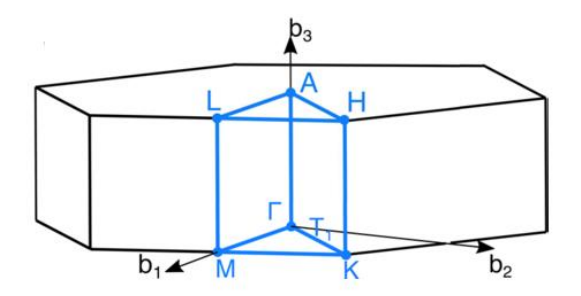


Figure .2.4 Brillouin zone in multilayer hBN 9.

Figure 2.6 shows the phonon dispersion relation in multilayer h BN  $^{12}$ . Both the acoustic (ZA, LA, TA) and optical phonon modes can be seen (ZO, LO, TO). Each phonon mode has been represented by its irreducible representation. The LO and TO phonons are responsible for the Raman G mode which is due to the  $E_{2g}$  vibrational mode of h BN. The  $E_{2g}$  vibrational mode is centered at 1366 cm $^{-1}$  (Stokes), in this mode, the boron and the nitrogen atoms move in the opposite directions in the same plane.

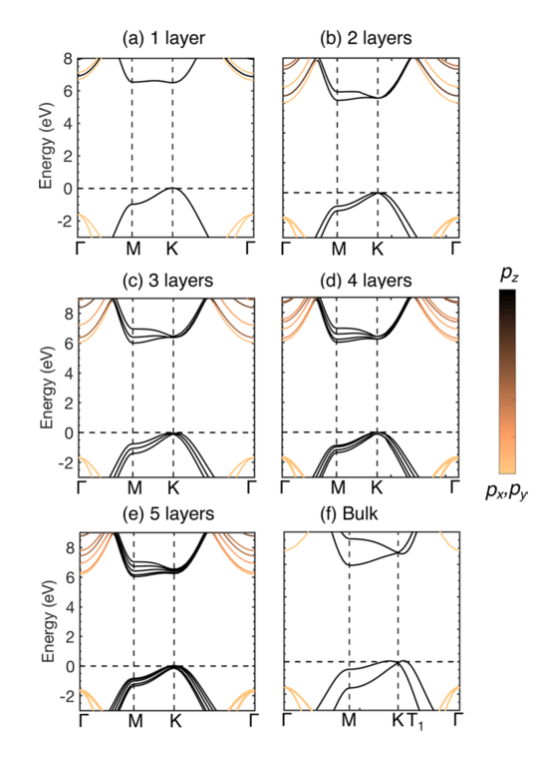


Figure .2.5 Electronic band structure of monolayer to bulk in hBN in AA' stacking (a-f). The colour of the band structure signifies the  $p_z$ ,  $p_x$ , and  $p_y$  character of the states  $^9$ .

Apart from this mode of vibration, there are two Raman active modes which are centered at  $-52.5 \text{ cm}^{-1}$  (anti-Stokes) and  $52.5 \text{ cm}^{-1}$  (Stokes), these modes also have  $E_{2g}$  symmetry but they arise due to interlayer shearing forces<sup>13</sup> (with 514.5nm laser excitation).

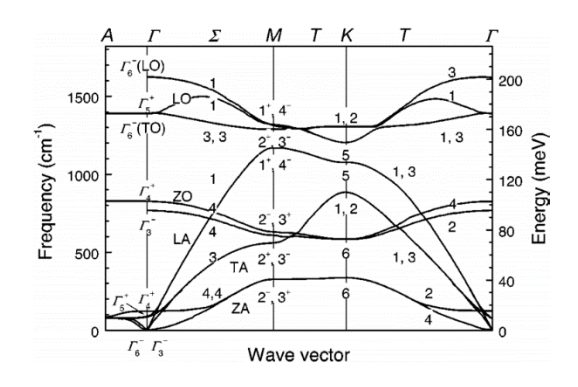


Figure 2.6. Phonon dispersion relation in hBN <sup>12</sup>.

Figure .2.7 shows the vibrational modes along with the Raman peaks in the case of a few-layer h BN  $^{13}$ . The most intense Raman mode is the  $E_{2g\,in}$  plane mode. The lower wavenumber modes are less intense when compared to the in-plane mode. This signifies that interplanar interaction in hBN is much weaker than in-plane interaction. And also the fact that unlike graphene or other TMDCS for hBN when the excitation wavelength is visible range resonant Raman condition is not achieved. As a result, the interlayer shearing mode is very faint when compared to the in-plane mode. Raman band shifts have been observed in hBN when transiting from monolayer to bulk. It has been reported that the in-plane  $E_{2g}$  peak of monolayer hBN is centered around 1372 cm $^{-1}$ , which is an upshift of about 6 cm $^{-1}$  from the bulk hBN $^{14,15}$ . This shift is generally due to the substrate-induced strain.

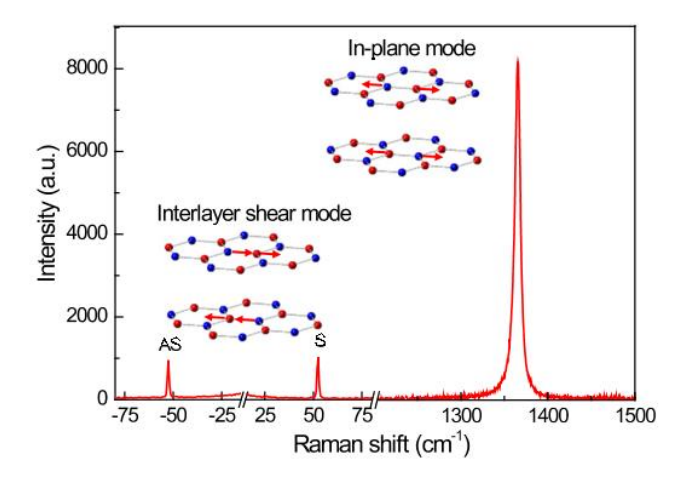


Figure .2.7. Raman spectrum of few-layer hBN <sup>13</sup>.

Hexagonal boron nitride has anisotropic thermal conductivity. The planar thermal conductivity ( $\kappa$ ) is 550 W/mK whereas for out of the plane it is 5W/mK<sup>16,17</sup>. For monolayer hBN, the  $\kappa$  value is 751 W/mK which is higher when compared to bulk hBN. For multilayer or bulk hBN, the increased interlayer interaction splits phonon branches, this creates more states for Umklapp scattering as a result the thermal conductivity decreases. Like in graphene the phonon modes

of ZO, LO, and TO don't contribute to the thermal conduction process. The major contribution arises from the (z-axis acoustic) ZA mode. Figure 2.8 shows the evolution of thermal expansion coefficient (TEC) from  $0^{\circ}$ C to  $1000^{\circ}$ C for 1-3 layer hBN<sup>17</sup>. Initially, the TEC was negative but it started to rise after  $550^{\circ}$ C. The negative thermal coefficient is one of the reasons for wrinkle formation in hBN synthesis in a CVD.

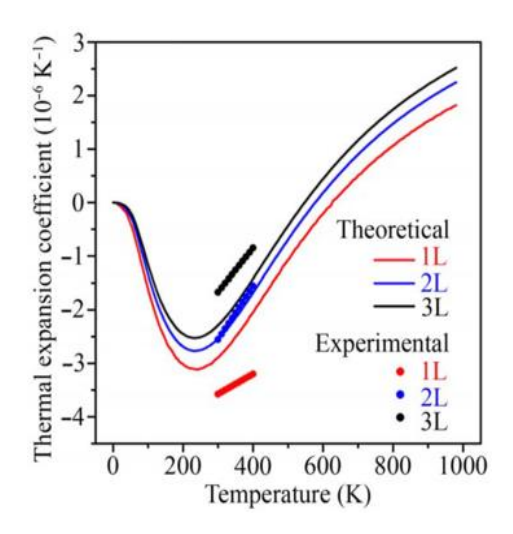


Figure .2.8 Theoretical and experimental thermal expansion coefficient of 1-3 layer hBN at different temperatures <sup>17</sup>.

Hexagonal boron nitride has a Young modulus of 0.865 TPa and fractures strength of 70.5 GPa <sup>18</sup>. The young modulus of standard construction A36 steel is about 200 GPa, which is about 4

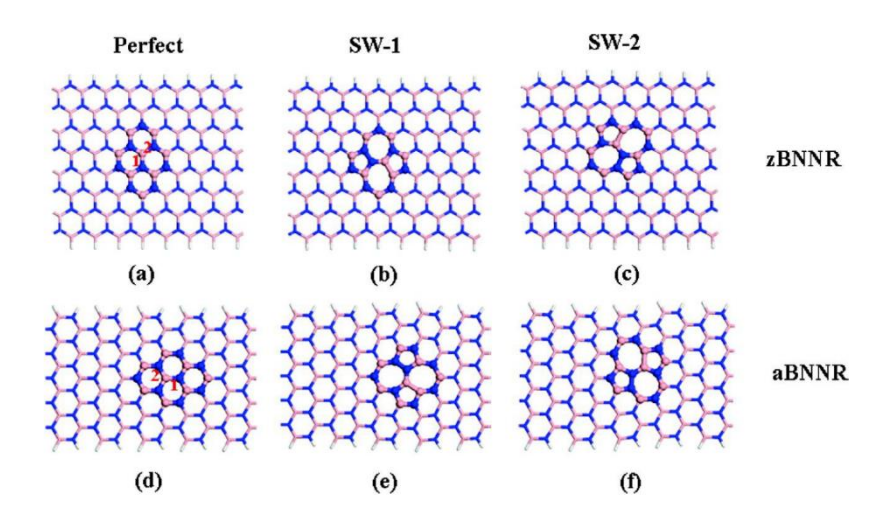
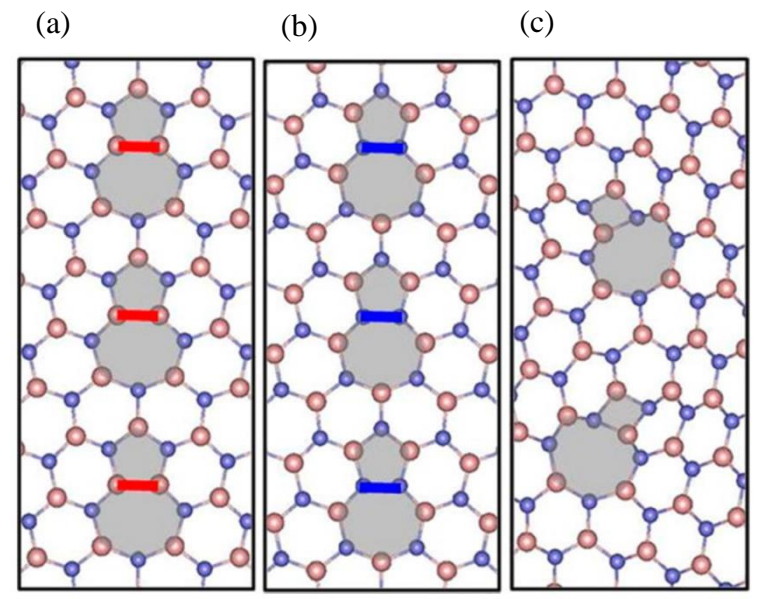


Figure .2.9 Two types of Stone-Wales defect in the armchair and zigzag edge hBN 19.

times less than that of hBN <sup>20</sup>. The strength remains constant up to 9 layers, which is in contrast with graphene. In graphene, the strength decreases with an increase in the number of layers. This is due to the difference in interlayer interaction. In graphene, the layers tend to slide when being indented but the hBN layer was glued at their position.

Defects in hBN- Pure hBN with no defects have astonishing mechanical and thermal

properties, but almost all synthesis techniques induce some sort of defects. Although defects are undesirable they have some specific applications in many fields. Like V<sub>N</sub>C<sub>B</sub> defects in hBN nanosheet are being explored for the source of single-photon emitters<sup>21</sup>. Stone-wale defects-Point defects originate in hBN and are known as Stone-Wales (SW) defects, in which point vacancies of either B or N give rise to pentagons and heptagons in the BN mesh. There are two types of B-N bonds in zBNNR and aBNNR, one is parallel to the axis and another is



perpendicular to the axis. Due to this fact, there are two types of SW defect namely SW1 and SW2.

Figure. 2.10 Grain boundaries, a) & b) polar grain boundaries with N rich and B rich respectively 5/7 construction. c) Nonpolar grain boundaries with 4/8 construction <sup>22</sup>.

Figure 2.9 shows two types of SW defect in both zBNNR and aBNNR. SW defects induce

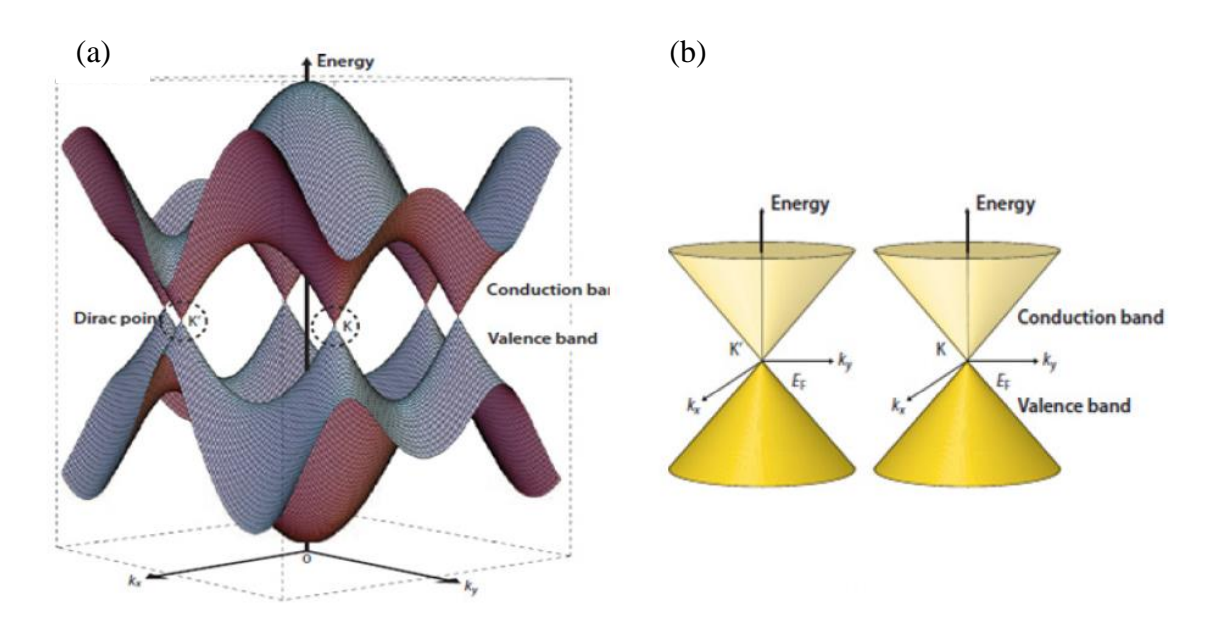


Figure .2.11 a) K and K' wave vectors at two sublattices. & b) Linear energy spectrum <sup>23</sup>.

structural deformation in the BN mesh, the B and N atoms are posed minutely outward plane. The site of SW defects is more reactive than the defects-free BN mesh. It also decreases the band gap of the defected species drastically, although the BN mesh is still a high band gap material. Defects also arise from dislocation and grain boundaries. Grain boundaries form because of the meeting of two grains that were propagating on a different growth route. The grain boundary may be polar or non-polar. If B: N=1 then the GB is nonpolar but may give rise to a 4/8 structure. The energy of dislocation in BN consists of topological strain and homoelemental bonding. 5/7 have homoelemental bonding with lower strain and 4/8 (figure 2.10 a-c) has no homoelemental bonding but has higher strain energy<sup>22</sup>. The formation of polar (B rich or N rich) or non-polar grain boundary depends upon the tilt angle between the grains.

**2.2.** Unique physics about 2D materials- In many cases two dimensional materials differ significantly from their bulk counterparts. The following are a few unique and exciting physical properties that are observed in 2D materials.

Linear dispersion relation in graphene- Graphene is zero band gap two-dimensional material which is described by a Dirac like Hamiltonian  $H=-i \hbar v_F \, \sigma \nabla$ , where  $v_F$  is the Fermi velocity and  $\sigma$  is the Pauli matrices. The charge carriers in graphene are not described by the usual Schrodinger-like wave equation rather by Dirac-like Hamiltonian is because of its crystal structure. Graphene structure consists of two interpenetrating subtleties A and B. Two energy bands are formed due to quantum mechanical hopping between these sublattices. Their intersection near the periphery of the Brillouin zone gives rise to a conical energy spectrum (Figure .2.11 shows the two wave vectors at two sublattices and the conical energy spectrum  $^{23}$ ). As a result, the quasiparticles in graphene behave like massless relativistic particles with linear dispersion relation of  $E=\hbar K v_F$ . This linear dispersion relation makes graphene special as generally, quasiparticles in semiconductors and metals have a parabolic energy spectrum  $^{24}$ .

Van Hove singularity- Van Hove singularity is a density of state singularity in which the density of states diverge <sup>25</sup>. This happens at the six M points in the Brillouin zone. The singularity has been found to have a direct correlation with the geometry, size, and edge profile of the structure. Moreover, it has also been reported that this singularity can withstand structural asymmetry by any vacancy <sup>26</sup>.

### 2.3. Synthesis techniques of 2D materials.

The fruits of hexagonal boron nitride can only be cherished if we have a reliable and scalable synthesis technique. There are many ways to synthesize hexagonal boron nitride nanosheets. Each of them has its pros and cons. In this section, we will discuss different synthesis methods available. Mainly the synthesis method can be divided into two branches, one is bottom-up synthesis and another one is top-down synthesis. In bottom-up synthesis hBN sheet is grown by assembling Boron and Nitrogen molecules whereas in top-down synthesis bulk hBN sheet

is broken down to get an ultrathin h BN sheet. Each one has their trade-off but is applicable for different fields.

**2.3.1. Bottom up synthesis techniques:** - In a comparison of the two techniques bottom-up technique is more suitable for and fitted for scalable production of 2D materials or hBN. The following are the major bottom-up synthesis techniques-

**Physical Vapor Deposition**- Physical vapour deposition is a line of sight deposition where molecules or monomers are ejected from the precursor material and deposited over the substrate. Hexagonal boron nitride has been synthesized by various PVD methods like by r.f and d.c spattering, by pulsed laser deposition, ion beam sputtering, and e beam evaporation method. Transition metals like Ru (0, 0,1), Ni, Rh (111), Au (111), and Cu have been used for the growth of hBN by PVD methods <sup>27,28,29,30,31</sup>. David *et al* employed reactive r.f magnetron sputtering to synthesize hBN over Ni substrate <sup>32</sup>. They observed the growth rate by varying the r.f power from 10W to 200W by negative biasing the substrate. Negative biasing has a positive effect on the growth rate. Reactive sputtering i.e the introduction of nitrogen along with argon is instrumental in maintaining the 1:1 (B: N) stoichiometry in hBN. Sputtering synthesis of hBN employs radio frequency as d.c sputtering is not possible with Boron or h BN targets.

The lattice mismatch between hBN and the substrate plays a crucial role in its synthesis. Uniform 1x1 hBN can only be grown over substrates with less than 0.5% lattice mismatch <sup>33</sup>. Substrates like Au (111) have a lattice mismatch of 14% with h BN. L Camilli *et al* have deposited h BN over Au(111) by r.f magnetron sputtering, where the registry is (8x8)Au/(9x9)BN <sup>33</sup>. hBN has also been deposited over the AIN template by pulsed sputtering by using Fe as a catalyst. Although the lattice mismatch (a for AIN= 0.311 nm, a for h BN=0.025 nm) is 19.6 % between AIN and hBN <sup>34</sup>. The iron catalyst is removed after BN growth by wet etching. Figure 2.12 shows the schematics of the growth <sup>34</sup>.

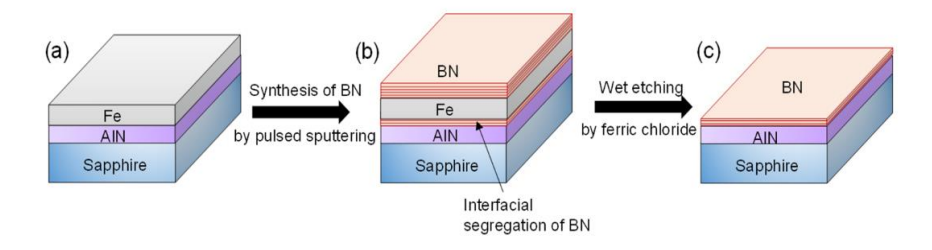


Figure .2.12 Steps of synthesis of hBN over AIN by pulsed sputtering <sup>34</sup>.

Ion beam sputtering (IBS) has also been employed to synthesize hBN over substrates like Cu and Ni<sup>31,35</sup>. Haolin wang *et al* employed two independent Kaufmann ion sources for the synthesis, one for the target and another one for the Ni substrate <sup>36</sup>. They achieved h BN domains whose sizes are comparable with CVD-grown ones. 1.0 KeV Ar ion source has been used in most IBS deposition of h BN. Pulsed laser deposition of hBN has been carried out by some groups. Nicholas *et al* have deposited hBN over highly ordered pyrolitic graphite (HOPG) and sapphire (001)<sup>37</sup>. Fiber-oriented Ag(111)/SrTiO3 (001) has been used as a substrate for PLD synthesis of h BN <sup>38</sup>. There is no successful study of large area hBN film growth over transition metals by PLD. Substrates used for the PLD growth of hBN have drawbacks when it comes to transferring the film. This is a deterrent to use PLD to obtain h BN for application purposes. Although there have been successful attempts in synthesizing h

BN via PVD methods, it is still not the popular choice among researchers. This is because PVD methods like IBSD, PLD require complex machinery and high to ultrahigh vacuum for their operation. And the synthesis process is difficult to reproduce or replicate. Among all PVD methods, r.f magnetron sputtering is the most studied synthesis process. The major advantage of r.f sputtering is that it is highly scalable and doesn't deal with as many variables as in PLD or IBSD.

Chemical Vapor Deposition- Perhaps the most popular synthesis method for large-scale hexagonal boron nitride is via chemical vapour deposition. The first known study of synthesizing boron nitride nanosheets was published in 1968, where they used diborane and ammonia as precursors<sup>39</sup>. Substrates like Si, Ta, Mo, Ge, and fused silica were used for deposition at temperatures ranging from 600-1080°C. CVD synthesis of hBN employs either single-source precursors where B and N are both present or two precursors which separately contain B and N. Most common single-source precursors are ammonia borane, borazine, and borazine. Borazine is toxic and most difficult to handle<sup>40</sup>. Ammonia borane is the safest single-source precursor to use. Which is not toxic and can be stored at ambient conditions. Common pairs of separate precursors which provide B and N are BF3-NH<sub>3</sub>, BCl<sub>3</sub>-NH<sub>3</sub>, B<sub>2</sub>H<sub>6</sub>-NH<sub>3</sub>. The use of a single precursor is a lot less cumbersome. CVD growth of hBN can be further categorized into the working pressure during growth. Which are as follows:

Low-Pressure CVD- hBN has been successfully grown at various low-pressure environments and as low as at 10<sup>-7</sup> mBar pressure <sup>41</sup>. Generally, a rotary pump in conjugation with an ion pump or turbomolecular pump is used to achieve such low pressure. Single sources like ammonia borane or multiple precursors can be used for this synthesis method <sup>42,41</sup>. The advantage of synthesizing hBN at UHV is that the obtained crystallinity of the film is of better quality. But

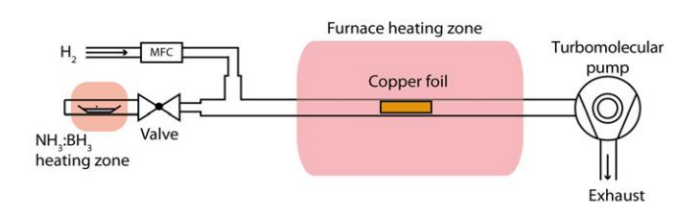


Figure. 2.13- Schematic diagram of a low-pressure CVD for h BN growth 41.

at UHV, film growth is not scalable and only 1-2 layer thick hBN can be grown. Nonetheless, hBN films grown at UHV conditions have less contamination when compared to films grown at  $10^{-3}$  mBar pressure. At  $10^{-3}$  mBar pressure the backflow of hydrocarbons from the rotary pump is more evident. These hydrocarbons can contaminate the hBN film<sup>43,44</sup>. Figure 2.13 shows the schematic diagram of UHV CVD, where a turbo molecular pump has been used to achieve  $10^{-7}$  mBar pressure<sup>41</sup>.

Atmospheric CVD- Atmospheric pressure CVD or APCVD implies the growth of hBN at ambient pressure though in a reducing atmosphere. Generally, a mixture of Argon and Hydrogen is used as the ambient gas. There are several advantages associated with the APCVD growth of hBN. It is easier to set up which doesn't require any complex pumping arrangements.

The absence of any pumping system irradiates the possibility of any contamination from the hydrocarbon backflow of the pumps. As there is no vacuum, a less expensive mass flow meter can be used which doesn't have to withstand a high differential pressure. But there are several drawbacks associated with the APCV growth of hBN. Like deposition rate is high which is detrimental in achieving high-quality crystallinity. Also synthesizing 1-2 layers is difficult in an APCVD. The gas flow effect is more evident in an APCVD when compared to LPCVD<sup>45</sup>. Maintaining a streamlined flow is difficult in APCVD, turbulence in the gas flow can have ill effects on the growth. LPCVD on the other hand doesn't suffer from this type of problem. Nevertheless, there have been many reports of successful synthesis of large-area hBN over different transition metals via APCVD <sup>46,47</sup>. Majharul *et al* synthesized hBN over liquefied Cu by using Ammonia Borane powder as a precursor. Where they formulated a way to reduce cracks that originate in APCVD <sup>48</sup>.

Atomic Layer Deposition-\_The successful synthesis of 2D materials like MoS<sub>2</sub> and WS<sub>2</sub> by atomic layer deposition made the way for the synthesis of hBN via this process. ALD has several advantages over CVD, like low-temperature growth at 250-300°C, high uniformity, and greater control over thickness<sup>49</sup>. Precursors used in CVD processes like ammonia borane are not used in ALD. Precursors like tris(ethylmethylamino) borane (TEMAB, C<sub>9</sub>H<sub>24</sub>BN<sub>3</sub>), and trichloroborazine (TCB) are used for ALD growth. The precursor handling in ALD is completely different from that of CVD. These precursors must satisfy certain conditions like thermal stability, inertness towards each other (when multiple precursors are used), and sufficient vapour pressure <sup>50</sup>. These restrictions over the choice of precursor and the inherent complexity of the ALD process didn't make it the popular choice for large-scale synthesis of hBN.

**Molecular Beam Epitaxy-**Molecular beam epitaxy has been applied to the synthesis of a few-layer h BN over many transition metals like Ni and Co<sup>51</sup>. Owing to its UHV growth conditions the h BN film has superior crystallinity and very little impurity. In situ characterization is also easier to perform in an MBE chamber. Furthermore, the growth of hBN in CVD is self-limited, as the catalytic activity of the substrate decreases with the growth. This is not the case with MBE, the hBN growth in MBE is not self-limited <sup>52</sup>. Many groups have reported the wafer-scale synthesis of hBN via MBE. Despite its positive accountability on various fronts of hBN growth, the process itself is very complex which falls behind CVD for large area growth <sup>53</sup>.

### 2.3.2. Top down synthesis techniques: - Two-dimensional materials like graphene and

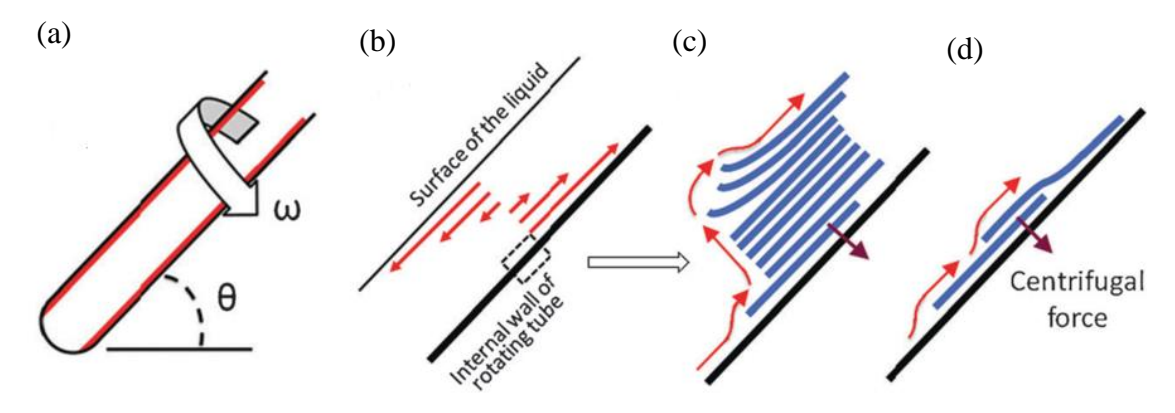


Figure .2.14 (a) Schematics of a vortex fluidic device (b) Fluid direction inside the test tube indicated by red arrows (c) exfoliation process (d) Slippage process <sup>54</sup>.

hexagonal boron nitride has its bulk counterparts. Through various techniques, these bulk materials can be thinned down to a single layer. Some of the techniques are discussed below.

**Solid Phase Exfoliation-** There are two prominent solid-phase exfoliation techniques. One is exfoliation by scotch tape from hBN powder another one is the ball milling method.

Recitative scotch tape peeling from hBN crystals or powder is an excellent method to get ultrathin hBN or graphene. As the Van der Waals force between the layers of hBN is very poor, they easily cleave. Details about this method have been described in the experimental method section.

Production of exfoliated 2D materials by ball milling is more scalable than the scotch tape peeling method. The ball milling energy is controlled by the size of the balls and rotation speed. During the milling process, benzyl benzoate is used as a protective layer to protect the hBN flakes from ball impacts and contamination. It has similar surface energy to that of hBN when compared to water, ethanol, or acetone. This prohibits the agglomeration of freshly dissociated hBN nanosheets. Low energy ball milling has yielded 67% of a few-layer BNNS<sup>55</sup>.

**Liquid Phase Exfoliation** – In Liquid-based exfoliation, the shearing or the centrifugal force of fluid is used to dissociate the BNNS from their bulk. Generally, there are two types, fluid shearing and sonication inside a fluid, these are described below-

Fluid shearing is a process in which precursor-like hBN powder or graphite flakes are dissolved in solvents like DMF or chloroform inside a test tube. When the test tube is rotated at very high r.pm like at 7500, the interplay of gravity and centrifugal force tears the 2D material into thinner portions. Figure 2.14 shows the basic outline of the fluid shearing process<sup>54</sup>.

Sonication of hexagonal boron nitride in polar solvents with surface energy close to hBN produces few-layer BNNS and even monolayer hBN. The sonication energy is varied for different solvents. Most general solvents are water, organic solvents, and acids like strong

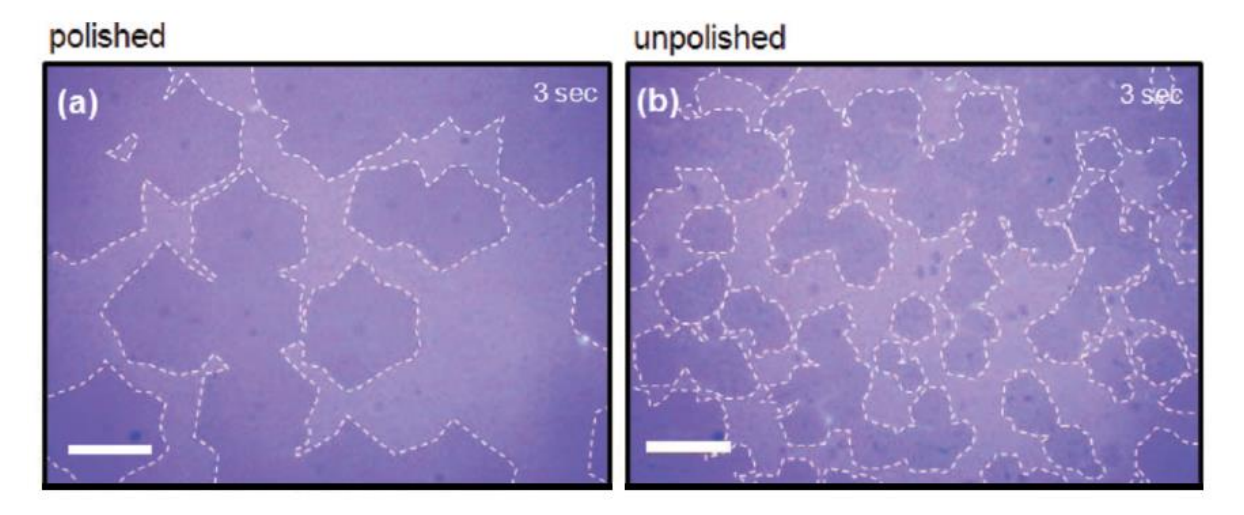


Figure .2.15 Optical micrographs of transferred graphene from Cu foil to SiO<sub>2</sub> /Si substrate. a) synthesized over electropolished copper and b)over nonelectropolished copper <sup>58</sup>.

protic acids. Organic solvents like ethanol, acetone, methanol, 1 propanol, 2 propanols, and tert-butanol have been used as a solvent for hBN exfoliation <sup>56</sup>.

**Unzipping BN nanotubes-**\_Unzipping of carbon nanotubes by plasma etching or cutting by catalysts has produced high-quality carbon Nanoribbons. This made bedrock for cutting multiwall boron nitride nanotubes either by plasma etching or by catalytic reactions. Multiwall BNNT (MWBNNT) is by coating over Si substrate with MWBNNT followed by PMMA spin coating. This assembly PMMA/MWBNNT is etched in Ar plasma and further PMMA removal by acetone followed by calcination at 600°C for 6hr. The MWBNNT bottom and sides were embedded in PMMA, so the plasma etched only the top surface which gave rise to unzipped BNNT<sup>57</sup>.

**2.3.2** Substrate effect on synthesis of 2D materials- CVD Synthesis of 2D materials like graphene and hBN has repeatedly revealed that the surface of the substrate has a decisive effect on the quality, uniformity, and even possibility of growth. The most critical surface features are the surface roughness, grain size, and crystallographic orientation. The nucleation density and choice of nucleation sites are dependent upon the substrate morphology. With low nucleation density, graphene grains tend to be bigger which is beneficial for device-based application<sup>59</sup>. Figure 2.15 shows the difference in graphene grain size over electropolished and nonelectropolished copper<sup>58</sup>. Clearly, the graphene grains are bigger when synthesized over electropolished copper. This is because electropolishing smoothens the surface and decreases the sticking coefficient of the surface, which decreases the nucleation density. As nucleation density decreases the graphene grain size increases. Not only electropolishing but physical/mechanical polishing has also positive effects on the grain size of graphene<sup>60</sup>.

The size of substrate grains also has an effect on the quality and size of graphene grains. This is because smaller grains of copper leads to an increased number of grain boundaries. As graphene islands also nucleate in the vicinity of the grain boundaries, smaller grains lead to high nucleation density. Which in turn reduces the size of the graphene grains. This same phenomenon is exhibited by hBN synthesis over metals like copper, nickel, Pt, Ru<sup>61</sup>. Apart from the surface roughness synthesis of hBN over Cu (111), Ni (111), Pt(111) has produced uniform commensurate layers. This reduces strain in the film and decreases the amount of wrinkle formation. As hBN and Cu (111) have a lattice mismatch of less than 1.8%, commensuration is much greater when compared to other lattice facets<sup>62</sup>. The substrate plays a role as a catalyst in synthesis in CVD, that is why after the growth of few layers the growth in z-direction stops.

### 2.4. Applications of 2D materials and hBN.

The hype and craze regarding two dimensional material and hBN can be attributed to their unique application in varied fields. Single-layer graphene which perhaps the most famous 2D material was isolated from bulk graphite in 2004, and then within a decade i.e by 2015 the number of accumulative publications over graphene attained more than 50,000 <sup>63</sup>. This phenomenal interest in graphene is primarily due to the exciting potential of its application. The application of graphene has been investigated in fields like renewable energy, saltwater desalination, nanoelectronics, flexible electronics, Raman enhancement, and many more. Needless to say this avalanche in curiosity regarding graphene spilled over other 2D materials like hBN. Some of the important and significant application areas of hBN are discussed in this section. Which are as follows:-

**2.4.1. Novel electronic devices-.** Atomically thin hexagonal boron nitride is free of dangling bonds and has an ultra-smooth surface and the minimal lattice mismatch makes it an excellent substrate for graphene-based electronics. The shift from Si-based electronic industry to graphene-based one requires an appropriate substrate like h BN where graphene can display its illusive abilities. Graphene-based field-effect transistors (FET) have displayed better efficiency in terms of carrier mobility than graphene/Si FET. Graphene in conjugation with hBN has found its way in many electronic devices. The effective carrier mobility of Si channel MOSFET is about  $1000-2000 \text{ cm}^2 \text{ V}^{-1} \text{ s}^{-1}$ , whereas it is about  $5000-10000 \text{ cm}^2 \text{ V}^{-1} \text{ s}^{-1}$  for graphene channel FET over SiO<sub>2</sub> substrate <sup>64,65</sup>. The effective mobility of graphene channel FET further increases 4-6 times when hBN is used as a substrate <sup>66</sup>. But these results have been obtained with exfoliated hBN and graphene when the carrier mobility

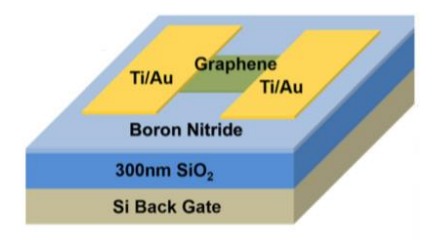


Figure 2.16 Schematics of a graphene FET

of CVD grown graphene is measured, it is only in the range of  $3000-5000 {\rm cm}^2~{\rm V}^{-1}~{\rm s}^{-1}$ , this massive reduction in carrier mobility in the case of CVD grown graphene is due to induction of defects<sup>67</sup>. Figure 2.16 shows the simple schematics of a back gated graphene channel FET over hBN. Gold/titanium metal electrodes have been used as a drain and source terminal<sup>68</sup>. Although exfoliated graphene over hBN shows magnificent carrier mobility as it is not a scalable process and fit for industrialization. Even if the ideal carrier mobility of graphene is  $200,000 {\rm cm}^2~{\rm V}^{-1}~{\rm s}^{-1}$  due to lack of scalability graphene channel FET over hBN substrate is still at its nascent stage <sup>69</sup>.

Apart from assisting graphene FET as an excellent substrate, hexagonal boron nitride nanosheets have also been used as an encapsulating layer. hBN encapsulated graphene device has reported carrier mobilities of 140,000 cm² V $^{-1}$  s $^{-1}$  in hBN-C-hBN configuration  $^{71}$ . Encapsulation of graphene devices with hBN provides added advantages when compared with other encapsulating layers like Al<sub>2</sub>O<sub>3</sub>, as graphene and hBN have a lattice mismatch of less than 2%. Hexagonal boron nitride film in conjugation with graphene in C-BN-C configuration has also been used as field-effect tunneling transistor device  $^{72}$ . Tunneling current measurements through hBN nanosheets even for a single layer is about  $10^4\,\mu\text{A}/\mu\text{m}^2$  at 1.0V bias  $^{73}$ . hBN is an excellent material for the prevention of tunneling current through electronic junctions which can provide exceptional electrical insulation. Hexagonal boron nitride in conjugation with graphene is proving to be a disruptor in wearable technology also. Wearable technology is highly coveted and two dimensional materials have a lot to offer in this field.

**2.4.2. Photonic application**- Hexagonal boron nitride is a hyperbolic metamaterial. Both pure hBN and its defects have potential in fields like deep UV optoelectronics, infrared photonics, single-photon emitters, and many more. Below are the few major applications of h BN for light-based devices.

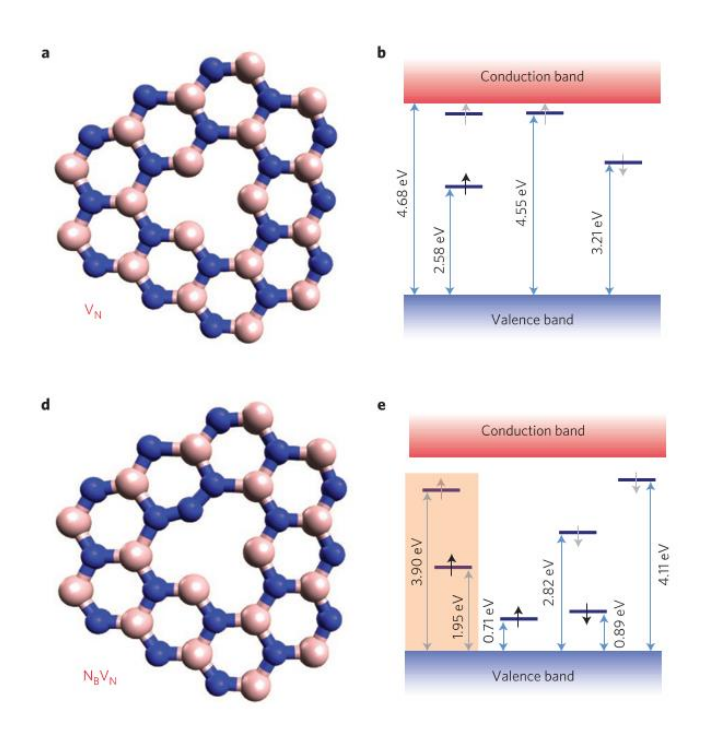


Figure .2.17 Defects in hBN and their respective electronic structure <sup>70</sup>.

**Single photon emitter-** With the increase in research in the field of quantum computing, light-based quantum computing has taken the lead. Recently working abilities photon-based quantum computer has been demonstrated which is far ahead of any other classical computer

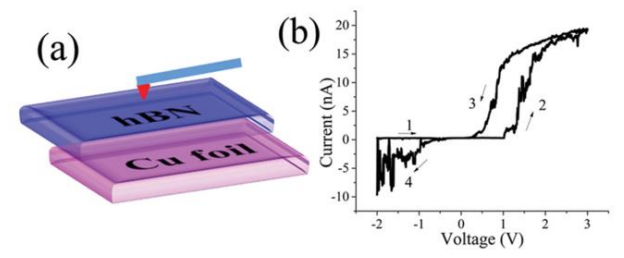


Figure .2.18 Resistive switching study. a) Device geometry b) I-V hysteresis loop of hBN 75.

<sup>74</sup>. Single photon emitters are of immense importance in a light-based quantum computer. As they are the key components to produce single photons which act as a qubit. Single photon emitters or SPE are non-classical sources of light that only emits one photon in a single excitation cycle. Defects sight in hBN has been attributed for the generation of

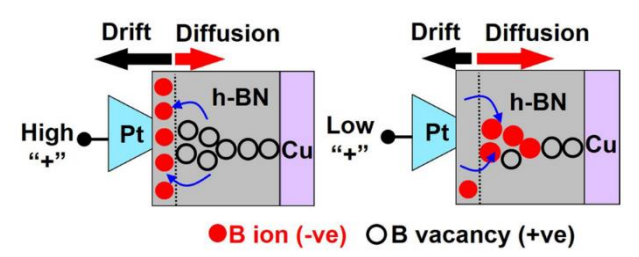


Figure .2.19 Drift and diffusion of B and B (+ ve) ions due to the application of voltage 77.

single photon. It has been stipulated that electronic band formation between valence and conduction band due to defect sites like  $V_NC_B$  (antisite carbon vacancy),  $V_N$ ,(boron vacancy)  $N_BV_N$  is the cause of single-photon emission<sup>76,70</sup>. When the hBN mesh has  $V_N$  or  $N_BV_N$  defects

extra electronic states appear between the conduction and valance band (Figure 2.17). Some of the energy differences like 2.58eV for  $V_N$  and 1.95eV for  $N_BV_{N \text{ are}}$  similar to the zero phonon line of photoluminescence spectra of hBN which is centered at 623nm or at 2 eV  $^{70}$ .

**Deep UV optoelectronic devices-** Hexagonal boron nitride has an absorption peak at 202nm, this particular feature has propelled for its exploitation in fields of deep UV photonics<sup>78</sup>. h BN has been proposed both for deep UV lasing and as well as for UV photodetection. UV photodetection is an important aspect in areas like water purification, UV flame sensing, space communication etc<sup>79</sup>. When hBN film-based devices were irradiated with 212nm laser under application of 0-20 V dc. There is a considerable difference between the photocurrent and the dark current.

**2.4.3. Memory devices**-Two dimensional materials like hBN and graphene have a lot of potential in memory devices like in fields of resistive switching, RRAM, and memristors.

Resistive switching- Hexagonal boron nitride has shown resistive switching properties in many studies<sup>80,75</sup>. Figure 2.18 shows the device geometry and current-voltage hysteresis loop which signifies resistive switching properties of a few-layer hBN film <sup>75</sup>. Atomically thin and few-layer hBN has an outstanding edge over other RS active materials in terms of flexibility, transparency, high endurance, and low power consumption. Nanocomposites of hBN have also been studied for resistive switching studies<sup>81</sup>. Primarily there are two prescribed mechanisms to explain the resistive switching mechanism. One is based on the formation and dissolution of conductive filaments and the other is based on the movement of boron ions<sup>82</sup>. When hBN films over metal substrates like copper are studied for RS properties, during the low resistance state that is ON state conducting filaments protruded from cathode to anode. During the high resistance state (due to the application of reverse voltage) that is the OFF state the conducting filaments dissolved due to oxidation.

The other mechanism is based on the drift and diffusion of B<sup>-</sup> ions. Figure 2.19 shows the schematics of the mechanism<sup>77</sup>. Here the hBN is over Cu foil, during the application of high voltage through the Pt tip of the conductive AFM the B<sup>-</sup> ions migrate towards the Pt electrode, in this case drifting of the B<sup>-</sup> ions has an upper hand over diffusion. This is the ON state with low resistance. Now upon reversing the polarity the B<sup>-</sup> ions recombine with the B vacancy

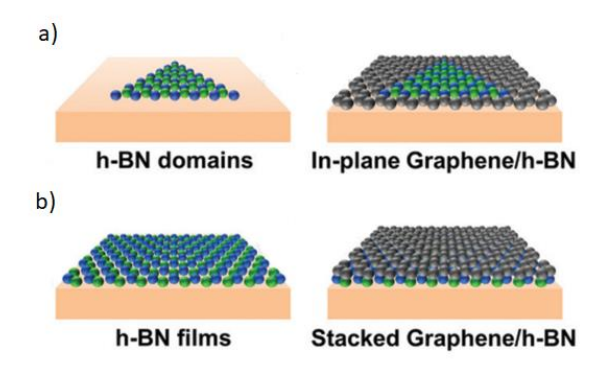


Figure. 2.20 In-plane hBN/ Graphene heterostructure 84.

states through diffusion and gives rise to the OFF state with high resistance. Ab initio calculations have shown that the occurrence of B vacancies is more favourable than N vacancies <sup>83</sup>. And also low affinity of boron when compared to the first ionization energy tends to give rise to B<sup>-</sup> ions.

**Graphene memristors** – For a new generation of computing like neuromorphic computing or neural networks graphene-based memristors are becoming a potential candidate for better efficacy. GFET hysteresis has been used to demonstrate vector-matrix multiplication with high retention endurance, high precision, low power consumption, and have a much smaller coverage area than conventional Si FET<sup>85</sup>.

## 2.4.4. Miscellaneous applications of hBN and other 2D materials.

**Desalination-** Pure drinkable water is becoming scarcer as the day passes, the need to have a reliable and cost-effective source of drinkable water is stronger than ever before. The evil irony is that we have an enormous amount of saltwater present in our plain sight, but is not drinkable. Hexagonal boron nitride has the potential to be a game-changer in this field, through selective ion filtration and defect modification it is slowly emerging as a viable alternative to the existing process of desalination<sup>86</sup>.

**Field emission-** Boron nitride nanotubes are able to emit electrons from their tips under the influence of strong electric filed<sup>87</sup>. Porous BN sheets and BN ribbons are also able to produce electrons under the similar influence. The presence of a finite zigzag edge is the cause for electron emission.

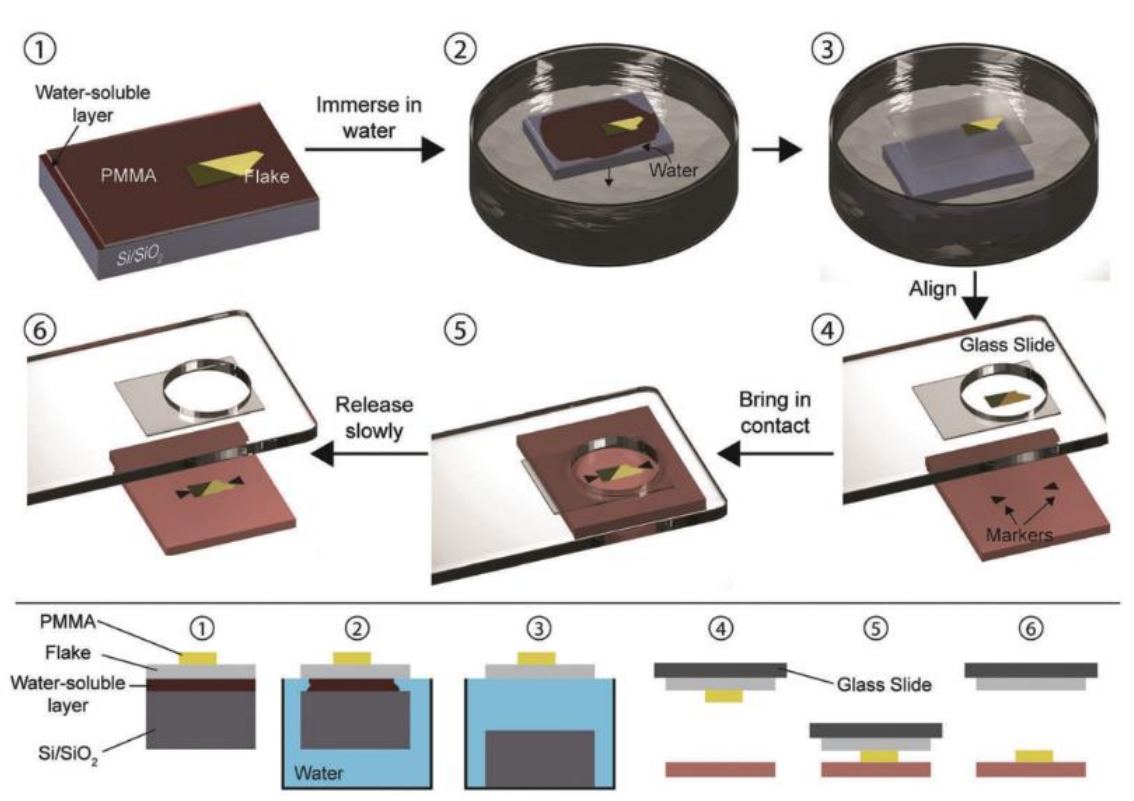


Figure .2.21 Schematics of different steps in transferring a flake from one substrate to another by using water-soluble stamps and PMMA  $^{89}$ .

**Neutron detection-** Hexagonal boron nitride is emerging to be an excellent neutron detector material<sup>88</sup>. Neuron detectors have numerous applications like in nuclear power plants, geothermal studies, etc. Generally, <sup>3</sup>He pressurized gas tube detectors are used, which has some shortcomings. Like they are bulky, require high operational voltage (1000V), slow speed for a response. These limitations are detrimental to flexible detector design. That is why solid-state

detectors are coming forth<sup>90</sup>. This is because <sup>10</sup>B an isotope of Boron has a high capture cross-section of 3840 b for thermal neutrons. When <sup>10</sup>B atom absorbs a neutron the following reaction happens-

 $^{10}$  B+ $^{1}$ n= $^{7}$ Li\*(0.84MeV) + $^{4}$  $\alpha$ \* (1.47MeV) -94% excited state ---1a  $^{10}$  B+ $^{1}$ n= $^{7}$ Li\*(1.015MeV) + $^{4}$  $\alpha$ \* (1.777MeV) -6% ground state ---1b

Li, 
$$\alpha \rightarrow N(e^{-}) + N(h^{+}) N \sim 10^{5} - -2$$

Equation 2 summarises the process of charge carrier generation by Li and alpha particles and the entrapment of the produced electron and holes. The two processes 1 and 2 happen in the same layer in hBN. This makes hBN a more efficient detector.

**Surface-enhanced Raman spectroscopy** (**SERS**) – Hexagonal boron nitride flakes and at the large film has convincingly shown Raman enhancement capabilities over various molecules like R6G, CuPc etc<sup>91,92</sup>. Chemical enhancement is observed in hBN. Although the factor of enhancement is far less than that of other SERS agents like metal nanoparticles, the durability, ease of storage in ambient conditions, and resistance to oxidation are remarkable. Hexagonal boron nitride has also been used as a passivating layer for gold and silver nanoparticles to protect them from degradation in the air and thereby increasing their life span<sup>93</sup>.

**2.5. Heterostructures-** Hexagonal boron nitride is an excellent 2D material for heterostructure templates. It has been used to make heterostructures with graphene, MoSe<sub>2</sub>, WSe<sub>2</sub>, WSe<sub>2</sub>, VO<sub>2</sub>, and many more <sup>94,95,96</sup>. There are mainly two ways to make a heterostructure. One is either by the synthesis in CVD or any other deposition system and another is by fabricating a layered composite structure by using dry transfer methods. Both of the processes have their specific advantages and disadvantages. Heterostructures can be of two

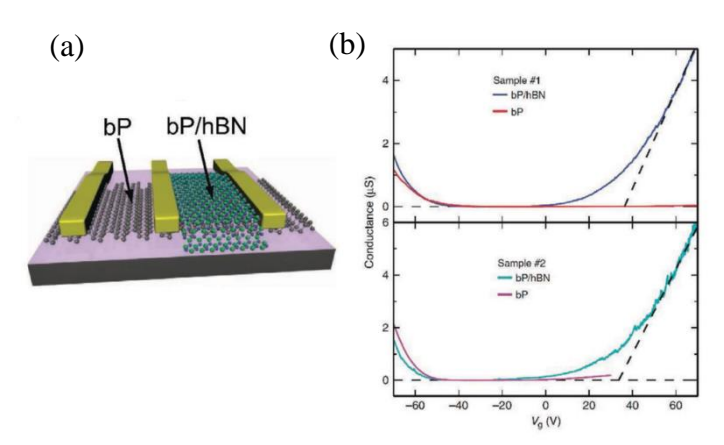


Figure .2.22 a) Schematics of BP device with and without hBN encapsulation. b) Conductance study of two samples with and without encapsulation of hBN <sup>97</sup>.

types geometrically, inplane and vertical heterostructures. Vertical heterostructures of 2D materials are also known as van der Waals heterostructures, as van der Waals forces hold the layers in place. Figure 2.20 a)shows the geometry of inplane hBN- Graphene heterostructure, b) shows the schematic vertical hBN/ Graphene heterostructure <sup>84</sup>.

**2.5.1. Synthesis of heterostructure-** Synthesis of heterostructure generally refers to the

growth of two different materials via CVD or any other synthesis techniques. Currently, CVD and PVD are the most popular techniques. Synthesis of vertical and inplane heterostructures can be done both in-situ and ex-situ. Insitu vertical structure is done by successive growth of two materials from two different precursors. Teng *et al* reported synthesis of both in-plane and vertical hBN/ Graphene in situ. Where they regulated temperature during growth to switch between in-plane and vertical heterostructures <sup>98</sup>.

**2.5.2. Fabrication of heterostructure-** Generally a micromanipulator associated with a microscope or a mask aligner is used to fabricate heterostructures. Fabrication of heterostructure is the process of assembling 2 or more layers of 2D materials on top of each other. Stamps like PPC, PMMA, and PDMS to pick and drop flakes at the desired position of another flake. Figure 2.21 shows the transfer process of one from one substrate to another step by step<sup>89</sup>. Where they used a water-soluble layer and PMMA film for transferring. As PMMA is dissolved in acetone it can be easily removed in the end step. This particular process can be repeated to make bilayer or trilayer structures. The hot pickup and release technique is also used to transfer flakes. Here the stamp is heated to a certain temperature for releasing the top flake is applied generally<sup>99</sup>. For electron or hole mobility studies gold contacts are made over the substrate. By aligning the flake over the contacts, mobility studies and capacitive studies can be easily done<sup>100</sup>.

Several advantages are associated with the synthesis way of making heterostructures. The interface between the two materials is cleaner as no dry polymer is used to fabricate them. Inplane heterostructure cannot be made by the fabrication process. But in the fabrication process, the purity of the two materials in question can be controlled as mostly exfoliated samples are used. The degree of rotation can be precisely controlled when fabricating heterostructures. Moiré patterns between the two materials can be better studied when using fabricated samples rather than the synthesized heterostructure<sup>101</sup>. Furthermore, as a synthesis of heterostructure is mainly done over transition metals there is no possibility to study their electrical properties before transferring them to dielectric substrates. In this case, the fabrication process edges out as it is mostly done over dielectric substrates where Au/Pt contacts can be easily done.

**2.5.3. Application of heterostructure.** Two-dimensional materials are already taking the leap towards large-scale application in different fields. The combination of different 2D materials in forms of heterostructure provides unique applicability, and thus they are getting popular day by day. The major areas where hBN plays a crucial role is-

Encapsulation- Unlike hBN many two-dimensional materials are not stable. Black phosphorous (BP), Indium Selenium (InSe), Hafnium Disulphide (HfS<sub>2</sub>) are sensitive to ambient conditions, as the roughness of BP flakes increases when stored in air. Encapsulation with hBN flakes considerably preserves BP flakes with little to zero change in their surface characteristics. hBN is able to do so by screening the effects of moisture and air. The electron mobility of hBN encapsulated BP, Graphene, and InSe devices have a considerable difference from non-encapsulated devices <sup>102,103</sup>. Figure 2.22 shows the BP channel FET with and without hBN encapsulation. Sample 1 and sample 2 are of two different channel thickness, 4.5 nm, and 5.7 nm respectively. The conductance study at room temperature both for the hole side (negative gate voltage) and electron side (positive gate voltage) showed better conductance for the encapsulated BP channel. For the electron side, it is one order more than the non-

encapsulated device<sup>97</sup>. hBN Encapsulated InSe devices have also shown improved device performance. The measured electron mobility of non-encapsulated InSe at 4K is 10,000 cm<sup>2</sup> V<sup>-1</sup> s<sup>-1</sup>. InSe is very sensitive to oxygen, water, and organics both from the ambient air and also contaminations during device fabrication. Thus an excellent way to improve device performance by encapsulation, Geim et al have reported electron mobility of 12700 cm<sup>2</sup> V<sup>-1</sup> s<sup>-1</sup> by fully encapsulating the InSe channel. Figure 2.23 shows the cross-sectional schematics of the InSe field-effect transistor where few-layer graphene has been used as an extended contact<sup>104</sup>.

**2.6.** New age characterization of hBN and 2D materials - Apart from the conventional/popular characterization techniques like XPS, AFM, FESEM, TEM, Raman, Optical microscopes, etc to analyze the structural, morphological, and stoichiometric properties of a 2D material, several other advanced techniques which have been in practice to study bulk material are slowly making their way to study 2D materials. Techniques like in-situ low energy electron diffraction (LEED), near field scanning optical microscopy (SNOM), ellipsometry, atom probe tomography (APT), etc are being used on a small scale to study properties of 2D materials or their heterostructure.

Ellipsometry- Ellipsometry is a non-destructive study relying on optical reflectance of a

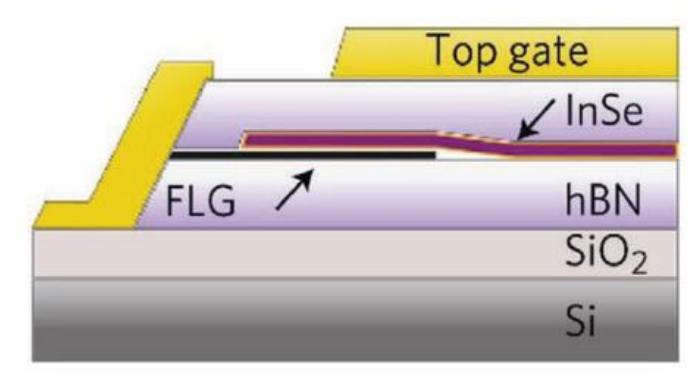


Figure .2.23 Cross schematic of hBN encapsulated InSe FET <sup>104</sup>.

surface. Through it, we can get valuable information about a 2D material film like its thickness and uniformity<sup>105</sup>. Although there are several methods by which these parameters can be measured, ellipsometry is one of the best possible ways to measure the thickness of the film with wafer-scale efficacy. As synthesis and transfer of hBN or graphene is approaching for wafer scales ellipsometry is getting an increasing attention<sup>106,107</sup>.

SNOM- In near field imaging, the excitation laser is focused through a tip aperture whose dimension is smaller than the excitation wavelength itself, which results in an evanescent field or near field. The attainable vertical resolution is 2-3 nm and lateral resolution is 20 nm. Hyperbolic phonon polaritons of hBN allow us to use these materials for SNOM studies. Advancement in infrared nano-imaging and generation (excitation wavelength is 780cm<sup>-1</sup> for hBN) has further enriched this technique for 2D materials <sup>108</sup>. Plasmons in graphene have also been imaged by SNOM <sup>109</sup>.

LEED and LEEM- LEED or low energy electron diffraction is an important tool to study in situ crystal growth. When it is combined with low energy electron microscopy (LEEM), it gives a detailed picture of the growth procedure. LEEM and LEED have been employed to study the growth of hBN over Cu (111), the advantage of these techniques is that they provide

real-time analysis of the growth process <sup>110</sup>.

**2.7. Future scope.** Two-dimensional materials have come a long way since the inception of graphene in 2004. Millions of papers have been published about graphene, hBN, and other 2D materials since then. The next big step in the 2D world will be its application in emerging fields like quantum computing. Quantum informatics, artificial intelligence, space technology, and many more. Another big push came from the discovery of new 2D materials. Nevertheless, the prospect of 2D materials with all the promises it has shown is bright.

## 2.8 Motivation and Objectives.

This thesis work is the outcome of intensive experiments in conjugation with an extensive literature review. This work tries to fill the research gaps regarding the synthesis and applications of hBN. The prime motivations of the work undertaken are –

- Owing to its unique properties hBN has an array of applications in fields like optoelectronics, memory devices, electrochemistry, neutron detection that has been discussed in detail in the earlier sections. Scalable synthesis of hBN is coveted due to its enormous potential in many fields. Synthesizing it via r.f sputtering could pave the way to fully harness its potential as the r.f sputter deposition method is highly integrated with the semiconductor industry. There is a lack of research material in the synthesis of hBN via r.f sputtering over the copper foil. This thesis work tries to address this issue by exploring the synthesis of hBN via r.f magnetron sputtering.
- Apart from the study of the synthesis process of hBN via r.f sputtering synthesis
  through CVD has also been undertaken. This was to elucidate the effect of the
  amount of precursor material over the thickness of the hBN film. Another
  motivation was to observe the formation of thermally induced wrinkles over hBN
  film as very few studies have addressed this issue.
- The as-synthesized hBN films via CVD were subjected to different applications. The motivation behind their use is as follows
  - a) Surface-enhanced Raman spectroscopy- The use of two dimensional materials as a Raman enhancement material is getting traction over the years. The efficacy of hBN as a SERS probe has also been investigated by many researchers. But lion shares of the work has been done in conjugation with metal nanoparticles and hBN films. Almost no report has investigated the Raman enhancement properties of only hBN films, let alone study the effect of thickness variation over enhancement factor. Abiding by this fact we tried to put ourselves to study the effect of CVD grown hBN ultrathin films over the Raman enhancement of organic dye molecules.
  - b) Oxygen reduction reaction (ORR) Hexagonal boron nitride is emerging to be an electrocatalyst in oxygen reduction reaction. It has the potential to replace the most common electrocatalyst Pt .There are a few reports which have explored the efficiency of CVD grown hBN over Cu foil as an electro catalyst in ORR reaction. We explored this field and have presented the initial results.

c) Resistive switching- Neuromorphic or non Von Neuman computing is getting popular day by day. Two-dimensional materials are being explored for their application in this field too. It has been reported that hBN exhibits resistive switching behaviour. We explored neuromorphic characteristics like potentiation for the hBN/Cu system by using a conductive AFM. Our results here are preliminary which can form the foundation for future research.

Setting the motivation of the work the major objectives of this study are :

- We studied the synthesis process over Cu foil via r.f sputtering. How the crystallographic orientation of the copper substrate surface plays a role in determining the phase of the BN film. And also how surface roughness of the copper substrate plays a role in the wettability and uniformity of the synthesized film. The results are discussed in chapter 4.
- Another objective was to synthesize hBN via atmospheric pressure CVD by using ammonia borane powder. Films of different thicknesses have been synthesized. Surface morphology investigation like wrinkle and grain size has also been carried on.
- Regarding SERS study with the hBN film our objective was to exhibit how Raman
  enhancement factor varies with the thickness of hBN film. We have shown that
  hBN as a SERS substrate is more durable than metal particles based SERS probes.
  Our results show that hBN films can stay stable for more than 7 months after their
  synthesis and still maintain their efficacy as a SERS probe. These results have been
  discussed in chapter 6 in detail.
- With regard to resistive switching behaviour of hBN our objective was to see how stable the I-V loop was so that we can venture for more sensitive studies like potentiation.
- We used cyclic voltammetry to study the electrocatalytic behaviour of hBN over Copper electrode in both nitrogen saturated environment and oxygen saturated environment. Our objective was to study the behaviour of the cathodic current with and without hBN for copper electrodes.

#### 2.9. References.

- 1. Naguib, M. *et al.* Two-dimensional nanocrystals produced by exfoliation of Ti 3AlC 2. *Adv. Mater.* **23**, 4248–4253 (2011).
- 2. Ashton, M., Paul, J., Sinnott, S. B. & Hennig, R. G. Topology-Scaling Identification of Layered Solids and Stable Exfoliated 2D Materials. *Phys. Rev. Lett.* **118**, 1–6 (2017).
- 3. Pakdel, A., Bando, Y. & Golberg, D. Nano boron nitride flatland. *Chem. Soc. Rev.* 43, 934–959 (2014).
- 4. Ahmed, R., Fazal-e-Aleem, Hashemifar, S. J. & Akbarzadeh, H. First principles study of structural and electronic properties of different phases of boron nitride. *Phys. B Condens. Matter* **400**, 297–306 (2007).
- 5. Pakdel, A., Zhi, C., Bando, Y. & Golberg, D. Low-dimensional boron nitride nanomaterials. *Mater. Today* **15**, 256–265 (2012).
- 6. Cassabois, G., Valvin, P. & Gil, B. Hexagonal boron nitride is an indirect bandgap semiconductor. *Nat. Photonics* **10**, 262–266 (2016).
- 7. Evans, D. A. *et al.* Determination of the optical band-gap energy of cubic and hexagonal boron nitride using luminescence excitation spectroscopy. *J. Phys. Condens. Matter* **20**, (2008).
- 8. Watanabe, K., Taniguchi, T. & Kanda, H. Direct-bandgap properties and evidence for ultraviolet lasing of hexagonal boron nitride single crystal. *Nat. Mater.* **3**, 404–409 (2004).
- 9. Wickramaratne, D., Weston, L. & Van De Walle, C. G. Monolayer to Bulk Properties of Hexagonal Boron Nitride. *J. Phys. Chem. C* **122**, 25524–25529 (2018).
- 10. Sharma, S., Kalita, G., Vishwakarma, R., Zulkifli, Z. & Tanemura, M. Opening of triangular hole in triangular-shaped chemical vapor deposited hexagonal boron nitride crystal. *Sci. Rep.* **5**, 1–9 (2015).
- 11. Doan, T. C., Li, J., Lin, J. Y. & Jiang, H. X. Charge carrier transport properties in layer structured hexagonal boron nitride. *AIP Adv.* **4**, 0–9 (2014).
- 12. Reich, S. & Ferrari, A. C. Resonant Raman scattering in cubic and hexagonal boron nitride. 1–12 (2005) doi:10.1103/PhysRevB.71.205201.
- 13. I. Stenger, L. Schué, M. Boukhicha, B. Berini, B. Plaçais, A. L. and J. B. Low frequency Raman spectroscopy of few-atomic-layer thick hBN crystals. **0**, 302 (1385).
- 14. Gorbachev, R. V. *et al.* Hunting for monolayer boron nitride: Optical and raman signatures. *Small* **7**, 465–468 (2011).
- 15. Cai, Q. *et al.* Raman signature and phonon dispersion of atomically thin boron nitride. *Nanoscale* **9**, 3059–3067 (2017).
- 16. Yuan, C. et al. Modulating the thermal conductivity in hexagonal boron nitride via

- controlled boron isotope concentration. *Commun. Phys.* **2**, 1–8 (2019).
- 17. Cai, Q. *et al.* High thermal conductivity of high-quality monolayer boron nitride and its thermal expansion. *Sci. Adv.* **5**, 1–9 (2019).
- 18. Falin, A. *et al.* Mechanical properties of atomically thin boron nitride and the role of interlayer interactions. *Nat. Commun.* **8**, 1–9 (2017).
- 19. Xiao, F. Hexagonal boron nitride nanosheets synthesis and applications. (2016).
- 20. Veeredhi, L. S. B. & Ramana Rao, N. V. Studies on the Impact of Explosion on Blast Resistant Stiffened Door Structures. *J. Inst. Eng. Ser. A* **96**, 11–20 (2015).
- 21. Sajid, A. & Thygesen, K. S. VNCB defect as source of single photon emission from hexagonal boron nitride. *arXiv* (2020).
- 22. Liu, Y., Zou, X. & Yakobson, B. I. Dislocations and grain boundaries in two-dimensional boron nitride. *ACS Nano* **6**, 7053–7058 (2012).
- 23. Garg, R., Dutta, N. & Choudhury, N. Work Function Engineering of Graphene. *Nanomaterials* **4**, 267–300 (2014).
- 24. Novoselov, K. S. *et al.* Electronic properties of graphene. *Phys. Status Solidi Basic Res.* **244**, 4106–4111 (2007).
- 25. Van Hove, L. The occurrence of singularities in the elastic frequency distribution of a crystal. *Phys. Rev.* **89**, 1189–1193 (1953).
- 26. Zhou, A. & Sheng, W. Van Hove singularities in graphene nanoflakes. *J. Appl. Phys.* **112**, (2012).
- 27. Camilli, L., Sutter, E. & Sutter, P. Growth of two-dimensional materials on non-catalytic substrates: h-BN / Au (111) Growth of two-dimensional materials on non-catalytic. (2014) doi:10.1088/2053-1583/1/2/025003.
- 28. Zhang, K., Feng, Y., Wang, F., Yang, Z. & Wang, J. Two dimensional hexagonal boron nitride (2D-hBN): Synthesis, properties and applications. *J. Mater. Chem. C* **5**, 11992–12022 (2017).
- 29. Sutter, P., Lahiri, J., Zahl, P., Wang, B. & Sutter, E. Scalable synthesis of uniform few-layer hexagonal boron nitride dielectric films. *Nano Lett.* **13**, 276–281 (2013).
- 30. Stewart, D. M. & Lad, R. J. Enhanced Crystallinity of h-BN Films Induced by Substrate Bias During Magnetron Sputtering. *Phys. Status Solidi Basic Res.* **255**, 1–5 (2018).
- 31. Wang, H. *et al.* Controlled Growth of Few-Layer Hexagonal Boron Nitride on Copper Foils Using Ion Beam Sputtering Deposition. *Small* **11**, 1542–1547 (2015).
- 32. Stewart, D. M. & Lad, R. J. Enhanced Crystallinity of h-BN Films Induced by Substrate Bias During Magnetron Sputtering. **1700458**, 1–5 (2018).
- 33. Camilli, L., Sutter, E. & Sutter, P. Growth of two-dimensional materials on non-catalytic

- substrates: H-BN/Au(111). 2D Mater. 1, (2014).
- 34. Ohta, J. & Fujioka, H. Sputter synthesis of wafer-scale hexagonal boron nitride films via interface segregation. *APL Mater.* **5**, (2017).
- 35. Liu, H. *et al.* High-performance deep ultraviolet photodetectors based on few-layer hexagonal boron nitride. *Nanoscale* **10**, 5559–5565 (2018).
- 36. Wang, H. *et al.* Synthesis of Large-Sized Single-Crystal Hexagonal Boron Nitride Domains on Nickel Foils by Ion Beam Sputtering Deposition. *Adv. Mater.* **27**, 8109–8115 (2015).
- 37. Glavin, N. R. *et al.* Synthesis of few-layer, large area hexagonal-boron nitride by pulsed laser deposition. *Thin Solid Films* **572**, 245–250 (2014).
- 38. Velázquez, D., Seibert, R., Man, H., Spentzouris, L. & Terry, J. Pulsed laser deposition of single layer, hexagonal boron nitride (white graphene, h-BN) on fiber-oriented Ag(111)/SrTiO3(001). *J. Appl. Phys.* **119**, (2016).
- 39. Rand, M. J. & Roberts, J. F. Preparation and Properties of Thin Film Boron Nitride. *J. Electrochem. Soc.* **115**, 423 (1968).
- 40. Park, S. *et al.* Facile Synthesis of Highly Crystalline and Large Areal Hexagonal Boron Nitride from Borazine Oligomers. *Sci. Rep.* **7**, 1–8 (2017).
- 41. Wood, G. E. *et al.* Van der Waals epitaxy of monolayer hexagonal boron nitride on copper foil: Growth, crystallography and electronic band structure. *2D Mater.* **2**, 1–9 (2015).
- 42. Ismach, A. *et al.* Toward the controlled synthesis of hexagonal boron nitride films. *ACS Nano* **6**, 6378–6385 (2012).
- 43. Qing, F. et al. Graphene growth with 'no' feedstock. 2D Mater. 4, (2017).
- 44. Mirzaei, M., Hedayat, S. M., Karimi-Sabet, J. & Towfighi Darain, J. Graphene growth with no intended carbon precursor feeding into the LPCVD process: causes, solutions, and effects. *Nanotechnology* **32**, 025604 (2021).
- 45. Kim, K. K. *et al.* (2011) Synthesis of Monolayer Hexagonal Boron Nitride on Cu Foil Using CVD.pdf. (2012).
- 46. Tay, R. Y. *et al.* Synthesis of aligned symmetrical multifaceted monolayer hexagonal boron nitride single crystals on resolidified copper. *Nanoscale* **8**, 2434–2444 (2016).
- 47. Oh, H. et al. Centimeter-sized epitaxial h-BN films. NPG Asia Mater. **8**, e330–e330 (2016).
- 48. Khan, M. H. *et al.* Carbon- and crack-free growth of hexagonal boron nitride nanosheets and their uncommon stacking order. *Nanoscale* **8**, 15926–15933 (2016).
- 49. Park, H. *et al.* Large-scale synthesis of uniform hexagonal boron nitride films by plasmaenhanced atomic layer deposition. *Sci. Rep.* **7**, 1–8 (2017).

- 50. Matsoso, B. *et al.* Synthesis of hexagonal boron nitride 2D layers using polymer derived ceramics route and derivatives. *J. Phys. Mater.* **3**, 034002 (2020).
- 51. Nakhaie, S. *et al.* Synthesis of atomically thin hexagonal boron nitride films on nickel foils by molecular beam epitaxy. *Appl. Phys. Lett.* **106**, 1–6 (2015).
- 52. Xu, Z. *et al.* Large-area growth of multi-layer hexagonal boron nitride on polished cobalt foils by plasma-assisted molecular beam epitaxy. *Sci. Rep.* **7**, 1–7 (2017).
- 53. Kim, K. K., Lee, H. S. & Lee, Y. H. Synthesis of hexagonal boron nitride heterostructures for 2D van der Waals electronics. *Chem. Soc. Rev.* **47**, 6342–6369 (2018).
- 54. Chen, X., Dobson, J. F. & Raston, C. L. Vortex fluidic exfoliation of graphite and boron nitride. *Chem. Commun.* **48**, 3703–3705 (2012).
- 55. Li, L. H. *et al.* Large-scale mechanical peeling of boron nitride nanosheets by low-energy ball milling. *J. Mater. Chem.* **21**, 11862–11866 (2011).
- 56. Marsh, K. L., Souliman, M. & Kaner, R. B. Co-solvent exfoliation and suspension of hexagonal boron nitride. *Chem. Commun.* **51**, 187–190 (2015).
- 57. Zeng, H. *et al.* 'White graphenes': Boron nitride nanoribbons via boron nitride nanotube unwrapping. *Nano Lett.* **10**, 5049–5055 (2010).
- 58. Han, G. H. *et al.* Influence of copper morphology in forming nucleation seeds for graphene growth. *Nano Lett.* **11**, 4144–4148 (2011).
- 59. Kwon, G. D. *et al.* Influence of the copper substrate roughness on the electrical quality of graphene. *Mater. Res. Express* **4**, (2017).
- 60. Zhan, L. *et al.* Preparation of Ultra-Smooth Cu Surface for High-Quality Graphene Synthesis. *Nanoscale Res. Lett.* **13**, (2018).
- 61. Lu, G. *et al.* Synthesis of large single-crystal hexagonal boron nitride grains on Cu-Ni alloy. *Nat. Commun.* **6**, (2015).
- 62. Joshi, S. *et al.* Boron nitride on Cu(111): An electronically corrugated monolayer. *Nano Lett.* **12**, 5821–5828 (2012).
- 63. Sung JS, A. S. & Sung YK, K. H. Emerging Analysis on the Preparation and Application of Graphene by Bibliometry. *J. Mater. Sci. Eng.* **04**, (2015).
- 64. Kim, E., Jain, N., Jacobs-Gedrim, R., Xu, Y. & Yu, B. Exploring carrier transport phenomena in a CVD-assembled graphene FET on hexagonal boron nitride. *Nanotechnology* **23**, (2012).
- 65. Olusegun, A. *et al.* We are IntechOpen, the world 's leading publisher of Open Access books Built by scientists, for scientists TOP 1 %. *Intech* **i**, 38 (2012).
- 66. Dean, C. R. *et al.* Boron nitride substrates for high-quality graphene electronics. *Nat. Nanotechnol.* **5**, 722–6 (2010).

- 67. Wei, W. et al. Fabrication and characterization of CVD-grown graphene based Field-Effect Transistor. Eur. Microw. Week 2014 Connect. Futur. EuMW 2014 Conf. Proceedings; EuMC 2014 44th Eur. Microw. Conf. 367–370 (2014) doi:10.1109/EuMC.2014.6986446.
- 68. Uddin, M. A. *et al.* Mobility enhancement in graphene transistors on low temperature pulsed laser deposited boron nitride. *Appl. Phys. Lett.* **107**, (2015).
- 69. Raimond, J. M., Brune, M., Computation, Q., Martini, F. De & Monroe, C. Electric Field Effect in Atomically Thin Carbon Films. **306**, 666–670 (2004).
- 70. Tran, T. T., Bray, K., Ford, M. J., Toth, M. & Aharonovich, I. Quantum emission from hexagonal boron nitride monolayers. *Nat. Nanotechnol.* **11**, 37–41 (2016).
- 71. Shautsova, V., Gilbertson, A. M., Black, N. C. G., Maier, S. A. & Cohen, L. F. Hexagonal Boron Nitride assisted transfer and encapsulation of large area CVD graphene. *Sci. Rep.* **6**, 1–8 (2016).
- 72. Concerning, D. *et al.* References and Notes 1. **335**, 947–951 (2012).
- 73. Britnell, L. *et al.* Electron tunneling through ultrathin boron nitride crystalline barriers. *Nano Lett.* **12**, 1707–1710 (2012).
- 74. Zhong, H.-S. *et al.* Quantum computational advantage using photons Downloaded from. *Science* (80-.). **8770**, 1–9 (2020).
- 75. Qian, K. *et al.* Hexagonal Boron Nitride Thin Film for Flexible Resistive Memory Applications. *Adv. Funct. Mater.* **26**, 2176–2184 (2016).
- 76. Caldwell, J. D. *et al.* Photonics with hexagonal boron nitride. *Nat. Rev. Mater.* **4**, 552–567 (2019).
- 77. Ranjan, A. *et al.* Conductive Atomic Force Microscope Study of Bipolar and Threshold Resistive Switching in 2D Hexagonal Boron Nitride Films. *Sci. Rep.* **8**, 1–9 (2018).
- 78. Li, L. H. & Chen, Y. Atomically Thin Boron Nitride: Unique Properties and Applications. *Adv. Funct. Mater.* **26**, 2594–2608 (2016).
- 79. Jiang, H. X. & Lin, J. Y. Hexagonal boron nitride for deep ultraviolet photonic devices. *Semicond. Sci. Technol.* **29**, (2014).
- 80. Pan, C. *et al.* Coexistence of Grain-Boundaries-Assisted Bipolar and Threshold Resistive Switching in Multilayer Hexagonal Boron Nitride. *Adv. Funct. Mater.* 27, (2017).
- 81. Rehman, M. M. *et al.* 2D nanocomposite of hexagonal boron nitride nanoflakes and molybdenum disulfide quantum dots applied as the functional layer of all-printed flexible memory device. *Mater. Res. Bull.* **105**, 28–35 (2018).
- 82. Jeong, H. *et al.* Resistive Switching in Few-Layer Hexagonal Boron Nitride Mediated by Defects and Interfacial Charge Transfer. *ACS Appl. Mater. Interfaces* **12**, 46288–

- 46295 (2020).
- 83. Zobelli, A., Ewels, C. P., Gloter, A. & Seifert, G. Vacancy migration in hexagonal boron nitride. *Phys. Rev. B Condens. Matter Mater. Phys.* **75**, 1–7 (2007).
- 84. Meng, J. H. *et al.* Synthesis of in-plane and stacked graphene/hexagonal boron nitride heterostructures by combining with ion beam sputtering deposition and chemical vapor deposition. *Nanoscale* **7**, 16046–16053 (2015).
- 85. Schranghamer, T. F., Oberoi, A. & Das, S. Graphene memristive synapses for high precision neuromorphic computing. *Nat. Commun.* **11**, 1–11 (2020).
- 86. Gao, H. *et al.* Rational Design and Strain Engineering of Nanoporous Boron Nitride Nanosheet Membranes for Water Desalination. (2017) doi:10.1021/acs.jpcc.7b06480.
- 87. Cumings, J. & Zettl, A. Field emission and current-voltage properties of boron nitride nanotubes. *Solid State Commun.* **129**, 661–664 (2004).
- 88. Li, J., Dahal, R., Majety, S., Lin, J. Y. & Jiang, H. X. Hexagonal boron nitride epitaxial layers as neutron detector materials. *Nucl. Instruments Methods Phys. Res. Sect. A Accel. Spectrometers, Detect. Assoc. Equip.* **654**, 417–420 (2011).
- 89. Frisenda, R. *et al.* Recent progress in the assembly of nanodevices and van der Waals heterostructures by deterministic placement of 2D materials. *Chem. Soc. Rev.* **47**, 53–68 (2018).
- 90. Maity, A., Grenadier, S. J., Li, J., Lin, J. Y. & Jiang, H. X. Hexagonal boron nitride neutron detectors with high detection efficiencies. *J. Appl. Phys.* **123**, (2018).
- 91. Xia, M. A Review on Applications of Two-Dimensional Materials in Surface-Enhanced Raman Spectroscopy. *Int. J. Spectrosc.* **2018**, 1–9 (2018).
- 92. Cai, Q. *et al.* Boron Nitride Nanosheet-Veiled Gold Nanoparticles for Surface-Enhanced Raman Scattering. *ACS Appl. Mater. Interfaces* **8**, 15630–15636 (2016).
- 93. Kim, G. *et al.* Hexagonal Boron Nitride/Au Substrate for Manipulating Surface Plasmon and Enhancing Capability of Surface-Enhanced Raman Spectroscopy. *ACS Nano* **10**, 11156–11162 (2016).
- 94. Dai, S. *et al.* Phase change materials for nano-polaritonics: A case study of hBN/VO2 heterostructures. *arXiv* **1900251**, 1–6 (2018).
- 95. Wang, L. *et al.* New Generation of Moiré Superlattices in Doubly Aligned hBN/Graphene/hBN Heterostructures. *Nano Lett.* **19**, 2371–2376 (2019).
- 96. Yu, J. *et al.* Observation of double indirect interlayer exciton in WSe 2 /WS 2 heterostructure . *Opt. Express* **28**, 13260 (2020).
- 97. Doganov, R. A. *et al.* Transport properties of pristine few-layer black phosphorus by van der Waals passivation in an inert atmosphere. *Nat. Commun.* **6**, (2015).
- 98. Gao, T. et al. Temperature-triggered chemical switching growth of in-plane and

- vertically stacked graphene-boron nitride heterostructures. *Nat. Commun.* **6**, 1–8 (2015).
- 99. Pizzocchero, F. *et al.* The hot pick-up technique for batch assembly of van der Waals heterostructures. *Nat. Commun.* **7**, (2016).
- 100. Zhao, Q., Wang, T., Ryu, Y. K., Frisenda, R. & Castellanos-Gomez, A. An inexpensive system for the deterministic transfer of 2D materials. *arXiv* 0–5 (2020) doi:10.1088/2515-7639/ab6a72.
- 101. Wang, Z. *et al.* Composite super-moiré lattices in double aligned graphene heterostructures. *arXiv* 1–8 (2019).
- 102. Zhang, J. *et al.* Atomically Thin Hexagonal Boron Nitride and Its Heterostructures. *Adv. Mater.* **2000769**, 1–28 (2020).
- 103. Song, X. *et al.* Graphene/h-BN Heterostructures: Recent Advances in Controllable Preparation and Functional Applications. *Adv. Energy Mater.* **6**, 1–7 (2016).
- 104. Bandurin, D. A. *et al.* High electron mobility, quantum Hall effect and anomalous optical response in atomically thin InSe. *Nat. Nanotechnol.* **12**, 223–227 (2017).
- 105. Airaksinen, V. M. Silicon Wafer and Thin Film Measurements. Handbook of Silicon Based MEMS Materials and Technologies: Second Edition (Elsevier Inc., 2015). doi:10.1016/B978-0-323-29965-7.00015-4.
- 106. Crovetto, A. *et al.* Nondestructive Thickness Mapping of Wafer-Scale Hexagonal Boron Nitride Down to a Monolayer. *ACS Appl. Mater. Interfaces* **10**, 25804–25810 (2018).
- 107. Wurstbauer, U. et al. Imaging ellipsometry of graphene. Appl. Phys. Lett. 97, 18–21 (2010).
- 108. Li, P. *et al.* Hyperbolic phonon-polaritons in boron nitride for near-field optical imaging and focusing. *Nat. Commun.* **6**, 1–9 (2015).
- 109. Xu, Q. *et al.* Effects of edge on graphene plasmons as revealed by infrared nanoimaging. *Light Sci. Appl.* **6**, e16204-9 (2017).
- 110. Felter, J., Raths, M., Franke, M. & Kumpf, C. In situ study of two-dimensional dendritic growth of hexagonal boron nitride. *2D Mater.* **6**, (2019).

### Chapter 3

### **Experimental Details**

Experiments performed for this thesis work can be broadly classified into categories like synthesis techniques, microscopy techniques, spectroscopic experiments and diffraction studies. Each of these techniques shall be discussed in this chapter. Instrument details and materials used for the thesis are also mentioned in this chapter.

#### 3.1 Cleaning and Electropolishing of copper foil:

Cleaning of the substrate (25-micron thick copper foil for our case) is vital for any sort of deposition. The precaution was taken to clean the copper substrate thoroughly. It was cleaned in dilute nitric acid (6.9 %) to clean the copper oxide layers and other metal contaminates <sup>1</sup>. Followed by rinsing in deionised water is done to get rid of copper nitrate and other byproducts. Deionised water was used because as it is almost free (about 18 mega ohm resistance) on any ions, which diminishes the probability of unwanted metal ions sticking to the freshly cleaned copper surface. The cold roll copper foil contains metallic and non-metallic dust particles like Si, Ca, Pt, Ru and Ce <sup>2</sup>.

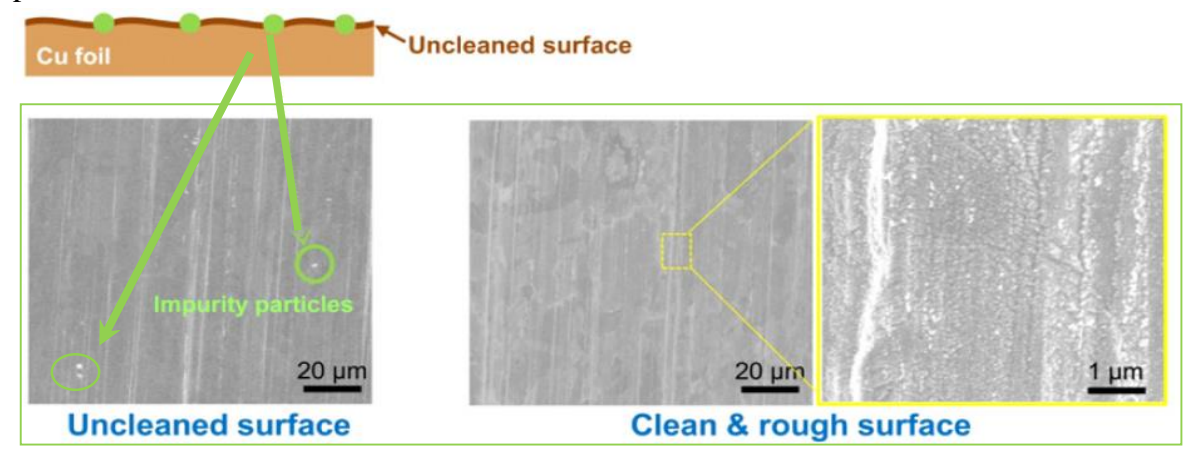


Figure .3.1 FESEM images of copper foil before and after cleaning with dilute Ni etchant.

Figure 3.1 shows the copper surface before and after treating Ni etchant. The effect of dilute nitric acid is similar to that of Ni etchant <sup>2</sup>.

$$Cu(s) + 4HNO_3 (aq) \rightarrow Cu (NO_3)_2 (aq) + 2NO_2 (g) + 2H_2O - (1)$$

Eq.1 shows the reaction of the copper substrate with dilute nitric acid. During the reaction, copper nitrate is produced along with nitrogen dioxide gas. The vigorous evolution of nitrogen dioxide gas washes of the impurity particle along with the copper oxide layers. The production of copper nitrate in aqueous form etches away the copper. This process of etching makes the copper substrate rougher. This roughness can be eliminated by electropolishing the copper foil. After cleaning with dilute nitric acid and DI water the sample was cleaned with acetone and isopropyl alcohol. This was done to get rid of the organic contaminants.

Electropolishing - As received copper foil was very rough after cleaning, to reduce the roughness of the copper surface electropolishing was done. Orthophosphoric acid (H<sub>3</sub>PO<sub>4</sub>) 85%

purity was used for electropolishing. Both the anode (+ electrode) and cathode (- electrode) were cleaned copper foil. The state of the electrolyte can be static or it can be dynamic. Static electrolyte refers to the condition that the electrolyte is not stirred upon during electropolishing. In the case of the dynamic condition, the electrolyte is stirred so that the viscous layer in the vicinity of the electrodes is not formed <sup>3</sup>.

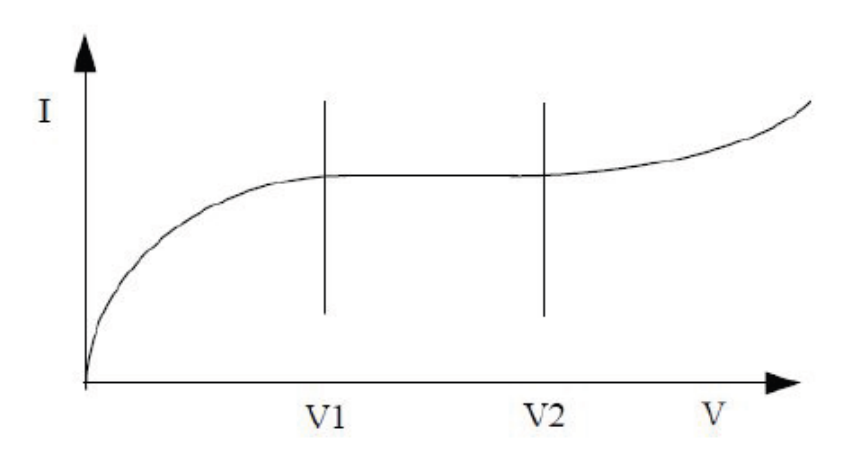


Figure .3.2 Current-voltage relationship during electropolishing in a static state.

Figure .3.2 shows the relationship between current and voltage during electropolishing when the electrolyte is static. At voltages below V1 etching occurs and at voltages below V2 pitting occurs. Polishing is obtained at the region between V1 and V2. For our case electropolishing was done for 50 s at 6.8-7.2 V (source voltage). The duration of electropolishing was chosen by adhering to the fact that over polishing may form pits that will depict the purpose. A proper balance was maintained to achieve a polished surface without the formation of pits and also to minimise etching. 85% pure phosphoric

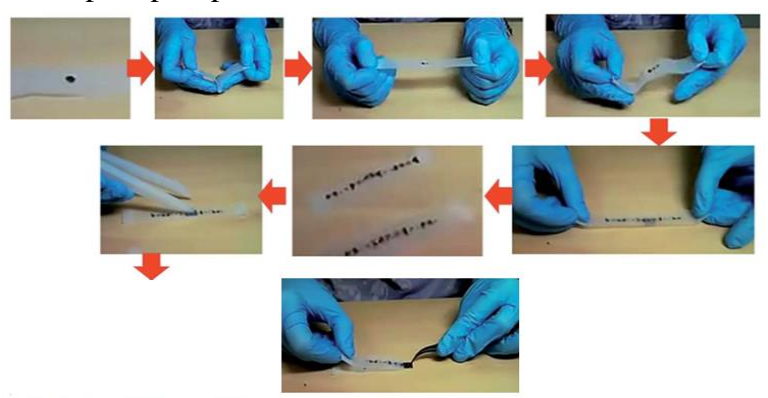


Figure 3.3 Simple steps of mechanical exfoliation.

acid, as well as a combination of phosphoric acid, isopropyl alcohol and acetic acid, was also used. For this combination, the electropolishing was done for 45 min with 4.7 mA/ cm<sup>2</sup>.

## 3.2 Synthesis techniques.

Hexagonal boron nitride has been synthesized by radio frequency (r.f) magnetron sputtering and by chemical vapour deposition. Mechanical exfoliation of hBN has also been done to fabricate graphene/hBN heterostructure.

**3.2.1 Exfoliation**: It is an easy process to obtain good quality 2D materials. hBN powder of 10-micrometre sized flakes has been used for exfoliation. For graphene exfoliation, HOPG crystal was used. We followed a simple route for exfoliation <sup>4</sup> where scotch tape has been used to peel the layers. At first, the SiO<sub>2</sub> capped Si substrate was cleaned by ultra-sonication in acetone and then in isopropyl alcohol and deionised water respectively. The scotch tape along with the powder (or graphite flake from HOPG) was peeled multiple times before placing it on SiO<sub>2</sub>/Si substrate. Figure 3.3 shows the simple peeling procedure by using the tape and placing it over the substrate <sup>5</sup>. The substrate along with the tape was heated to 80°C and then cooled down to room temperature to release the tape. Excess adhesive over the substrate was cleaned by acetone.

#### **3.2.2.** Radio frequency (r.f) magnetron sputtering:

Principle of operation- Radio frequency magnetron sputtering is a type of physical vapour deposition (PVD), where deposition occurs only at the line of sight. Figure 3.4 shows the simple schematics of r.f magnetron sputtering system <sup>6</sup>. The magnets were used to concentrate plasma ions near the target material. The concentrated plasma increases the efficiency of the deposition process.

Instrumentation and deposition parameters - Deposition by sputtering requires a dedicated system. The sputtering system basically has two variations, one is radiofrequency sputtering (r.f) and another one is direct current (d.c) sputtering. R.F sputtering is used for materials which have an insulating target and d.c sputtering is used for materials that have a conducting target. Thin metal films are deposited by d.c sputtering where any insulating material like

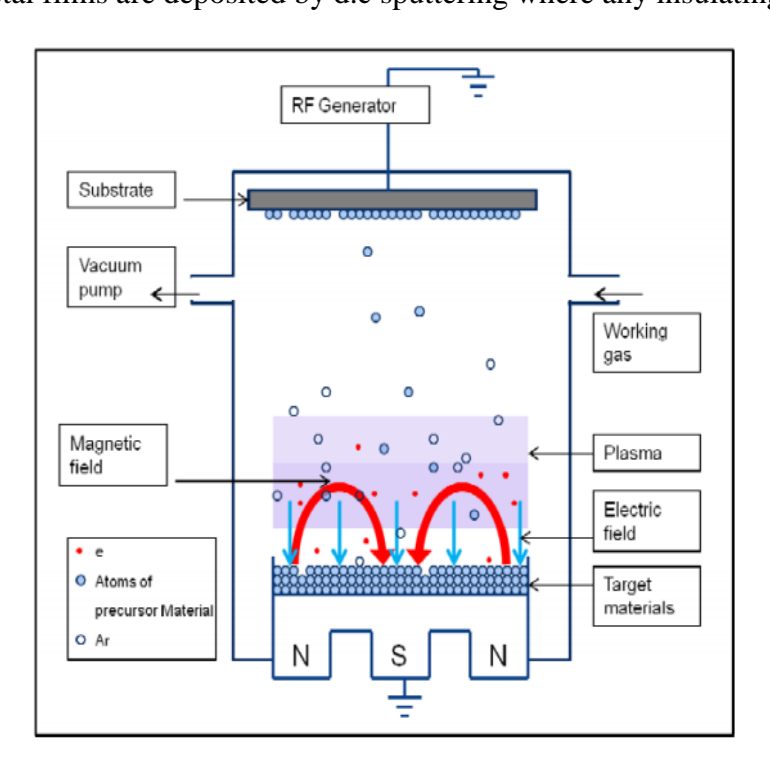


Figure 3.4 Schematic diagram of r.f magnetron sputtering <sup>6</sup>

zinc oxide is deposited by r.f sputtering. Hexagonal boron nitride is an insulating material therefore we used the r.f sputtering system for deposition. The main components of a sputtering

system are a vacuum chamber, pumping system, power supply, gas supply, substrate and target material. D.C power supply is used for d.c magnetron sputtering whereas 13.56 MHz r.f power supply is used for r.f magnetron sputtering. High vacuum (10<sup>-7</sup> mBar base pressure) or ultrahigh vacuum (10<sup>-9</sup> mBar base pressure) is maintained inside the sputtering chamber. h BN target is used for the growth of h BN film over copper. As h BN is highly insulating r.f magnetron process was used. When targets are conducting like for metal targets d.c magnetron sputtering can be used. A load lock assembly system was used to load and unload the sample.

# 3.2.3. Chemical vapour deposition:

Principle of operation- Principle of operation- Chemical vapour deposition is the process of deposition of solid materials over another material (substrate) by means of a chemical reaction. The precursor material is feed to the system in the form of gas or in the vapour phase. The substrate acts as a catalyst for the chemical process that takes place inside a CVD. The deposition is not a line of sight deposition, as chemical vapour can reach any corner of the substrate material provided it has a proper flow of the precursor material. The gas species in a CVD consists of two separate entities, one is the precursor material and another one is the carrier gas. The role of the carrier gas is to transit the precursor species to the desired reaction chamber.

The basic idea about CVD is to deposit or coat any material by altering/breaking the chemical bonds of the precursor material and forming new chemical bonds to make the new material that shall coat the substrate. Now, this process of breaking and making chemical bonds require a huge amount of energy. This energy is supplied by raising the temperature of the reaction zone of the CVD system. Like the growth of GaAs in MOCVD (metal-organic chemical vapour deposition) requires a temperature of 650° C <sup>7</sup>. High temperature in the reaction zone serves two purposes a) it helps to achieve the chemical breakdown of the precursor species, b) high temperature increases the surface mobility of the substrate which increases the wettability and provides a homogenous coating. The energy can be supplied in different ways also, like creating plasma and by applying UV radiation. To achieve a continuous and homogeneous coating by CVD the following conditions should be met 1) a steady flow of the precursor material, 2) homogeneous ant constant temperature at the reaction zone, 3)proper venting of the byproducts of the chemical reaction.

CVD types, Elements of a CVD, type of reactions involved and instrumentation used – Different types of CVD can be classified according to their working condition, the temperature of operation, precursor nature and gas flow. Some common types of CVD are as follows-

LPCVD- This stands for low-pressure chemical vapour deposition. The CVD operates in the region of the rough vacuum of the order of 10<sup>-3</sup> mBar. A tubular furnace is used with a rotary pump at one side and gas supply and precursor material on the other side. The reaction zone can be one or two or more depending upon the process.

UHVCVD- Ultra-high vacuum CVD operates in the pressure region of 10<sup>-8</sup>-10<sup>-9</sup> mBar. It was devised to a grown ultrapure single crystal. The growth rate very slow in these type of CVD. APCVD- Atmospheric pressure CVD works in ambient pressure without the application of any vacuum apparatus. The growth rate is generally higher than in UHVCVD.

MOCVD- Metal organic chemical vapour deposition uses organometallic precursor. The precursor is evaporated and is transported by a neutral gas like nitrogen or argon to the deposition chamber.

PECVD- Plasma enhanced CVD is similar to LPCVD; the main difference is the type of activation energy. In LPCVD heat energy is solely used to break /make chemical bonds, but in PECVD apart from heat energy plasma is also introduced. The ions of the plasma in conjugation with heat energy supplied bring down the reaction temperature for a coating to form. As a result, PECVD can operate at a lower temperature.

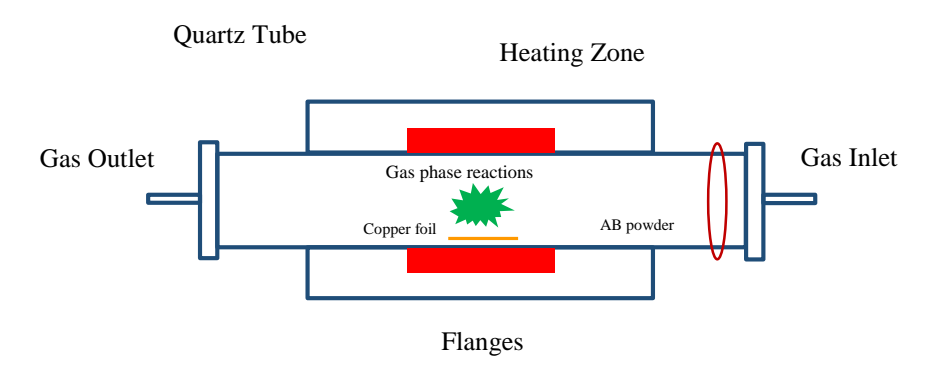


Figure 3.5- Schematic Diagram of APCVD system.

Instrumentation used for the production of hBN - Figure 3.5 shows a schematic of the APCVD chemical vapour deposition chamber which has been extensively used for the growth of hBN. The CVD system used for the deposition of h BN is custom made. Tube furnace (quartz tube used for deposition), gas manifold and gas cylinders, mass flow controllers are the main parts of the CVD set up. The horizontal quartz tube is fitted with flanges at the end through which gas is introduced. The substrate (Cu foil) is placed within the heating zone and the reactant is transported over to the substrate with the help of the carrier gas. The reaction takes place over the Cu foil at high temperatures. A heating tape is used to heat the ammonia borane powder (precursor for hBN growth) to 90-120° C. The powder is heated when the copper substrate inside the furnace is at 1040° C. A mixture of argon and hydrogen in the ratio of 9:1 is used as a carrier gas. The heating ramp rate was fixed at 8° C/ min and natural uninterrupted cooling was performed. The quartz was baked at 1060° C after cleaning it with dilute nitric acid, D.I water, IPA and acetone. The baking was done to remove residual deposition from the sublimation of AB powder. Proper cleaning and baking are necessary to get rid of secondary deposition from the inner walls of the quart tube. This CVD system is operated at atmospheric pressure. The copper foil was placed at the centre of the furnace and the AB powder was placed 55 cm upstream. After loading the copper foil and AB powder, the system was purged with Ar gas at 200 SCCM for 60 min. The purging is done to decrease the amount of oxygen inside the tube. A steady flow of 200 SCCM Ar is maintained up to 600° C. At 600° C Argon is replaced by 200 SCCM of Ar: H<sub>2</sub> (90:10). During the growth of h BN at 1040° C 50 SCCM of Ar: H<sub>2</sub> (90:10) is used. After growth when the furnace starts cooling the flow of Ar: H<sub>2</sub> (90:10) is increased to 200 SCCM until it reaches room temperature. CVD synthesis is not a line of sight deposition only like physical vapour deposition systems. The deposition also occurs in the out of sight places from the precursor. This is why deposition occurs at the underside of the copper foil.

#### 3.3 Microscopy.

Different types of microscopy methods have been employed to investigate the characteristics of hBN film both over the copper substrate and also after transferring the film over dielectric substrates. Optical microscopy, electron microscopy (both scanning and transmission) and atomic force microscopy has been applied to study the film from an array direction.

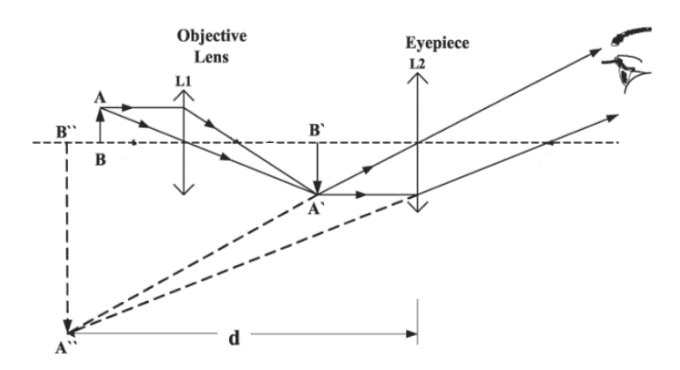


Figure 3.6- Schematic Diagram of CVD system.

#### 3.3.1. Optical Microscope:

Principle of operation- Inarguably the oldest microscopy technique is optical microscopy. Light microscope exploits the wave nature of light where a magnified image is formed by a combination of lenses. We have extensively used the light microscope for the thesis work. Figure 3.6 shows the simple light diagram of an optical microscope <sup>8</sup>. Where L1 is the objective lens and L2 is the eyepiece, AB is an object and A" B" in the image. If we neglect the optical aberration then the resolution (d) is given by  $d=\lambda/2NA$ . Where  $\lambda$  is the wavelength of light and N.A is the numerical aperture of the lens. The highest possible resolution with an optical resolution to date is about 100 nm.

Instrumentation- A standard light microscope consists of the objective lens, ocular lens, CCD camera, lens tube, stage and reflector. We used an Olympus BX53M microscope fitted with a DP73 CCD camera. The objectives used have magnification of 100x, 50x, 20x and 10x with numerical aperture (NA) of 0.90, 0.75, 0.40 and 0.25 respectively. One long working distance (10 cm between the object and the objective lens) 50x objective with 0.50 NA was used for the flake transfer by using the micromanipulator establishment.

Application of optical microscopy in 2D materials research – The thickness of SiO<sub>2</sub> film over Si determines the colour of the substrate. This dependence of the colour over thickness is due to interference. Interference occurs due to two distinct reflection paths, 1) air to SiO<sub>2</sub> and 2) SiO<sub>2</sub> –Si interface <sup>9</sup>. Depending upon the thickness of the SiO<sub>2</sub> layer the path difference will be different and thereby different phase shifts. As a result, different thickness of SiO<sub>2</sub> over Si produces a different colour. This same phenomenon is reproduced when flakes of 2D materials like graphene, hexagonal boron nitride etc. are exfoliated over Si/SiO<sub>2</sub> substrate. Here the interface is air- flake and flake –SiO<sub>2</sub>. Different thickness of the flake gives rise to different

path difference and as a result, appears to be of a different colour when viewed through the microscope. The thickness of graphene and other 2D material flakes can be easily estimated by their optical micrographs.

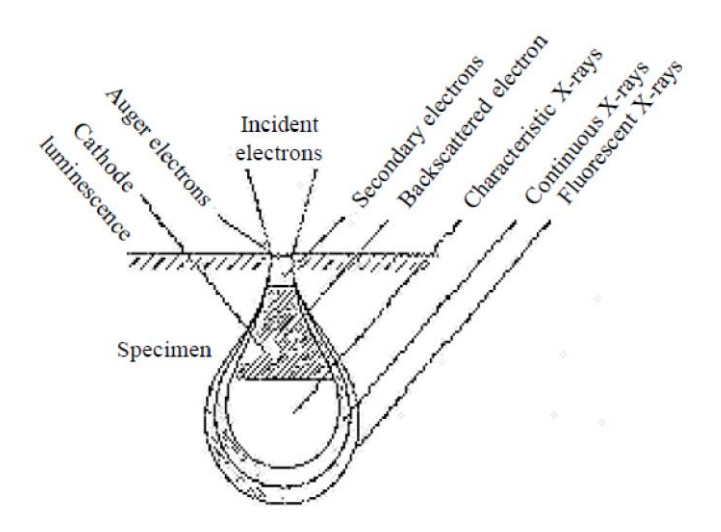


Figure .3.7 Interaction volume of the electrons with the sample surface.

For performing optical microscopy over our samples like hBN /SiO<sub>2</sub>/Si or hBN/ Cu no special sample preparation was needed, only a cleaned sample was sufficient enough for imaging. We performed optical imaging over nearly all transferred hBN films (from both types of deposition CVD and sputtering) that is over 100 transferred film. This is the primary technique to estimate the merits of the transfer process. The best results are incorporated in the thesis work.

#### 3.3.2. Field emission scanning electron microscopy:

Principle of operation - Scanning electron microscopy is a form of microscopy where electrons are extracted from a material (filament inside the electron gun) and then accelerated before they hit the sample. The particle nature of electron is exploited in this

microscopy to generate a very high magnified image. The reflected electrons are used to get an intensity mapping of the sample. A SEM image is an intensity map of the number of electrons reflected from a certain area of the sample. Figure 3.7 shows the interaction volume between the incoming electrons and the sample surface. The detectors of a scanning electron microscope deal with the secondary electrons and the backscattered electrons as they provide morphological information about the surface.

Instrumentation - The extraction of electrons can be done in two ways, one is by applying an electric field (for field emission scanning electron microscopy FESEM) and another is by thermionic emission. FESEM has better lateral resolution when compared to SEM. Zeiss Once the electrons are emitted from the electron gun they are collimated and accelerated with a certain voltage then focused into a spot, before they hit the sample. Upon hitting the sample the electrons are reflected and are detected by the detectors. The reflected electrons can be broadly classified into two categories —elastically scattered electrons and non-elastically scattered electrons.

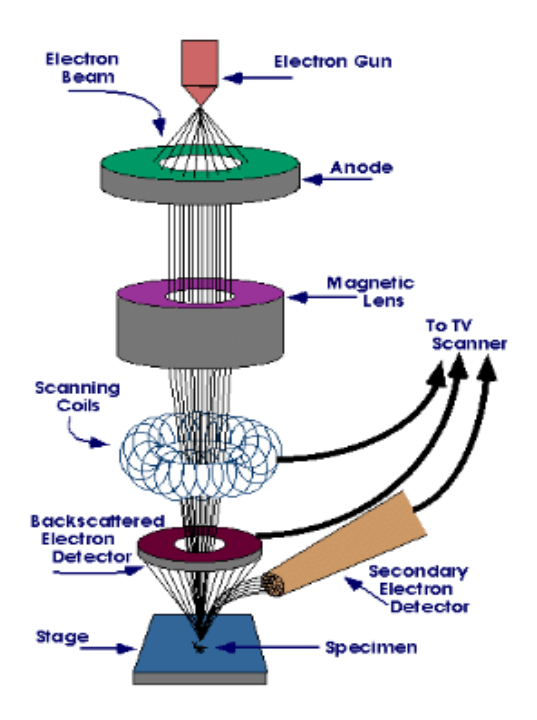


Figure. 3.8 Scanning electron microscope

Detectors - Inlens and SE (secondary electron detector) detectors are used to detect inelastically scattered electrons and BSE (backscattered electron detectors) detector is used to detect the elastically scattered electrons. Inlets detector is best to examine the surface morphology of the sample having similar phases. Whereas BSE detector is best suited to examine the a sample which has different phases, as different phases produce different contrast.

Image formation, magnification and resolution - In FESEM the obtained image is the intensity mapping produced by the scattered electrons coming from the sample. The reflected electrons from the sample are fed to a scintillator inside the detector. The signal from the scintillator is amplified and transduced to a video signal.

Resolution of the image depends upon this accelerating voltage generally called EHT (extra high tension). The resolution also depends upon the working distance (distance between the electron gun and sample). At very short working distance the electron spot becomes very small. The smallest spot produces very high resolution, but the depth of field decreases (depth of field is the range of focus in the vertical direction). Magnification depends upon the ratio of the raster over the sample and raster of the display module (i.e monitor). The scan coil is used to regulate the scan size, the smaller the scan size higher is the magnification. The dimension of the TV screen remains same, only the scan size is verified to regulate the magnification. Ultra 55 FESEM has been extensively used for the thesis work. Hexagonal boron nitride is highly insulation, most of the times thick h BN samples were coated with gold/palladium before scanning. This coating provided a proper grounding for the incident electrons. As the maximum thickness of the as-synthesized h BN films were no more than 10 nm we kept the EHT at 3 KV for very thin films (1-3 nm) and 5 KV for 4-10 nm thick films. An aperture of 30 µm was used for all measurements. A copper tape (adhesive on both sides) was used to affix the sample on the stub. Carbon adhesive tapes were not used as the conductivity is a lot less than the copper

adhesive tapes and the copper tapes are a lot less sticky than the carbon tapes. This made the samples reusable as they can be easily plucked from the stub. About 150-200 samples were imaged with FESEM.

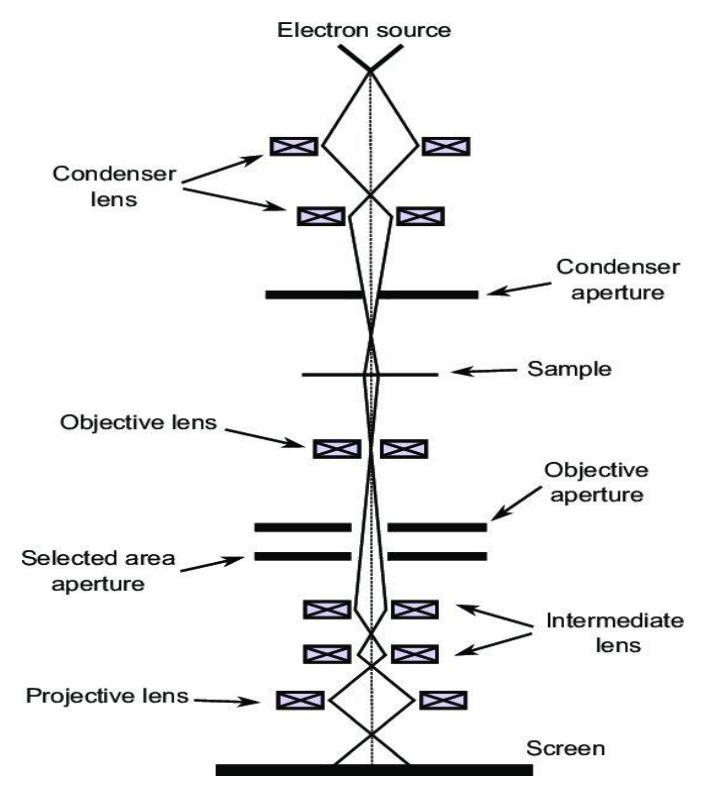


Figure .3.9 TEM schematics <sup>6</sup>

### 3.3.3. Transmission electron microscope:

Principle of operation - As the name suggests TEM or transmission electron microscopy deals with the transmitted electrons through the sample. It exploits the wave nature of electrons . As we know the resolution of any microscopy applying electromagnetic waves is given by  $d=\lambda/2NA$ . The lesser the wavelength higher is the resolution.

Instrumentation- Figure 3.9 shows the schematic diagram of a standard TEM <sup>10</sup>. Electron are emitted from the electron source (emission of electrons can be done by both ways, either by thermionic emission or by field emission), then they are tightly focussed by using magnetic lenses. After leaving the sample the transmitted electron—beam is again focused and then enlarged by magnetic lenses. After enlargement the electrons are projected over a phosphorous screen and an image is formed in a similar way like photography. Transmission electron microscope offers both bright field and dark field images. The current thesis work focuses on bright-field images only. Lesser the wavelength of the incident electrons i.e higher the accelerating voltage more is the resolution obtained. Standard TEM offers a resolution of 0.2 nm. Holey copper grids (with no amorphous carbon film), lacey copper grids (copper grids coated with carbon mesh) and copper grids with carbon coatings, these three types of grids are generally used to load the samples.

TEM analysis cannot be performed directly over hBN/Cu so the hBN film was transferred over TEM grids with carbon coating. 200 kV accelerating voltage was used for imaging. Wet transfer process was applied to transfer the hBN film from the copper substrate to the TEM grids. A FEI Tecnai G<sup>2</sup> 20 TWIN TEM was used for our experiments. A total of 10-12 hBN samples were transferred over TEM grids for imaging.

## 3.3.4. Atomic force microscopy:

Principle of operation-When two particles are bought in close proximity with each other, the potential between them varies with the distance and this variation is governed by Lennard-Jonnes potential (Figure 3.10)<sup>11</sup>. The mathematical form of the potential is given by :  $V=A[(r_m/r)^{12}-2(r_m/r)^6]$ , where r is the distance between the two particle (the tip and the sample surface for AFM), A is the depth of the potential and  $r_m$  is the distance where the potential is minimum. Atomic force microscopy is based on this interaction i.e the interaction between the tip and the sample.

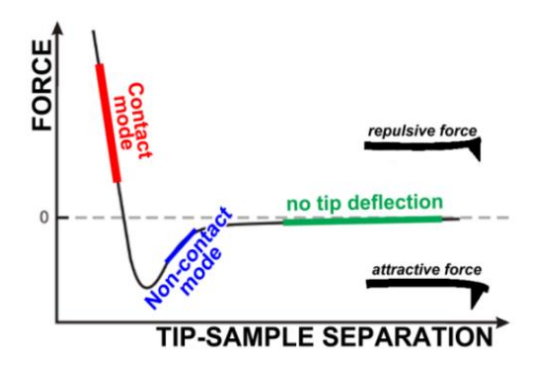


Figure. 3.10 Force regime in AFM.

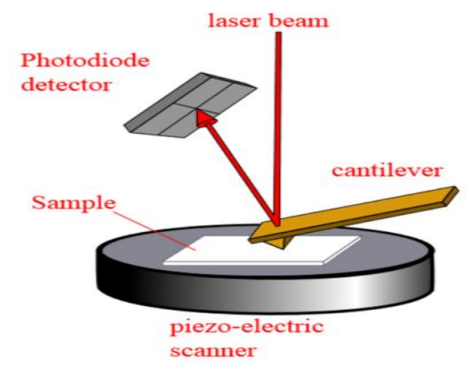


Figure. 3.11 Schematic of an AFM.

Instrumentation - Figure 3.11 shows the schematic of an AFM. AFM consists of a very fine tip (generally tip radius of about 20 nm) attached to a cantilever <sup>11</sup>. Once the tip is bought in the vicinity of the sample it interacts with sample surface. (Figure. 3.10) First there is no tip deflection, then it is attracted (region where non-contact mode of operation) towards the sample and on further reduction of the tip-sample distance it is repelled (region for contact mode of operation). A laser is incident over the cantilever top surface, which is reflected back to a photo

diode. As the tip raster the sample surface due to the variation of height of the surface features, the tip gets deflected with a different force. This deflection in turn changes the position of the laser in the photo diode. The deflection in the photo diode is quantified in terms of electric voltage which gives a near perfect estimate about the height and depth of the surface feature. False colour is used to generate AFM image which is obtained from the voltages recorded from the raster of the tip. Every AFM image is accompanied with a colour bar which is the height scale for that particular image.

Modes of operation - Generally AFM work in three different modes, contact and non-contact mode and tapping mode. Each mode has their specific advantages and disadvantages, like non-contact mode is most suitable for biological samples and other soft samples.

Contact mode - In contact mode AFM the tip is dragged through the surface. Generally, hard surfaces, which have a lesser chance of being damaged or scratched by the tip are studied by this mode. The contour of the surface is measured either by measuring the deflection of the cantilever or from the feedback signal from the cantilever by keeping it at a constant height. Only a height image is obtained in this mode.

Non-contact mode- Non-contact mode AFM is done for soft materials like biological samples, ultrathin film, microbes etc. In this mode, the AFM tip does not come into contact with the sample surface. Here the cantilever is oscillated at its resonant frequency or just above it with amplitudes less than 10 nm. Vander Waals forces which are strongest in the range of 1-10 nm, or any other forces tend to change the frequency of vibration of the cantilever. Along with the feedback loop system and the decreased vibrational frequency, the tip maintains a constant distance from the sample surface. Generally in most AFM systems non-contact mode gives 3 images one is the height image, amplitude image and the 3<sup>rd</sup> one is the phase image. Phase image refers to the phase difference between the actual frequency of vibration and the resonant frequency of the tip.

Tapping mode – Tapping mode is also called intermittent mode. It is almost similar to that of non-contact mode. Here also the cantilever is oscillating near its resonant frequency but the amplitude of vibration is from 100-200 nm. Interaction forces like Vander Waals force, electrostatic force etc. tends to decrease the amplitude of vibration of the cantilever. With the help of an electronic servo, the piezoelectric actuator maintains a constant height during scanning.

Advantages and disadvantages of AFM over electron microscopy <sup>12</sup> – There are many advantages of using an AFM over an electron microscope. Electron microscopes require a high vacuum to operate and typically require sample coatings for imaging. Coating samples makes them useless for other characterization and creating and maintain a high vacuum is expensive. AFM can perfectly work in ambient conditions and doesn't require any coatings. The biggest advantage of AFM over electron microscopy is that it provides a three-dimensional image of the sample surface which is crucial for studying surface properties of the material like roughness, morphology and depth of any surface feature.

Atomic force microscopy brings several disadvantages along with its pros. The scan rate of AFM is too slow when compared to a FESEM. Also, the scan size in a FESEM can be of the order of a few millimetres, whereas the maximum scan size of most AFM is of the order of  $100 \times 100 \, \mu m$ . Figure 3.12 shows typical artefacts that occur in AFM imaging. A tip with a high

radius of curvature can't image objects which have a lower radius of curvature. Instead, we get a blunt shape of the object like shown in figure 3.12 (b). Similarly surfaces having very steep wells cannot be imaged by an AFM. As shown in figure .3.12 (c).

AFM is primarily used to measure the thickness of the transferred film and also to obtain surface images of hBN/Cu. Two AFM system have been used for this thesis work one from Asylum research and another from SEIKO instruments. Cleaned transferred samples were used for thickness measurements by recording the AFM image at the edge of the film. At least 15 transferred samples from different batches were used to record the height profile. For obtaining the AFM images of hBN/Cu preferably the samples directly loaded from their respective deposition chambers to the AFM station. This was done to reduce the chance of humidity adsorption. Nearly 40-50 hBN/Cu systems experimented with AFM.

### 3.3.5. Scanning Kelvin probe microscopy:

Principle of operation – Contact potential difference of a solid's surface can be measured by using Kelvin probe microscopy. It is a type of atomic force microscopy where a conducting tip is used to measure the contact potential difference between the tip and the sample ( $V_{CPD}$ ). Figure 3.13 shows the electronic energy levels of the tip and the sample at different configuration  $^{13}$ . Contact potential difference is given by  $-V_{CPD} = (\phi_{tip} - \phi_{sample})/e$ , where  $\phi_{tip}$  and  $\phi_{sample}$  is the work function of tip and sample respectively. If the work function of the tip is known the work function of the sample can be calculated.

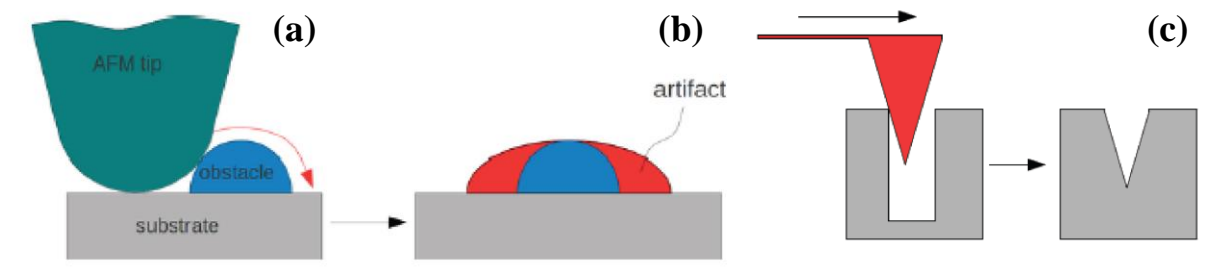


Figure. 3.12 Artefacts in AFM produced by high curvature tip and artefacts arising in case of a steep sample.

Instrumentation- A conducting AFM tips are applied for scanning Kelvin force probe microscopy. Both AC and DC voltage is applied to the AFM tip, AC voltage generates an oscillating electrical force between the tip and the sample, DC voltage nullifies the oscillating electrical forces that originated from the contact potential difference (CPD) between the sample and the tip. The AFM tip raster the sample surface, which generates a map of CPD of the scanned area of the sample. Initially, we get an image of CPD with a pseudo colour scale in eV or mV. By applying the work function of the tip it is possible to get work function mapping from the CPD image. KPFM was performed over hBN/Cu system. 3-4 samples from sputter deposition were used for this measurement. No special preparation technique was required prior to the measurement.

### 3.3.6. Conductive atomic force microscopy:

Principle of operation - Conductive atomic force microscopy or CAFM is a scanning probe microscopic technique in which an atomic force microscope is used to map the current obtained from a sample surface.

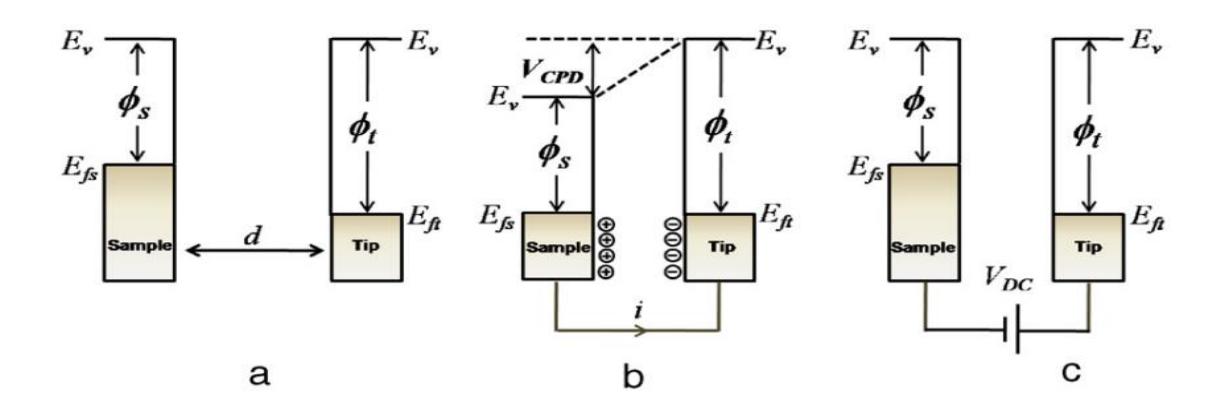


Figure. 3.13 AFM tip-sample electronic energy levels: (a) tip-sample separated by distance d without any electrical contact, (b) electrical contact between tip and sample and (c) To nullify the CPD a voltage (Vdc) is applied between tip and sample.  $E_v$  is the vacuum energy level,  $E_{fs}$  and  $E_{ft}$  are Fermi energy levels of the sample and tip, respectively.

A conducting tip is used for CAFM, and a bias is applied between the CAFM tip and sample <sup>14</sup>. The total current I is given by I= J.Ae<sub>ff</sub>, where J is the current density and A<sub>eff</sub> is the effective total area from which electrons are flowing. The lower the effective total area higher is the resolution of the CAFM. The applied bias is responsible for the flow of electrons.

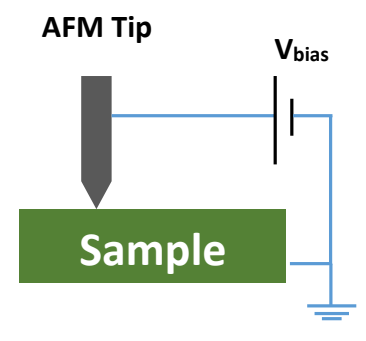


Figure .3.14 Tip sample configuration in a conductive AFM.

Instrumentation – Generally the applied bias varies from 1-5 V and the compliance current of CAFM is 20 nA. The CAFM tip raster the selected sample area and generates a current map of the selected area. At the same time, a topography map is also generated of the same selected area. The voltage can be varied during the raster of the sample or it can be kept constant. The feedback loop, raster process and piezo are similar to that of an AFM. Generally, a Pt/Ir coated tip is used for CAFM with a 20 nm tip radius. CAFM can be performed both in ambience condition and in ultrahigh vacuum. In an ultra-high vacuum the effective area for electron flow decreases (as very little humidity is present) which increases the resolution. Figure 3.14 shows the tip-sample configuration in a cafe.

cAFM is primarily used to investigate the I-V loop characteristic of hBN/Cu systems and thereby studying the resistive switching properties. NO special preparation is needed for this experiment. 4-5 samples from a different batch of deposition (both CVD and sputtering) was used for cAFM studies.

## 3.4 Spectroscopy.

The study of the interaction of matter with electromagnetic radiation is called spectroscopy. This current work deals with mainly X-ray photoelectron spectroscopy, Raman spectroscopy, Fourier transform infrared spectroscopy and UV-visible spectroscopy. Each technique has been used to gather specific information about the sample in question.

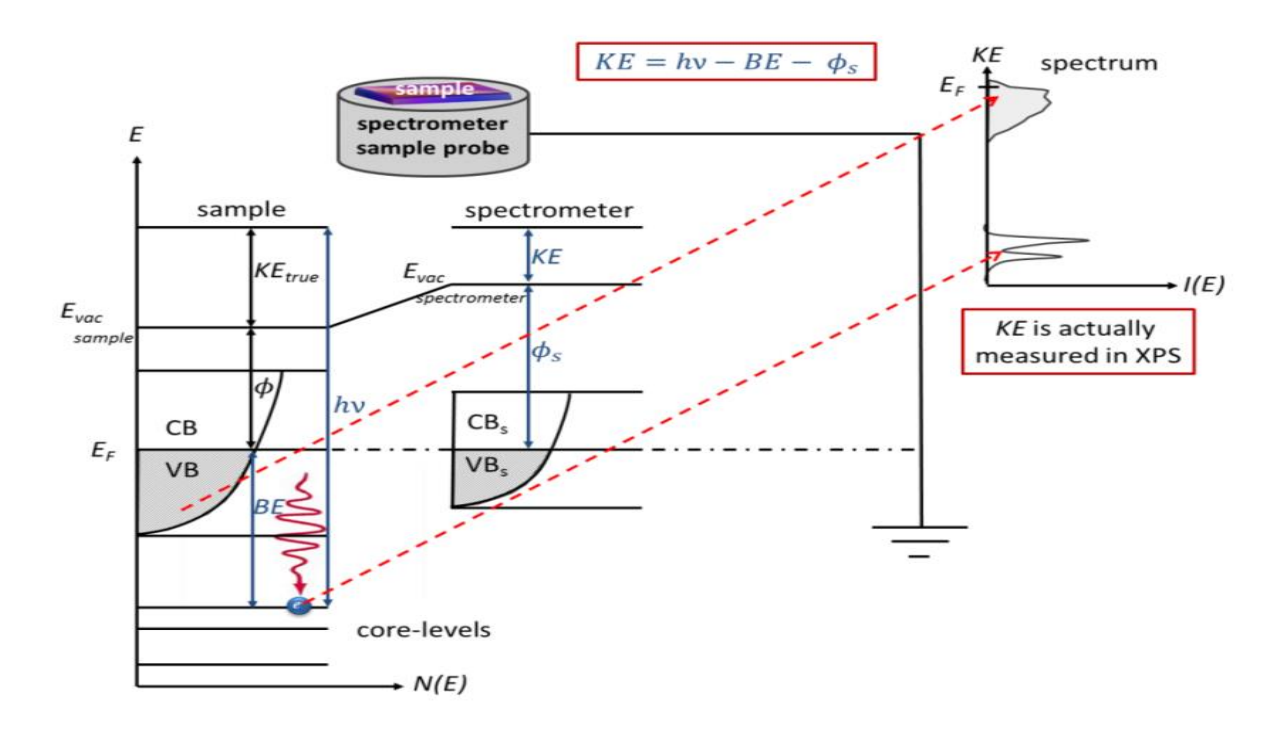
# **3.4.1.** Energy-dispersive X-ray spectroscopy:

Principle of operation- Energy-dispersive X-ray spectroscopy (EDS or EDAX) is an analytical technique used to determine the elemental or chemical nature of a material. It works on the principle of identifying an element from its characteristic X-ray spectrum. When the electron from the electron gun of the FESM strikes the sample, some of the incident electrons ejects the core level electron of the sample. This creates a vacancy in the core level, to fill this vacancy electron from the higher level jumps to it. This process releases energy in the form of X-rays. As the energy difference between the different stationary orbits of an atom is the characteristic of an element, so is the X-ray emitted due to the transition between them. By registering this X-ray with a detector EDS technique enables us to identify the elements present in the sample. Instrumentation - In our work, we used the EDS detector which was fitted to the FESEM chamber. For the EDS measurement in our work, we used 20kV of EHT and the working distance was 10 mm. High EHT is required as the impinging electrons should have enough kinetic energy to strike off a core level electron of the sample material. A detector is used to detect the X rays and is converted to voltage signals which are further processed. The detector is maintained at cryogenic temperature. The cooling of the detector is either done by liquid nitrogen or by Peltier cooling.

#### 3.4.2. X-ray photoelectron spectroscopy:

Principle of operation - When any material is irradiated with photons, three incidents may occur, 1) the photons may not interact with the material, 2) the photons may take part in inelastic scattering with the material atoms – Compton effect, 3) photoelectric effect- where the photons transfer all their energies to eject an electron from any of the stationary orbits of the material atom. The photoemission of the electron will only occur if the energy of the incoming photons is greater than the binding energy of the irradiated electron. X-ray photoelectron spectroscopy is basically a photoelectric effect where high energetic X-rays strike a material surface and ejects a core level electron. Figure 3.15 shows the energy level diagram for XPS with the sample spectrometer in electrical contact <sup>15</sup>. The sample and the spectrometer are in electrical contact, this makes their Fermi level equal. The equation to obtain the binding energy of a core of an element is B.E=hv-K.E-φ<sub>s</sub>, where hv is the energy of the

incident photo electrons, K.E is the kinetic energy of the ejected electrons coming from the sample and  $\phi_s$  is the work function of the spectrometer. The spectrometer is calibrated by using an Au sample. We measure the kinetic energy of the ejected electrons and calculate the binding energy of the sample.



 $Figure.\ 3.15.\ Energy\ level\ diagram\ for\ XPS\ with\ sample\ and\ spectrometer\ probe\ in\ contact.$ 

Instrumentation and data analysis -A standard XPS instrument consists of a vacuum chamber, X-ray source, energy analyser and data system. The XPS system used was from Axis Ultra, equipped with a monochromatic Al Kα X-ray source (1486.6 eV). The vacuum inside the chamber was maintained at 10<sup>-9</sup> mBar and a load lock system was used to load the samples inside the chamber. The use of load lock decreased the pumping time considerably. The binding energy of carbon C1s which is at 284.6 eV is used as a reference for the analysis of the biding energy of other elements. When C1s is in question Au is taken as the reference element. The obtained data is the collection of electrons of different energies named as count per second (cps), this cps is plotted with respect to the binding energy. Along with the respective binding energy peaks, a background is obtained. This back ground is due to the inelastic scattering of electrons. This background has to be subtracted during data analysis. Generally, three types of background removal are applied in XPS data analysis. Which are linear, Shirley and Tougaard background. Background removal and peak fitting can be done by many software like origin, casa XPS, peak fit pro etc.

Type of peaks obtained in XPS –Different types of peaks are observed in an XPS spectrum. Some of them are fundamental ones related to the XPS technique and some of them are sample-specific. Also, a few peaks appear due to the effect of the instrument. The following are the different major types of peak that can appear in XPS  $^{16}$  –

a) Photoelectron lines - The photoelectron lines arise due to the core-shell electrons. They are most intense and sharp in nature. They are mostly symmetrical in nature but in some metals

due to electron coupling, they become asymmetrical. The photoelectron lines of non-conductors are 0.5 eV wider than that of conductors.

- b) Auger lines The incoming X-ray photon ejects a core level electron, the outer shell electrons fill up the vacancy at the core-shell by releasing energy in the form of X-ray. Sometimes these X rays knock out an electron from another shell, this electron is called an Auger electron and the process is called the Auger process. The four main Auger lines are KLL, LMM, MNM and NOO, these lines are identified by the initial and final vacancy states. Like in the KLL shell the initial vacancy is at the K shell and the final two vacancies is at the L shell. Auger lines are independent of the photo ionization energy.
- c) Satellite X-ray peaks If the X-ray source is not strictly monochromatic apart from the characteristic X-ray line some other minor components also appear at higher photon energies.
- d) Shake up lines Sometimes the photo emission of an electron leaves the ion in the excited state. In this process the kinetic energy of the photo electron is reduced, the difference being equal to the difference between the ground state and the excited state of the ion. This

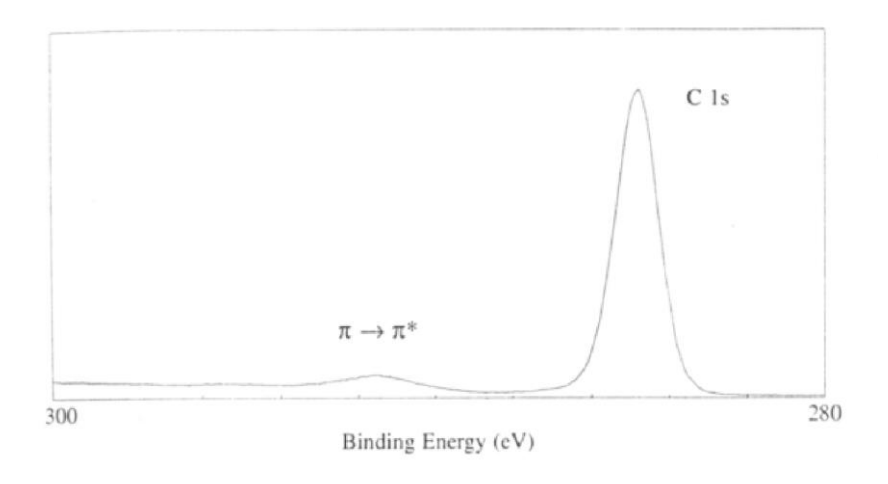


Figure. 3.16 A typical XPS spectra exhibiting C1s

results in the appearance of satellite peaks at binding energy higher than the main peak. In figure. 3.16 we can see a shakeup line in C1s as  $\pi$ - $\pi$ \* (HOMO-LUMO) peak. The main peak is at 284.6 eV respective to sp<sup>2</sup> hybridisation.

XPS has performed over hBN/Cu samples. 8-10 samples from different batches of deposition (both sputtering and CVD) were used for XPS measurement. The samples were not processed before the XPS measurement.

### 3.4.3. Raman spectroscopy:

Raman spectroscopy deals with the inelastic scattering of photons by matter. It is a highly versatile characterization method that can be employed in solid, liquid and gaseous phases. Due to its versatility, it is widely used in fields of physics, chemistry, material science, explosive research and biomedical application. Raman scattering has a major application in pharmaceutical research. Raman spectroscopy has proved to be a major player in two-dimensional materials research most notably in graphene research. The layer dependence of the Raman spectrum of graphene has made it one of the hall mark to identify pristine graphene.

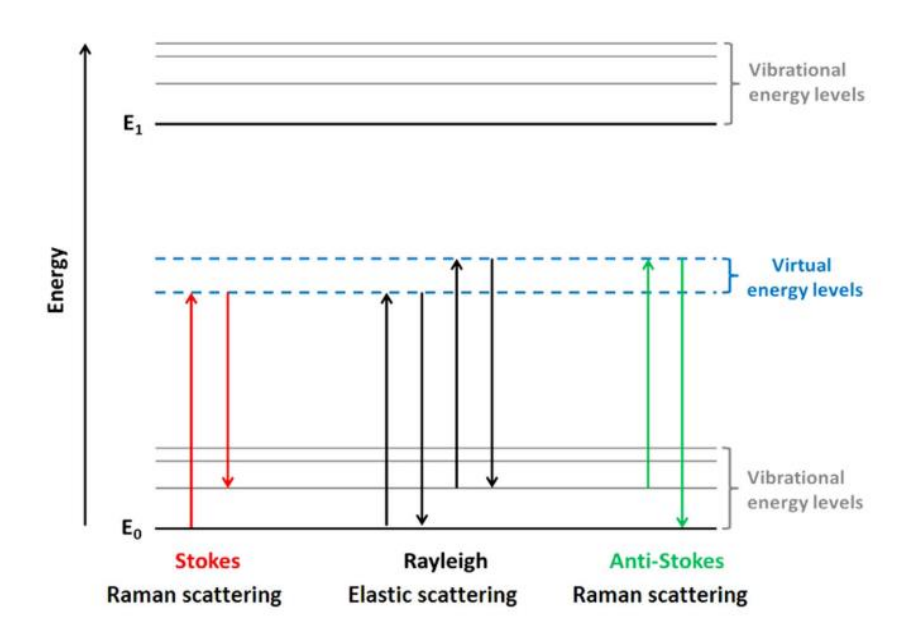


Figure. 3.17 Energy transitions in Raman scattering.

Principle of operation - When incident light interacts with any molecule, it excites it to a virtual energy state, most of the time the excited molecule relaxes back to the ground state by emitting the same amount of energy as that of the incident one. Sometimes the molecules undergo inelastic scattering releasing the different amount of energy, this inelastic scattering is the basis of Raman spectroscopy. Figure 3.17 depicts the energy transitions involved in Raman scattering <sup>17</sup>. Raman scattering comprises of Stokes and Anti Stokes scattering. When the excited molecule belonged to the ground state it gives rise to stoke lines. Due to thermal distribution initially, some molecules resides at a higher vibration energy level, these molecules are responsible for anti-Stoke lines. The Raman shift is given by  $\Delta\lambda = 1/\lambda_0 - 1/\lambda$ , where  $\lambda_0$  is the wavelength of the incident beam and  $\lambda$  is the wavelength of the stokes line. The Raman shift is plotted along the X-axis and the number of detected due to Raman scattering is plotted in the Y-axis.

Instrumentation - Due to this inherent nature of weak interaction several methods has come up to enhance the Raman signal coming out of the material. One of the popular methods to enhance Raman signal is surface-enhanced Raman spectroscopy or "SERS", SERS is basically a Raman spectroscopy where enhancement of Raman spectrum of a material is done by the surface activity of another material. Mostly gold and silver Nano particle (10 nm) used for this purpose. Hexagonal boron nitride is also be used for enhancement of Raman signal. Generally, a monochromatic laser source is used as the incident light source in Raman spectroscopy. Laser is used as it produces coherent and high-intensity monochromatic light, 532 nm, 514 nm, 633 nm and 785 nm are among the wavelengths used for Raman spectroscopy. We have used a 532 nm laser (100 mW) for our experiments (Horiba labram Raman spectrometer) along with a 100X objective (0.9 NA). The as-grown h BN film over the copper substrate did not produce the Raman spectrum, as the fluorescence background was dominant, so it has to be transferred over dielectric substrate like SiO<sub>2</sub>/Si to obtain the Raman spectrum.

### 3.4.4. Fourier transform infrared spectroscopy:

Principle of operation - Fourier transform infrared spectroscopy or FTRIR is an analytical spectroscopic technique to obtain the infrared spectrum of a sample in absorption or emission

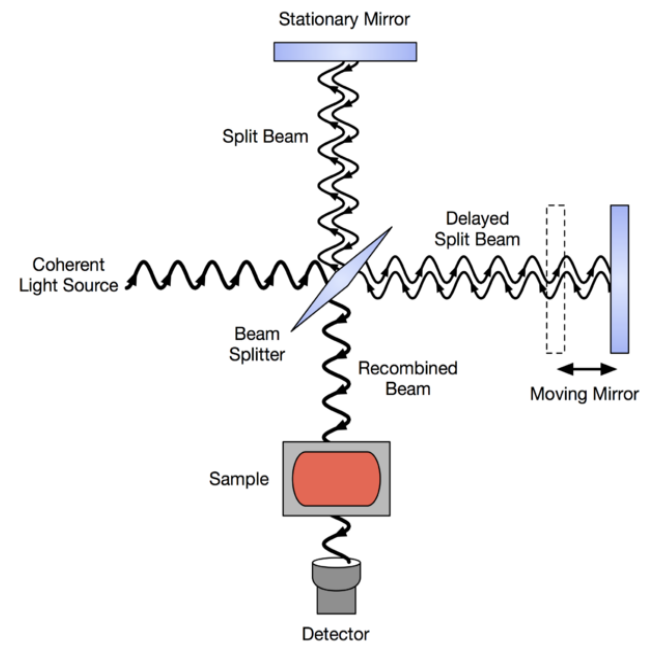


Figure. 3.18 Schematics of FTIR.

mode. Solid, liquid and gaseous samples can be used for spectroscopy. When a material is irradiated with the infrared spectrum, energy is absorbed and the wavelength of the absorbed energy is a function of vibrational states. By recording the spectrum vibrational modes and molecules which generates these states can be identified.

Instrumentation - In FTIR full spectrum light is irradiated and shines a Michelson interferometer. The mirror in the Michelson interferometer is moved periodically, as it moves it blocks and transmits each wavelength of light. The intensity of the light rays coming from the sample is recorded by the detector and the distance moved by the mirror is also recorded. Fourier transform is used to generate the spectrum from the length scale of the mirror movement. Figure. 3.18 shows the schematics of an FTIR in transmittance mode. Although FTIR can be performed in both reflectance and transmittance mode we performed FTIR of hexagonal boron nitride in reflectance mode. The films were transferred by wet etching from the copper substrate to SiO<sub>2</sub>/Si substrate for FTIR measurements.

**3.4.5. UV-visible spectroscopy:**\_Ultraviolet-visible spectroscopy or simply UV-Vis spectroscopy is an absorbance or reflectance spectroscopy where electromagnetic radiation from 200 nm to 800 nm is irradiated over a sample and the scattered radiation is recorded. During spectroscopy, if the energy of the incoming photon exactly matches with the band gap of the sample material then we observe a peak at the corresponding wavelength. This absorbance can be used in a quantitative manner to obtain the concentration in the case of liquid samples. The band gap of the material can be determined from the absorbance spectrum by using a Tauc plot.

Instrumentation - This technique can be applied to solid, liquid and gaseous samples alike. A typical UV-Vis spectrometer uses a deuterium lamp for wavelengths from 170-335 nm and a tungsten lamp for the visible spectrum. During spectroscopy, if the energy of the incoming

photon exactly matches with the band gap of the sample material then we observe a peak at the corresponding wavelength. This absorbance can be used in a quantitative manner to obtain the concentration in the case of liquid samples.

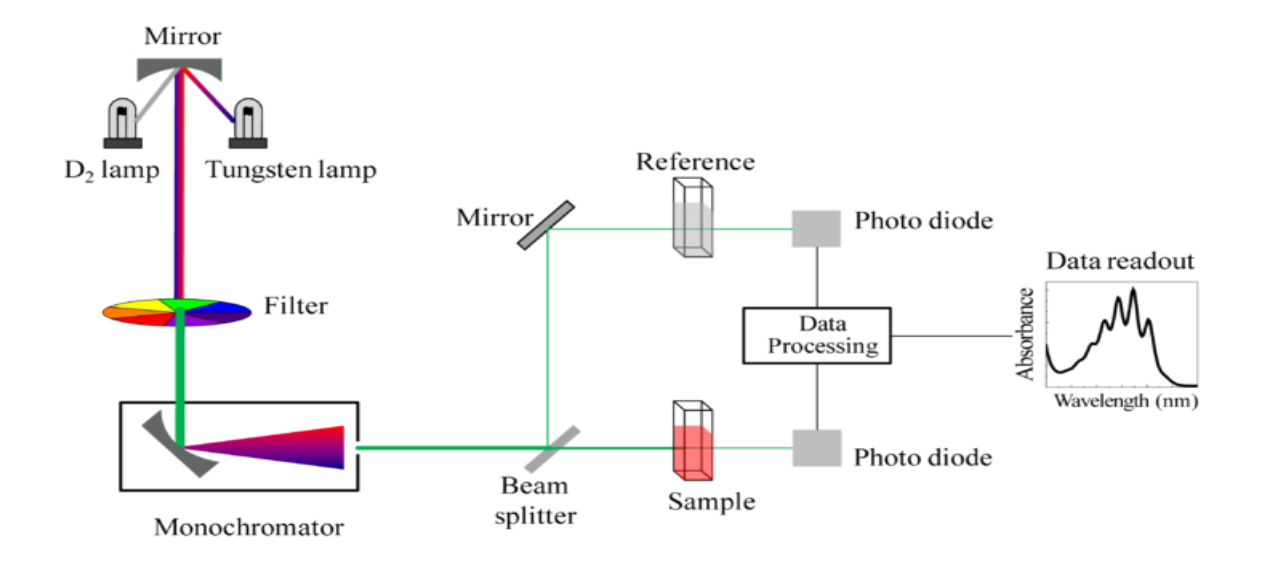


Figure. 3.19 Schematic diagram of a UV-Vis spectrometer.

The band gap of the material can be determined from the absorbance spectrum by using a Tauc plot. Figure 3.19 shows the schematic diagram of a UV-Vis spectrometer. For the practical spectroscopic purpose, both the sample/substrate and a reference substrate is used. The reference substrate is used to subtract the absorbance produced by it so that we get the absorbance data coming from the sample only. For hexagonal boron nitride samples, the film was transferred from copper substrate to quartz substrate and an empty quartz substrate was used as a reference sample. The wet transfer method was followed for the transfer process. As glass is opaque to ultraviolet radiation quartz substrate was necessary for obtaining the spectra in absorbance mode <sup>18</sup>.

For spectroscopic studies like Raman, FTIR and UV-Vis the hBN film was transferred from the copper substrate to dielectric substrates like SiO<sub>2</sub>/Si and quartz plate. Raman measurement was performed over at least 50 samples. FTIR and UV-Vis have performed over 3-4 samples. Apart from the transfer of the sample, no special preparation is needed for these three spectroscopic studies.

#### 3.5 Diffraction studies.

Electron back scattered diffraction and X-ray diffraction of the substrate (25-micron thick copper) has been studied. X-ray diffraction provided crystallographic information about bulk whereas electron back scattered diffraction provided information about the surface of the foil only.

### 3.5.1. X-Ray diffraction:

Principle of operation - X-Ray diffractometer is readily used to obtain crystallographic information about a known or unknown material. It is one of the oldest technique to obtain

such information. Figure 3.20 and 3.21 shows the schematics Bragg diffraction condition in crystal planes and an X-ray diffractometer <sup>19</sup>.

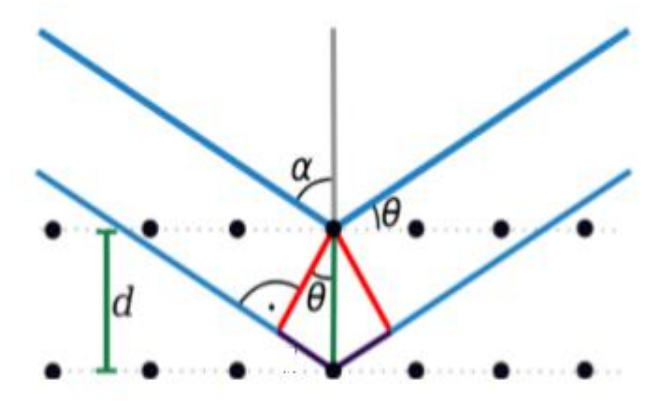


Figure. 3.20 Schematics of an x-ray diffractometer.

When Bragg condition is satisfied the incident X rays produces constructive interference. As the  $\theta$  is measured and wavelength is known the inter planar spacing d can be obtained. Instrumentation - The x-ray diffractometer roughly consists of an x-ray source, collimator detector and a sample stage. The x-ray is produced by a cathode ray tube, after they are produced the slits are used to make them monochromatic.

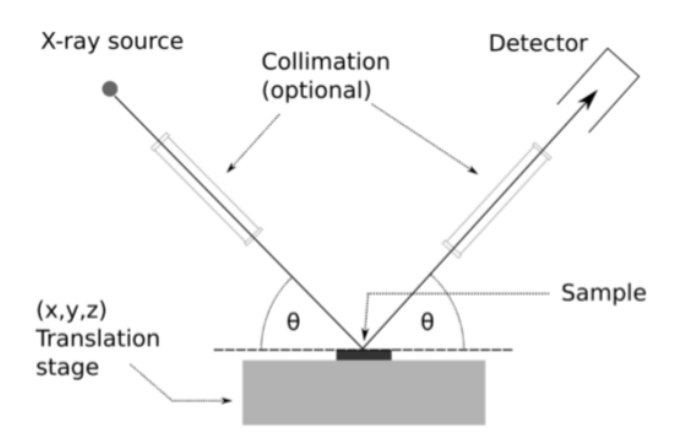


Figure. 3.21 X-ray scattering through Bragg angle.

Once they are diffracted from the sample they are detected by the detector. If the sample is crystalline the diffracted photons when detected from sharp spikes at certain angles respective to the sample, and if it was amorphous a noisy background occurs. The penetration depth of the X-ray is about 50-200  $\mu$ m<sup>20</sup>. To reduce the penetration depth of X rays GIXD (glancing incidence x-ray diffraction) is performed. In this technique, the angle of incidence  $\theta$  is reduced to a very small value (like 0.5°) so that majority of the X-ray photons are diffracted by the first few layers of the material. We performed x-ray diffraction to study the crystallographic nature of the as-received copper foil and also their nature after annealing. X-ray diffraction provides information about the crystallographic nature of the sample in bulk, by no means can it be used to properly identify the crystal orientation of the surface (down to a depth of 20-40 nm).

X-ray diffraction was carried out to estimate the crystallographic orientation of the copper foil. As received copper foil and annealed copper foil, both were used for XRD measurement. The foils were cleaned with dilute nitric acid before XRD measurement to remove the native oxide layer. 20-30 samples were tested with XRD measurements.

#### 3.5.2. Electron back scattered diffraction (EBSD):

Principle of operation - Electron backscattered diffraction is an analytical technique by which the crystallographic orientation of a surface of a material can be determined. EBSD is done in conjugation with scanning electron microscopy. The incoming electron beam collides (inside the FESEM chamber) with the sample and creates both elastic and non-elastic collisions. The elastically rebound electrons produce a diffraction pattern and the diffraction pattern depends upon the crystallographic nature of the sample. As in X-ray diffraction here too Brag's condition has to be satisfied for a diffraction pattern to occur. The electrons after diffraction form Kikuchi bands, each Kikuchi band can be traced back to the Miller indices of the crystal plane from which it originated.

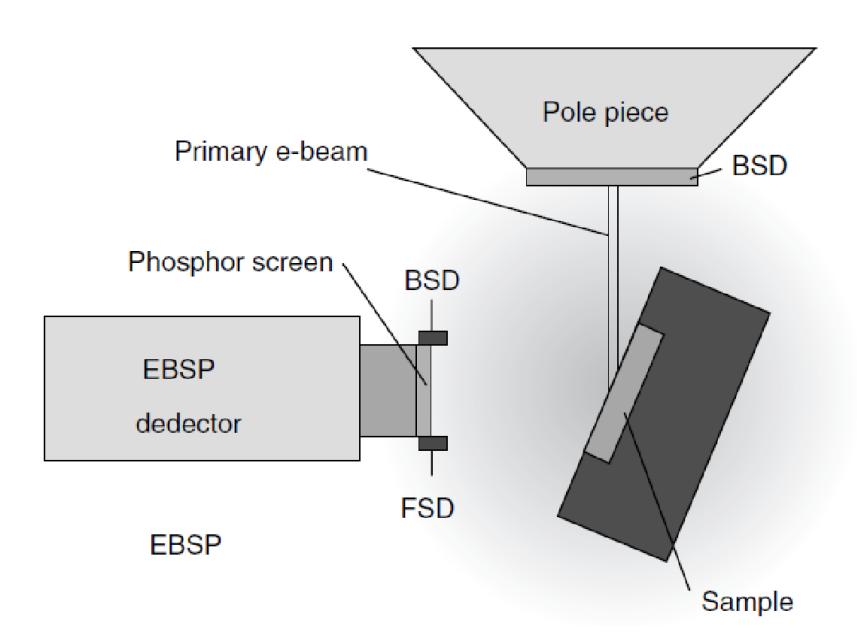


Figure. 3.22. Schematic diagram of the sample arrangement inside SEM chamber for EBSD measurement.

Instrumentation - EBSD detector is attached to FESEM chamber in which electrons with accelerating voltage is irradiated over the sample surface. The accelerating voltage is typical of the order of 15-25 kV. The sample is tilted by 20° with the electron beam. First, a SEM image is obtained over which EBSD scan is done. A CMOS/CCD sensor is used to collect the patterns that originated from the diffraction pattern. Once the pattern has been collected indexing is done. Figure 3.22 shows the schematic diagram of the sample and detector arrangement for EBSD mapping. Hough transformation is used to detect the crystal orientation from the pattern. For EBSD we require a highly polished sample as too much surface corrugation blocks the diffracted electrons from reaching the detector. We performed EBSD over the electropolished copper substrates and h BN / Cu substrate.

Typical data presentation – An inverse pole figure is used to read EBSD data. A pole figure is a tool for plotting 3D information in 2D.

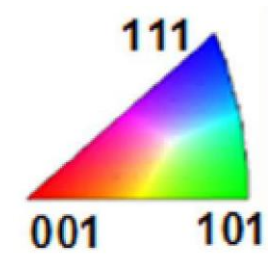


Figure. 3.23 IPF map of cubic system.

A pole figure represents the crystal direction of a material with respect to the sample's reference system. But an inverse pole figure represents the sample's direction with respect to the crystal's reference system. The rolling direction (RD) of the sample can be represented with respect to any major crystal axis like (111), (100) and (110). Due to the symmetry of the crystal system in most cases, the inverse pole figure map can be reduced to a triangle. Inverse pole figure is generally used as a default colour scheme for EBSD orientation maps. Figure 3.23 shows the IPF map for the cubic system. Complete blue refers to (111) planes, complete red is for (001) and green for (101). Different crystal system has different IPF maps as their stereographic projections are different.

EBSD was performed over as received copper foil after electropolishing it. Electropolishing was done to decrease the surface roughness as EBSD requires a highly polished surface. EBSD was also done for annealed copper foils and hBN films to estimate the grain size of the film. A total of about 20 samples experimented with EBSD.

### 3.5.3. Selected area electron diffraction:

Principle of operation - Selected area electron diffraction (SAED) is a crystallographic technique that is very effective in determining the crystallographic orientation of samples which has a smaller dimension. SAED is performed with the help of a transmission electron microscope. The accelerating voltage of the TEM can be set at 100 kV or 200 kV, depending upon the sample. The incoming electrons behave like waves and the array of lattice points of the sample behaves like a grating. This interaction between the electron waves and the sample lattice points gives rise to a diffraction pattern. The diffraction pattern obtained depends upon the crystal structure of the sample. Each obtained spot in the TEM image is a satisfied diffraction condition.

A standard TEM IS used to obtain a SAED pattern. Instead of recording the image formed by the transmitted electrons, the diffraction pattern is recorded. Just like TEM imaging here too thick a sample has to be thinned down to obtain the diffraction pattern. Different crystal systems generate different diffraction pattern. The obtained SAED image is in reciprocal space, d spacing and lattice constant can be calculated by using the column length and resolution of the electron wave.

# 3.6 Miscellaneous experiments

In conjugation with characterization and synthesis techniques, other complementary experiments were carried out. These experiments include electro polishing of the copper foil, setting up a micromanipulator and transfer of the h BN film from the copper substrate to different dielectric substrates.

## 3.6.1. Transfer process:

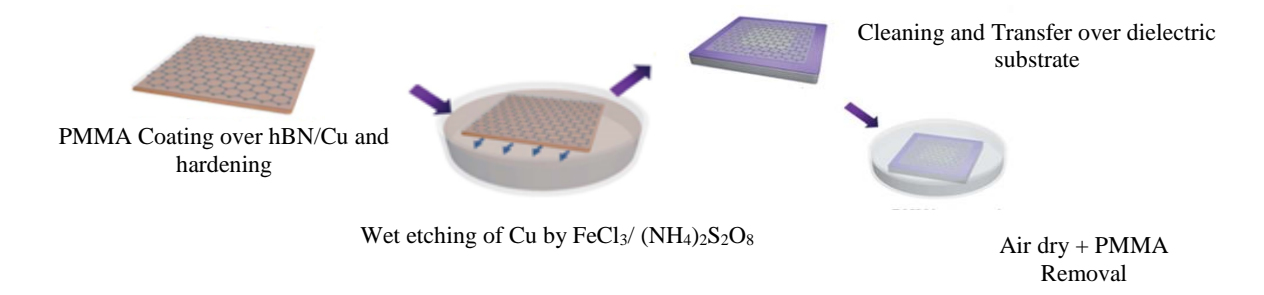


Figure .3.26 Steps for wet transfer of h BN over dielectric substrates.

Transfer of h BN from copper substrate over dielectric substrates has been done by wet etching of the copper foil. Figure 3.26 shows the steps of hBN transfer <sup>21</sup>. For wet etching 1M solution of ferric chloride (FeCl<sub>3</sub>) and in some experiments 0.1 M solution of Ammonium persulphate ((NH<sub>4</sub>)<sub>2</sub>S<sub>2</sub>O<sub>8</sub>) has been used. 1% PMMA (Poly (methyl methacrylate)) solution in anisole has been used as a protective layer coating over h BN. After coating h BN/Cu with 1% PMMA solution it was annealed in air at 60°C for 1 min to harden the PMMA layer. Then PMMA/hBN/Cu composite was floated over the etchant solution. Once the copper is fully etched the floating PMMA/hBN layer is scooped with a clean SiO<sub>2</sub>/Si substrate and the film is once again floated over deionised water. This is done to clean the etchant from the PMMA/h BN layer. Finally, the PMMA/hBN film is scooped from D.I water with a desired dielectric layer and air-dried for 8-10 hr. After drying the PMMA layer was removed by dipping in hot acetone (40°C). Acetone dip was followed by isopropyl alcohol dip and D.I water dip. The transfer has been done over SiO<sub>2</sub>, GaAs and quartz plate.

### 3.7 Materials used

List of chemicals used for synthesising hexagonal boron nitride, to clean the copper substrate and other miscellaneous chemicals:

Name	Purity	Make	
Ammonia Borane	97%	Sigma Aldrich	
Powder			
Nitric acid	70%	FINAR	
Isopropyl alcohol	Sisco research	99%	
	laboratories		
Acetone	99.9%	SRL	

Ferric Chloride	98%	Avra			
(anhydrous)					
25 micron thick	99.8%	Alfa Aesar			
copper foil					
100 micron thick	99.9%	Alfa Aesar			
copper foil					
Name	Purity	Make			
Ortho phosphoric	85%	SRL			
acid					
Ammonium	98%	Sigma Aldrich			
Persulphate					
Crystal violet powder	95%	Sigma Aldrich			
Methylene Blue	82%	Sigma Aldrich			
powder					
Malachite green	97&	Sigma Aldrich			
powder					
PMMA Powder	99%	Sigma Aldrich			
Anisole	99.7%	Sigma Aldrich			

### 3.7 References:

- 1. Liu, Z. *et al.* 2011\_Direct Growth of Graphene-Hexagonal Boron Nitride Stacked Layers.pdf. 2032–2037 (2011).
- 2. Kim, S. M. *et al.* The effect of copper pre-cleaning on graphene synthesis. *Nanotechnology* **24**, (2013).
- 3. Manual, I. Electron Microscopy Sciences INSTRUCTIONAL MANUAL Twin Jet Electropolisher Model 501B. 0–25.
- 4. Huang, Y. *et al.* Reliable Exfoliation of Large-Area High-Quality Flakes of Graphene and Other Two-Dimensional Materials. *ACS Nano* **9**, 10612–10620 (2015).
- 5. Yi, M. & Shen, Z. A review on mechanical exfoliation for the scalable production of graphene. *J. Mater. Chem. A* **3**, 11700–11715 (2015).
- 6. Bosco, R., Van Den Beucken, J. V., Leeuwenburgh, S. & Jansen, J. Surface engineering for bone implants: A trend from passive to active surfaces. *Coatings* **2**, 95–119 (2012).
- 7. Takahashi, Y., Hattori, S., Soga, T., Sakai, S. & Umeno, M. Mechanism of MOCVD Growth for GaAs and AlAs. *Jpn. J. Appl. Phys.* **23**, 709–713 (1984).
- 8. Chen, X., Zheng, B. & Liu, H. Optical and digital microscopic imaging techniques and applications in pathology. *Anal. Cell. Pathol.* **34**, 5–18 (2011).
- 9. Roddaro, S., Pingue, P., Piazza, V., Pellegrini, V. & Beltram, F. The optical visibility of graphene: Interference colors of ultrathin graphite on SiO2. *Nano Lett.* **7**, 2707–2710 (2007).
- 10. Marturi, N. Vision and visual servoing for nanomanipulation and nanocharacterization in scanning electron microscope. 180 (2013).
- 11. Maver, U. *et al.* Polymer Characterization with the Atomic Force Microscope. *Polym. Sci.* (2013) doi:10.5772/51060.
- 12. Atomic Force Microscopy. Science (80-. ). 1–14.
- 13. Melitz, W., Shen, J., Kummel, A. C. & Lee, S. Kelvin probe force microscopy and its application. *Surf. Sci. Rep.* **66**, 1–27 (2011).
- 14. Avila, A. & Bhushan, B. Electrical measurement techniques in atomic force microscopy. *Crit. Rev. Solid State Mater. Sci.* **35**, 38–51 (2010).
- 15. Naturwissenschaften, D. Der. In-operando hard X-ray photoelectron spectroscopy study on the resistive switching physics of HfO 2 -based RRAM. (2014).
- 16. Moulder, J. F., Stickle, W. F., Sobol, P. E. & Bomben, K. D. Handbook of X-ray Photoelectron Spectroscopy Edited by. *Handb. X-ray Photoelectron Spectrosc.* 261

(1992).

- 17. Ember, K. J. I. *et al.* Raman spectroscopy and regenerative medicine: a review. *npj Regen. Med.* **2**, (2017).
- 18. De Caro, C. UV / VIS Spectrophotometry. *Mettler-Toledo Int.* 4–14 (2015).
- 19. Kuhlmann, K. Development and Commissioning of a Prototype Neutron Backscattering Spectrometer with an Energy Resolution Enhanced by an Order of Magnitude using GaAs Single Crystals. (2018).
- 20. Liu, J., Saw, R. E. & Kiang, Y. H. Calculation of effective penetration depth in X-ray diffraction for pharmaceutical solids. *J. Pharm. Sci.* **99**, 3807–3814 (2010).
- 21. Choi, Y. *et al.* The effect of the graphene integration process on the performance of graphene-based Schottky junction solar cells. *J. Mater. Chem. A* **5**, 18716–18724 (2017).

### Chapter 4

# Hexagonal BN synthesized by RF magnetron sputtering

Hexagonal boron nitride is a wide band gap-meta material. hBN has a layered structure similar to graphite with an in-plane lattice mismatch of 1.7% only, structural aspects of hBN has been discussed in detail in chapter 2 <sup>1,2</sup>. hBN with its atomically smooth surface and homogeneous charge distribution became popular as the preferred dielectric substrate for graphene-based devices <sup>3,4,5</sup>. Since then it has firmly established its place as one of the members of the expanding 2D materials family. It is now frequently used as tunnel barriers and encapsulation layers for nanoelectronic devices <sup>6,7,8</sup>. It has a thickness-dependent photoluminescence property, with bulk hBN exhibiting high exciton luminescence in the deep UV region making it suitable for deep-UV photonics applications <sup>9,10</sup>. It is also a hyperbolic metamaterial with a dielectric constant same in the basal plane but having opposite signs in the normal plane <sup>11</sup>. To achieve the full potential of hBN scalable and high yield growth procedures are required. Here, we demonstrate the synthesis of hBN by reactive R.F magnetron sputtering over the copper foil. Copper foil is used as a substrate which is less expensive and the wet etching transfer process can easily be applied. Copper foil preparation conditions determine the crystallographic orientation of BN films. Synthesis of hBN over copper will provide an excellent platform for scalable synthesis of multilayer hBN for both research and industrial purpose.

Large area hexagonal boron nitride thin films can be synthesized by a number of methods-like chemical vapour deposition (CVD), molecular beam epitaxy (MBE) and radio frequency (RF) sputtering. The crystallinity and crystal orientation of the substrate plays a crucial role in determining the quality of the hBN films. CVD is the most popular method to synthesize large area 2D materials including hBN <sup>12,13</sup>. In CVD synthesis different kinds of transition metal substrates are utilized for the growth of 2D materials <sup>14,15,16</sup>. Copper foils are the most popular choice as a substrate for the synthesis of hBN since they are relatively inexpensive and the carbon solubility in copper is also low <sup>17,18</sup>. However, in CVD it is difficult to get repeatable growth rates and high processing temperatures are required to produce high-quality films. The growth of hBN films by CVD shall be discussed in the next chapter. Physical Vapor Deposition method like RF sputtering can be used to synthesize uniform films of 2D materials over large areas <sup>19</sup>. With RF magnetron sputtering we can deposit hBN films at a lower temperature with precise control over the growth rate and it is also scalable in nature. Unlike CVD where hBN films are synthesized on metallic substrates which act as a catalyst, with RF sputtering hBN films can be deposited on noncatalytic substrates also<sup>20</sup>. In this chapter, we discuss the growth of ultrathin hBN films on weakly interacting metal substrates like Cu using reactive RF sputtering. We employed cyclic deposition at low temperatures followed by annealing to synthesize multilayer hBN films on commercially available Cu foils. We also elucidate the impact of the Cu foil preparation on the synthesis of continuous films of uniform thickness. We investigated how the Cu foil surface termination plays a deciding role in the phase selection of BN film.

### 4.1. Deposition by radio frequency sputtering.

We have employed a radio frequency sputtering method to deposit hBN over the copper substrate. The frequency of the applied alternating voltage is 13.7 MHz. Various parameters of

the deposition were involved, which are discussed below-

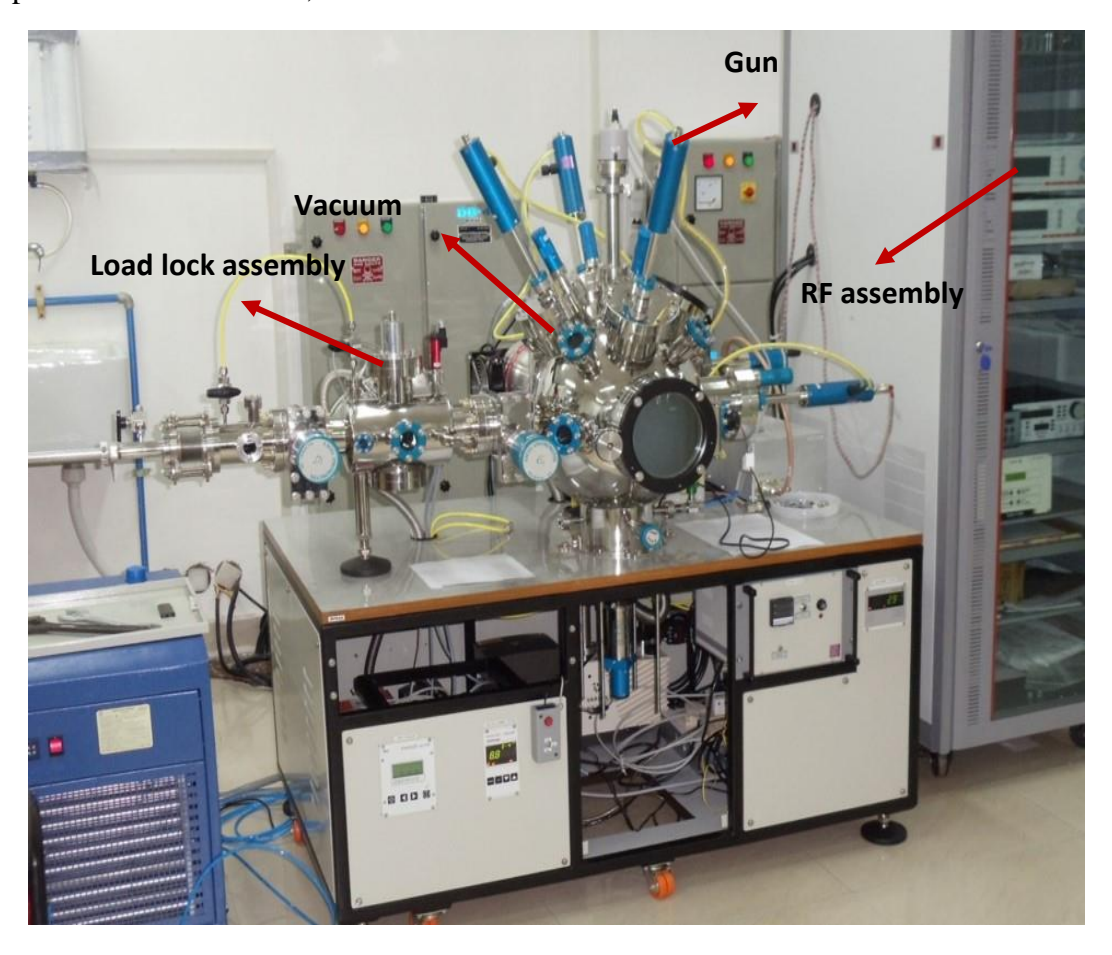


Figure 4.1 R.F sputtering set up which is used for deposition.

**4.1.1. Deposition parameters-** Deposition by sputtering requires a dedicated system. The sputtering system basically has two variations, one is radio frequency sputtering (r.f) and another one is direct current (d.c) sputtering. R,F sputtering is used for materials which have an insulating target and d.c sputtering is used for materials that have a conducting target. Thin metal films are deposited by d.c sputtering where any insulating material like zinc oxide is deposited by r.f sputtering. Hexagonal boron nitride is an insulating material therefore we used the r.f sputtering system for deposition. There were a number of parameters that has to be precisely controlled to obtain the film. The parameters that were monitored and controlled for an optimized growth that is repeatable are as follows:

**Power & impedance matching** - R.F power is an important parameter for the success and repeatability of hexagonal boron nitride deposition. The magnitude of power determines the deposition rate, high power like more than 40 W leads to faster deposition and low power results in slower deposition. High power leads to greater heat generation in the target and very efficient cooling is required to carry out deposition at high power. At the high power rate of ionization of the sputter gas increases and this increases the rate of bombardment of the ions in the target. This process heats up the target quickly. Inefficient cooling may lead to the crack of the target which will contaminate the deposited material and shall make the target useless for further deposition. We kept the target temperature at 18°C by using a water-cooled chiller. The chiller started cooling when the target temperature reached 20°C. The applied power constitutes only forward power, an impedance matching box is used to match the impedance of the circuit

with the source impedance. The source impedance is attributed to the plasma formed by the sputtering gas and is categorized into three components (capacitive, inductive and resistive). The impedance matching is important as an unmatched impedance shall give rise to a definitely reflected power. A nonzero reflected power will unnecessarily increase the target temperature and decreases the effectivity of the true power. Ideally, the reflected power should be zero.

**Substrate temperature** — The temperature of the substrate during deposition is generally referred to as the substrate temperature. The substrate (25-micron thick copper foil) was placed over a substrate holder (made up of stainless steel). The copper foil was fixed with the substrate holder by pins made up of stainless steel. No adhesive was used to hold the substrate, as at high temperature the adhesive might have melted and contaminated the deposition. Resistive heating was applied to heat the substrate holder which in turn heats up the substrate. A PID temperature controller was used to precisely control the temperature of the substrate holder. The temperature of the substrate during deposition plays a crucial role. This shall be discussed in further sections.

**Deposition Time-** The duration of the deposition is referred to as the deposition time. A digital stopwatch was used to measure the deposition time. At the end of the deposition, the r.f power supply was switched off which immediately stopped the deposition. The deposition time has to precisely controlled to ensure repeatability of the entire experiment.

Sputter gas- Sputter deposition occurs by ionizing a gas species inside the sputtering chamber. Generally, ultra-pure argon is used as a sputtering gas species. In our case, we applied reactive sputtering. We used 30 sccm of argon and 3 sccm of nitrogen. The gas combination was constant for all our experiments. A calibrated mass flow controller was used to precisely measure the amount of each time.

**Substrate rotation** - For a uniform deposition in all direction over the substrate surface substrate rotation is important. The substrate was rotated at a rate of 3 r.p.m in a clockwise direction. The orientation of the rotation either clockwise or anti-clockwise has the same effect over the outcome of the deposition. Only the magnitude of rotation affects the uniformity of the deposition.

Substrate-target distance and angle - The distance between the substrate and target were fixed at 12 cm and the angle of deposition was 45°. These parameters were fixed for every deposition. **Base pressure, pre sputtering, chamber cleaning and degassing** — Although chamber cleaning is not a parameter that has to be regulated during the deposition. But proper chamber cleaning is very important for the growth of hexagonal boron nitride by r.f sputtering. As the same deposition chamber was used to deposit other materials like cadmium telluride, zinc oxide etc. So it is crucial to remove any reminiscent material stuck to the inner walls of the deposition chamber. If the chamber is not properly cleaned, then some portion of the previously deposited material may contaminate the current deposition. Therefore it is necessary to neatly clean the inner walls of the deposition chamber and any other surface which is at the line of sight of the substrate and the target.

The base pressure is the pressure inside the chamber before pre-sputtering starts. The lower the base pressure more pure the deposition is. For our case, the base pressure was  $2x10^{\Lambda-7}$  mBar. After cleaning it took 24-36 hour to reach that pressure. A higher base pressure indicates the presence of water vapour inside the chamber. For every deposition this base pressure was constant.

After loading the sample and after the desired base pressure the substrate was degassed at 800°C for 30 min. We noticed an order change in the total pressure of the chamber at the end

of the degassing. This change in pressure can be attributed to the release of the surface adsorbed gases over the substrate as well as over the inner walls of the chamber. Although the chamber itself was not heated due to radiative heat transfer from the substrate holder the inner walls were also heated to about 50-55 degrees. Degassing serves several purposes in one go. Firstly it cleans the substrate surface and the chamber inner surface; secondly, it helps to achieve a cleaner vacuum.

After degassing, purging of the connecting tubes and pre sputtering in important. A tiny amount of air sweeps into the connecting tubes and this air has to be purged out before deposition starts. So both the argon and nitrogen connecting pipes were purged with 20 and 10 sccm of respective gases for 20 min.

Presputtering is a process where sputtering starts but without deposition, this is done by closing the shutter of the target and the substrate is closed. During handling the target and storing

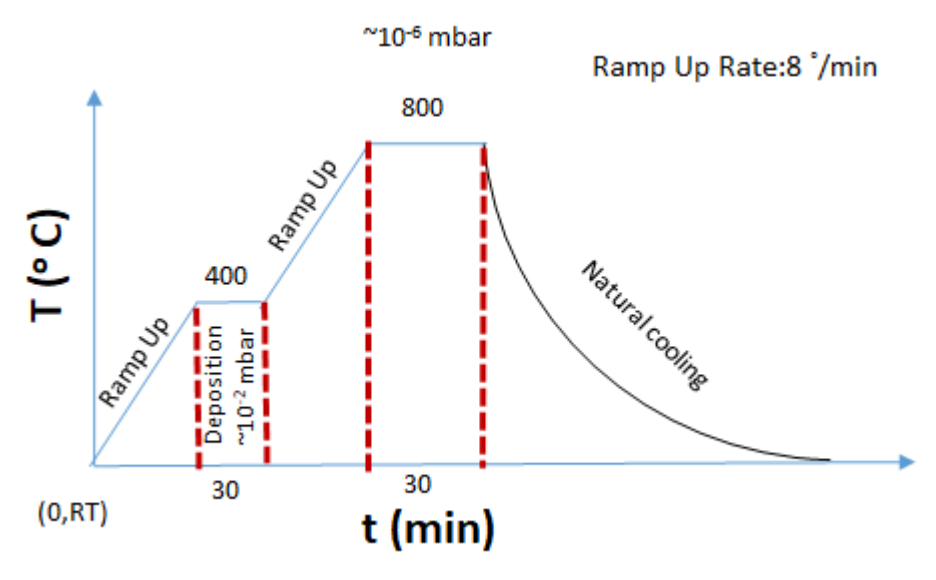


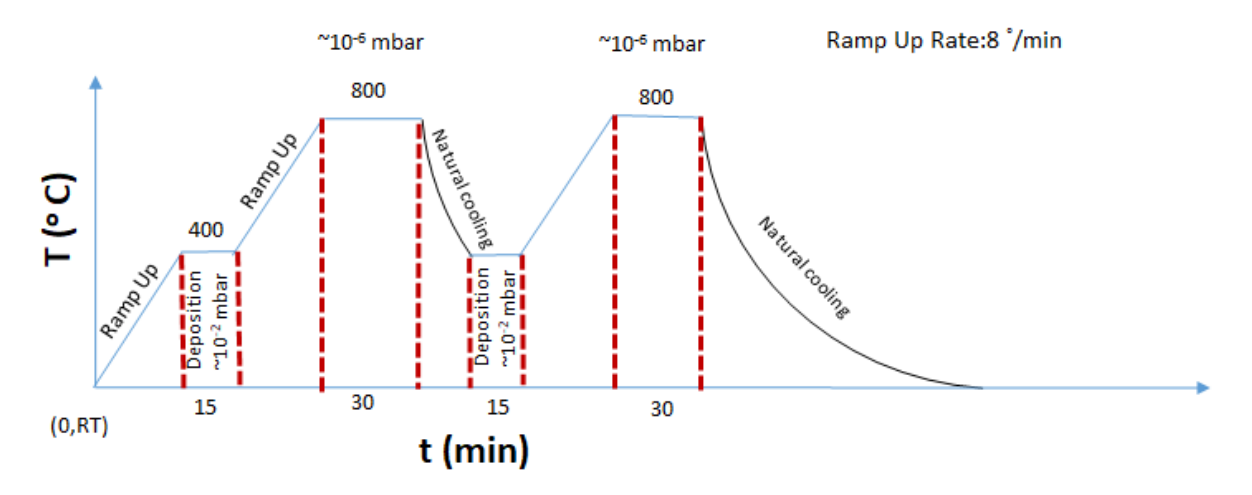
Figure 4.2 Schematics of a single step deposition of 30 min at 400° C with 30 min post-annealing at 800° C. gases and other contaminants accumulate over the target. To get a pure deposition is necessary to clean the target surface. The is cleaning was done by pre sputtering at 25 W, 30 sccm Ar, 3 sccm N2 for 6hr. The duration is important, we have noticed it takes about 5-6 hr to completely clean the target surface. Any less amount of presputtering contaminates the first deposition.

**4.1.2 Single step deposition-** Single step deposition is a process where sputtering deposition is carried out only once. The deposition is done either at high temperature or at room temperature. Following the deposition post annealing is done. For all our experiments post annealing is done at  $800^{\circ}$  C for 30 min. Fig 4.2 shows a typical one step deposition at  $400^{\circ}$  C, and was followed by deposition for 40 min ( $T_1$ ) post annealing is done at  $800^{\circ}$  C. The deposition was carried out at  $10^{-2}$  mBar pressure at  $400^{\circ}$  C for 30 min. After deposition the sputtering gas flow was stopped and the pressure during post annealing was about  $10^{-6}$  mBar.

During a single step deposition at room temperature (RT) creates mostly three-dimensional structures, as after nucleation there less surface mobility for the nucleated island to coalesce and to form bigger grains. The problem of deposition at RT is partially solved when deposition temperature increased. At high temperature deposition like that of in Fig.4.2 the higher temperature provides surface mobility for the nucleated sites to collapse. Post annealing further increases the grain size and enhances the crystallinity of the film. One problem associated with single step deposition is that the nucleation density is large and the size of the nucleated island

is comparatively small. The reason for large nucleation density is that during the total time of deposition the process of nucleation goes on because before post annealing the island dimensions are quite small and do not wet the surface completely.

**4.1.3. Multiple step deposition-** Multiple step deposition is a two or more number of deposition with post annealing after each deposition. Figure 4.3 shows a typical two step **Figure** 



4.3 Schematics of a two-step deposition of 15+15 min at 400°C with 30 min post annealing at 800°C after each set of deposition.

deposition, where a 30 min deposition is broken down into two 15 min  $(T_1+T_2)$  deposition. With an equal duration of post annealing after each set of deposition. The first deposition step acts for the formation of nucleation sites. Then first after post annealing these nucleated sites create bigger islands by coalescing. In the second stage  $(T_2)$  incoming BN monomer/ dimer/ sputtered species had bigger islands over the substrate to adhere to and this increases the size of the islands. Thus in the second step, the process of growth of the islands dominates the nucleation process. Multiple step deposition is helpful for layered growth of h BN/Cu.

#### 4.2. Results and discussion-

The 25 micron thick as the received copper foil was thinned down to this thickness by cold rolling process. This process leaves rolling marks over the surface. The SEM image in figure 4.4 (a) shows the rolling lines. The presence of rolling lines in the as-received Cu foil makes it very rough (roughness ~ 96 nm from figure 4.4 b) .The XRD plot in figure 4.4 (c) shows that the dominant crystallographic orientation of the foil is (200) , although the EBSD map in figure 4.4 (d) shows the presence of other orientations. The inset of figure 4.4 (d) is the inverse pole figure for the EBSD map, The presence of mixed colour orientation in the EBSD map tells us that the foil surface is polycrystalline in nature. But the image has a dominant red hue which tells us that although the Cu foil is polycrystalline in nature but the dominant orientation is (200). The grain size is 10- 20  $\mu m$  . The black patch is due to the un-mapped portion of the foil. EBSD is a surface-sensitive technique and as the copper surface has high average roughness some portions are not flat enough to generate consistent diffraction pattern which can be mapped.

## Copper foil processing

The as received copper foil (25  $\mu$ m thick, 99.8% purity sourced from Alfa Aesar) was first cleaned in dilute nitric<sup>21</sup> acid for about 20s for removing the native oxide from its surface. It was then rinsed with deionized water followed by cleaning with acetone and isopropyl alcohol for removing any organic contaminants (Details of the cleaning process has been discussed in chapter 5) .Different methods were followed to further process the Cu foil which are described in the table below

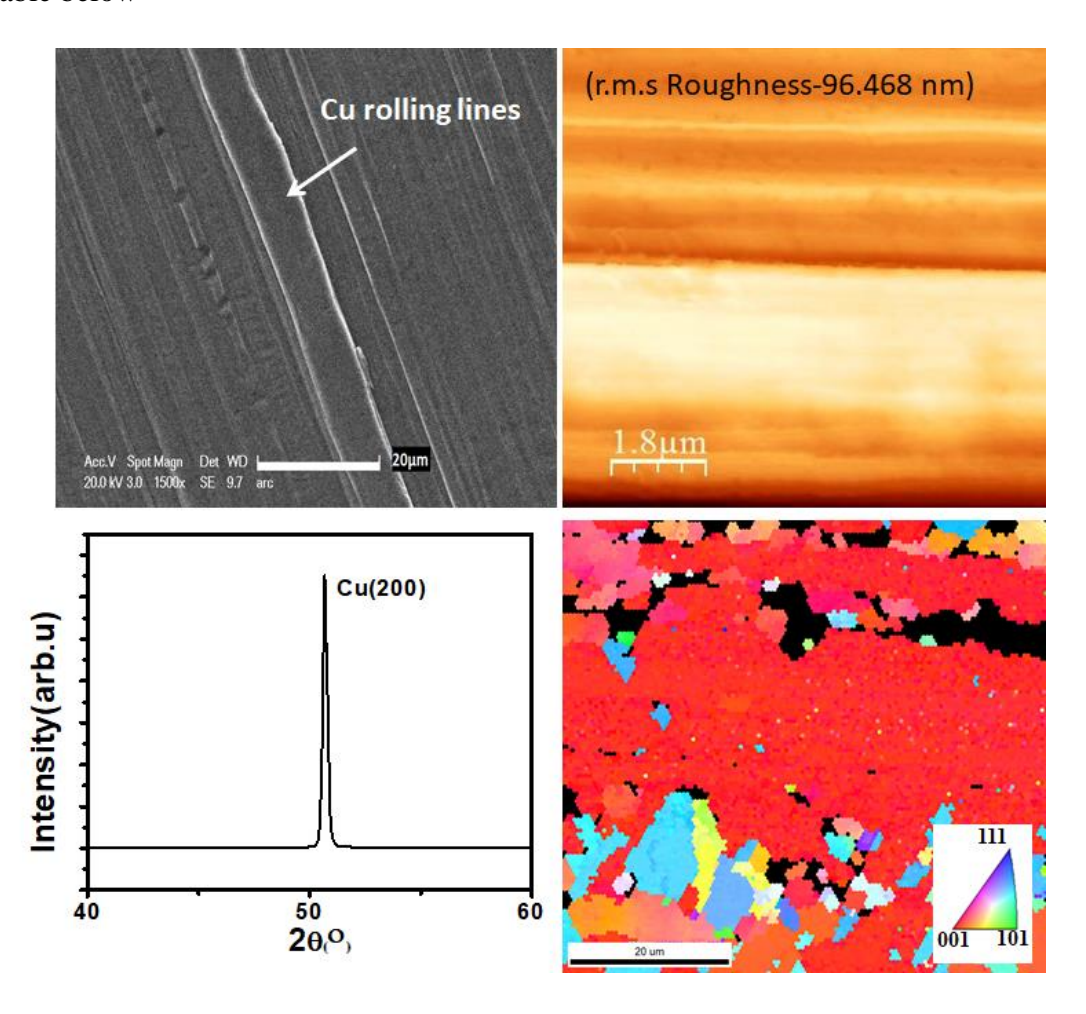


Figure 4.4 Characterization of the as received copper foil. (a) SEM  $\,$  (b) AFM  $\,$  (d) EBSD image  $\,$  (c) XRS of the as received copper foil.

Table 1:

Method I	The non-electropolished Cu foil was annealed at 900°C in Ar gas for 120 min.
Method II	The electropolished Cu foils were annealed at 900°C in Ar:H <sub>2</sub> (90:10) gas for 60 min.
Method III	The electropolished Cu foils were annealed at 1040°C in Ar:H <sub>2</sub> (90:10) gas for 60 min.

In the text i.e in this chapter, Cu foils processed using these methods are labelled as Cu M II and Cu M III respectively. Boron nitride films were synthesized on these copper foil with reactive radio frequency (rf) magnetron sputtering of h BN target (2 inch diameter with 99.99% purity) in high purity  $\text{Ar:N}_2$  (10:1) gas mixtures with total pressure  $10^{-2}$  mBar, with 25 W rf power (if not mentioned). For all depositions these parameters were kept constant. During growth the deposition time (t) was varied from 30 min to 3 hours while substrate temperature ( $T_s$ ) was varied from RT to  $400^{\circ}\text{C}$  respectively. After deposition the substrate was annealed at  $800^{\circ}\text{C}$  for 40 min. Single step and cyclic/multiple step (deposition alternated by post annealing at  $800^{\circ}\text{C}$  for 40 min) deposition were used for synthesizing hBN films.

#### 4.2.1. Film characterization-

## Characterization methods

The crystallographic orientation of the copper foil was studied by X ray diffraction using XRD, PAN analytical: X'Pert<sup>3</sup> Powder with Cu Kα line (Kα1 and Kα2 with 2:1 ratio). Electron back scattered diffraction (EBSD) using AMETEK EBSD detector fitted to FEI NOVA NANO 460 FESEM, the imaging was done at 20 KeV, sample tilted at 70°). X-ray photoelectron spectroscopy was recorded using Axis Ultra system equipped with monochromatic Al Ka Xray source (1486.6 eV). The energy resolution was set at 0.1 eV. For Raman and AFM measurements, the hBN film was transferred to SiO<sub>2</sub>/Si substrate using wet transfer method<sup>22</sup>. Atomic force microscopy (Asylum Research) was applied for AFM measurements. Raman spectra was acquired using Witec Alpha 300 spectrometer with 532 nm laser, 100X objective (675 nm laser spot) and 1mW input power. Transmission Electron microscopy (TEM) analysis was done using a FEI Tecnai G<sup>2</sup> 20 TWIN transmission electron microscope and has been used to obtain the SAED pattern. The aperture was 20 µm and accelerating voltage was 200 kV. The film from copper substrate was transferred over a copper grid with carbon nanomesh by wet transfer method which has been applied in previous transfers. Conductive atomic force microscopy (cAFM) measurements were carried out over the h BN/Cu film. Asylum Research cAFM has been used for the I-V measurements by using a Pt/Ir conductive tip with compliance current of 20 nA.

(Every characterization method has been discussed in detail in chapter 3 and the above mentioned instruments have been used for all other similar experiments carried out in the subsequent chapters)

### Results and discussion

The EBSD map (figure 4.5 a) of the Cu foils prepared by Method I (that is after annealing non-electropolished Cu foil in Ar for 120 min at  $900^{\circ}$  C) shows that it has mixed texture, with average grain size of ~50  $\mu$ m .We performed XRD of the annealed copper foil for different duration of annealing. This has been shown in figure 4.5 (c), the foil was annealed for 2 hr, 3 hr and 4 hr . Although the (111) phase increased in proportion the (200) phase is still present.

### hBN films on non-electropolished and annealed Cu foil (MI)

The hBN film synthesized on Cu substrate (MI) at RT for 60 min (40 W) is very discontinuous and with small grains nucleated all over the substrate (Figure 4.6 (a)) From SEM (figure 4.6 a) image we observed mostly hexagonal or octagonal BN islands which are crystalline in nature

with sharp facets. However, BN is not deposited uniformly on Cu substrate. In some areas it shows a preferential alignment relative to the substrate while in some it is randomly oriented Directionality Analysis measures (shown in figure 4.6 b) the orientations of edges within an image, producing histograms of the total length of edges at a given angle. In the histogram, three peaks (A, B, C) can be observed. The most intense peak(A) is separated from the other two peaks by 30° and 40° respectively. The width of peak A is the narrowest, indicating the long edge of the BN islands prefer to orientation along a certain direction with respect to the Cu grains. The underlying Cu grains can have either Cu (111) or Cu (100) orientation.

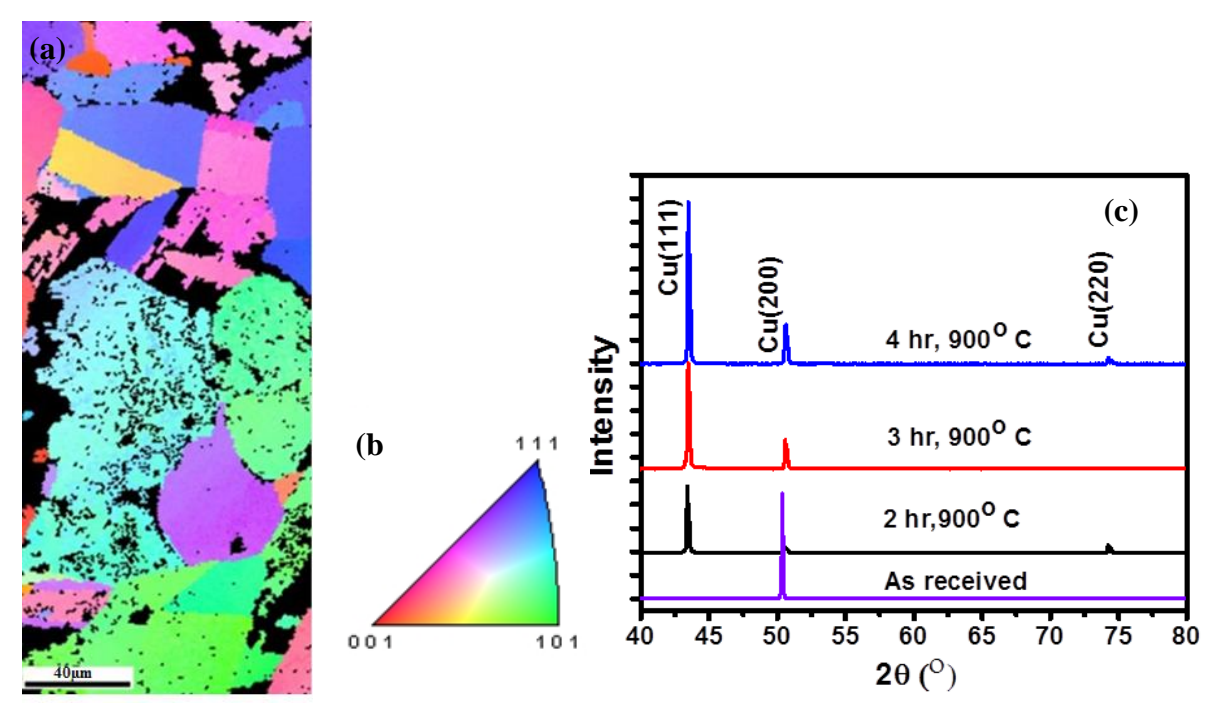


Figure 4.5 (a) EBSD map of the Cu foil prepared by method I (b) IPF for cubic crystal system (c) Comparison of XRD of annealed and as received copper foil.

Decreasing the sputtering power to 25 W the size islands was reduced as shown in figure 4.7 (a). Figure 4.7(b) and (c) shows the high resolution XPS spectra of B1S and N1s XPS of this

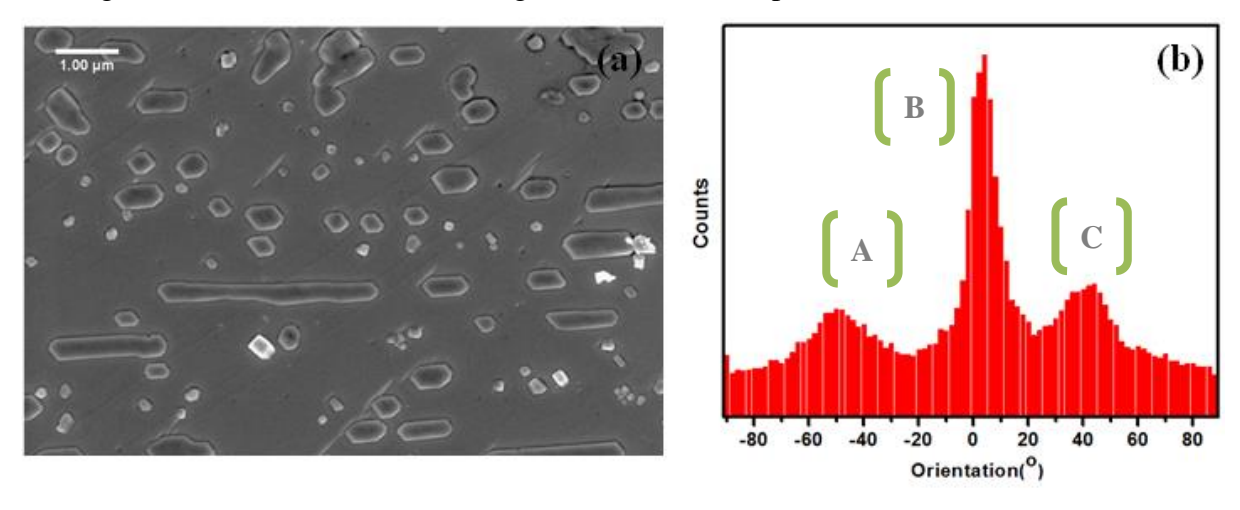


Figure 4.6 FESEM micrograph (a) and directionality analysis (b) of the deposition doe for 60 min,  $T_s$ =RT, 40W, in Ar plasma, substrate prepared by M I.

film. From the fitting, we can deconvolute the N1s (B1s) peak into 2 components at 398.4 eV (190.8 eV) and 399.6 eV (191.9 eV). The low energy peaks correspond to multilayer hBN films and the peak positions are similar to that reported for multilayer hBN films synthesized on Cu foils

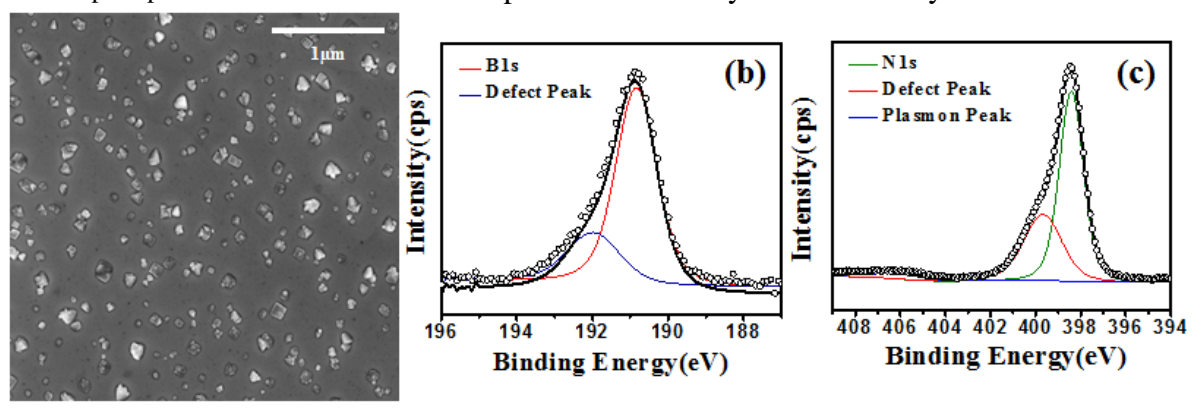


Figure 4.7. hBN deposited on non-electropolished Cu substrate M I (a) FESEM micrographs of hBN grains deposited at Ts= RT for 60 min. (b) and (c) High resolution XPS spectra of B1s and N1s of the sample in panel (a).

using  $CVD^{23}$ . The peaks at higher binding energy can be attributed to defects in the deposited hBN film<sup>23</sup>.

In the N1s spectra, we also observe the characteristic  $\pi$  plasmon loss peak at 406.2 eV associated with sp<sup>2</sup> bonded materials. Figure 4.8(a) shows AFM micrograph of hBN synthesized on Cu substrate (MI) for total 60 min in two steps (t<sub>1</sub>=30 min, t<sub>2</sub>=30 min) at substrate temperature  $T_s = RT$ . The inset is the height profile of the triangular grain which shows a height of 120nm. Figure 4.8 (b) is the corresponding phase image of the AFM micrograph. The contrast is completely different from the Cu substrate. The FESEM image of this particular place has been shown in figure 4.8 (c). Here along with the large triangular grain we can see some secondary nucleation in the remaining area. The presence of the triangular island indicates the formation of hBN which is equilibrium shape of hBN islands with N-terminated zig zag (ZZ) edges on strongly interacting substrates like Ni(111), Ru(0001), Co(0001) <sup>24,25,26</sup>. We also observe smaller islands with semi hexagonal shape (white circles). Depending on the partial pressure of Nitrogen and Boron atoms the shape of the hBN islands can vary from triangular (Nitrogen rich), truncated triangular to hexagonal (Boron rich) <sup>27</sup>. In our growth condition we have higher Nitrogen partial pressure so the triangular shaped islands have grown at the cost of semi hexagonal shaped islands. These discontinuous hBN islands imply that the BN adatoms are not wetting the Cu surface. Increasing the substrate temperature during deposition resulted in lower nucleation and higher wetting of the substrate, however the surface diffusion of hBN adatoms during post growth annealing is not high enough to overcome the high surface roughness. The discrete triangular hBN islands, therefore grow in 3D manner. Figure 4.8(d) shows the FESEM micrograph where we can see that at 400°C substrate temperature for total 60 min in a two-step growth (t<sub>1</sub>=30min, t<sub>2</sub>=30 min). We now observe a higher density of nucleated hBN islands with a mixture of triangular and trapezoidal shape. In addition to the chemical potential of B and N atoms, the energetically stable shape of hBN islands also depends on the step morphology of the underlying substrate. hBN films synthesized by CVD on most transition metal substrates have asymmetric growth rates in different crystallographic directions resulting in preferential triangular like hBN island shape <sup>27</sup>. On substrates Ir(111) and Pt (111) with fairly weaker interaction with hBN (similar to Cu),

trapezoidal shapes of hBN have also observed in addition to the triangular islands. The authors stated that in case of Ir(111) the Ir step edges reorient themselves to align parallel to the long edges of the hBN island step edges and the growth hBN island is truncated in the step up direction to produce trapezoidal shaped islands <sup>28</sup>.

### hBN deposited on electropolished Cu substrate (MII & MII)

To improve the surface roughness, the Cu foils were electropolished and then annealed at high temperature. The electropolished Cu foil prepared by MII showed a remarkable improvement in texture with now dominant (001) orientation with grain size ranging from 50-100 μm (Figure 4.9(a)). Figure 4.9 (c) shows the FESEM micrograph of the cBN film over the copper substrate. We can observe the faceted pyramidal shape of the grain in the film both triangular and square facets corresponding to {111} and {100} lattice plane of cBN. Similar cBN grain growth with four "quasi" {111} faces was observed on Si(001) substrate by CVD<sup>29</sup>. Figure 4.9 (c) shows the Raman spectrum of the film after transferring it over SiO<sub>2</sub>/ Si substrate. Here we can see a clear LO peak of cubic BN cantered at 1303 cm<sup>-1</sup>. Cubic BN is the most stable phase at low temperature while hexagonal BN is the stable phase at ambient temperature and atmospheric pressure <sup>30</sup>.

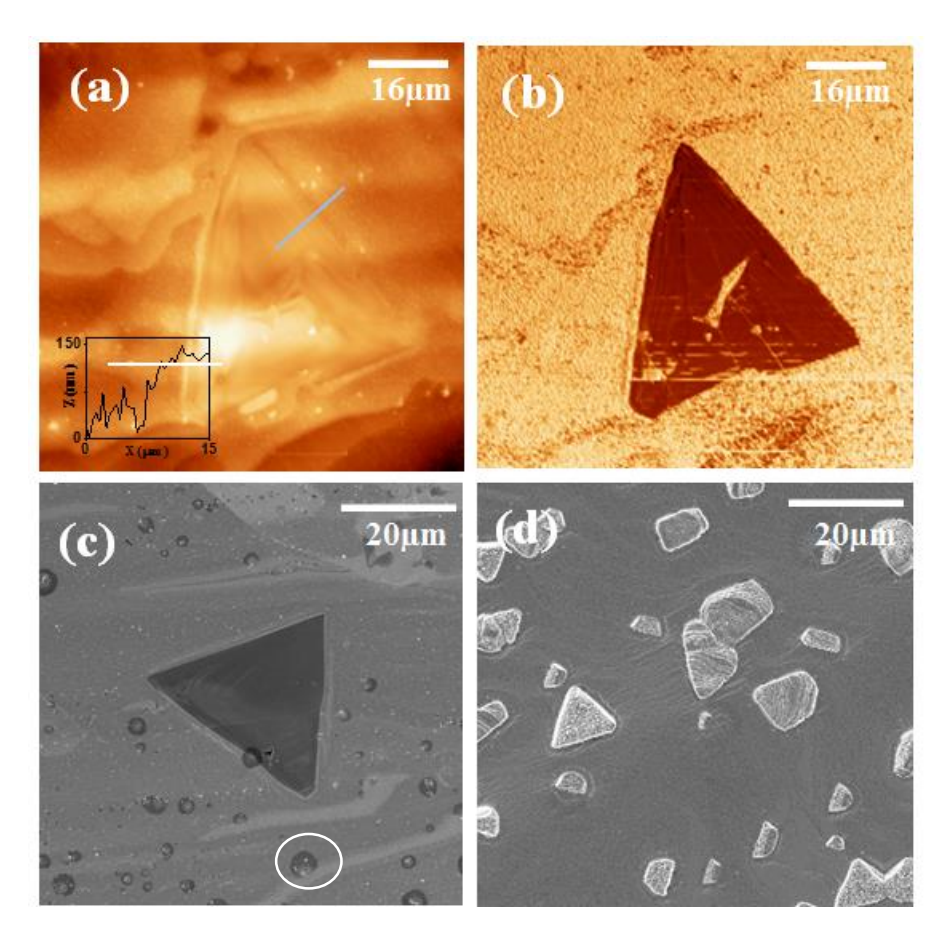


Figure 4.8 Micrographs of hBN over substrate prepared by method I (a) AFM topography image of a triangular hBN island deposited at RT using two step deposition ( $t_1$ =30min,  $t_2$ =30 min). Inset shows the height profile of the BN islands. (b) AFM phase image of the grain in (a). (c) FESEM micrograph of the same hBN island. (d) FESEM micrographs of hBN deposited at  $T_s$ = 400°C using two step deposition ( $t_1$ =30min,  $t_2$ =30 min).

Since the difference in free energies of formation of c-BN and h-BN is very low, the lattice mismatch with the substrate determines the phase of BN films. Figure 4.10 shows the

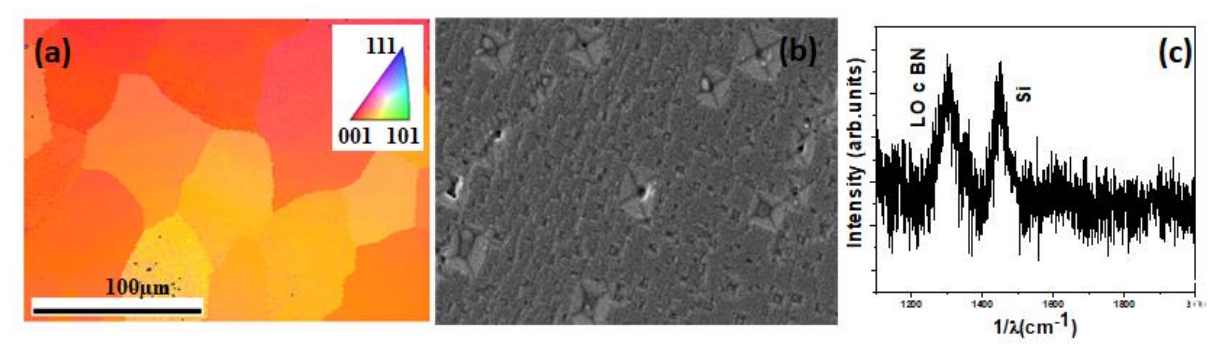


Figure 4.9 hBN deposited on electropolished Cu substrate MII (a) EBSD map of the copper substrate, Inset-IPF legend. (b) FESEM micrograph of the BN film over copper deposited at  $T_s$ = 400°C using two step deposition ( $t_1$ =30min,  $t_2$ =30 min). (c) Raman spectrum of the deposited film after transferring.

comparison with cBN and hBN with different Cu planes. The lattice mismatch between cBN and hBN with Cu(001) and Cu(111) surface is the lowest. Synthesis of pure cBN films However in the case of lattice matched substrates like diamond. On Cu(001) substrate cBN is the preferred phase while on Cu(111) the stable phase. On Cu(001) substrates it has 3D growth similar to cubic diamond films. On Cu(111) hBN grows proceeds by Van der Waals epitaxy. hBN nucleates to form triangular grains, which grow and coalesce to form continuous hBN film. XPS analysis was performed over this film. Figure 11 shows the high resolution N1s spectrum with a uniform peak cantered at 399.1 eV. This corresponds to cBN phase which is in accordance with reported value<sup>31,32</sup>. Increasing the annealing temperature from 900°C to 1040°C in MIII caused a marked increase in the (111) crystallographic orientation but other orientations were also present. In figure 4.12(c) the XRD plot shows the Cu(111) peak centred at 43.2° without the presence of (200) orientation. Although the EBSD map which elucidates over the surface orientation shows the substrate surface prepared by MIII are showing majority of the foil having (111) crystallographic orientation along with the presence of other orientation . The average grain size has increased to  $\sim 500 \ \mu m$  (Figure 4.12 (a)). From AFM image in Figure 4.12(d) we can see the surface facets on the Cu foil and the surface roughness has further reduced to ~3 nm. Low surface roughness reduces nucleation density and facilitates the growth of a homogeneous and uniform hBN film.

Bulk	Lattice Constant	Surface	Symmetry	Lattice Constant
(1)	(Å) (for column 1)	termination (2)		(Å) (for column 2)
(1)				
Cu	a = 3.59	Cu(001)	Square	a = 3.59
cBN	a = 3.61	Cu(110)	Rectangular	a = 3.59
				b = 2.53
				0 – 2.55
hBN	a = 2.50, c = 6.66	Cu(111)	Hexagonal	a = 2.53

Figure 4.10 Table comparing lattice constants different Cu crystal orientation with cBN and hBN.

Figure 4.13(a) shows the FESEM micrograph of the hBN film deposited on these Cu substrates (M III) at 400°C for a total 60 min in two step cyclic deposition ( $t_1$ =30 min,  $t_2$ =30 min). The hBN film synthesized is continuous and completely wets the substrate. Figure 4.13(b) shows the TEM image of the film after the film was transferred over copper grid with carbon-coated nano mesh. The crystallinity of the deposited hBN was investigated by using electron diffraction in TEM. Figure 4.13(c) shows the selected area diffraction pattern (SAED) of the particular area of the film. The diffraction pattern was taken over 0.9x0.9  $\mu$ m<sup>2</sup>. We can clearly see the hexagonal spots in the SAED pattern which is in accordance with the reported <sup>33</sup> SAED pattern on of single crystalline hBN .

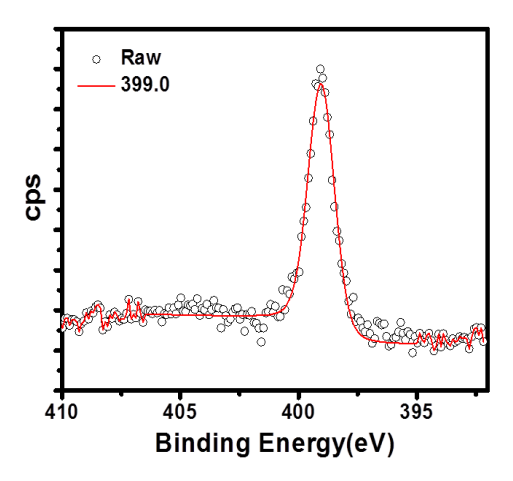


Figure 4.11 High resolution XPS N1s spectrum of cBN ( $T_s$ = 400°C using two step deposition ( $t_1$ =30min,  $t_2$ =30 min), MII)

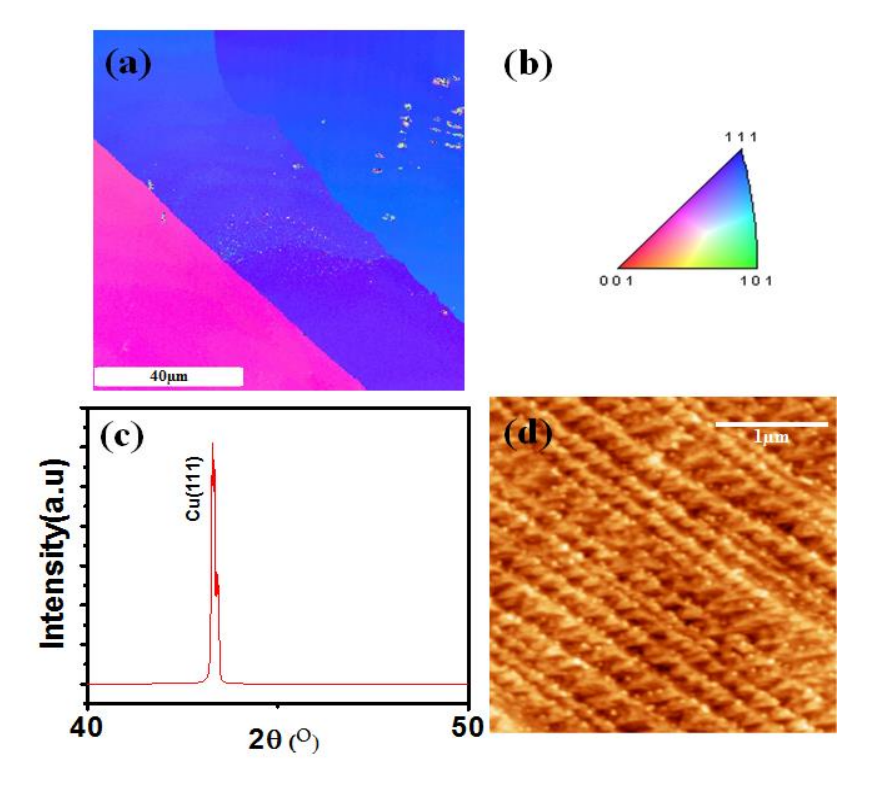


Figure 4.12 Copper foil preparation by MIII (a) EBSD orientation map of Cu substrate (b) IPF legend (c) XRD of the foil. (d) AFM of the Cu substrate.

Figure 14 (a) and (b) shows the optical and AFM micrograph of the film characterized for TEM. The film was transferred by wet etching method from copper foil to SiO<sub>2</sub>/Si substrate (the transfer methods has been described in details in chapter 3). In the optical image a clear contrast between the film and SiO<sub>2</sub> surface can seen, the contour of the film looks brighter as due to the presence of residual PMMA. The adjacent AFM image shows the thickness of the film is (inset) are 2 nm which is comprised of 3-4 layers of hBN.

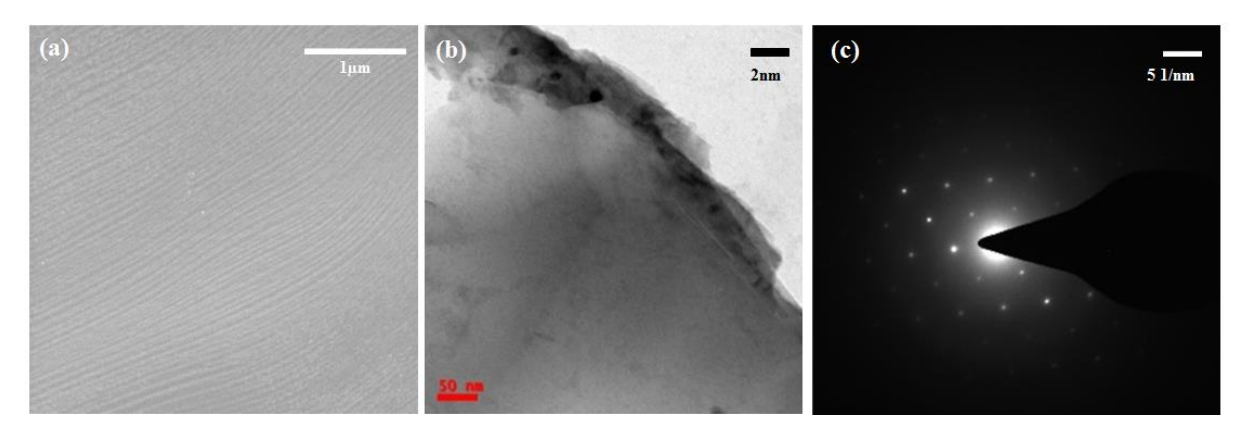


Figure 4.13 hBN deposited on electropolished Cu substrate MIII - (a) FESEM micrograph of hBN deposited at  $T_s$ = 400°C using two step deposition for a total of 60 min ( $t_1$ =30min,  $t_2$ =30 min) (b) TEM image of hBN and (c) SAED pattern of hBN film deposited for total 120 min in two step ( $t_1$ :60 min,  $t_2$ :60 min) at  $T_s$ : 400°C.

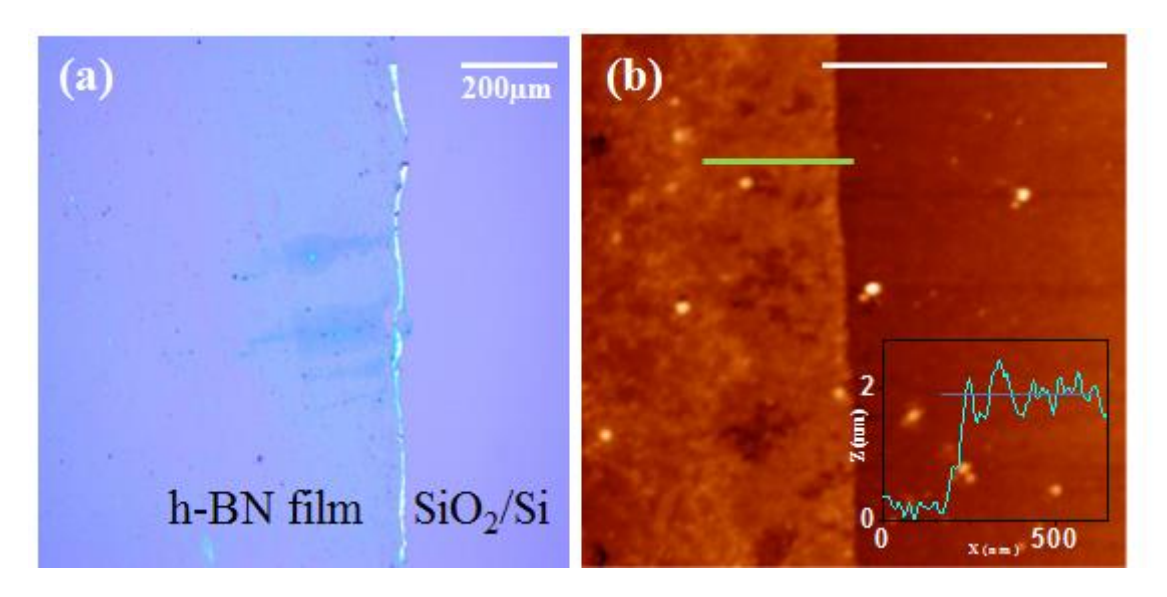


Figure 4.14 (a) Optical (b) and AFM image of the transferred of hBN film over  $SiO_2$  (300 nm)/Si. This hBN film was synthesized using two step (60 min +60 min) deposition for total of 120 min at 400°C (Substrate prepared by MIII) Inset: Height profile of the film. Scale bar 1 $\mu$ m.

We examined the surface morphology of a three step deposition, which is shown in figure 15(a) and figure (b). Figure 15(a) is the FESEM image of the film deposited for a total of 90 min divided in three equal portions (30+30+30 min). The surface of the film is homogeneous and continuous. We estimated the surface roughness of the film from the AFM image (figure 15 b), which is 4.44 nm. In the AFM image parallel copper facets can be seen which is due to the high temperature annealing of the hBN/Cu. A four-step deposition was used for kelvin force probe microscopy, which gives an idea of the work function of the hBN/Cu system. Figure 16

(a) is the height profile of the film and 16 (b), (c) is the contact potential map and work function map of the same place.

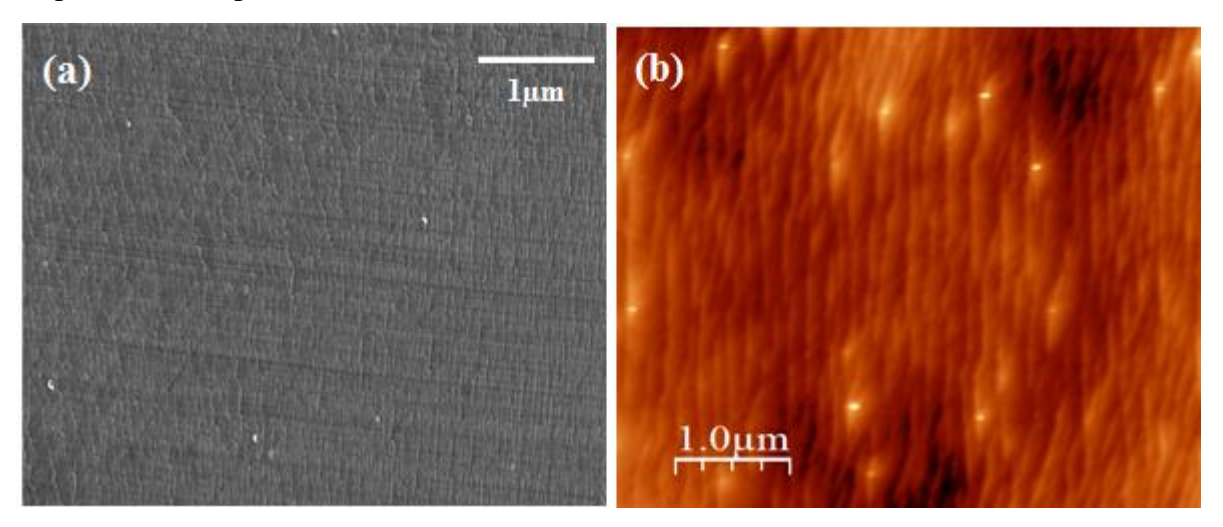


Figure 4.15 (a) FESEM and AFM (b) image of hBN deposited in three step ( $t_1$ :30 min,  $t_2$ :30 min,  $t_3$ :30 min,  $t_3$ :400°C). The r.m.s roughness of the film over copper is 4.44 nm.

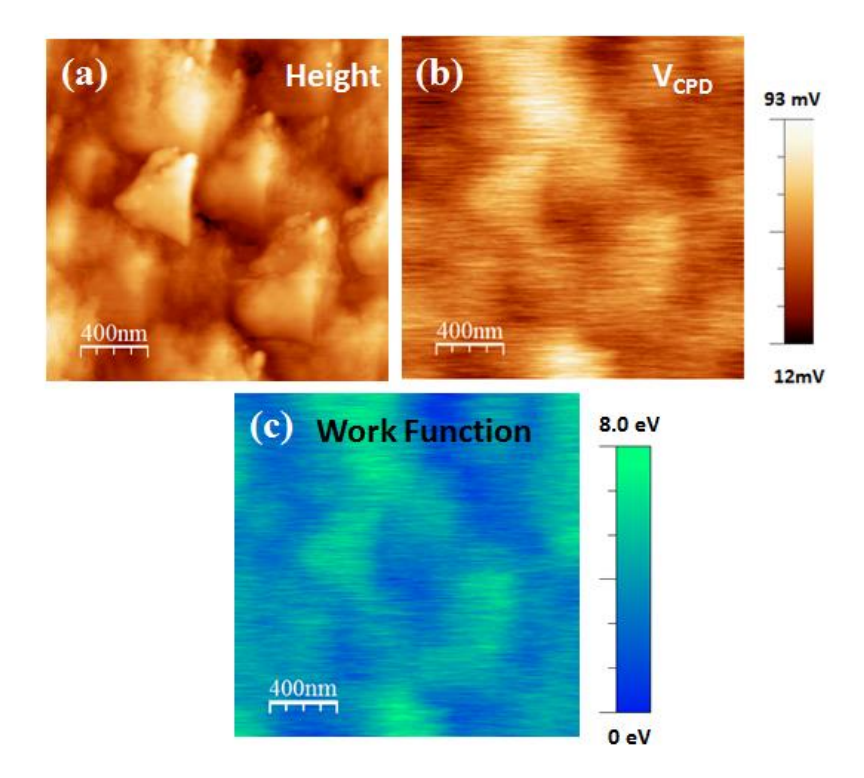


Figure 4.16 KPFM images of samples deposited in four step for 60\*4 = 360 min at 400°C,25 W. (a) height profile (b) contact potential mapping and (c) Work function mapping.

Contact potential difference is given by-

$$-VCPD = (\varphi tip - \varphi sample)/e$$
,

where  $\phi_{tip}$  and  $\phi_{sample}$  is the work function of tip and sample respectively. A Titanium/Iridium tip with work function of 4.6 eV was used for mapping purpose. The work function map has even contrast with average work function between 4.1-4.4 eV. This is in accordance with the reported value of work function in hBN/Cu system<sup>34</sup>.

## 4.2.2. Resistive switching properties-

We investigated electrical properties by using cAFM of hBN films OVER Cu foil ( prepared by method III). The current–voltage relationship (I–V) has been measured on hBN film synthesized for total 120 min (2 nm thick, 60 min +60 min , $T_s$  =400°C) and 360 (7nm thick,60 x 6 min,  $T_s$  =400°C) mins respectively. A typical I–V characteristic recorded on Pt/hBN/Cu devices is shown in Figure 4.17(a). The I-V response of 2 nm and 7 nm thick film show similar rectifying behaviour. The current saturates after 20 nA as the compliance current for the cAFM used was 20 nA. After 3-4 cycles the hysteresis loop collapsed due to the irreversible creation of defects. Figure 17(b) shows the schematics of the device geometry, the top contact was made with the cAFM tip over the film and the bottom contact was made with a gold clip pressure contact over the bare Cu foil .

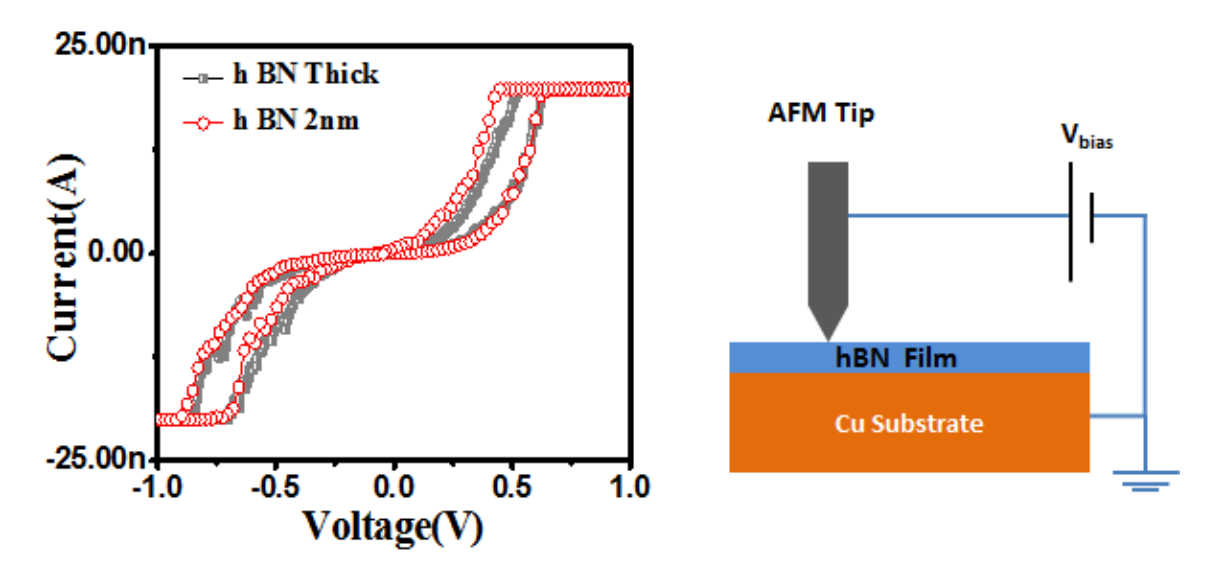


Figure 4.17 (a) I-V characteristic of hBN films of different thickness measured using cAFM (b) Device geometry used for I-V measurement.

Figure 4.18(a) shows the area of the hBN/Cu where I-V plot was recorded, figure 18(b) and (d) shows the cAFM image during off and on state. The on state image has an even contrast (apart from a few place) which shows that the film gives rise to uniform conduction current. Figure 4.18(c) shows the I-V loop recorded at the marked position in figure 18(a). The loop had a step 0 to +2, +2 to 0,0 to -2 and -2 to 0. The hBN/Cu device changes from high resistance state (HRS) to low resistance state (LRS) at 0.6 V which is in accordance with the value reported in literature  $^{35}$ . The device was reset by reversing the polarity.

### 4.3. Conclusion.

We have successfully synthesized multilayer hBN films from 2 nm (4 layers) to 7 nm thicker films (22 layers) over copper foil by radio frequency (RF) magnetron sputtering. We have

demonstrated how Cu foil preparation impacts the growth of hBN films. On non-electropolished Cu foil with (100) surface termination we get discontinuous hBN while on electropolished Cu foil with (111) surface termination we get continuous uniform hBN films. The synthesised film was subjected structural and morphological studies accompanied with electrical measurements. Resistive switching property of multilayer hBN film has been successfully demonstrated via conductive AFM method. This present work should have an impact on the realistic application of h BN by making it's synthesis more economic and thus pave the way for industrial-scale production.

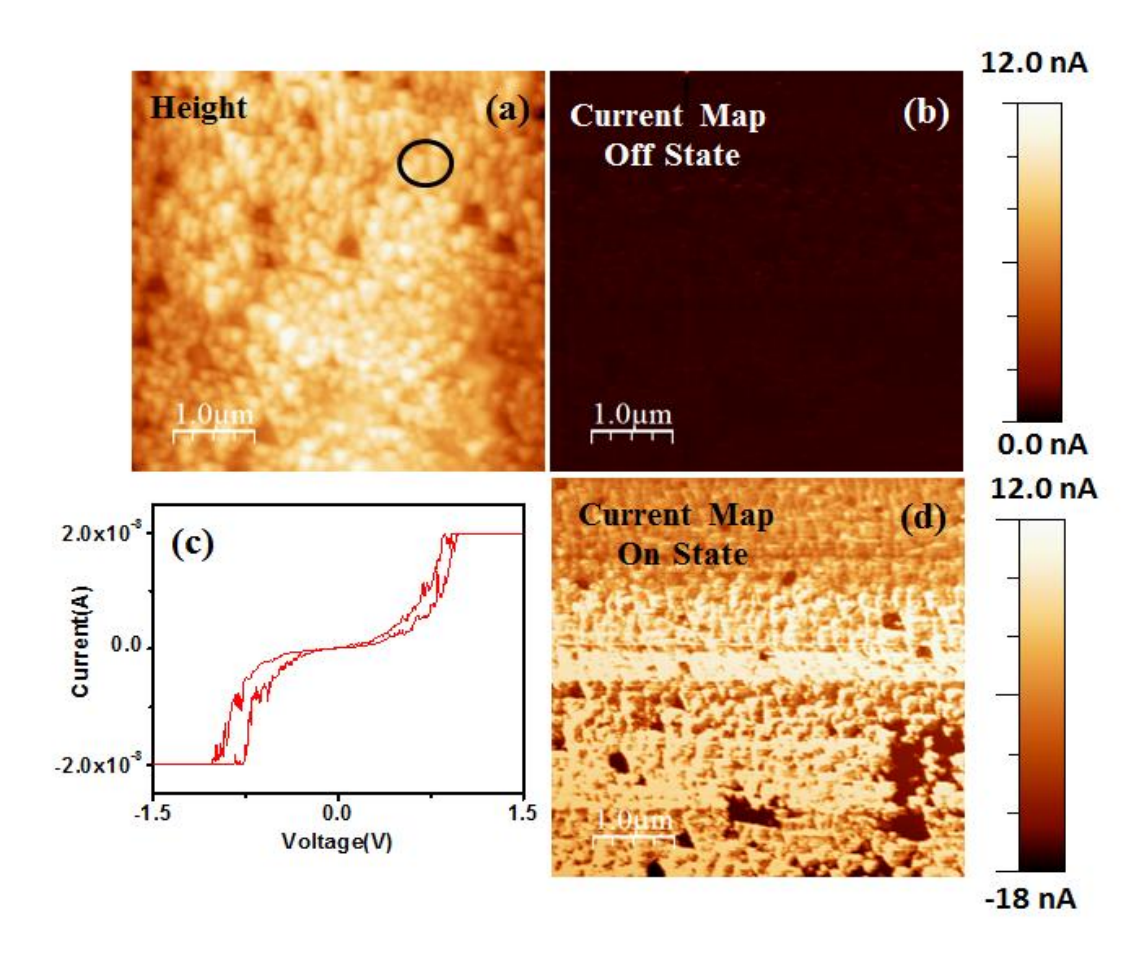


Figure 4.18 cAFM study of 2 nm thick film (60 min +60 min deposition,  $T_s$  =400°C) (a) Height image where current map is recorded. (b) & (d) Current map at off state and at on state. (c) I-V loop recorded at the marked position in (a).

### 4.4. References.

- 1. Cassabois, G., Valvin, P. & Gil, B. Hexagonal boron nitride is an indirect bandgap semiconductor. *Nat. Photonics* **10**, 262–266 (2016).
- 2. Wang, J., Ma, F. & Sun, M. Graphene, hexagonal boron nitride, and their heterostructures: properties and applications. 16801–16822 (2017) doi:10.1039/c7ra00260b.
- 3. Dean, C. R. *et al.* Boron nitride substrates for high-quality graphene electronics. *Nat. Nanotechnol.* **5**, 722–726 (2010).
- 4. Meric, I. *et al.* Graphene field-effect transistors based on boron-nitride dielectrics. *Proc. IEEE* **101**, 1609–1619 (2013).
- 5. Lee, K. H. *et al.* Large-scale synthesis of high-quality hexagonal boron nitride nanosheets for large-area graphene electronics. *Nano Lett.* **12**, 714–718 (2012).
- 6. Xu, Z. *et al.* Direct growth of hexagonal boron nitride / graphene heterostructures on cobalt foil substrates by plasma-assisted molecular beam epitaxy.
- 7. Singh, R. *et al.* Low temperature wafer-scale synthesis of hexagonal boron nitride by microwave assisted surface wave plasma chemical vapour deposition. *AIP Adv.* **9**, (2019).
- 8. Han, X., Lin, J., Liu, J., Wang, N. & Pan, D. E ff ects of Hexagonal Boron Nitride Encapsulation on the Electronic Structure of Few-Layer MoS 2. (2019) doi:10.1021/acs.jpcc.9b02549.
- 9. Caldwell, J. D. *et al.* Photonics with hexagonal boron nitride. *Nat. Rev. Mater.* **4**, 552–567 (2019).
- 10. Du, X. Z., Uddin, M. R., Li, J., Lin, J. Y. & Jiang, H. X. Layer number dependent optical properties of multilayer hexagonal BN epilayers. *Appl. Phys. Lett.* **110**, (2017).
- 11. Dai, S. *et al.* Tunable phonon polaritons in atomically thin van der Waals crystals of boron nitride. *Science* (80-. ). **343**, 1125–1129 (2014).
- 12. Yu, J., Li, J., Zhang, W. & Chang, H. Chemical Science Synthesis of high quality two-dimensional materials via chemical vapor deposition. *Chem. Sci.* **00**, 1–12 (2015).
- 13. You, J., Hossain, D. & Luo, Z. Synthesis of 2D transition metal dichalcogenides by chemical vapor deposition with controlled layer number and morphology. *Nano Converg.* (2018) doi:10.1186/s40580-018-0158-x.
- 14. Song, L. *et al.* Large scale growth and characterization of atomic hexagonal boron nitride layers. *Nano Lett.* **10**, 3209–3215 (2010).
- 15. Kim, G. *et al.* Growth of high-crystalline, single-layer hexagonal boron nitride on recyclable platinum foil. *Nano Lett.* **13**, 1834–1839 (2013).
- 16. Shi, Y. *et al.* Synthesis of few-layer hexagonal boron nitride thin film by chemical vapor deposition. *Nano Lett.* **10**, 4134–4139 (2010).
- 17. Khaksaran, M. H. & Kaya, I. I. Spontaneous Nucleation and Growth of Graphene Flakes on Copper Foil in the Absence of External Carbon Precursor in Chemical Vapor Deposition. (2018) doi:10.1021/acsomega.8b01652.
- 18. Mittemeijer, E. J. & L, G. A. The solubility of C in solid Cu. **51**, 1–5 (2004).
- 19. Muratore, C., Voevodin, A. A. & Glavin, N. R. Physical vapor deposition of 2D Van der Waals materials: a review. *Thin Solid Films* **688**, 137500 (2019).
- 20. Camilli, L., Sutter, E. & Sutter, P. Growth of two-dimensional materials on non-catalytic substrates: H-BN/Au(111). *2D Mater.* **1**, (2014).
- 21. Liu, Z. *et al.* 2011\_Direct Growth of Graphene-Hexagonal Boron Nitride Stacked Layers.pdf. 2032–2037 (2011).
- 22. Cabrero-vilatela, A., Weatherup, R. S., Braeuninger-weimer, P., Caneva, S. & Hofmann, S. Towards a general growth model for graphene CVD on transition metal

- catalysts †. 2149–2158 (2016) doi:10.1039/c5nr06873h.
- 23. Schloegl, R. *et al.* In Situ Observations during Chemical Vapor Deposition of Hexagonal Boron Nitride on Polycrystalline Copper. *Chem. Mater.* **26**, 6380–6392 (2014).
- 24. Liu, S. *et al.* Predicting the preferred morphology of hexagonal boron nitride domain structure on nickel from ReaxFF-based molecular dynamics simulations. *Nanoscale* **11**, 5607–5616 (2019).
- 25. Auwärter, W., Suter, H. U., Sachdev, H. & Greber, T. Synthesis of One Monolayer of Hexagonal Boron Nitride on Ni(111) from B-Trichloroborazine (ClBNH)3. *Chem. Mater.* **16**, 343–345 (2004).
- 26. Orofeo, C. M., Suzuki, S., Kageshima, H. & Hibino, H. Growth and low-energy electron microscopy characteri- zation of monolayer hexagonal boron nitride on epitaxial cobalt. **6**, 335–347 (2013).
- 27. Stehle, Y. *et al.* Synthesis of Hexagonal Boron Nitride Monolayer: Control of Nucleation and Crystal Morphology. (2015) doi:10.1021/acs.chemmater.5b03607.
- 28. Petrović, M., Hagemann, U., Horn-von Hoegen, M. & Meyer zu Heringdorf, F. J. Microanalysis of single-layer hexagonal boron nitride islands on Ir(111). *Appl. Surf. Sci.* **420**, 504–510 (2017).
- 29. O'Brien, P., Pickett, N. L. & Otway, D. J. Developments in CVD delivery systems: A chemist's perspective on the chemical and physical interactions between precursors. *Chem. Vap. Depos.* **8**, 237–249 (2002).
- 30. Cazorla, C. & Gould, T. Polymorphism of bulk boron nitride. 1–6 (2019).
- 31. Kidambi, P. R. *et al.* In Situ Observations during Chemical Vapor Deposition of Hexagonal Boron Nitride on Polycrystalline Copper. *Chem. Mater.* **26**, 6380–6392 (2014).
- 32. Berns, D. H. & Cappelli, M. A. Cubic boron nitride synthesis in low-density supersonic plasma flows. *Appl. Phys. Lett.* **2711**, 2711 (1995).
- 33. Khan, M. H. *et al.* Synthesis of Large and Few Atomic Layers of Hexagonal Boron Nitride on Melted. 21–24 (2015) doi:10.1038/srep07743.
- 34. Tuning Band Gap and Work Function Modulations in Monolayer hBN / Cu (111) Heterostructures with Moiré Patterns. (2018) doi:10.1021/acsnano.8b04444.
- 35. Jeong, H. *et al.* Resistive Switching in Few-Layer Hexagonal Boron Nitride Mediated by Defects and Interfacial Charge Transfer. (2020) doi:10.1021/acsami.0c12012.

### Chapter 5

### Hexagonal BN synthesized by CVD

Increasingly 2D materials are being investigated for their potential use in different fields but the biggest bottle neck in harnessing the full potential of hBN is its synthesis process. Atmospheric pressure CVD has a lot of potentials to overcome this hurdle. In this chapter, we have synthesized hBN of different thicknesses via APCVD for different applications like surface enhanced Raman spectroscopy (SERS), as an electrocatalyst for oxygen reduction reaction (ORR), as encapsulating layer for MoS<sub>2</sub> devices and we have also studied resistive switching properties of hBN film <sup>1,2</sup>. Characterization of the hBN film has been done and detailed analysis is presented here. Deposition and substrate cleaning methods along with the substrate preparation method has also been discussed here.

### 5.1. Growth of hexagonal boron nitride using APCVD.

Hexagonal boron nitride has been grown in an atmospheric pressure CVD. First, we shall discuss the copper substrate preparation for the growth of hBN.

### 5.1.1. Copper substrate preparation.

 $25 \mu m$  thick copper foil has been used for hBN growth. In three different steps, the copper was processed prior to hBN growth, which is as follows:-

### Step A

The following steps were followed in cleaning the copper foil-

- a) Rinsing in 6.9 % HNO<sub>3</sub> for 25 s followed by deionized (D.I) water wash three times.
- b) Washing with acetone and isopropyl alcohol.

### Step B

Cleaning and electropolishing-

In this method of substrate processing, the following steps were followed –

- a) Cleaning of the copper foil like in (1).
- b) Electropolishing –

The cleaning in dilute nitric acid even if for 25 s makes the copper surface rough . The rough surface creates high nucleation density which reduces film grain size and increases the number of grain boundaries this adversely affects the quality of the film. To reduce this roughness the film was electropolished.

The followed electropolishing procedure is –

- i) Electropolishing time -30 min ii) Anode (-) to cathode (+) distance -2 cm iii) Electropolishing voltage -1.2 V to 1.8 V iv) Current -20 mA or 4.6mA/ cm $^2$ .
- v) Electropolishing solution –

Two solutions were used – Orthophosphoric acid + Isopropyl alcohol all in ratio of 5:1

c) After electropolishing the substrate was cleaned in D.I water to wash the electropolishing solution. Further washing was done by using acetone and IPA to remove organic contaminants.

## Step C

The following are the steps for this method-

a) Cleaning similar like method A b) Electropolishing similarly like method B c) Post annealing of copper foil in non-contact form-

After step (a) & (b) the sample was annealed in Ar + H<sub>2</sub> atmosphere having 9:1 ratio (200



Figure 1. Copper foil placement for the non-contact annealing in argon+ hydrogen atmosphere.

SCCM flow rate) for 1 hr at 1040 °C. The sample was placed over the rims of an alumina

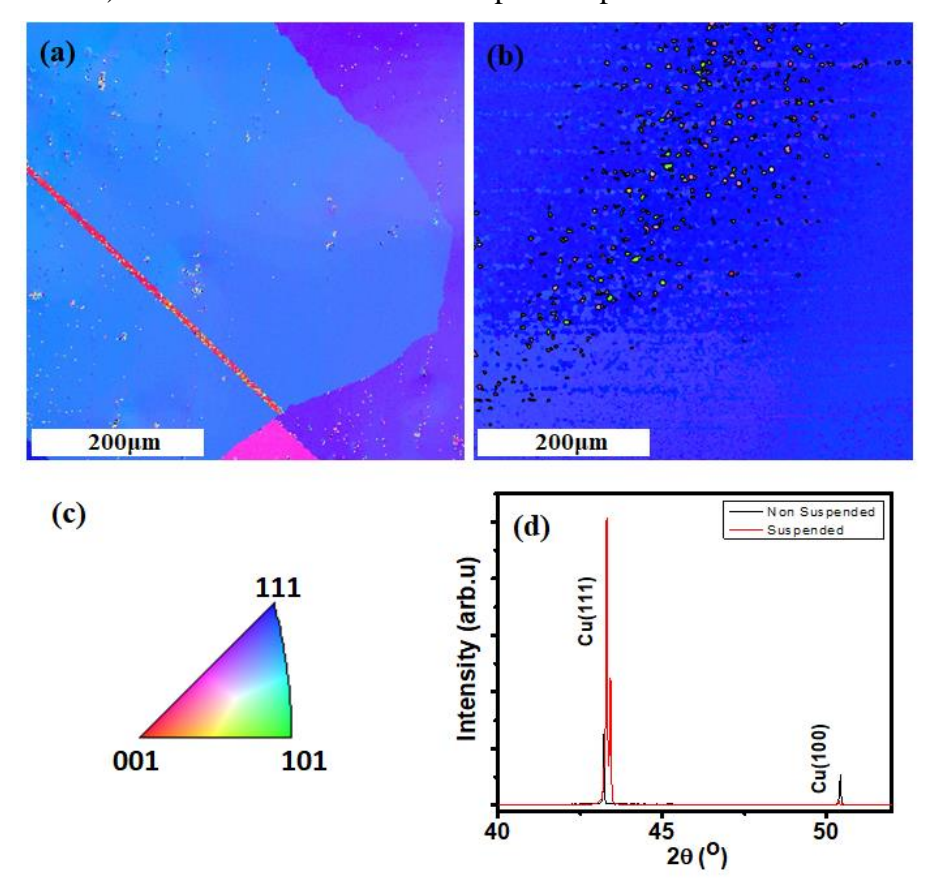


Figure 2. EBSD and XRS of annealed copper foil at 1040°C. a) Contact annealing for 30 min b) Non-contact annealing for 60 min. c) Inverse pole figure map for EBSD scans. d) Comparison of XRD plot.

crucible, as depicted in figure 1. Prior to annealing, the quartz tube was purged with 200 SCCM Ar for 1 hr. The ramping rate was 8° C /min and the furnace was left for natural cooling after the end of the annealing process.

The non-contact annealing was done to achieve a homogeneous and large grain sized Cu(111) surface. The Cu(111) surface has the lowest surface energy and during recrystallization at temperatures close to its melting point the surface restructures itself (111) configuration and achieves the highest packing fraction at the surface. The hanging copper foil in the middle during annealing at high temperature is free from touch induced stress. And as it has less stress over a large area it recrystallizes to (111) plane more homogeneously <sup>5</sup>. Contact-free annealing of Cu foil creates larger grains of copper. Due to epitaxial growth hBN grains are also bigger in size as hBN growth follows the texture of the underneath Cu foil. Larger grains of hBN reduces the amount of grain boundaries in hBN film, which is beneficial for applications like resistive switching. In other words contact-free annealing when compared to contact annealing (the Cu foil sits over the bottom of the crucible) enables us to get Cu(111) plane over a large area with more homogeneity. We performed XRD and electron back scattered diffraction (EBSD) to verify the same. Figure 2 shows EBSD and X Ray diffraction pattern of both annealed copper foil in non-contact (as shown in figure 1, in the middle portion) and contact way of annealing.

To investigate the surface orientation of the processed copper foil we employed EBSD, which is a surface-sensitive technique (details explained in the experimental methods section). Figure 2(a) shows the EBSD map of  $0.5 \times 0.5$  mm annealed (copper is in contact with the crucible) copper foil in presence of Ar+ H<sub>2</sub>. The foil was annealed at  $1040^{\circ}$  C for 30 min. Here the blue patch is the Cu(111) orientation, which is not homogenous over the whole area and other orientations are also present. In figure 2(b) the EBSD scan has been take over the same area of  $0.5 \times 0.5$  mm from the non-contact portion of the copper foil as shown in figure 1, here we can see that the overall area has a similar shade of blue confirming the presence of Cu(111) orientation over the full area. Clearly, non-contact annealing has greater efficacy in obtaining (111) orientation.

Figure 2(c) shows the X ray diffraction pattern of copper foil annealed in non-contact form (Red) and when placed over the crucible (Black). Clearly, the intensity of the Cu(111) is dominant for the non-contact one which is almost three times the contact one. The Cu(100) peak is also very faint for the non-contact one. XRD gives an overview of the bulk of the copper foil as it has high penetration depth, thereby we can say that the formation of (111) planes is not only restricted to surface but the bulk of Cu foil obtained the (111) configuration.

Carbon is present as an impurity present in the copper substrate. Carbon atoms segregate out during the cooling phase of the pre annealing process <sup>6</sup>. This segregated carbon is etched away by Ar/H<sub>2</sub> gas. In one way pre annealing of the copper foil (non-contact or not) reduces the amount of carbon in the substrate. This in turn decreases the chance of carbon impurity in the hBN film.

### 5.1.2 Atmospheric pressure CVD growth from Ammonia Borane.

Hexagonal boron nitride has been synthesized by using Ammonia Borane (AB) powder as a precursor material. Two separate constant heating zones were used for the growth of hBN. The

AB powder crucible was placed upstream, 55 cm (X) from the substrate and 15(X) from the edge of the quartz tube. For all of our experiments X and Y as shown in figure 3 were kept constant. A quartz crucible was used instead of a alumina one .This is because alumina is more porous than quartz and retains the residue of AB powder which makes it difficult to clean. The quartz crucible had no rims to facilitate the flow of precursor material. The decomposition of AB powder is well documented in the literature, upon heating between 80° C - 130° C AB powder decomposes to Ammonia (NH<sub>3</sub>),Borazine (N<sub>3</sub>B<sub>3</sub>H<sub>6</sub>), Borane (BH<sub>3</sub>) and diborane (B<sub>2</sub>H<sub>6</sub>)<sup>3,4</sup>. Further dissociation of these species into NxBy in the APCVD reaction chamber at growth temperature gives rise to hBN film. Detailed discussion about growth has been done in section 5.1.2

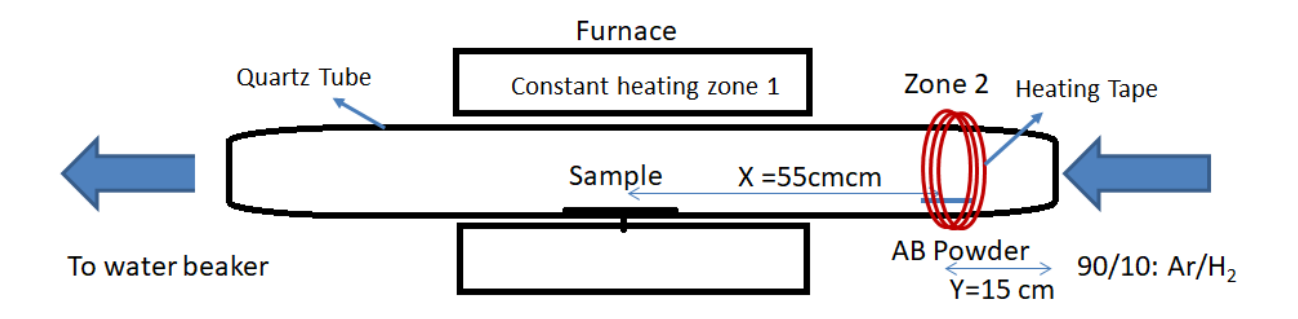


Figure 3. Schematic of the CVD used for h BN growth.

Atmospheric pressure chemical vapour deposition has been employed to synthesize hBN. As no pump is used to purge the system, to get rid of the atmospheric oxygen the quartz tube was purged with 200 SCCM of Ar for 1 hr before every deposition. The presence of oxygen is detrimental for the growth of hBN, as at high temperature it oxidises copper and inhibits the growth process.

Figure 4 shows a typical heating profile for the growth of hBN. Several parameters of the synthesis process were kept constant for all of our experiments in this chapter. Which are -

- 1) Growth temperature i.e 1050° C
- 2) Carrier gas composition (9:1 of Argon and Hydrogen)
- 3) Sublimation temperature of AB powder ( $130^{\circ}$  C), the sublimation temperature was achieved by using a heating tape in zone 2 (see figure 3). The heating tape was connected to a variac, which supplied a constant voltage of 120 V.
- 4) Ramp up the rate of the furnace to achieve 1050°C
- 5) The cooling rate is the natural cooling rate.

Hexagonal boron nitride has been synthesized using APCVD on a copper substrate (99.8%, 25  $\mu$ m thick sourced from Alfa Aesar. Ammonia Borne (AB) powder was used as a precursor material (Sigma Aldrich). Ammonia borane (NH<sub>3</sub>BH<sub>3</sub>) starts decomposing from 70-130 ° C into borazine (in very minute proportion), diborane and N<sub>x</sub>B<sub>y</sub> species. Dehydrogenation of the AB molecule gives rise to the N<sub>x</sub>B<sub>y</sub> species. The N<sub>x</sub>B<sub>y</sub> species at high temperature over copper

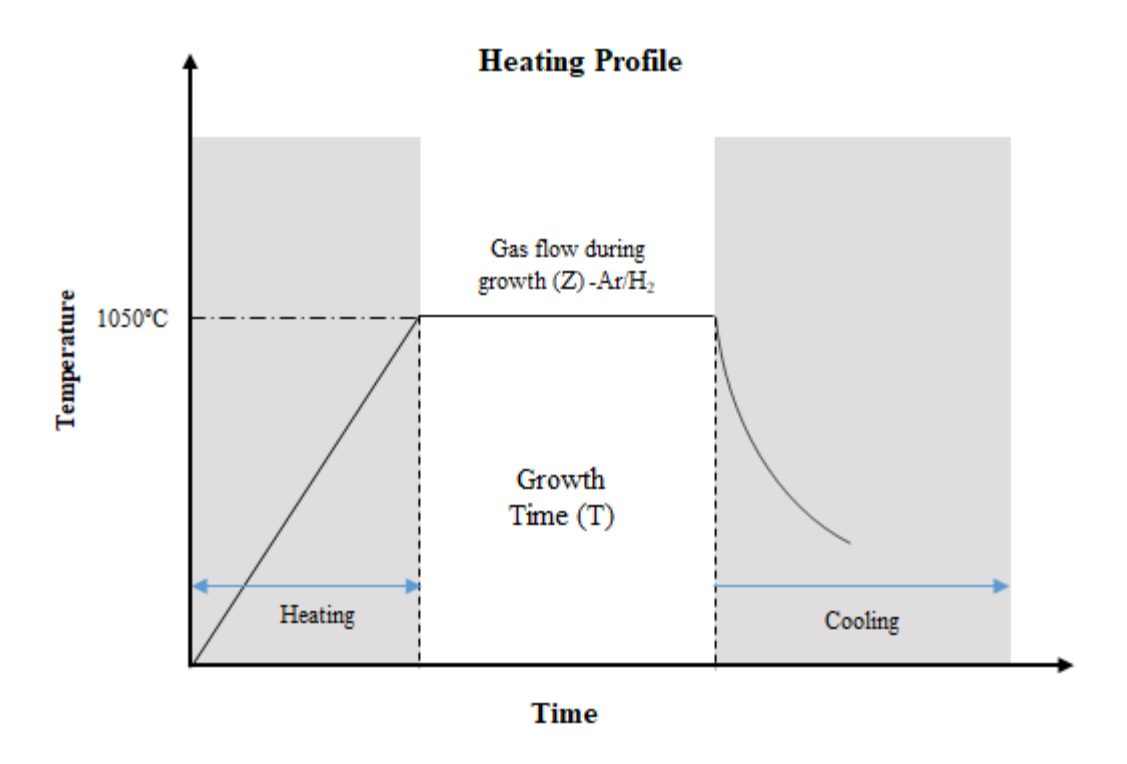


Figure 4. Typical heating profile for the growth of hBN.

the surface gives rise to hBN film. In this process, the copper surface acts as a catalyst. At first  $N_x B_y$  nucleates over the copper surface and then the growth of hBN from the nucleated species takes place. Some reports suggest that dehydrogenation takes place after adsorption over the copper surface  $^7$ . Other precursors like borazine is also used for hBN synthesis. But borazine is highly toxic in nature, handling it and disposing of the released chemical species requires special arrangements. On the other hand ammonia borane is a non-hazardous material and doesn't require special arrangements to work with.

A mixture of Argon and Hydrogen (9:1, 99.99% purity) was used as a carrier gas during the growth time. Different amounts of AB powder were used to synthesize different thicknesses of hBN Cu foil. The as-received Cu foil was prepared by the method described in the substrate preparation section. After substrate preparation, the Cu substrate was placed at the centre of a horizontal tubular furnace of 5 cm diameter and 1.2 m in length. The AB powder was placed 55 cm upstream from it. The system was purged using 200 sccm of Ar/H2 (90/10) gas mixture for 30 min. After purging, the Cu substrate was heated to 1050 °C with a heating rate of 8 °C/min from room temperature (RT) to 600 °C under 200 sccm Ar gas, and from 600 to 1050 °C under 200 sccm of Ar/H2 (9:1). Then, the gas flow rate was kept constant at 50 sccm Ar/H2 (9:1) until the reaction was over. The substrate was kept at 1050 °C for 30 min, and then, it was allowed to cool down naturally to RT. During the cooling phase, the gas flow rate was increased to 200 sccm Ar/H2 (9:1). The temperature profile used for synthesis is shown in figure 4. The precursor heating was initiated when the substrate temperature reached 1050 °C that is the variac was switched on. For varying the thickness of hBN films, the starting amount of precursor powder was varied while keeping all the other growth-related parameters constant. For 7, 6, and 1.5 nm thick hBN film, 10.8, 9, and 4.9 mg AB powder was used, respectively.

#### 5.2. Results and discussion.

The synthesized hBN film was characterized by an array of methods to investigate different aspects of the film like structural, stoichiometric, surface homogeneity etc. These aspects have been discussed in detail in this section.

### 5.2.1. Film characterization.

The broad classification of the characterization done can be categorized into a) spectroscopic studies b) diffraction studies and c) microscopic observation. We employed FESEM, AFM, TEM and an optical microscope to study the surface morphology and crystallographic nature of the film. XPS and Raman were used for spectroscopic studies.

### Micrographs-

Figure 5 shows the SEM (a) and optical micrographs (b) of a hBN deposition at 1050°C, the deposition was carried out for 10 min with 50 SCCM Ar+H<sub>2</sub> flow. The FESEM image shows

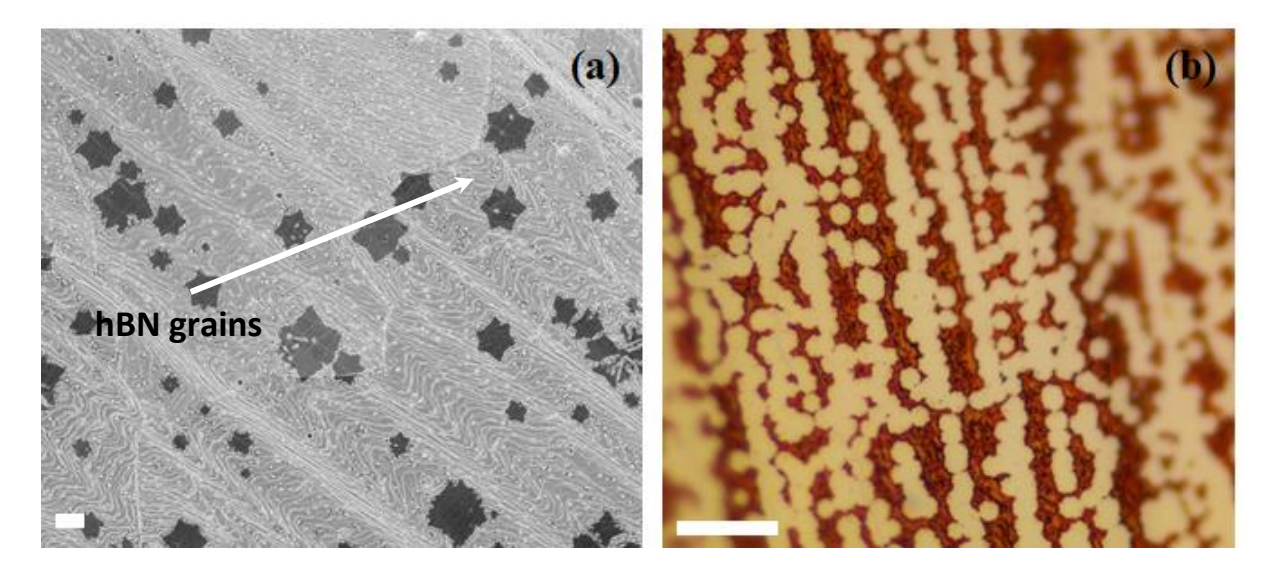


Figure 5. FESEM (a) and optical micrographs (b) of the hBN deposition over copper. Scale bar-10  $\mu$ m. [Deposition parameters - 10 min, 9 mg AB, 50 SCCM ]

hexagonal islands of hBN. As the growth time was intentionally kept short these nucleated islands didn't coalesce for a continuous film. After the growth, the hBN/Cu foil was heated at 200 °C to oxidize it. The optical micrograph in figure 5(b) shows copper foil was oxidized, the brown contrast in the optical micrograph is the oxidized Cu surface. The underlying copper foil of the deposited island is not oxidized as hBN inhibits oxidation <sup>8</sup>. This gives a sharp contour to the hexagonal island in the optical image. In the SEM image (figure 5, a) hBN islands with hexagonal contour are more prominent. The morphology of the islands is hexagonal this is due to the fact that N:B ratio is tilted towards B, when it is exactly 1 the morphology is triangular. The optical micrograph of hexagonal hBN islands over oxidized Cu (figure 5 b), shows that the islands have clear geometry of arrangement. They are linearly placed, this is because the nucleation takes place with respect to the orientation of the underneath copper facets.

To achieve a completely homogeneous and continuous large area hBN film the growth time

was increased to 15 min. and the length and breadth of the copper foil used were 40 x 8 mm keeping all other parameters constant. Efficient transfer of large are hBN film to other substrates is important for any application.

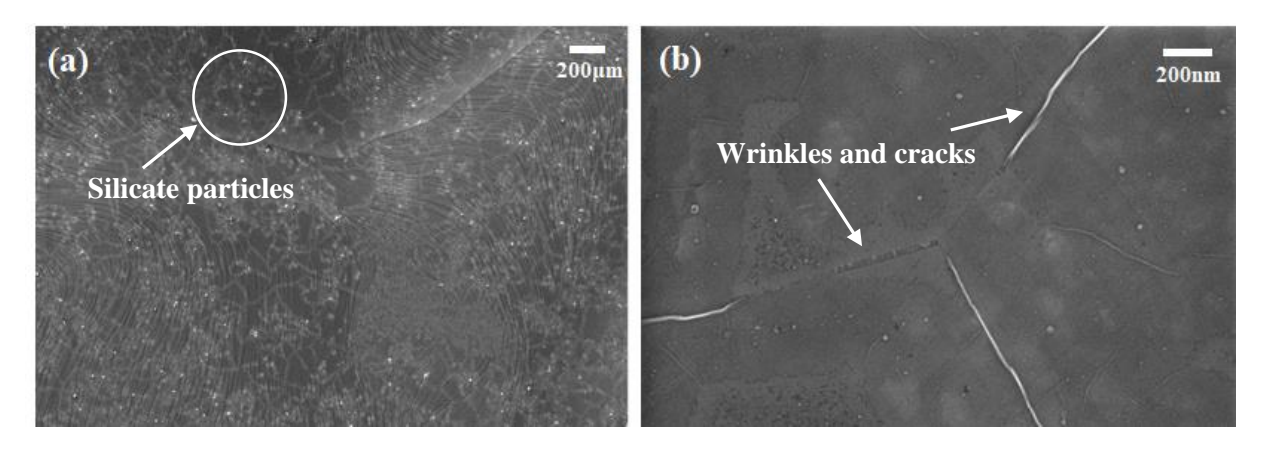


Figure 6. FESEM images for 15 min growth (a)lower magnification at  $10 \times (b)$  higher magnification at  $100 \times (b)$  higher magnification at

Figure 6 (a & b) shows the FESEM image of the synthesized hBN, which shows that it has a uniform and homogeneous morphology. In some locations over the film white particles which can be seen in figure 6(a), these particles are silicate particles <sup>9</sup>. They arise from the inside wall of the quartz tube. Denatured and older quartz tube contaminates sample to a high degree. Proper cleaning of the tube just prior to deposition is an efficient way of eliminating the possibility of silicate contamination. At higher magnification in figure 7(b) we can see wrinkles and small cracks about 10 nm in the lateral dimension. The film shows a considerable amount of surface homogeneity and uniformity.

Figure 7 shows the optical (a) and AFM (b) images of the transferred hBN film. The inset of the AFM image shows the height profile of the transferred film, the thickness is about 6.0 nm. This 6 nm thick film has been used for subsequent SERS application in the following sections. The transfer process employed here is mentioned in detail in the experimental details section. For this film figure 7, the deposition was carried out for 30 min and keeping all other parameters constant. The film has been transferred from copper substrate to over SiO<sub>2</sub>/Si substrate, the SiO<sub>2</sub> layer is 290 nm in thickness, this layer gives the necessary optical contrast to identify the hBN film. In figure 8(a) the pink contrast is the SiO<sub>2</sub> layer and the bluish-violet contrast is the hBN film, this is marked in the image.

We can also see some leftover PMMA residues in figure 7(a) which is present in a minute amount in some places of the film. This particular transfer was done by using 1M FeCl<sub>3</sub> solution as an etchant, we also used 0.1 M ammonium persulphate solution as a copper etchant. The (NH<sub>4</sub>)<sub>2</sub>S<sub>2</sub>O<sub>8</sub> solution has resulted in a more clean transfer with less presence of residual PMMA. Figure 7 (c & d) shows the optical micrographs of the transferred film where 0.1 M ammonium persulphate solution is used as an etchant. In both the images (image c is captured at the middle of the film and d is at the edge) the surface is relatively clean when compared to the transfer in figure 7 a. This reason for the clean surface can be attributed to the fact that 0.1 M (NH<sub>4</sub>)<sub>2</sub>S<sub>2</sub>O<sub>8</sub> etches copper very slowly when compared to 1M FeCl<sub>3</sub> solution. Fast etching for the FeCl<sub>3</sub> creates undulation to the film and as a result, the adhesion between the top PMMA and film

increases. On the contrary slow etching by ammonium, persulphate is almost like a quasistatic process and maintains the firmness of the film and has a less adverse effect over the transfer process.

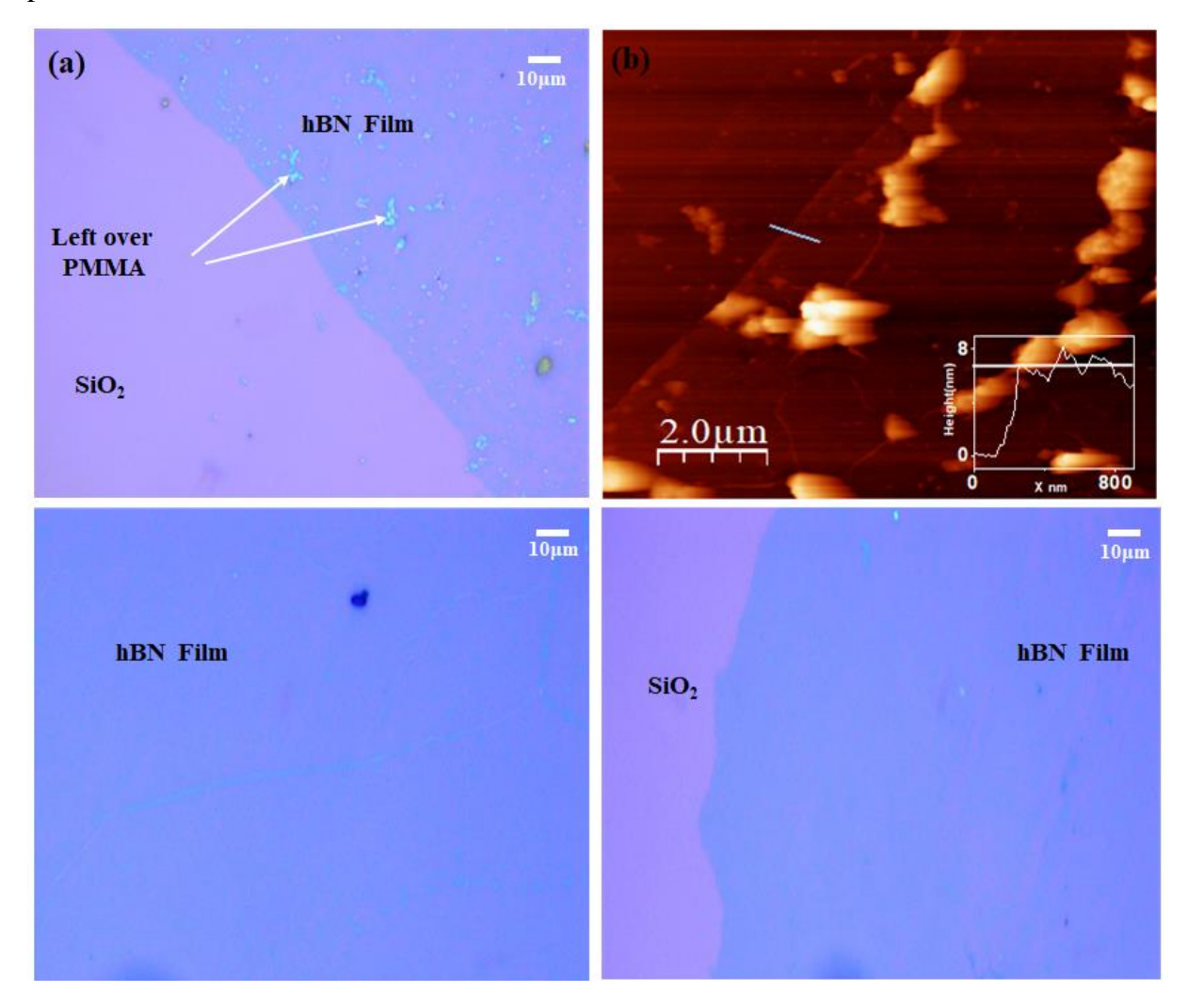


Figure 7. Optical (a,c,d) and AFM (b) images of the transferred sample, inset height profile through the marked line.[Deposition parameters - 30 min, 9 (for c,d 11 )mg AB , 50 SCCM ]

To understand the crystalline nature of the film we performed selected area diffraction pattern analysis (SEAD). For performing the TEM experiments the hBN film was transferred to a copper grid TEM grid with carbon layer support. The transfer process was similar to the process mentioned in the experimental details section and 1M FeCl $_3$  solution is used as an etchant. In figure 8(a) we can see the SEAD pattern of the transferred film and figure 8(b) shows the corresponding hBN film, the diffraction pattern has been recorded over an area of 0.003~x 0.003~mm.

The image shows concentric points in a hexagonal pattern. There are two white points close together, marked with a white circle. This is because of the polycrystalline nature of the film. As different family of crystal plane give rise to different diffraction pattern. We indexed two points in the diffraction pattern which are [011] and [112], the measured angle between them is 36° and the calculated angle is 38°.

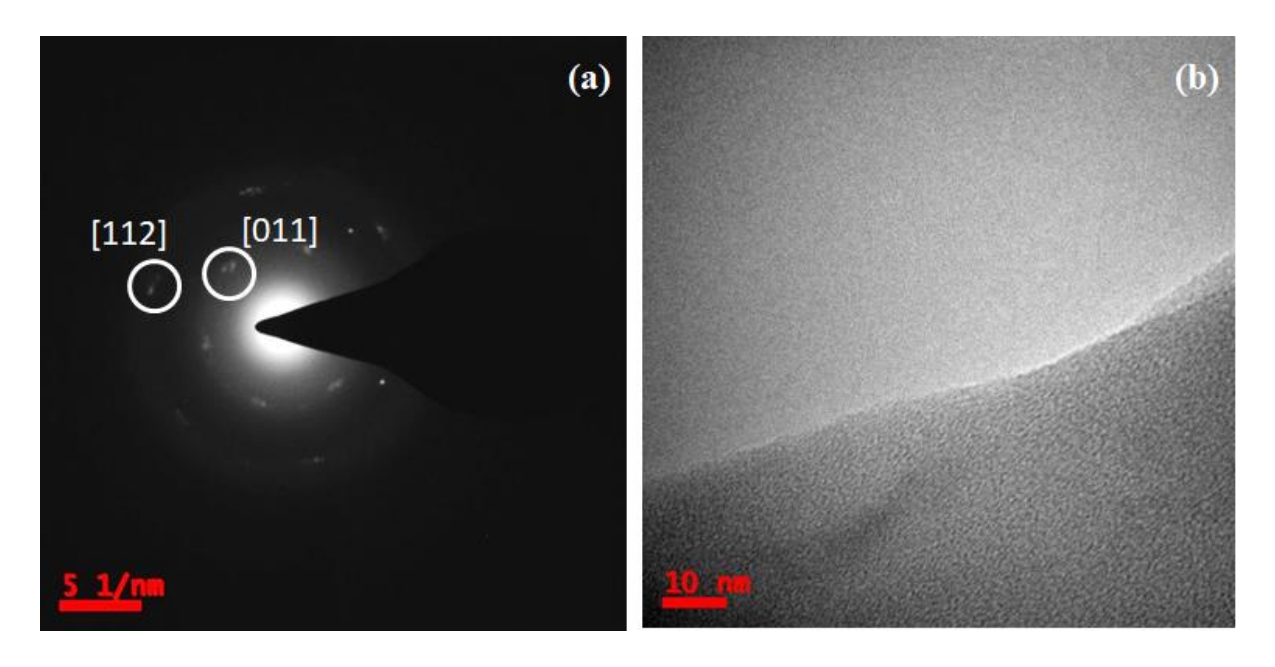


Figure 8. SEAD pattern (a) and the corresponding TEM image (b). [Deposition parameters - 30 min, 9 mg AB , 50 SCCM]

### Spectroscopic studies—

The synthesized film which was used for diffraction studies was also put to spectroscopic studies like FTIR, UV-Vis, Raman and XPS. For all these studies the transfer from copper to dielectric substrate was made by using the same transfer process as mentioned earlier. Figure

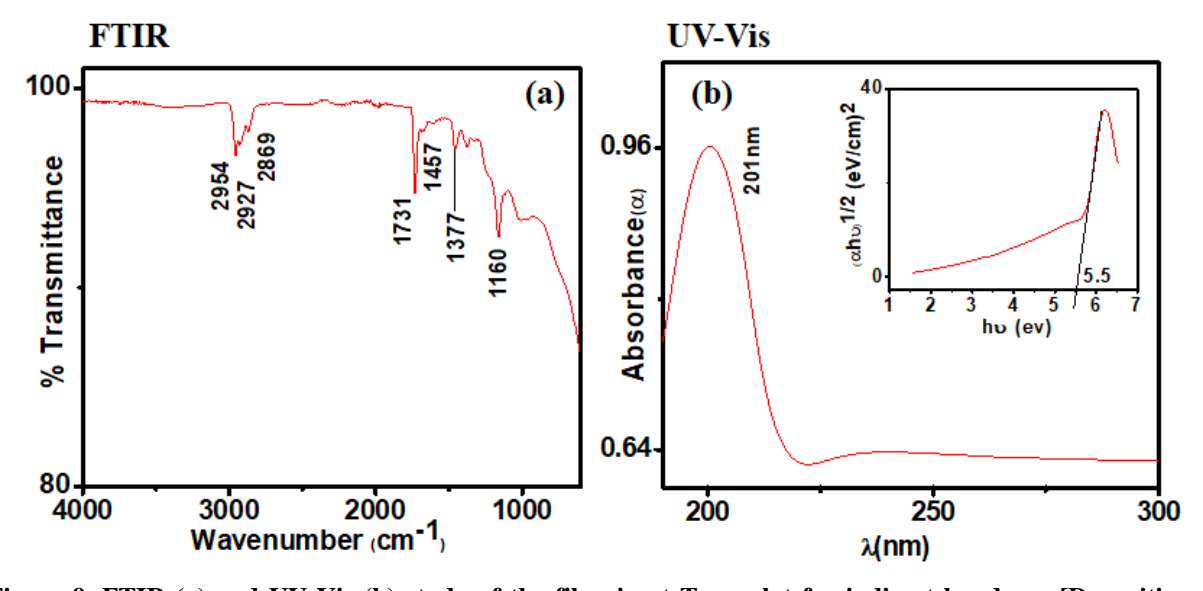


Figure 9. FTIR (a) and UV-Vis (b) study of the film, inset Tauc plot for indirect band gap.[Deposition parameters - 30 min, 9 mg AB, 50 SCCM]

9 (a), (b) shows the FTIR (a) and UV-Vis (b) spectroscopy of the transferred film. For FTIR studies the film was transferred to a SiO<sub>2</sub>/Si substrate and for UV-Vis spectroscopy, it was transferred over a transparent quartz plate. Quartz plate was used instead of glass as transmission spectroscopy was needed from UV (200 nm) range to IR range and as glass is opaque to UV rays so quartz plate was used. There are some distinct peaks that can be seen in the FTIR spectrum, the band centred near 2927 cm<sup>-1</sup> is for the leftover PMMA residues <sup>10</sup>. The

peak centered at 1160 cm<sup>-1</sup> corresponds to Si-O out of phase stretching and the peak at 1377 cm<sup>-1</sup> corresponds to the hBN film <sup>11,12</sup>.

UV-Vis spectra was obtained to determine the band gap of our synthesized film. In figure 10, (b) we can see the UV-Vis spectra of the film over quartz plate, it has an absorption peak at 201 nm. We used the Tauc equation –

$$c(h\nu - Eg) = (\alpha h\nu)^{1/2}$$

Where  $\alpha$  is the absorption coefficient, h is the planks constant,  $\lambda$  is the wavelength, C is a constant and Eg is the band gap. The inset of figure 9 (b) show the Tauc plot which is a plot of the Tauc equation, from this, we get a band gap of 5.5 ev, which is fairly consistent with prevailing literature <sup>13,14</sup>.

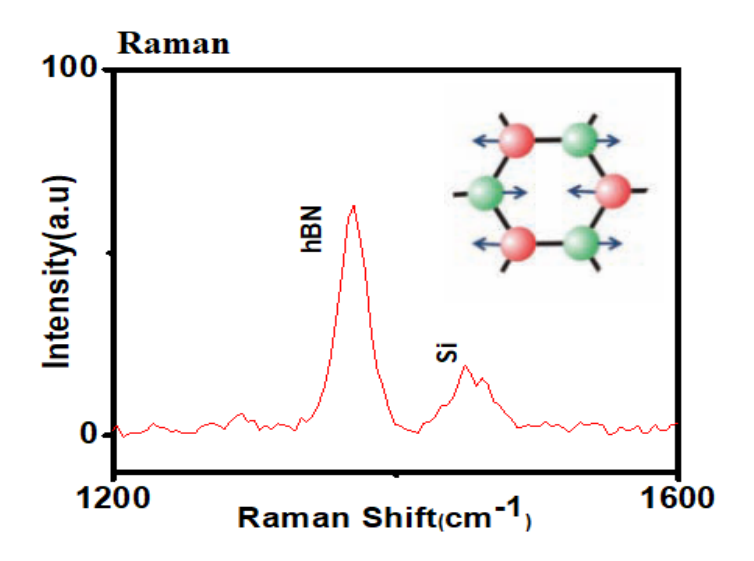


Figure 10. Raman spectra of the hBN film over  $SiO_2$  /Si substrate, inset shows the B and N vibrational modes <sup>15</sup> [Deposition parameters - 30 min, 9 mg AB, 50 SCCM]

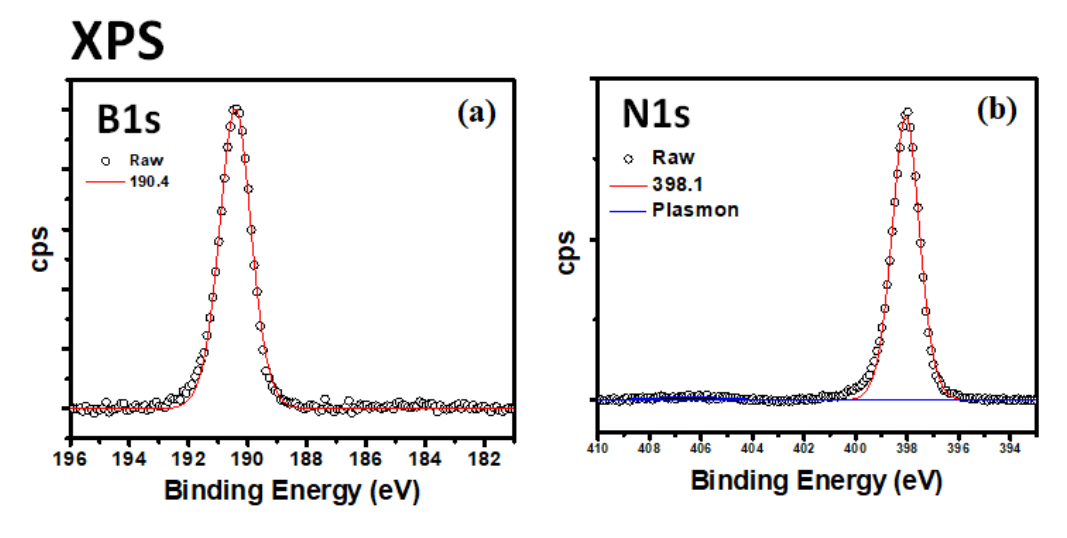


Figure 11. High resolution XPS spectra of the hBN film. a) N1S and b) B1s[Deposition parameters - 30 min, 9 mg AB, 50 SCCM]

The same film was used Raman measurements, figure 10 shows the Raman spectra of the transferred film. The hBN peak at  $1370 \, \text{cm}^{-1}$  is due to the in-plane stretching of B and N atoms. The sublattice of B atoms stretches to the opposite direction of the N atoms as shown in the inset of the figure  $11^{15}$ . The Si peak is present at  $1450 \, \text{cm}^{-1}$ , this is the third-order transverse optical mode of the underneath Si substrate  $^{16}$ . The interesting thing to note here is that the intensity of the hBN (E2g) peak is poor, just about 2.5 times to that of the third order Si peak. This is because the Raman scattering cross section of hBN is very low, to put it into perspective it is about 50 times lesser to that of graphene. Raman spectra are one of the identifying spectra of hBN. Full-width half maxima (FWHM) of the  $E_{2g}$  peak is  $24 \, \text{cm}^{-1}$  which is the value reported for most hBN films synthesized by APCVD  $^{17}$ .

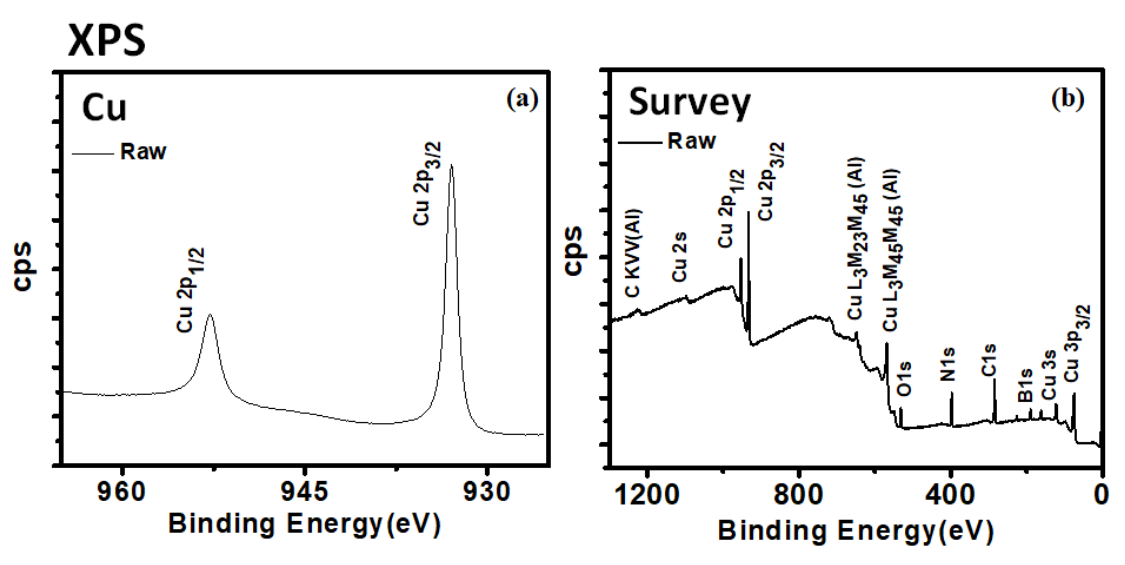


Figure 12. High resolution XPS spectra a) Cu and b) survey of the hBN film. [Deposition parameters - 30 min, 9 mg AB, 50 SCCM]

XPS analysis was performed over the hBN/Cu film. XPS is an excellent technique to understand the stoichiometric ratio of B and N in hBN film, it also provides important information about any impurities of different bonding phase in the film. Figure 11(a & b) and 12(a) are the high resolution XPS scans of B,N and Cu . Figure 12(b) is the survey spectrum of the film. The N1s peak at 398.1 eV and B1s peak at 190.4 eV (figure 11 a &b) correspond to few layer hexagonal boron nitride film and these values are similar to that of the reported literature <sup>18</sup>. The FWHM of these two peaks are B-1.26 eV and 1,3 eV for N. The pi plasmon peak in N1s spectrum can be seen at 406.5 eV, plasmon peak arises due to electron lone pair at the nitrogen site .For calculation of the stoichiometry, N1s and B1s peak was fitted with Gaussian-Lorentzian peak shape and ratio of the area under peak is divided by Relative Sensitivity Factors (RSF) as-

$$\frac{N}{B} = \frac{\frac{Area\ under\ peak\ N1s}{RSF\ of\ N}}{\frac{Area\ under\ peak\ B1s}{RSF\ of\ B}}$$

Relative sensitivity factor or RSF of an orbital is the photo-ionization cross section when normalised with respect the C1s value.. Boron K shell photoionization cross section for 1500 eV photon energy (we used 1486.6 eV Al lines) is - 6453.8 Barns and nitrogen K shell photoionization cross section for 1500 eV photon energy (we used 1486.6 eV Al lines)- 23914 Barns. Using these for the calculation of stoichiometry of the BN film it was found to be B: N= 0.94:1 which shows that the hBN film has nearly 1:1 B:N ratio. High resolution Cu spectrum (figure 12 a) shows two sharp symmetric peaks of Cu2p<sub>1/2</sub> and Cu 2p<sub>3/2</sub> with 1.0 eV and 1.2 eV FWHM respectively. There are no peaks related to the oxide phase of copper, this is due the fact that hBN acts as a protective layer for the copper substrate which inhibits oxidation. This same fact has been seen in the optical image in figure 5(b) where the copper underneath the hBN islands is not oxidized. The survey spectrum in figure 12(b) shows no extra contaminant peak, only adventitious carbon and adsorbed oxygen along with Auger lines can be seen.

## 5.2.2. Film thickness and morphology variation.

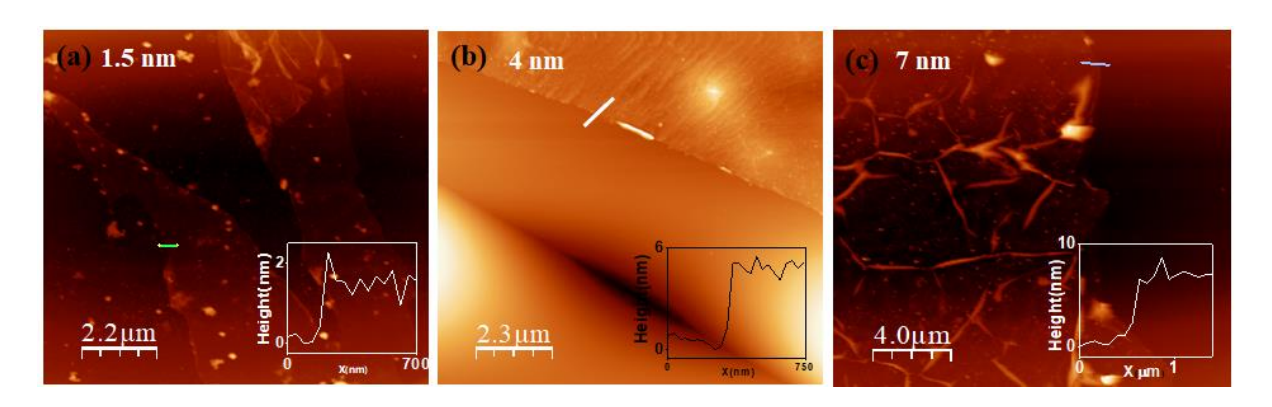


Figure 13. AFM micrographs of the transferred sample of three different thickness, inset showing their respective height profile, a) 1.5 nm b) 4 nm and c) 7 nm.

The film thickness was varied by changing the amount of precursor material. Figure 13 shows the AFM micrograph of three transferred films with different thickness, inset shows the height profile which is 1.5 nm, 4 nm and 7 nm respectively. For all three films, the substrate was pre annealed at 1040°C for 60 min. For synthesizing the 1.5 nm and 7 nm film the substrate was electropolished and 4 mg (figure 13 a) and 11 mg (figure 13c) AB powder was used. The substrate used for 4 nm film (figure 13b) was not electropolished and 10.5 mg AB powder was used. Interestingly the thickness is different although in figure 13(b) and 13(c) a similar amount of powder was used. This is due to the fact the substrate of the thicker film was electropolished and as electropolishing reduces the roughness of the substrate it facilitates layered growth and thereby increases the thickness of the film. There are wrinkles over the 7 nm film the origin is discussed in the following section.

The gas flow rate during the cooling phase has an important role in the surface morphology of the film. With a higher gas flow rate the cooling rate increases and wrinkles arise. Figure 14 gives us more insight into the formation of wrinkles. Figure 14(a) shows the AFM image of the wrinkled 7 nm hBN/Cu and (b) shows the corresponding FESEM image. The inset of figure 14(a) shows the height profile of the wrinkles. The wrinkles were made by rapid cooling of the

copper substrate after the growth. Thermally-induced wrinkles are fairly common in hBN synthesis  $^{19}$ . 200 SCCM Ar/H<sub>2</sub> was used during the cooling whereas only 50 SCCM Ar/H<sub>2</sub> was used for both the 1.5 nm and 4 nm film. This increased gas flow increased the cooling rate and caused the thermally induced wrinkles in the 7 nm film. The height of the wrinkle is 18 -20 nm and the lateral dimension is 100 nm. Figure 14 (b, c) shows the AFM and FESEM image of the 1.5 nm film . The r.ms roughness of the 7 nm film is 21 nm whereas it is only 7 nm for the 1.5 nm film.

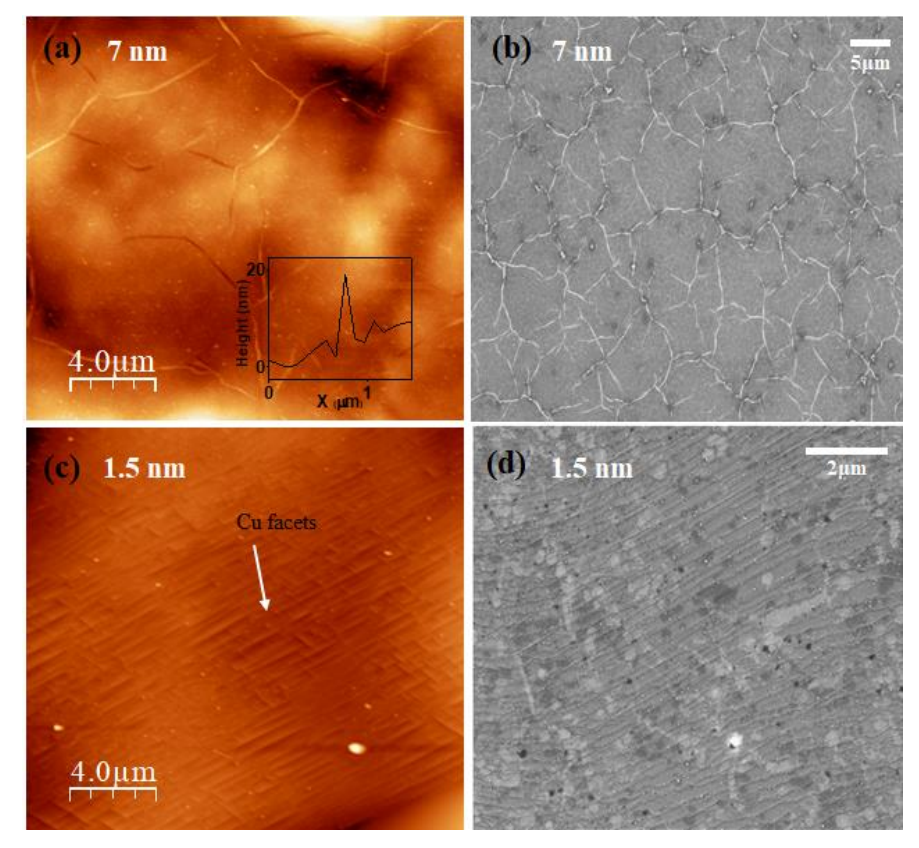


Figure 14. AFM (a, c) and FESEM (b, d) of different morphology of two films a) & b) 7 nm film and c) & d) 1.5 nm film.

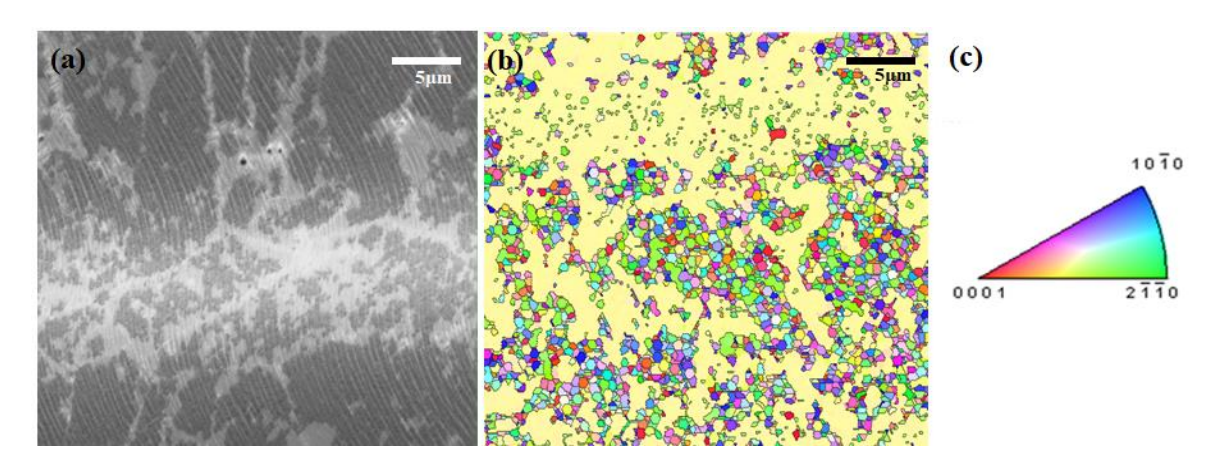


Figure 15. Grain size determination by EBSD mapping of hBN/Cu a) electron image where the EBSD map has been done.

From both the AFM image and FESEM image we can see the 1.5 nm film has homogeneous

and uniform syrface morphology without the presence of wrinkles. The AFM image of the 1.5 nm film shows copper facets with a clean surface.

To study the grain size of the film we performed an EBSD scan. The scan was performed at 10 Kv gun voltage. Figure 15 (a) shows the electron image where the EBSD scan was taken and figure 15(b) shows the EBSD map. The yellow colour in the plane where the scan results were not obtained in image 15(b), this due to the surface roughness of the film. As EBSD requires a very smooth surface for imaging. The coloured tiles in figure 15 (b) show the estimated grain size is 1-1.5  $\mu$ m and is polycrystalline in nature. Figure 15(c) shows the inverse pole figure for the hexagonal system.

The films of thickness 1.5 nm, 6 nm and 7 nm have been used for SERS study which is described in the following section.

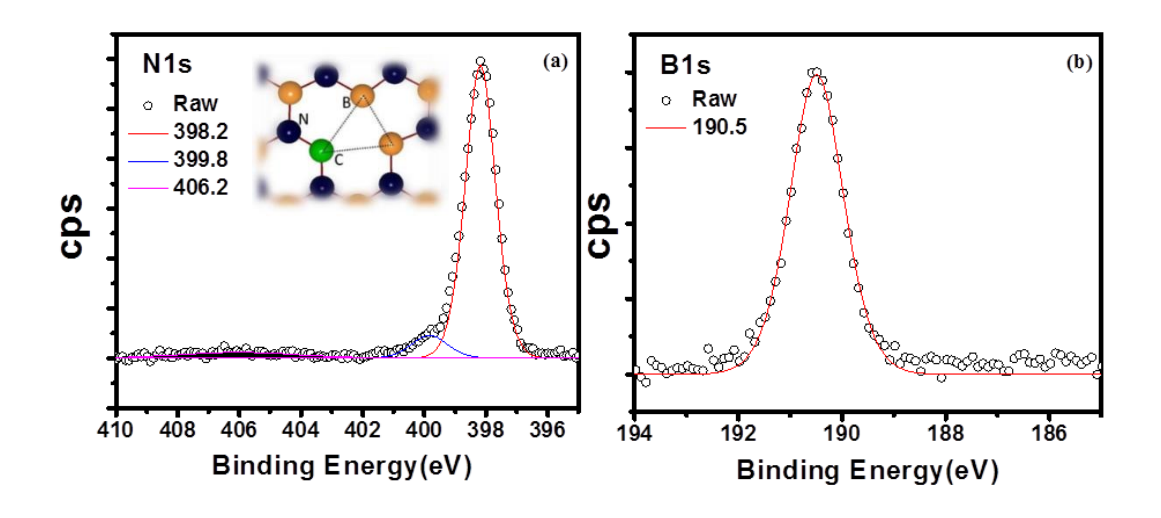


Figure 16. High resolution XPS spectrum of the 1.5 nm thick film, (a) N1s and (b) B1s.

The 1.5 nm film was subjected to XPS study. Figure 16 shows the high-resolution N1s and B1s spectra of film. The pair 398.2 eV / 190.25 eV belongs to few-layer hBN, this is similar to the XPS results obtained for the 6 nm film. Which is expected as both films are multilayer hBN The FWHM for the 398.2 eV peak is 1.2 eV and for the 190.5 eV is 1.25 eV. In figure 16(a) the pi plasmon peak is centered at 406.2. The peak centered at 399.8 eV is due to the C-N bonds present in the film. For thinner hBN films sometimes VNCB defects form. In VNCB defect one B site is replaced with C along with N site vacancy as depicted in the inset of figure  $16(a)^{20}$ . The stoichiometry of the 1.5 nm was determined in a similar way like that of the 6 nm film, the N:B ratio is 1: 0.913.

Figure 17 (a) shows the comparison of Raman spectrum of the 1.5 nm, 6 nm and 7 nm film. the E2g peak of hBN is centered at 1368 cm<sup>-1</sup>,1372 cm<sup>-1</sup> and 1368 cm<sup>-1</sup> respectively. The plots were fitted with Lorentzian shape. The FWHM of the three films is 19 cm<sup>-1</sup>, 24 cm<sup>-1</sup> and 31 cm<sup>-1</sup>. The high FWHM of the 7 nm film can be attributed to the fact that the film surface has wrinkles which is indicates that film was under stress and wrinkles emerged due to the stress-relieving process. The inherent stress affects the atomic bonds which in turn broadens the Raman peak.

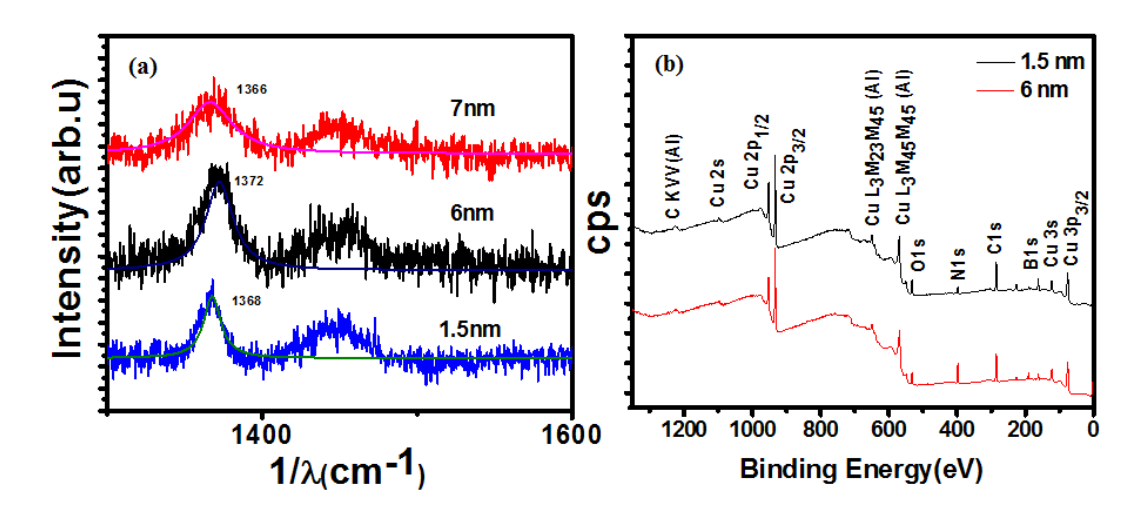


Figure 17. Comparison of (a) Raman spectrum of 1.5 nm, 6 nm and 7 nm film, (b) survey XPS spectrum of 1.5 and 6 nm film.

The peak at  $1450 \text{ cm}^{-1}$  is due to the third order Si peak like in previous Raman measurements. The survey spectrum of the 1.5 nm and 6 nm hBN has been compared in figure 17(b). Both the scans have been recorded under similar conditions like same dwell time and equal number of sweeps so that they can be measured. The  $\text{Cu}2p_{1/2}$  peak is more intense for the 1.5 nm film in comparison with 6 nm film. Which is excepted as the substrate peak intensity should be smaller for the thicker film.

#### 5.3 Conclusion.

We have successfully synthesized hexagonal boron nitride over copper foil by using ammonia borane powder as a precursor. Films of four different thickness have been deposited by varying the amount of precursor material. The synthesized films have been characterized by different analytical methods. The measured band gap from Tauc plot of the synthesized film is 5.5 eV. XPS scans reveal that the stoichiometry of the film is nearly 1:1 (calculated value is B:N 0.94:1). The hBN film synthesized over annealed (in contact with the crucible during annealing) copper substrate has a grain size of 2-4 µm. The grain size determination was done by EBSD scan of the hBN film. FESEM images show that the surface of the film has a homogeneous and uniform texture. Vibrational spectroscopy like Raman and FTIR was done by transferring the hBN film to SiO<sub>2</sub>/Si substrate. We employed two etching agents for wet etching of Cu foil, FeCl<sub>3</sub> and (NH<sub>4</sub>)<sub>2</sub>S<sub>2</sub>O<sub>8</sub>, with ammonium persulphate showing the best results. We have also synthesized wrinkled hBN film by increasing as flow during the cooling rate. Thermally-induced wrinkles have a lateral dimension of 100 µm and the height profile from the AFM images shows that the wrinkles are 35 nm in height. Our results elucidate that hBN film thickness can be varied by only varying the precursor material and keeping all other parameters constant. We varied the amount of ammonia borane powder from 4.5 mg to 11 mg to achieve 1.5 nm, 4 nm, 6 nm and 7 nm films.

#### 5.4. References.

- 1. Ahmed, K. *et al.* Growth of hexagonal boron nitride on (111) Si for deep UV photonics and thermal neutron detection. *Appl. Phys. Lett.* **109**, 1–5 (2016).
- 2. Lee, K. H. *et al.* Large-scale synthesis of high-quality hexagonal boron nitride nanosheets for large-area graphene electronics. *Nano Lett.* **12**, 714–718 (2012).
- 3. Babenko, V. *et al.* Time dependent decomposition of ammonia borane for the controlled production of 2D hexagonal boron nitride. *Sci. Rep.* **7**, 1–12 (2017).
- 4. Baitalow, F., Baumann, J., Wolf, G., Jaenicke-Roöβler, K. & Leitner, G. Thermal decomposition of BNH compounds investigated by using combined thermoanalytical methods. *Thermochim. Acta* **391**, 159–168 (2002).
- 5. Luo, D. *et al.* Adlayer-Free Large-Area Single Crystal Graphene Grown on a Cu (111) Foil. **1903615**, 1–13 (2019).
- 6. Khaksaran, M. H. & Kaya, I. I. Spontaneous Nucleation and Growth of Graphene Flakes on Copper Foil in the Absence of External Carbon Precursor in Chemical Vapor Deposition. *ACS Omega* **3**, 12575–12583 (2018).
- 7. Chang, R. J. *et al.* Growth of Large Single-Crystalline Monolayer Hexagonal Boron Nitride by Oxide-Assisted Chemical Vapor Deposition. *Chem. Mater.* **29**, 6252–6260 (2017).
- 8. Mahvash, F. *et al.* Corrosion resistance of monolayer hexagonal boron nitride on copper. *Sci. Rep.* **7**, 1–5 (2017).
- 9. Al-Kamiyani, S. & Mohiuddin, T. Improved control in elimination of white impurities on graphene by chemical vapor deposition (CVD). *AIP Adv.* **8**, (2018).
- 10. Vijayakumari, G., Selvakumar, N., Jeyasubramanian, K. & Mala, R. Investigation on the electrical properties of polymer metal nanocomposites for physiological sensing applications. *Phys. Procedia* **49**, 67–78 (2013).
- 11. Tay, R. Y. *et al.* Trimethylamine Borane: A New Single-Source Precursor for Monolayer h-BN Single Crystals and h-BCN Thin Films. *Chem. Mater.* **28**, 2180–2190 (2016).
- 12. F, A. M. D. FTIR and Photoluminescence of Annealed Silicon Rich Oxide films. *Superf. y vacío* **22**, 11–14 (2009).
- 13. Silly, M. G. *et al.* Luminescence properties of hexagonal boron nitride: Cathodoluminescence and photoluminescence spectroscopy measurements. *Phys. Rev. B Condens. Matter Mater. Phys.* **75**, 1–5 (2007).
- 14. Cai, Q. *et al.* Raman signature and phonon dispersion of atomically thin boron nitride. *Nanoscale* **9**, 3059–3067 (2017).
- 15. Gorbachev, R. V. *et al.* Hunting for monolayer boron nitride: Optical and raman signatures. *Small* **7**, 465–468 (2011).
- 16. Wang, L. *et al.* Water-assisted growth of large-sized single crystal hexagonal boron nitride grains. *Mater. Chem. Front.* **1**, 1836–1840 (2017).
- 17. Abidi, I. H. *et al.* Selective Defect Formation in Hexagonal Boron Nitride. *Adv. Opt. Mater.* **7**, 1–9 (2019).
- 18. Kidambi, P. R. *et al.* In Situ Observations during Chemical Vapor Deposition of Hexagonal Boron Nitride on Polycrystalline Copper. (2014) doi:10.1021/cm502603n.
- 19. Yu, J. S. *et al.* Structural analysis of graphene synthesized by chemical vapor deposition on copper foil using nematic liquid crystal texture. *Carbon N. Y.* **76**, 113–122 (2014).
- 20. Sajid, A. & Thygesen, K. S. V N C B defect as source of single photon emission from hexagonal boron nitride Introduction: (2007).

#### Chapter 6

#### Applications of hBN and its heterostructures

This chapter explores the application of CVD grown hBN. We have investigated the following applications of hBN-a) resistive switching properties of hBN, b) hBN as an electrocatalyst in oxygen reduction c) hBN heterostructure and d) surface-enhanced Raman spectroscopy. 6 nm thick hBN was used to study both ORR and resistive switching properties. For resistive switching conductive AFM was used. Resistive switching is the sudden change in the resistance state of a dielectric due to the action of electrical potential. This change is reversible and non-volatile in nature. This property has an interesting application in non-volatile resistive random-access memories (RRAM) devices. Resistive switching studies were carried out by using a conductive atomic force microscope. The copper substrate of the hBN/Cu was used as the bottom electrode and the cAFM tip acted as the top electrode. Our studies show that the I-V loop for 6 nm thick hBN film was stable for more than 100 cycles.

The oxygen reduction reaction is the most important reaction in a fuel cell. A fuel cell is a device that converts chemical energy to electrical energy. But unlike any conventional battery a fuel most commonly hydrogen is used. At the anode, with the help of catalyst hydrogen molecules are split into electrons and protons. These electrons are forced into a circuit that generates an electric current. At the cathode site, protons, electrons, and oxygen combine to form water by means oxygen reduction reaction. Fuel cells do not have any moving parts and are extremely efficient in making electricity. We have investigated the role of hBN as a catalyst in ORR reaction by using cyclic voltammograms.

We have also investigated the hBN heterostructure by fabricating them via micromanipulation by using organic stamps and also by using wet transfer techniques. Hexagonal boron nitride has shown remarkable performance as a substrate for graphene-based electronics and also in encapsulating devices. We have investigated the photocurrent behaviour of  $MoS_2$  with and without encapsulation by hBN. Finally, in this chapter, we have explored the SERS abilities of hBN films. For SERS drop-casting method was used to disperse the probe molecules onto the hBN substrate and measured the enhancement effect due to the substrate using a 532 nm excitation laser. The observed enhancement factors are consistent with theoretically calculated interaction energies of MB > R6G > MG with a single layer of hBN. We also observed that the enhancement is independent of the film thickness and surface morphology. We demonstrate that the hBN films are highly stable and even for older hBN films prepared 7 months earlier we were able to achieve similar enhancements when compared to freshly prepared films. Our detailed results and analyses demonstrate the versatility and durability of hBN films for SERS applications.

#### 6.1 Resistive switching application of CVD grown hBN.

Resistive switching materials (RSMs) exhibit tunable resistance states on the application of electrical bias. These RSMs materials can be used in Resistive random-access memory (RRAM) devices based on non-volatile memory technology. The RRAM device is a voltage/current controlled resistor, that can toggle between a low resistance state (LRS) and

high resistance state (HRS), usually has a metal-insulator-metal (MIM) vertical configuration. Electrical bias induced resistive switching is displayed by many organic and inorganic materials (metal oxides, chalcogenides, amorphous silicon and more)<sup>1,2</sup>. In addition to these conventional RSMs, low dimensional materials are also being explored for Resistive switching behaviour. hBN, a 2D material, shows a sudden change in resistance under the application of electric field and can be used in RRAM devices <sup>3</sup>. HBN has many advantages – it is an insulator that allows a larger operating window and has high thermal conductivity, thermal stability. hBN shows non-polar resistive switching property which is the coexistence of both unipolar and bipolar switching properties <sup>4,5</sup>. It has a high current on/ off ratio (10<sup>7</sup>) which is also beneficial for RRAM devices.

In this section, we have employed CVD grown multilayer hBN film for resistive switching study by conducting AFM. The synthesis process and substrate preparation were similar to that mentioned in chapter -5. For the resistive switching study, all hBN films were grown over the electropolished substrate.

Figure 6.1 (a) shows the schematics of the device geometry applied via CAFM to study the resistive properties. A Pt/Ir tip was used as the top electrode and the Cu substrate of the hBN/Cu structure as the bottom electrode. The compliance current of the CAFM was set at 20 nA. To mitigate the adverse effect of humidity and adsorbed moisture over hBN/Cu surface the CAFM chamber was air sealed and silica gel was kept inside the chamber to absorb the moisture.

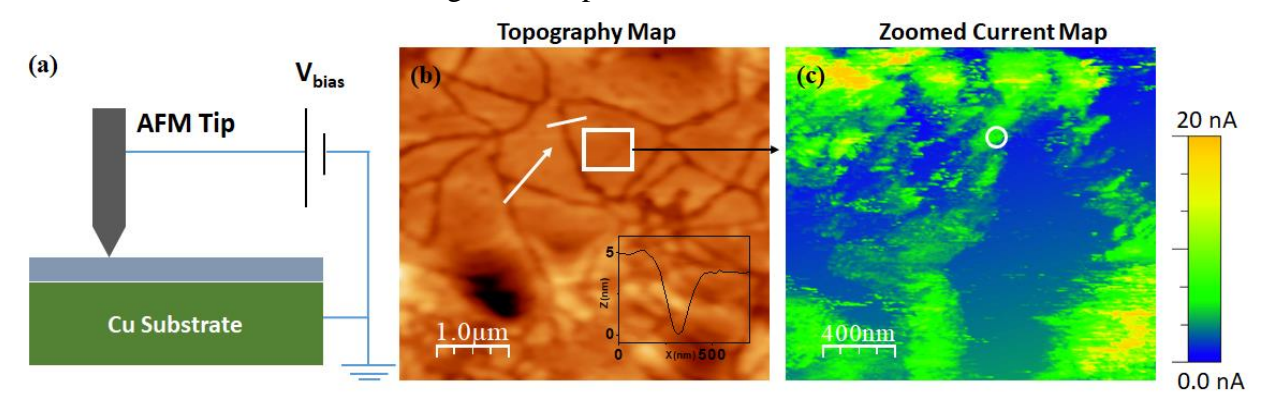


Figure 6.1 (a) Schematics of the device geometry used to study hBN film via CAFM. (b) Topography image of the hBN film, inset shows the height profile through grain boundary (c) Current map of the marked position in (b) under the influence of a bias of 10 V.

Figure 6.1(b) shows the topography map (b) and current map (c) of the film. In the topography image, we can see the grain boundaries (GB) shown by the white arrow. Oxygen intercalation takes place through these grain boundaries which can oxidize the copper substrate. The Cu foil starts oxidizing close to the GB's so for conductivity measurement we chose a position within a single hBN grain avoiding GB's. Figure 6.1 (c) shows the current map of the area marked in figure 6.1 (b) at a bias voltage of 10 V. We were unable to record currents at low bias voltage and had to increase the bias voltage to 10V to get a measurable current. hBN is a large band gap material with high electrical impedance and is used as a tunnel barrier in many van der Waals heterostructures. In addition, we also have copper oxide layers present at the back contact (hBN/Cu/Copper oxide) which also acted as a tunnel barrier to current conduction.

Therefore, a high bias voltage was required for the onset of current conduction through the film. In the current map shown in Figure 6(c), we observe areas with both high and low local conductivity, with current values varying from 4nA to 15 nA with the highest current at 20 nA. This inhomogeneity in local conductivity within a grain of hBN can be due to the presence of inhomogeneous local defect distribution or local variation in thickness over a single grain.

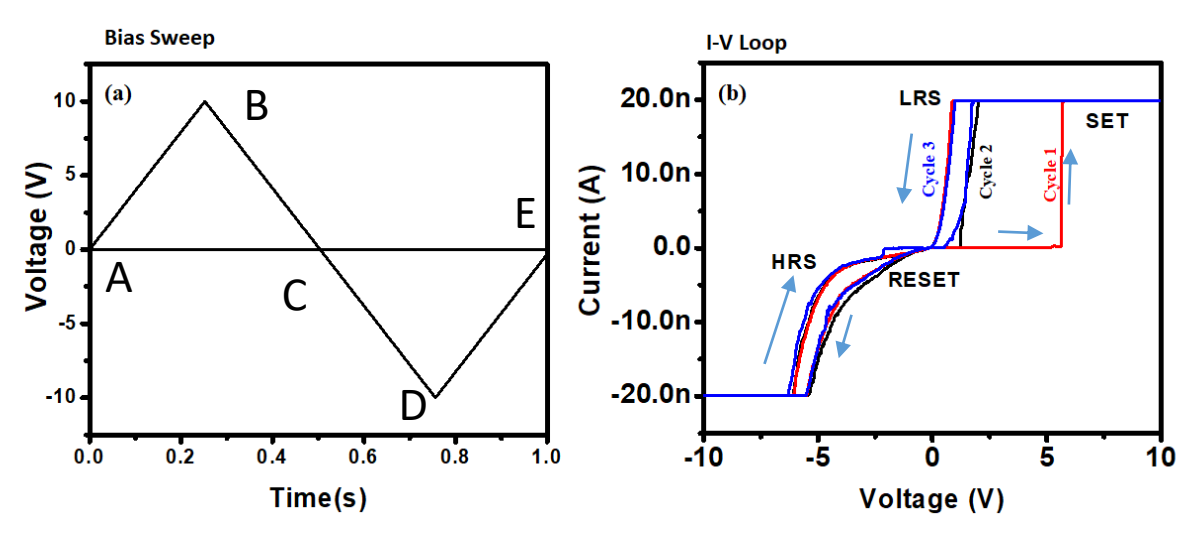


Figure 6.2: I-V study of 6 nm thick hBN film (a) Nature of the applied bias (b) I-V loop for first three cycles.

Figure 6.2 (b) shows the I-V characteristics under the influence of an applied DC sweep bias from 0V to 10 V. The circled area in figure 6.1 (c) shows the area where the I-V characteristics have been recorded. The nature of the bias has been shown in figure 6.2 (a). The bias is linear in nature reaching a maximum of 10 V in both polarities. It was increased linearly from 0 V to 10 V at a rate of 30 V/s and decreased at the same rate. Each I-V loop was recorded within a span of 1 s to minimize the drift of the cAFM tip (forming voltage). Cycle 1, in figure 6.2 (b) achieves the compliance current of 20 nA at a voltage of 6 V shown in the first quadrant (i.e. in +ve cycle). In the next two cycles, the compliance current is achieved around 2 V, which is significantly lower than the first cycle. The high voltage required in the first cycle is to achieve LRS (low resistive state) state from HRS (high resistive state) is because of the initial formation of conducting path through CF (conducting filaments). To test the endurance of the film it was subjected to multiple I-V measurements. Figure 6.3(a) shows 100 cycles, after 100 cycles the film retains its resistive switching properties exhibiting high quality and stability of the film. Figure 6.3 (b) shows that the SET and RESET voltages do not vary too much with each successive cycle. Other materials which exhibit resistive switching as TiO<sub>2</sub> has also been reported to show 100 I-V cycles <sup>6</sup>. Stability up to 100 cycles is considered stable enough for venturing into further studies.

The switching mechanism can be attributed to the formation/rupture of conductive filaments composed of either boron ions/vacancies or metal ions <sup>2,7,8</sup>. In a perfect 2D material film, metal atoms like Cu encounter a large energy barrier for diffusion across the basal plane. However, the presence of defects like vacancies, grain boundaries and edges lower the diffusion barriers and Cu can easily diffuse into the hBN film. Thus, when an external bias is applied, metal ions can now diffuse into the hBN film to form conducting channels resulting in the LRS of the

device. When the polarity of the applied voltage is reversed, the CFs rupture either by electrochemical dissolution or migration of ions due to Joule heating, resetting the device to HRS. As mentioned in the previous chapter, the hBN films synthesized by CVD here are slightly boron deficient. Another possibility is that the metals atoms can substitute the boron vacancies present and give rise to conducting channels. To get a better idea about the switching mechanism further comprehensive studies need to be undertaken.

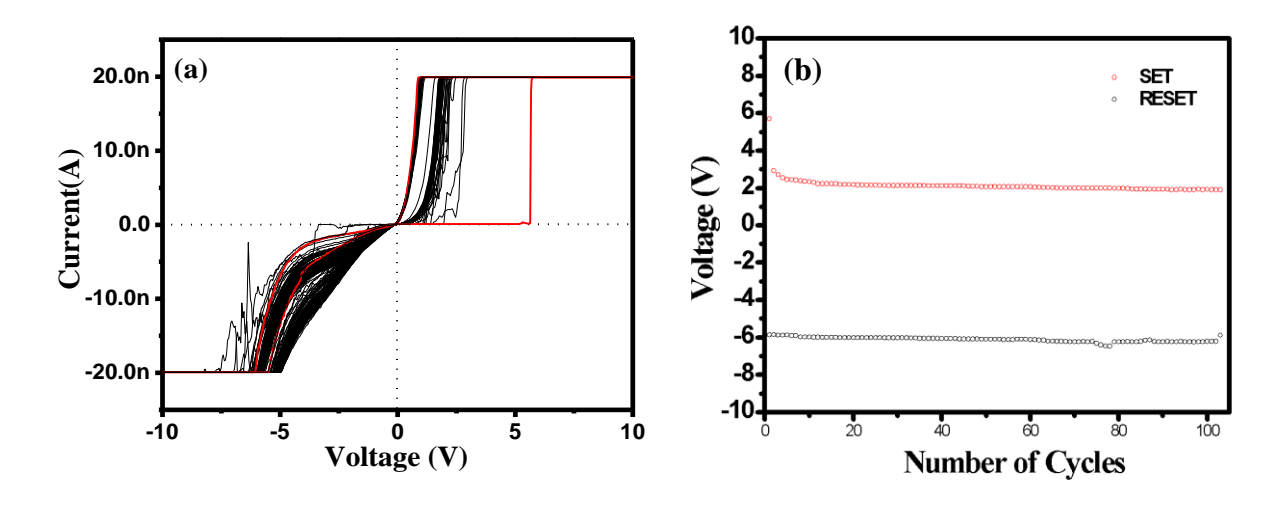


Figure 6.3 (a) I-V loop showing 100 cycles (b) SET & RESET voltages for first 100 cycles.

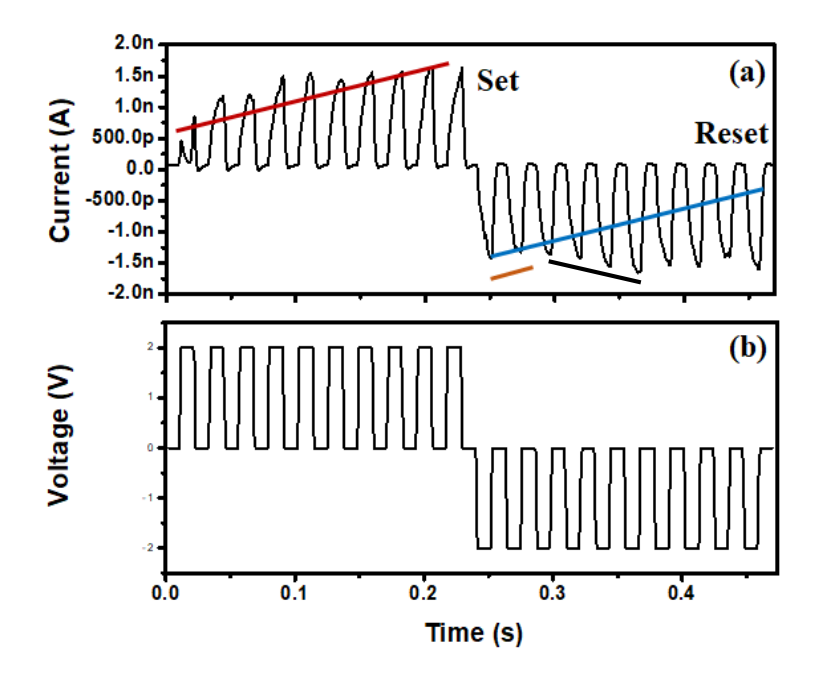


Figure 6.4: Learning behaviour study (a) I-V characteristics under the influence of pulsed DC. (b) Nature of the applied pulse D.C.

In recent times biological system inspired computing is getting traction. Computing systems that emulate the nervous system are more equipped to solve difficult problems and are sought after for pattern recognition and studying the interaction between non-biotic systems with the external environment. Among many such areas neuromorphic architecture in materials that

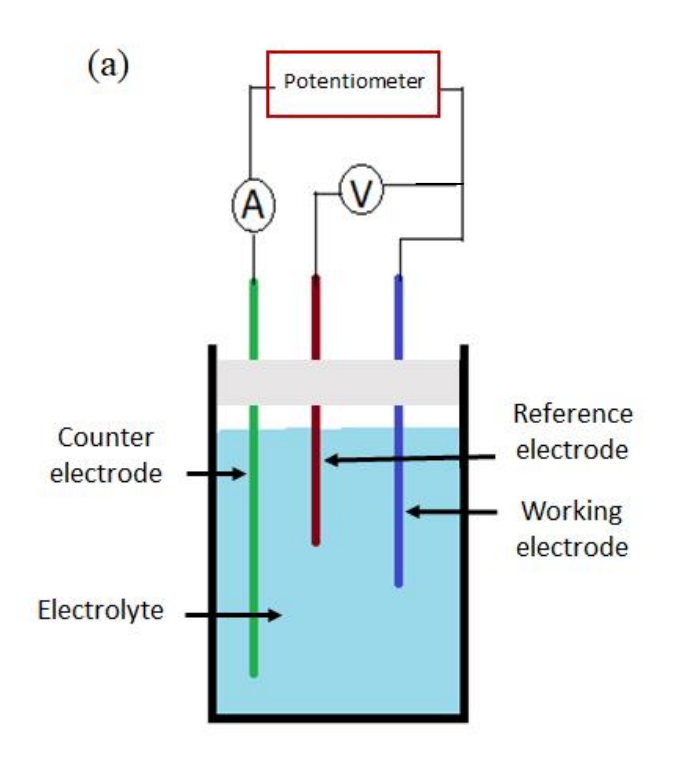
exhibit resistive switching like HfO<sub>2</sub> and ZnO has been studied in detail <sup>9,10,11,12</sup>. Several two-dimensional materials are being explored for non-von Neumann architecture, MoS<sub>2</sub> and graphene has shown promising results <sup>13,14,15</sup>. Recent studies about Graphene memristive synapses in crossbar architecture has shown that it can act as a powerful computing engine in artificial neural networks <sup>16</sup>.

We have studied neuromorphic potentiation and depression also known as the learning process of the 6 nm hBN film over Cu substrate <sup>17</sup>. Figure 6.4 shows potentiation (depression) in the +Ve and –Ve bias. For both the positive half and negative half of the applied voltage the magnitude of the applied bias is 2 V with 25 ms between each pulse as shown in figure 6.4 (b). The current in the +Ve half gradually rises (follows the red line) with each pulse and the device is SET to a low resistive state, this is due to the formation of CF. Upon the change of polarity, during the first 2 potentiations (depression) the current gradually decreases (yellow line). The current should have followed the blue line and should be zero and RESET the device. But instead, it fluctuates. This can be attributed to the drift of the cAFM tip. Due to the drift of the tip new CF may arise in the –Ve bias which creates new filaments. This can be seen just after the first 2 potentiations (depression) in the –Ve half, i.e the black line, the current increases with each pulse. Again when the tip drifts back to its original position the current starts decreasing (green line).

Potentiation studies in neuromorphic computing resemble the learning process in biological systems. Just as with increased frequency of action potential through neurons enables us to learn new things more quickly. The difference between the two applied electric pulses in figure 6.4 (b) affects the time taken by hBN/Cu system (in figure 6.4 (a)) to achieve the LRS state (set) from HRS (reset) state.

#### 6.2. hBN as an electrocatalyst in oxygen reduction reaction (ORR).

Fuel cells have always been a sought after technology since their inception because of their high energy density, remarkable efficiency and next to zero gas emission. Now with the rise of electrification of vehicles fuel cells have become a hot topic of scientific research. In simple terms a fuel cell is an electrochemical cell where chemical energy is converted to electrical energy by using a fuel and an oxidizing agent. The oxygen reduction reaction is the most important reaction that happens in a fuel cell <sup>18</sup>. Oxygen reduction reaction or ORR is a chemical reaction in which oxygen molecules are reduced to either water or hydrogen peroxide. It is also an important reaction in biological respiration like in aerobic systems. Electrocatalysts like Pt is used in ORR reaction, but due to high cost and low stability, the search for alternative electrocatalysts is always on <sup>19</sup>. The search for electro-catalysts like nonmetallic, alloys or oxides of precious metals (like Pd-Pt) and nitrogen coordinated metals has dominated research efforts <sup>20,21</sup>. Nitrogen-doped graphene and hBN are the two most promising 2D materials which have been explored as an electro-catalyst in ORR reaction <sup>22,23</sup>. The metal oxide or metal-based catalysts generally suffer from sintering and agglomeration when operating inside a fuel cell, these degrade the catalysts.



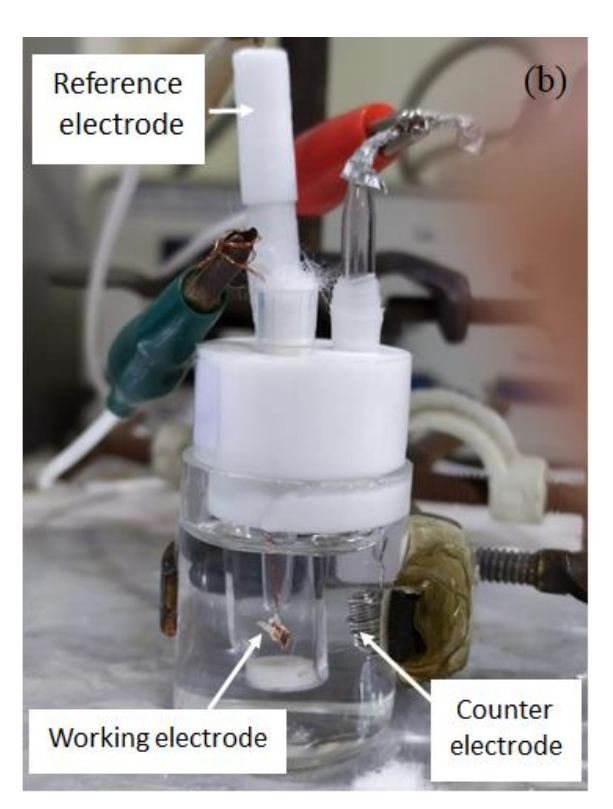


Figure 6.5 schematics (a) and image of the electrochemical cell used for ORR study of hBN.

To overcome such scenarios nonmetallic carbon-based catalysts has been developed. hBN and N doped graphene provide more surface area for electrocatalytic activity as well as they are stable in a varied chemical environment. In an aqueous solution Oxygen reduction reaction happens mainly in two pathways:

- 1) Reduction through 4 electrons from O<sub>2</sub> to H<sub>2</sub>O
- 2) Reduction through 2 electron O<sub>2</sub> to H<sub>2</sub>O<sub>2</sub>

It has been observed in hBN/Ni systems that the energetically favoured path is a 2 electron process, where hBN acted as an electrocatalyst <sup>24,25</sup>. Hexagonal boron nitride has also been studied as an electrocatalyst for Au electrodes <sup>18</sup>. In this work, we have studied the electrocatalytic activity of hBN over copper electrode by using cyclic voltammetry. 6 nm thick hBN film has been synthesized over one surface of the Cu substrate.

The thickness of the copper foil is 25 micrometre. The Copper was cleaned and was not electropolished for this ORR experiment. Details of the hBN growth have been discussed in chapter- 5. Figure 6.5 (a & b) shows the schematics and cell used for cyclic voltammetry (CV), 0.1 M KOH solution was used as an electrolyte with hBN/Cu as a working electrode and Pt wire as a counter electrode. Ag/AgCl was used as a reference electrode. Currently, there are two conventions about reporting CV data, the US and IUPAC convention. Figure 6.6 (a & b) shows both of the conventions. In the US convention potential is scanned from high to low whereas in the IUPAC convention it is the opposite. In our study, we have used the US convention in presenting the CV data.

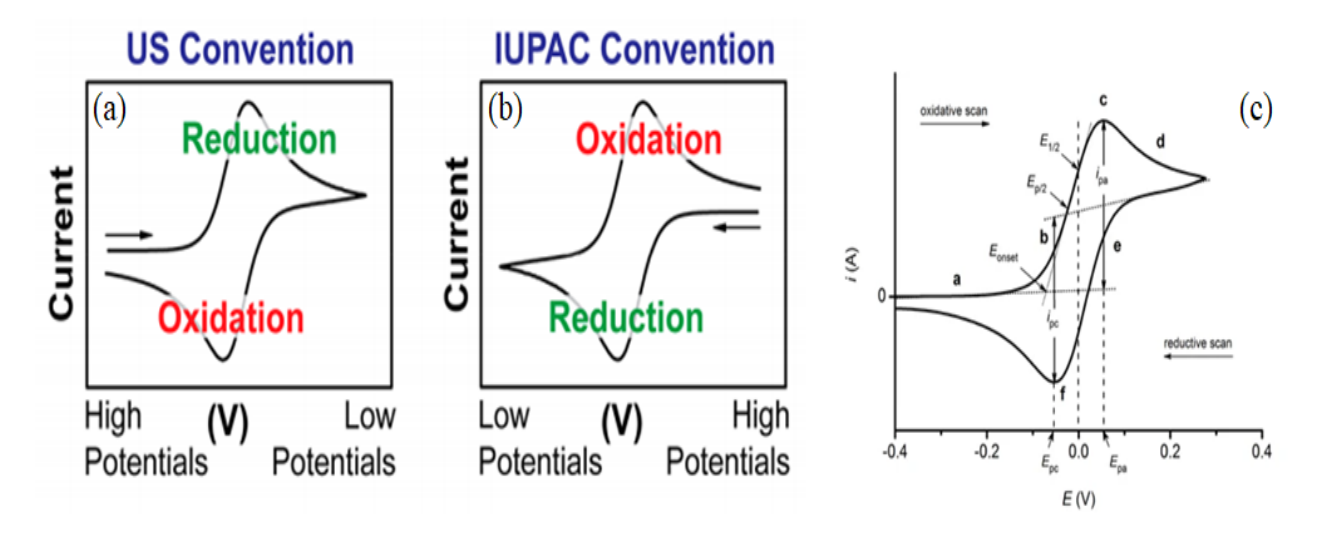


Figure 6.6 Two different conventions to report CV (cyclic voltammetry) data, (a) US convention which has been used in this chapter and (b) IUPAC convention <sup>26</sup>. (c) Duck shaped cyclic voltammogram.

Explaining the duck shape CV curve-

Let us consider the plot in figure 6.6 (c), the scan starts from high potential then reaches low potential. Initially, there is no increase in current as the potential is not enough to oxidize the analyte. With the onset of oxidation the increases exponentially because of the oxidation of the analyte at the working electrode surface. Under the steady electrochemical condition, the current rises linearly with the applied voltage. This is the due presence of a constant concentration gradient of the analyte within the vicinity of the electrode surface's double diffuse layer. With the depletion of the analyte, the current response loses its linearity along with the increase in the diffuse double layer. Now the current attains a maximum point at c which the peak anodic current (Ipa) for oxidation at peak potential (Epa). From this point the decreasing flux of analyte causes less mass transport of analyte from bulk to diffuse double layer interface, as a result, the current starts decreasing and a steady state is reached when a further increase in positive potential has no effect over the current. The reductive scan is a mirror image of the oxidative scan.

Figure 6.7 shows the voltammograms of different scan rate ranging from 20 mV/s to 100 mV/s. The voltammograms have been recorded by using bare Cu foil as the working electrode in 0.1 M KOH solution under oxygen saturated condition. The maximum anodic current is of the order of 1  $\mu$ A. Figure 6.8 compare the cyclic voltammograms recorded for bare copper and hBN/Cu in both oxygens saturated and nitrogen saturated conditions. It has been observed that with the presence of hBN over Cu foil the maximum anodic current (for scan rate 20 mV/s) has increased to 4  $\mu$ A and to 8  $\mu$ A for oxygen saturated and for nitrogen saturated environment respectively. This maximum anodic current further increases with the increase in scan rate to 50 mV/s and then to 100 mV/s. At 100 mV/s the anodic peak current under a saturated nitrogen environment reached 20  $\mu$ A, this is similar to other reports where the electrocatalytic activity of hBN has been investigated  $^{27}$ .

The two electron process of oxygen reduction to hydrogen peroxide is more probable than 4 electron process in the case of hBN systems <sup>18</sup>. B and N atoms of the hBN film provide higher

number of sites for O<sub>2</sub> molecule attachment and as a result, it reduces the overpotential for ORR and thereby acts as a catalyst. There are very few studies over CVD grew hBN/ Cu system in oxygen reduction reaction studies. Our results are at the preliminary stage, further investigation shall shed light on the catalytic mechanism of hBN in increasing the cathodic current.

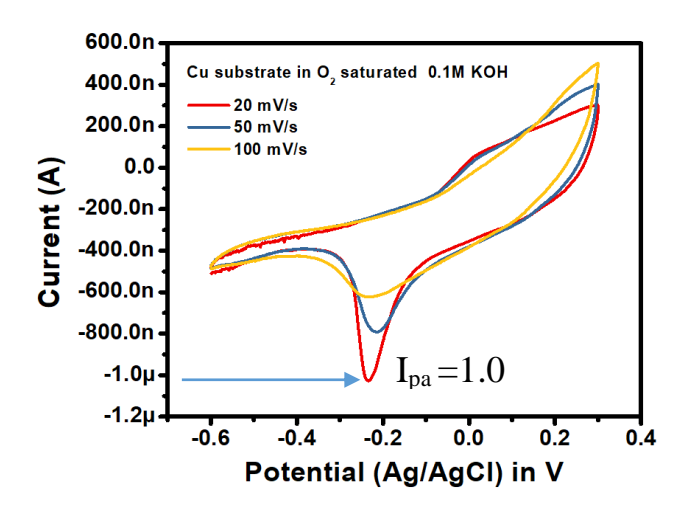


Figure 6.7 Cyclic voltammograms recorded in oxygen saturated 0.1 M KOH with bare copper foil as a working electrode.

#### 6.3. Heterostructure and MoS<sub>2</sub>/hBN devices.

The heterostructure is the fabrication or growth of two different materials in either vertical stacking or in-plane. Encapsulation of electronic and optoelectronic devices by hBN has also promising results. hBN has been used as a passivating layer for metal nanoparticle-based SERS substrates. A thin layer of hBN protects the metal nanoparticles from degradation from the environment. We have fabricated hBN and MoS<sub>2</sub> vertical heterostructure by the wet transfer method. The heterostructure of 2D materials has a different application in many fields. Transport properties of 2D materials like graphene or MoS<sub>2</sub> is greatly enhanced when hBN is used as a substrate. The effective mobility of graphene channel FET increases 4-6 times when hBN is used as a substrate instead of SiO<sub>2</sub>. This is due to the fact hBN is free of dangling bonds and no trapped states like in SiO<sub>2</sub>, and hBN surface are ultra-smooth which decreases the collision points.

We have experimented with transferring CVD grown hBN and MoS<sub>2</sub> films. This transfer method has been depicted in figure 6.9. Figure 6.9 (1 & 2) Shows 6 nm hBN film over Cu and 0.7 nm MoS<sub>2</sub> film over SiO<sub>2</sub>/Si substrate. Figure 6.9 (3) shows device structure i.e hBN/MoS<sub>2</sub>/hBN which has been made by the wet transfer method from the respective substrates of hBN and MoS<sub>2</sub>. At first, hBN was transferred over SiO<sub>2</sub>/Si substrate then MoS<sub>2</sub> was transferred on top of it. Gold contacts were made over this hBN/MoS<sub>2</sub> structure. And finally, the whole device was encapsulated with another hBN layer.

Figure 6.10 shows the photocurrent response of the MoS<sub>2</sub> device encapsulated in hBN. 532 nm laser was used to illuminate the device, 100 % of the laser means is 45 mW. Both in the case of pulsed lasing and continuous lasing we can see enhancement in photocurrent. For 100%

lasing power the photocurrent for pulsed lasing under 0.9 V is 800 nA (for the bare device it was 11 nA, figure 6.10 a). Similarly, for continuous lasing at 100% power output, the recorded current is 25 nA (for the bare device it was 12 nA, figure 6.10 b). This increase in photocurrent of the encapsulated device can be attributed to less scattering of charge carriers. When hBN is the substrate instead of SiO<sub>2</sub> it provides an ultra-smooth surface that is free of trapped states like in SiO<sub>2</sub>. This enhances the photo responsively of MoS<sub>2</sub>. The encapsulated MoS<sub>2</sub> exhibits better photocurrent behaviour than the bare one. This is because the top surface of the MoS<sub>2</sub> is protected from humidity and surface adsorption. This reduces the charge scattering centres which enhances the carrier mobility and photocurrent. Moreover, the use of hBN substrate also shields MoS<sub>2</sub> from the trapped states in SiO<sub>2</sub>, this also positively affects the photocurrent behaviour.

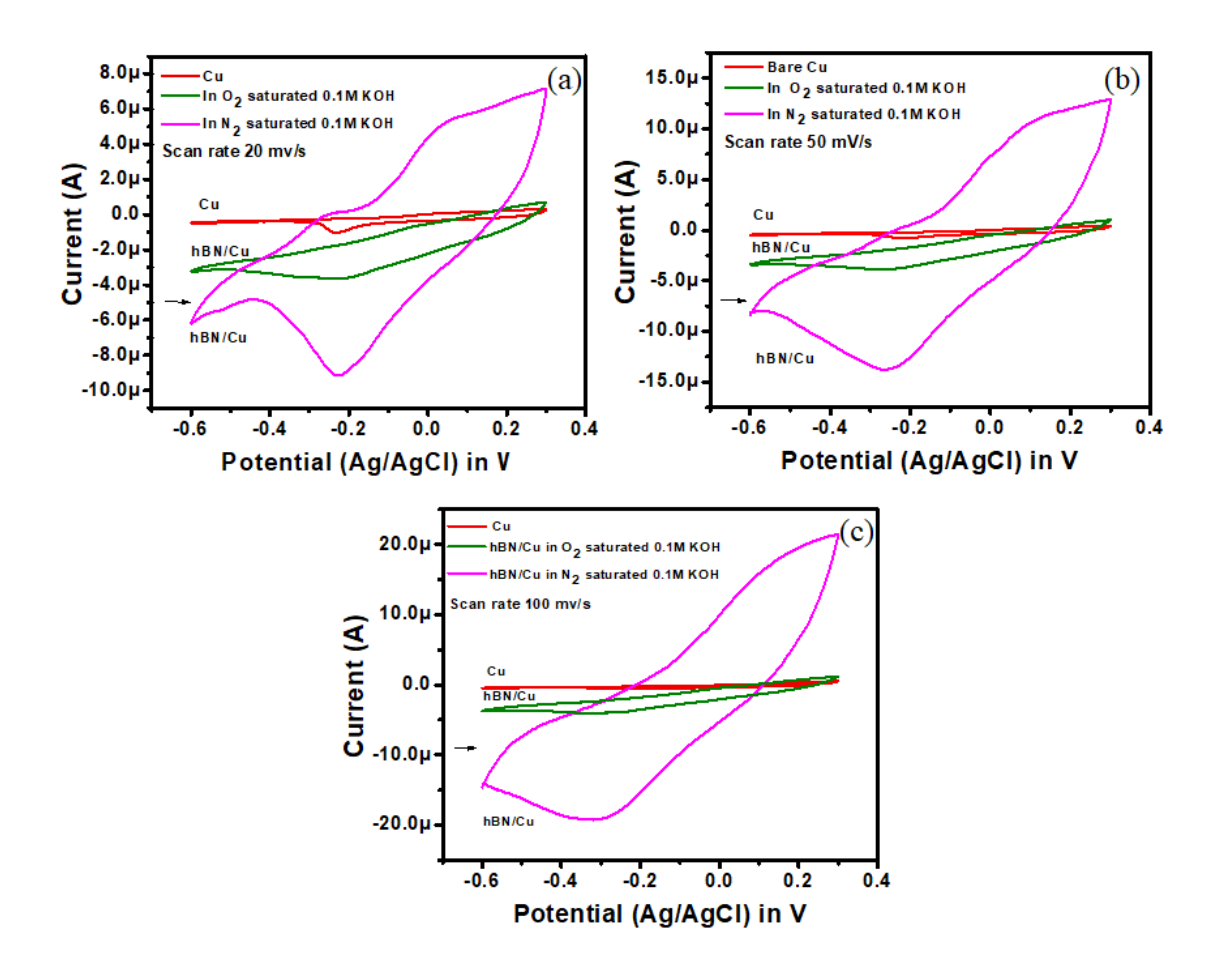


Figure 6.8 Comparison of cyclic voltammograms of bare Cu and hBN/Cu recorded both under nitrogen and oxygen saturated conditions.

#### 6.4. Surface-enhanced Raman spectroscopy by using hBN film.

The synthesized hBN film of different thickness was used to investigate their Raman enhancement capabilities. Surface-enhanced Raman spectroscopy/scattering (SERS) is an offshoot of Raman spectroscopy which is commonly used in chemical sensors to detect trace

quantities of analyte molecules and can trace down to single-molecule <sup>28,29</sup>. Here when analyte molecules adsorb on SERS substrate, its Raman signal is amplified such that the signal intensity becomes comparable to that of fluorescence. The two most accepted mechanism about SERS enhancement is an electromagnetic enhancement (EM) and chemical enhancement (CM). The EM enhancement has origins from (i) the local field enhancement produced from the excitation of surface plasmons and (ii) the re-radiation enhancement <sup>30</sup>. The EM enhancement can result in an enhancement factor as high as  $10^8$ - $10^{11}$  and is independent of the nature of the analyte molecule. The chemical enhancement is strongly dependent on the chemical nature of the analyte molecule. It has contributions from (i) charge transfer resonances between the substrate and the adsorbed analyte and/or (ii) adsorption-induced non-resonant modifications of molecular polarizability of the analyte molecule <sup>31,30</sup>. The contribution of the chemical enhancement is much smaller than the electromagnetic enhancement and, its magnitude may reach 10<sup>2</sup>–10<sup>4</sup>. Commonly used SERS substrate are roughened noble metal substrates (Ag, Au, Cu), metal nanoparticles in suspension and metal nanoparticles immobilized on substrates <sup>32</sup>. In these metal-based substrates, the electromagnetic enhancement is so strong that it overshadows any chemical enhancement effect. Metallic substrates also suffer from some drawbacks like low oxidation resistance, catalytic activity, photobleaching effect <sup>33,34</sup>. To overcome these problems passivating or encapsulation layers composed of inert materials like ultra-thin Al<sub>2</sub>O<sub>3</sub>, SiN, dithiocarbamate and other dielectric films are used <sup>35,36,37</sup>. Semiconductors and dielectrics have also been explored as alternative SERS active substrates <sup>31</sup>. Recently two dimensional (2D) materials are being investigated for the next generation of SERS substrate <sup>38,39</sup>. 2D materials have a large specific surface area, high oxidation resistance, high chemical inertness, high thermal conductivity, high flexibility and good biocompatibility, which are all highly desirable features required for SERS substrate 40,41. In addition, the largescale uniform coatings of 2D materials can be synthesized using controllable and cost-effective methods, thus ensuring better reliability and reproducibility of Raman signals. In 2D materials, CM is the dominant mechanism of enhancement, the enhancement factors (EFs) are sensitive to the molecule type, molecule orientation, molecule concentration, laser wavelength, substrate type 42,43.

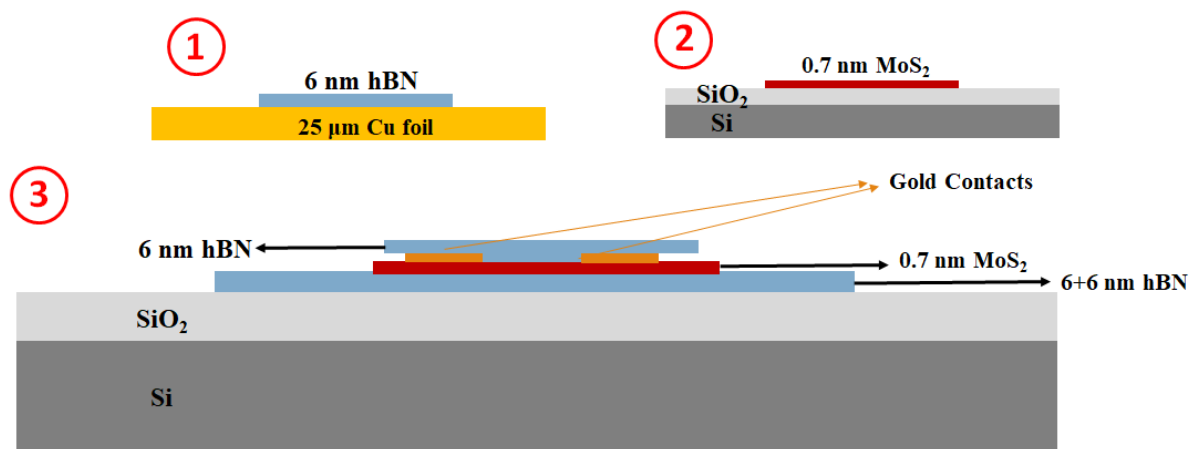


Figure 6.9 Schematic diagram depicting steps of heterostructure fabrication by wet transfer method.

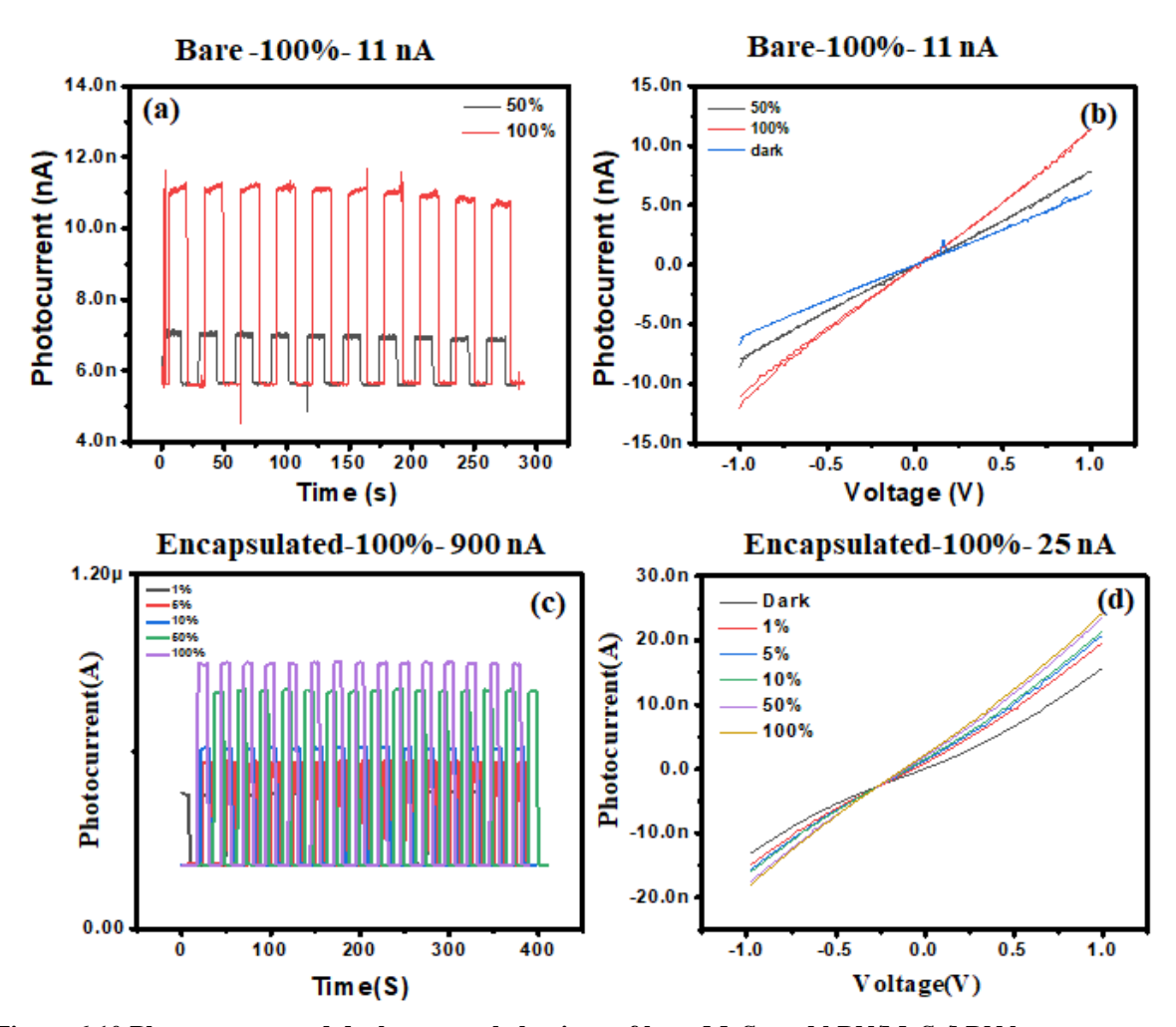


Figure 6.10 Photocurrent and dark current behaviour of bare  $MoS_2$  and  $hBN/MoS_2/hBN$  heterostructure. (a, b) Bare  $MoS_2$  under pulsed lasing and Continuous lasing respectively. (c,d) encapsulated  $MoS_2$  under pulsed lasing and Continuous lasing respectively.

In this work about Raman enhancement, we have investigated the SERS activity of few-layer hexagonal Boron Nitride (hBN) films. hBN, an analogue of graphene, has a similar layered structure with Boron and Nitrogen atoms arranged in a hexagonal lattice. Graphene has a covalent C-C bond while hBN has a polar B-N bond. hBN is also an electrical insulator with band gap of 6 eV <sup>44</sup>. It has an atomically smooth surface free of dangling bonds and high thermal conductivity <sup>45</sup>. It is a metamaterial which has found its way to an array of application <sup>46</sup>. Exfoliated hBN has also been used as an effective insulating and passivating layer for SERS substrates <sup>47,48</sup>. Its exceptional chemical inertness ensures good stability against photothermal and oxidative damages, high thermal conductivity helps in heat dissipation. Previous literature in Surface-Enhanced Raman spectroscopy (SERS) about hBN mostly deals with composite materials using exfoliated hBN flakes as a passivating layer for metal nanoparticles <sup>33,49,50</sup>. We used three standard dye molecules – Methylene blue (MB), Malachite green (MG) and Rhodamine 6G (R6G) with high Raman scattering cross-section as probe molecules. We observed enhancement of the order ~10<sup>3</sup> for MG and ~10<sup>4</sup> for 1 μM concentration of MB and

R6G dyes. We also studied the effect of film thickness and film morphology on the Raman enhancement of MB molecules. The enhancement observed due to these films is comparable to that of exfoliated hBN flakes. We were able to reuse the hBN substrates multiple times for SERS measurements after cleaning the substrates with ethanol without any loss insensitivity. The chemical inertness of hBN films ensured that we were able to observe the same order of enhancement even for films synthesized 10 months ago. The SERS enhancement could be reliably reproduced for different hBN films synthesized in different batches thereby demonstrating the versatility of hBN as SERS substrates.

#### **6.4.1. SERS experiment**

The Raman spectra were acquired using Horiba Labram Raman spectrophotometer with 532 nm laser, 100 X objective (532 nm; estimated laser spot size of ~720 nm) and typically 100 mW input power for all Raman measurements. For each Raman spectra, data was accumulated for 2 cycles and the integration time was set at 5s. All these parameters are kept constant unless otherwise mentioned. The 4 µl dye solution (in ethanol) were drop cast on hBN substrate and allowed to dry, before recording Raman spectra. For enhancement factor calculations the Raman spectra were measured on at least 10 different positions on the same sample. During each and every Raman measurement for a particular set of film thickness and particular dye, every aspect of the measurement like laser power, wavelength, objective lens, grating, spectrometer etc. all was kept the same. Figure 6.11 shows the schematics of the SERS experiment study where the few drops of the analyte was drop casted over the transferred hBN film and the subsequent spectrum was recorded by the Raman spectrometer.

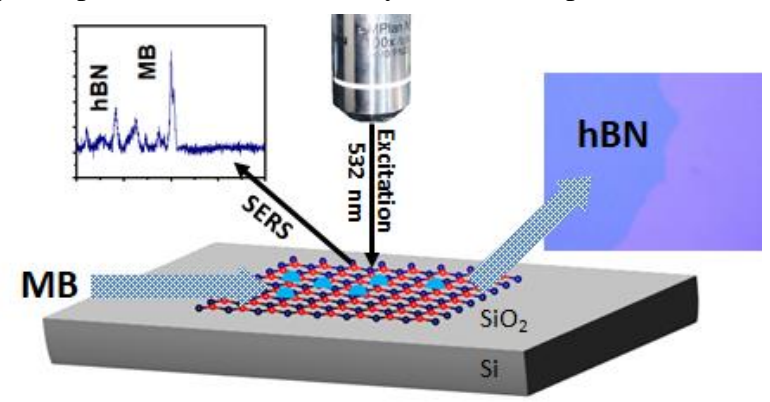


Figure 6.11 Schematic diagram of the SERS experimental setup.

#### 6.4.2. Discussion and enhancement factor.

To probe Raman enhancement effects by the hBN substrate we used three standard model dyes-Methylene Blue, Malachite Green and Rhodamine 6G. The dye solutions (in ethanol) were drop casted on hBN substrate and allowed to dry, then Raman spectra were recorded. To compare the enhancement effect, Raman spectra of the dyes was recorded on hBN film coated SiO<sub>2</sub>/Si substrate and blank SiO<sub>2</sub>/Si (reference substrate). Figure 6.12 (a) shows a representative Raman spectrum of 1 μM MB over 6 nm thick hBN films (the synthesis and

characterization of this 6 nm thick film have been discussed in chapter -5) where we can clearly observe the enhancement effect due to the presence of hBN films. For 1  $\mu$ M solution of MB, no signal was detected for MB on SiO<sub>2</sub>/Si substrate but a large signal at 1601 cm<sup>-1</sup> was detected on hBN/SiO<sub>2</sub>/Si substrate. Figure 6.12(b) shows the SERS spectra of 50  $\mu$ M R6G with and without hBN over SiO<sub>2</sub>/Si substrate and figure 6.12(c) shows the Raman enhancement of 1  $\mu$ M solution malachite green at three positions. To quantify the enhancement effect of hBN substrate, analytical enhancement factor (AEF) was calculated as-

$$AEF = \frac{I_{SERS} X C_{Raman}}{I_{Raman} X C_{SERS}}$$

Where I<sub>SERS</sub> is the Raman intensity of the probe molecule on hBN substrate

 $C_{SERS}$  is the corresponding concentration of the probe molecule in ethanol  $I_{Raman}$  is the Raman intensity of the probe molecule on a reference substrate  $C_{Raman}$  is the corresponding concentration of the probe molecule in ethanol

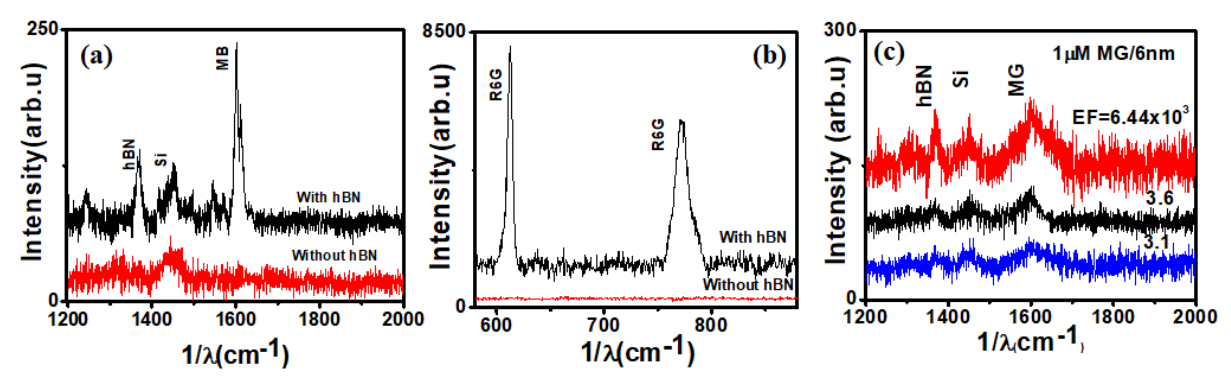


Figure 6.12 a),b ) Raman spectrum of 1 $\mu$ M MB and 50  $\mu$ M R6G with 6 nm hBN and without hBN over SiO<sub>2</sub>/Si c)Raman spectrum 1  $\mu$ M MG/6 nm hBN/SiO<sub>2</sub>/Si .[ 532 nm and 100 mW]

MB has 14 distinguishable Raman peaks between 250 cm<sup>-1</sup>-1750 cm<sup>-1</sup> with the most intense peak at 1624 cm<sup>-1</sup>. The band at 1618 cm<sup>-1</sup> (C-C stretching) was taken as the reference for the calculation of AEF's. Figure 6.13 shows Raman spectra of MB on different positions for the 6 nm and 1.5 nm thick hBN and the spectra are offset for clarity. The AEFs for 1.5 nm and 6 nm hBN film were calculated for over 8 positions and they varied from (0.9-2.2)×10<sup>4</sup> and (1.18-1.47)×10<sup>4</sup>, respectively [see data presented in Figures 6.13(a) and 6.15(b)]. The standard deviation of AEF for 1.5 nm and 6 nm film was 0.4 and 0.11 and mean AEFs were 1.37×10<sup>4</sup> and 1.29×10<sup>4</sup>, respectively. To ensure the reproducibility of our results the Raman measurements were repeated with samples from different synthesis batches and all of the measurements showed similar results [Figure 6.13(c)], where the mean AEF was 1.34×10<sup>4</sup> with a standard deviation of 0.27. Clearly, the enhancement results are consistent with different batches of hBN for different hBN film thickness.

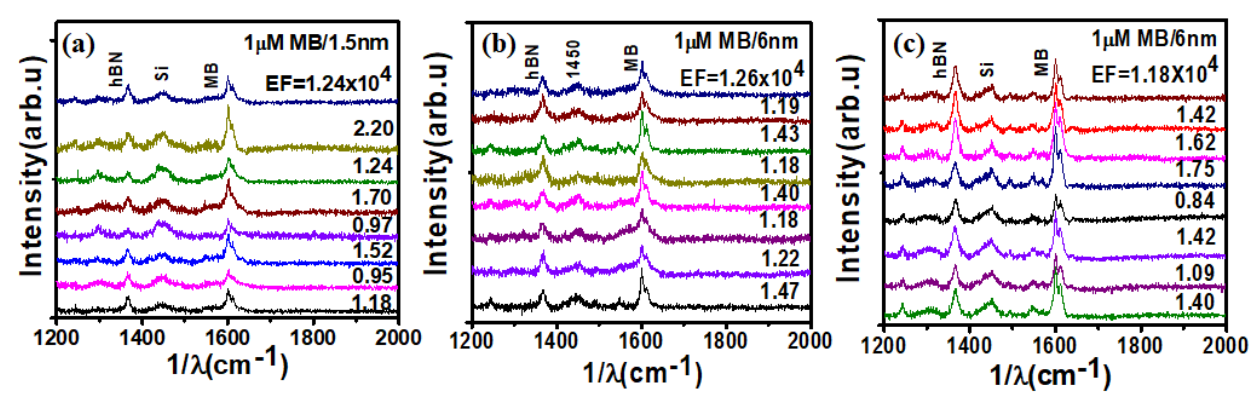


Figure 6.13 a), b) Raman enhancement of 1  $\mu$ M MB by 1.5 nm and 6 nm film at different positions of the film. c) Reproducibility studies - Raman enhancement of 1  $\mu$ M MB by a different 6 nm film at different positions.

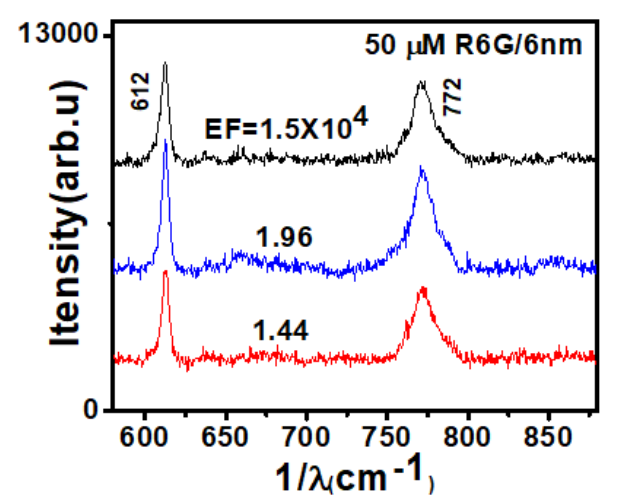


Figure 6.14 Raman spectrum 50  $\mu$ M R6G/6 nm hBN/SiO2/Si. [532 nm excitation, 100 x objective, Integration -5s, Accumulation - 2, 25 mW]

We investigated two more organic dye Malachite green (MG) and R6G as a SERS probe with the 6 nm film. Malachite green has a sharp Raman band near 1617 cm<sup>-1</sup>, which has been used as a reference for enhancement studies <sup>51</sup> (See figure 6.12 c). Figure 6.14 depicts a representative Raman spectrum of 50  $\mu$ M R6G over 6 nm thick hBN films where enhancement is observed for in the presence of hBN film. We estimated the analytical enhancement factor at different spots on the sample to get an average AEF  $1.5 \times 10^4$  for R6G and  $6.44 \times 10^3$  for MG (Figure 6.12 c). This is an order less than the AEF obtained for methylene blue. The difference in the order of enhancement can be explained by the strength of interaction of dyes with hBN substrate. It is believed that the polar nature of hBN induces an interfacial dipole in the adsorbed organic molecules which increases the transition probability that gives rise to the enhancement in Raman enhancement effect <sup>34,40</sup>. In this case, the interaction between hBN and Methylene Blue having a  $\pi$  conjugated aromatic structure is primarily determined by the  $\pi$ - $\pi$  interaction. For MG and R6G dyes the interaction with hBN is relatively weaker resulting in lower enhancements.

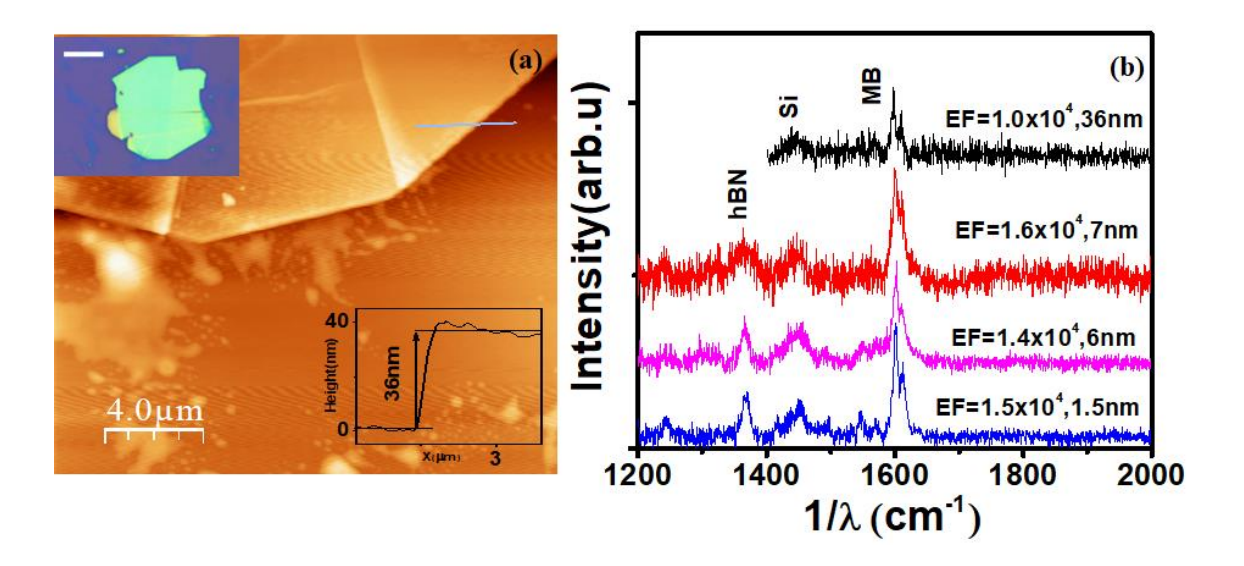


Figure 6.15 a) AFM image of the exfoliated flake, Inset- height profile shows its thickness of 36 nm and optical micrograph- scale 10  $\mu$ m b) Raman enhancement of 1  $\mu$ M MB by 1.5 nm, 6 nm and 7 nm film and 36 nm hBN flake. [532 nm excitation, 100 mW, 100 x objective, Integration -5s, Accumulation - 2.]

Figure 6.15 shows the AFM image of the flake with height profile and optical image in the inset. The thickness of the film is 36 nm. These particular flakes were used to study the Raman enhancement capabilities. Figure 6.15 (b) shows the Raman spectra of 1 µM MB on hBN films of different thickness. For the hBN films synthesized using CVD, the calculated average EFs for 1.5 nm, 6 nm and 7 nm films were  $1.37 \times 10^4$ ,  $1.29 \times 10^4$  and  $1.5 \times 10^4$ , respectively. The MB peak splits into two peaks centred at 1601 cm<sup>-1</sup> and 1612 cm<sup>-1</sup> and downshifts. This downshifts and splitting of the 1618 cm<sup>-1</sup> peak are evident in both the CVD prepared film and in the hBN flake. This shift and splitting of the 1618 cm<sup>-1</sup> peak has been reported in earlier SERS studies of MB 52. The AEF's are similar for both 1.5 nm, 6 nm and 7 nm thick hBN film indicating that the film thickness has no impact on the enhancement factors for hBN film, which is similar to previously reported results. Ling et. al had observed no change in enhancement factor for mechanically hBN flakes of different thickness since there was no absorption of light in the visible region <sup>34</sup>. We also compared the enhancement effect of our hBN films synthesized by APCVD with mechanically exfoliated hBN flakes. The 36 nm thick hBN nanosheet was exfoliated from hBN powder and used for SERS measurement. For 1 µM MB dye, we also observed a similar degree of enhancement similar to that of 1.5 nm, 6 nm and 7 nm film synthesized by APCVD film. The surface morphology (roughness) usually plays an important role in the creation of local hot spots which leads to an even higher enhancement of Raman signal of adsorbed analyte <sup>53,54</sup>. Interestingly, for the case of a highly wrinkled surface of 7 nm thick hBN film (with highest surface roughness), we observed a similar enhancement of ~10<sup>4</sup> for MB molecules compared to the flat hBN films. Even though the enhancement factors are not comparable to those of plasmonic substrates but they are much better than other 2D materials like MoS<sub>2</sub>.

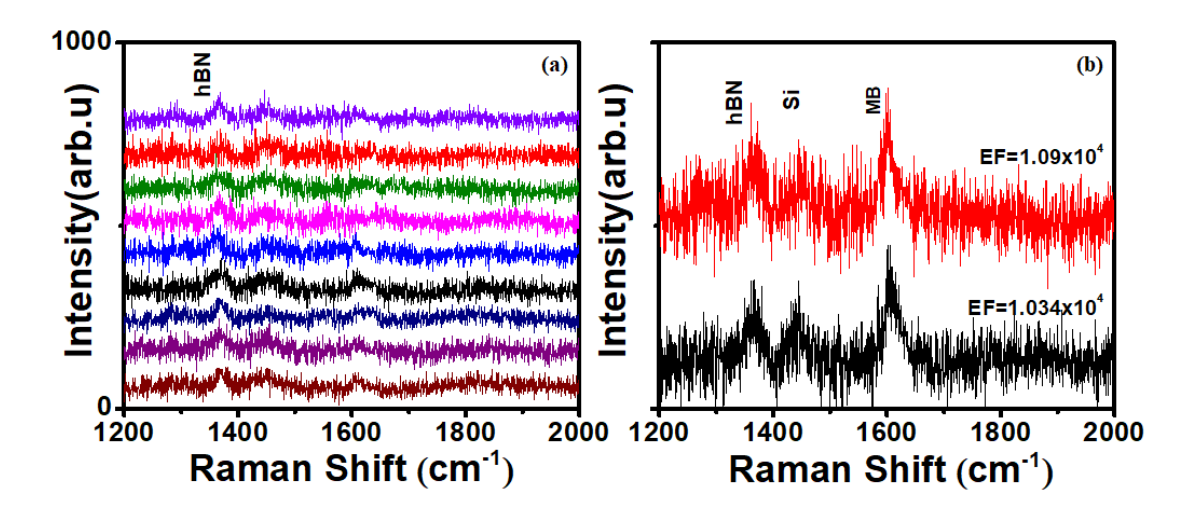


Figure 6.16 a) Raman spectrum of 1  $\mu$ M /7 nm hBN film after cleaning in ethanol for 45 min at 10 positions. Apart from the hBN and Si peak no other peak can be seen. b) Regenerated 7 nm film for enhancement of 1  $\mu$ M MB at two positions. [532 nm excitation,, 100 x objective, Integration -5s, Accumulation - 2, 100 mW ]

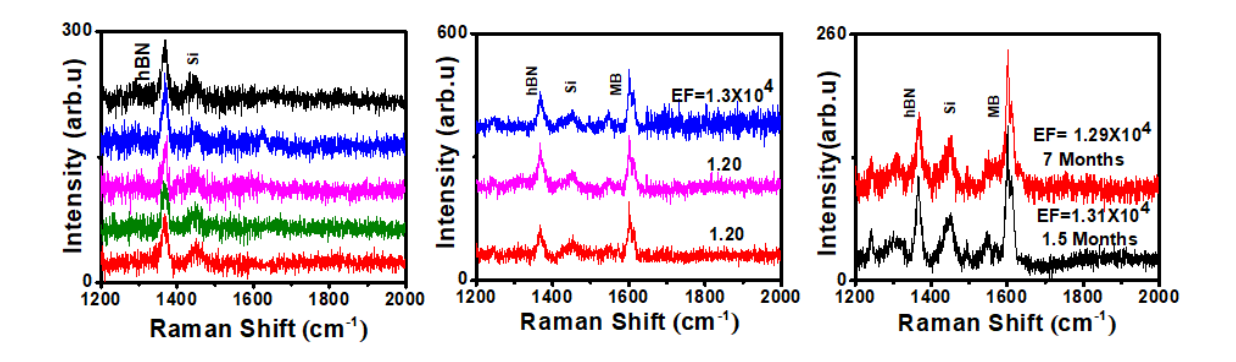


Figure 6.17 a) Raman spectrum of the 1  $\mu$ M MB/6 nm after washing in ethanol for 45 min. b) Re-drop casting 1  $\mu$ M MB over the film in a) Clearly regeneration has been achieved. c) Raman enhancement of 1  $\mu$ M MB by 6 nm film at different time duration after their growth.

In addition to enhancement factors, stability and reusability are some of the important parameters to keep in mind while choosing SERS substrate. Figure 6.16(a) shows the Raman spectra of MB on 7 nm thick hBN film after cleaning with alcohol. It shows no other peak than the h BN peak, after re drop-casting 1  $\mu$ M MB in figure 6.16 (b) the same enhancement was achieved. This indicates that the substrate can be regenerated without any loss of sensitivity. A regenerative study was also carried out with the 6 nm thick hBN film for MB dye. Here also after washing the dye from the 6 nm hBN film, we were able to reproduce enhancement results we obtained enhancement factors of the order ~  $10^4$ . This has been presented in figure 6.17 (a) & (b). We also performed Raman enhancement measurements at different time spans after the growth of 6 nm thick hBN films [after 1.5 months and 7 months] as shown in figure 6.17(c). We observe the same order of enhancement (~ $10^4$ ) compared to freshly prepared hBN films. It shows that these hBN films are highly stable in an ambient atmosphere. Compared to plasmonic

substrates which are prone to oxidation, hBN films tend to have a long self-life. hBN films being chemically inert and very resistant to oxidation can thus be regenerated and reused multiple over a large time duration. Our results thus show that APCVD synthesized large area hBN films to be highly reliable and durable SERS substrate which can be used in sensors.

The enhancement from the sole hBN film can be further improved by using hBN in conjunction with Au nanoparticles. We used a hybrid substrate with Au nanoparticles deposited on hBN films and then measured the SERS signal of MB. Figure 6.18 shows the Raman spectra of MB on hybrid Au/hBN substrate for 532 nm and 633 nm laser excitation. We estimated the mean AEF to be  $2.6 \times 10^5$  for 532 nm and for 633 nm excitation, the mean enhancement factor increased by one order to  $1.3 \times 10^6$ . These values are similar to those reported earlier  $^{33}$ .

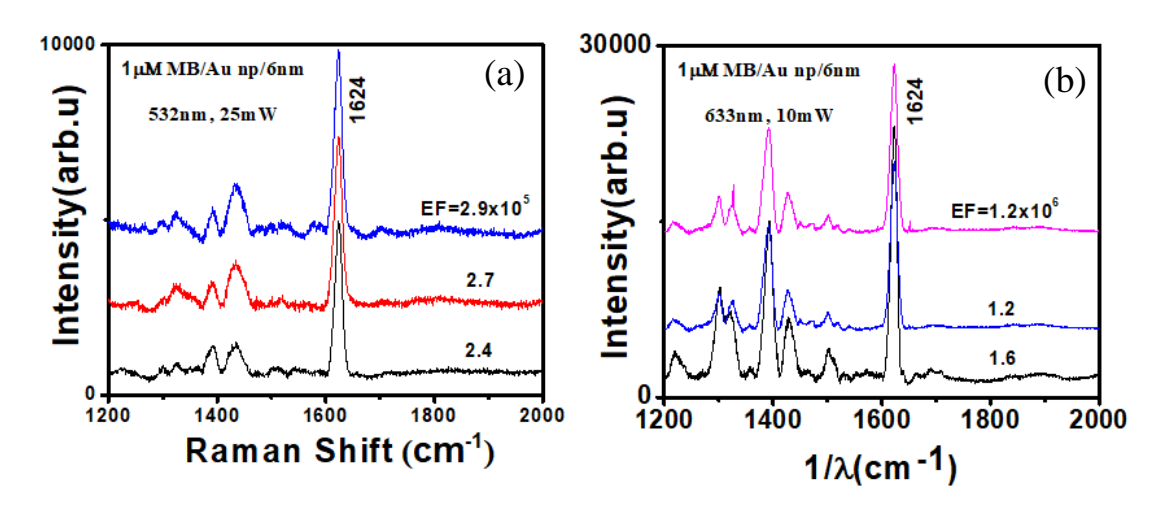


Figure 6.18 Raman enhancement of 1 micro molar MB with Au nano particles and hBN a) with 532 nm excitation, 25 mW and b) 633 nm excitation with 10 mW.

#### **First Principle MD Calculations**

The enhancement factor is strongly dependent on the substrate-molecule interactions. The interaction energy between single layer hBN and different dye molecules were calculated using first-principle molecular dynamics simulation techniques. The interaction of a hBN layer is energetically more favourable with MB (-6.8 eV) rather than R6G (-4.8 eV) and MG (-2.9 eV) as shown in Figure 6.19. The methylene blue molecule shows parallel orientation to hBN layer as compared to the inclined orientation of MG and R6G molecules to hBN layer respectively. This occurs due to rotational flexibility of benzene rings and steric hindrance of side groups; dimethylamine (MG and R6G) and ester group (R6G). Furthermore, the interaction between R6G and hBN is further enhanced over MG and hBN due to the presence of ester functionality where carboxylate oxygens show interaction with hBN layer. The effective overlap between

the orbitals is higher in MB due to parallel orientation than R6G and MG that adopt inclined orientation as shown in the HOMO electron density profiles.

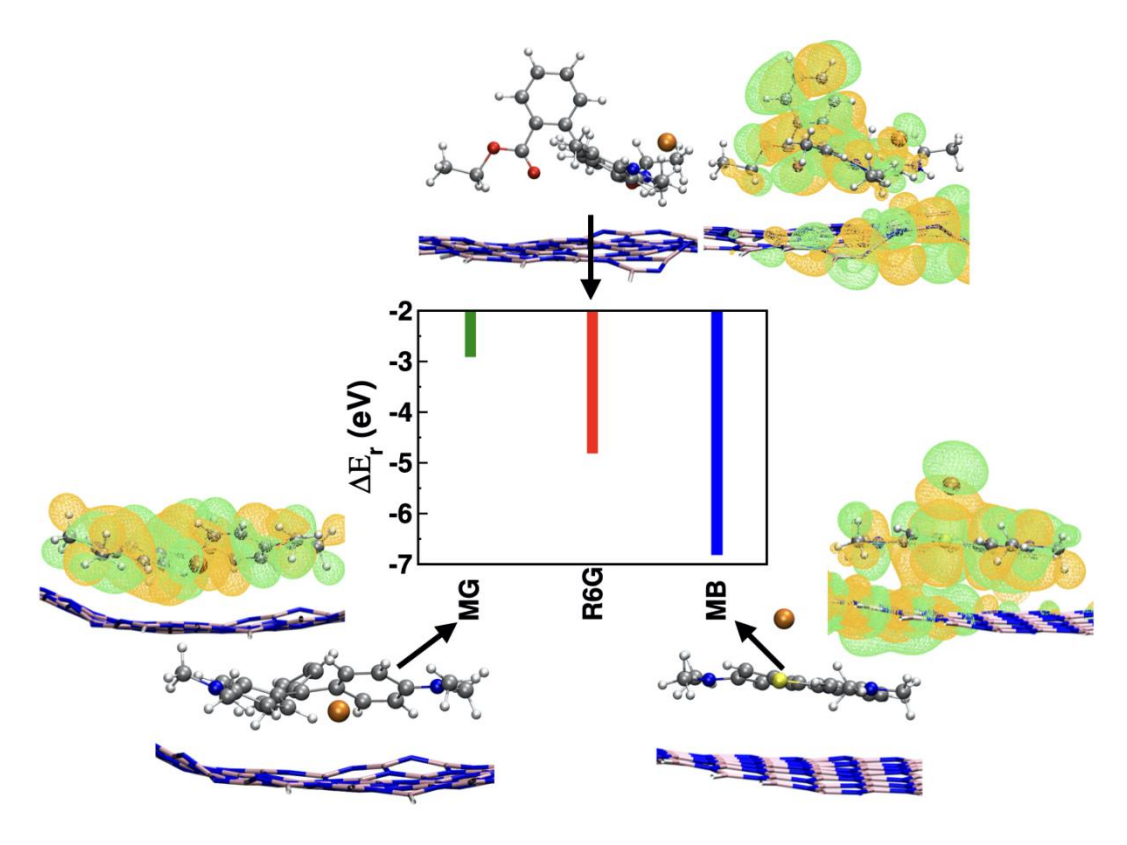


Figure 6.19 Full view of the optimised geometries of complexes of a single layer of hBN and dye (a) methylene blue (MB), (b) Rhodamine 6 G (R6G) and machalite green (MG).

Figure 6.19 Relative interaction energy, E<sub>d</sub> between single layer of hBN and dye molecule that are MB, R6G and MG are methylene blue, Rhodamine 6G and malachite green. The grey, white blue, pink, crimson and red colours represent C, H, N, B, Cl and O atoms. The HOMO electron density surfaces of the complexes are plotted for isodensity value of 0.007 a.u. (full view images are available in Figures 6.21 and 22).

#### **Simulation Details:**

System	E <sub>complex</sub> (Hartree) Set 1	E <sub>complex</sub> (Hartree) Set 2
hBN + MB	-1077.257814077	-1077.257582858
hBN + R6G	-1181.169304485	-1181.171273989
hBN + MG	-1100.931727326	-1100.932009555

Figure 6.20 Table showing combination of three systems.

The effect of the system was also tested by simulating all the systems with larger box dimensions (Set 2) of 3.2 nm x 2.0 nm x 4.0 nm. The total energy ( $E_{complex}$ ) of the complexes for all the systems are consistent with Set 1 ( 3.2 nm x 2.0 nm x 3.0 nm) and has an error of +/-0.001 Hartree as shown in the figure 6.20 table.

We have synthesized hBN four different thickness via APCVD out of which we used three films to sturdy the Raman enhancement abilities of the APCVD grown hBN film hBN films with different surface morphology have also been synthesized and have been studied about their behaviour over Raman enhancement. We have successfully demonstrated the Raman enhancement capability of few layer APCVD grown hexagonal boron nitride over Methylene blue, R6G and Malachite green dissolved in ethanol. All sets of 1.5 nm film, 6 nm film and 7 nm thick hBN films exhibited similar enhancement factors. . The enhancement factors are in agreement with the theoretically calculated interaction energies of dyes with a single hBN layer (MB-hBN > R6G-hBN > MG-hBN). The MB molecule adopts parallel conformation as compared to R6G and MG molecules that show inclined conformations on the surface of hBN. The Raman enhancement from hBN is found to be independent of the thickness of the film. In our case, hBN films synthesized by APCVD is of high quality and its enhancement effect is comparable to that of exfoliated hBN flakes. Our result provides valuable insights for understanding the Raman enhancement by hBN films, and would thus be useful for developing hBN-based SERS substrate. Figure 6.23 shows a table which compares the enhancement factor of different 2D materials and composites of 2D materials with our hBN film.

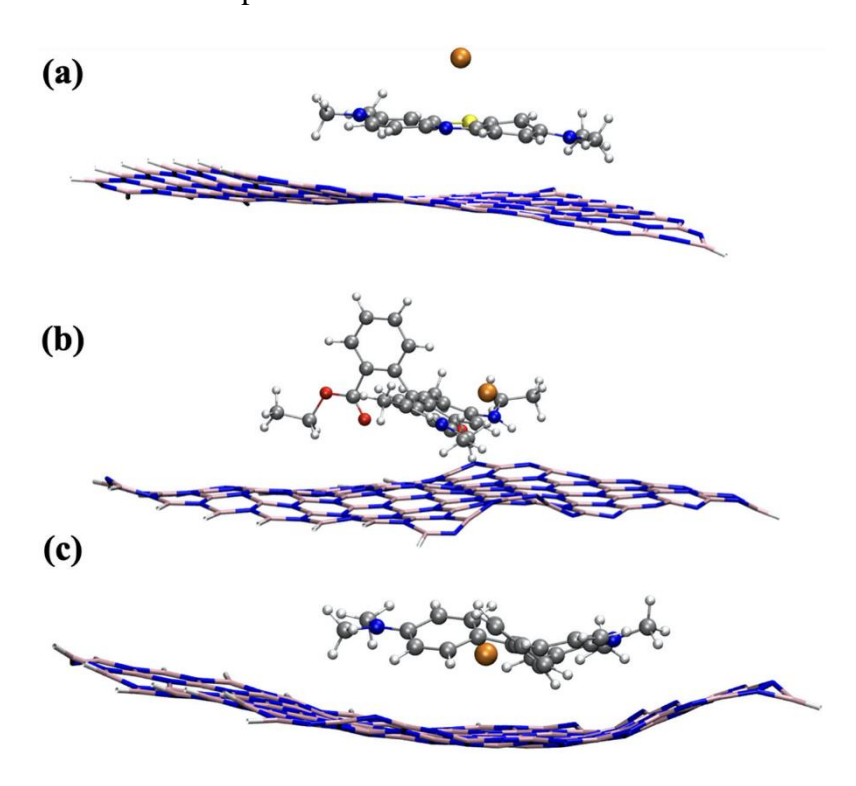


Figure 6.21: Full view of the optimized geometries of complexes of a single layer of hBN and dye (a) methylene blue (MB), (b) Rhodamine 6 G (R6G) and malachite green (MG).

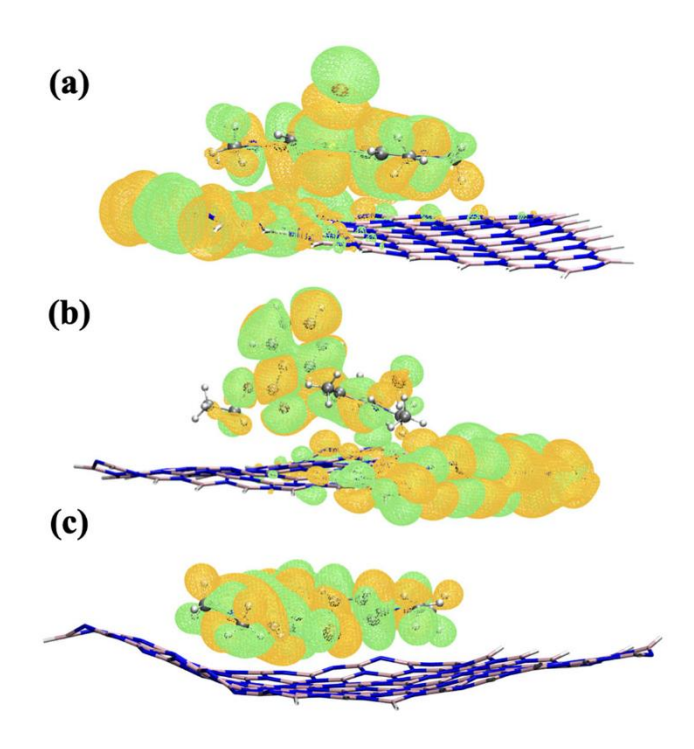


Figure 6.22: Full view of HOMO electron density surfaces for isodensity value of 0.007a.u. of the optimized geometries of complexes of a single layer of hBN and dye (a) methylene blue (MB), (b) Rhodamine 6G (R6G) and malachite green (MG).

The comparison shows that our results about enhancement factor are at at par if not ahead of many 2D materials.

Sl. No	Substrate	Probe Molecule	Excitation wavelength (nm)	Laser Power (mW)	Enhancement Factor
1.	CVD Graphene on Ag nanoparticles over Si <sup>55</sup>	R6G	633	20	8.3 x 10 <sup>6</sup>
2.	Exfoliated hBN on Au nanoparticles <sup>33</sup>	R6G	514.5		2.5 x 10 <sup>5</sup>
3.	CVD hBN film	MB	532	100	1.4 x 10 <sup>4</sup>
	(Our work)	MG	532	100	6.4 x10 <sup>3</sup>
		R6G	532	25	1.5 x10 <sup>4</sup>
4.	CVD hBN film + Au	MB	532	25	2.9 x 10 <sup>5</sup>
	Nanoparticles		633	10	$1.6 \times 10^6$
	(Our work)				
5.	Graphene Flake <sup>34</sup>	CuPc	632.8	1	63

6.	hBN Flake 34	CuPc	632.8	1	13
7.	MoS <sub>2</sub> Flake <sup>34</sup>	CuPc	632.8	1	16
8.	Monolayer MoS <sub>2</sub> <sup>56</sup>	4- mercaptopyridine	488	0.6	3.8 x 10 <sup>5</sup>

Figure 6.23 Table comparing enhancement factors of other 2D materials and composite materials with our hBN film.

#### 6.5 Conclusion.

In this chapter, we have investigated the four specific application of CVD grown hBN namely, in surface-enhanced Raman spectroscopy, resistive switching, oxygen reduction potential and heterostructure assembly. We have successfully shown that different thicknesses of hBN film do not have any effect on the Raman enhancement abilities of hBN. That is the Raman enhancement by hBN nanosheet is independent of their thicknesses. We have used three different organic dyes, methylene blue malachite green and Rhodamine 6G, all of them showed similar enhancement factors. The Raman signal enhancement of MB molecule is slightly ahead of others. Molecular dynamics study shows that MB molecule aligns more horizontally with the hBN nanosheet than MG and R6G molecules. As a result, greater overlapping of molecular orbital takes place which increases the chemical enhancement of the Raman signal. We have also experimented with the durability of the hBN film by registering SERS spectra at the different period after their synthesis. hBN films also shown regenerative properties, i.e one film can be reused after proper cleansing via ethyl alcohol.

Resistive switching studies of the films shows that the hBN film is stable up to 100 I-V cycles. The CVD grown film is stable and further studies like potentiation and depression were carried out with the same film. hBN as a catalyst in ORR reaction has been investigated in both oxygen saturated and nitrogen saturated condition. Where hBN/Cu system showed enhancement in peak anodic current when compared to only Cu electrodes. We have also investigated the photocurrent by bare  $MoS_2$  and encapsulated  $MoS_2$  by hBN film. Our results show that encapsulated devices shown higher photocurrent than bare devices.

•

#### 6.6. References.

- 1. Liu, G. *et al.* Recent Advances in Resistive Switching Materials and Devices: From Memories to Memristors. *Eng. Sci.* 4–43 (2018) doi:10.30919/es8d779.
- 2. Qian, K. *et al.* Hexagonal Boron Nitride Thin Film for Flexible Resistive Memory Applications. *Adv. Funct. Mater.* **26**, 2176–2184 (2016).
- 3. Li, J. *et al.* Symmetric Ultrafast Writing and Erasing Speeds in Quasi-Nonvolatile Memory via van der Waals Heterostructures. *Adv. Mater.* **31**, 1–8 (2019).
- 4. Wu, X. *et al.* Thinnest Nonvolatile Memory Based on Monolayer h-BN. *Adv. Mater.* **31**, 1–7 (2019).
- 5. Huang, H. H., Shih, W. C. & Lai, C. H. Nonpolar resistive switching in the Pt/MgO/Pt nonvolatile memory device. *Appl. Phys. Lett.* **96**, (2010).
- 6. Biju, K. P. *et al.* Improved resistive switching properties of solution processed ti O 2 thin films. *Electrochem. Solid-State Lett.* **13**, 2–6 (2010).
- 7. Siddiqui, G. U., Rehman, M. M., Yang, Y. J. & Choi, K. H. A two-dimensional hexagonal boron nitride/polymer nanocomposite for flexible resistive switching devices. *J. Mater. Chem. C* **5**, 862–871 (2017).
- 8. Ranjan, A. *et al.* Conductive Atomic Force Microscope Study of Bipolar and Threshold Resistive Switching in 2D Hexagonal Boron Nitride Films. *Sci. Rep.* **8**, 1–9 (2018).
- 9. Chandrasekaran, S., Simanjuntak, F. M., Panda, D. & Tseng, T. Y. Enhanced Synaptic Linearity in ZnO-Based Invisible Memristive Synapse by Introducing Double Pulsing Scheme. *IEEE Trans. Electron Devices* **66**, 4722–4726 (2019).
- 10. Covi, E., Brivio, S., Fanciulli, M. & Spiga, S. Synaptic potentiation and depression in Al:HfO2-based memristor. *Microelectron. Eng.* **147**, 41–44 (2015).
- 11. Covi, E. *et al.* HfO2-based memristors for neuromorphic applications. *Proc. IEEE Int. Symp. Circuits Syst.* **2016-July**, 393–396 (2016).
- 12. Wang, Q. *et al.* Interface-engineered reliable HfO2-based RRAM for synaptic simulation. *J. Mater. Chem. C* **7**, 12682–12687 (2019).
- 13. He, C. *et al.* Artificial Synapse Based on van der Waals Heterostructures with Tunable Synaptic Functions for Neuromorphic Computing. *ACS Appl. Mater. Interfaces* **12**, 11945–11954 (2020).
- 14. Sun, L., Wang, W. & Yang, H. Recent Progress in Synaptic Devices Based on 2D Materials. *Adv. Intell. Syst.* **2**, 1900167 (2020).
- 15. Yi, S. G. *et al.* Artificial Synaptic Emulators Based on MoS2 Flash Memory Devices with Double Floating Gates. *ACS Appl. Mater. Interfaces* **10**, 31480–31487 (2018).
- 16. Schranghamer, T. F., Oberoi, A. & Das, S. Graphene memristive synapses for high precision neuromorphic computing. *Nat. Commun.* **11**, 1–11 (2020).
- 17. Zeng, F., Li, S., Yang, J., Pan, F. & Guo, D. Learning processes modulated by the interface effects in a Ti/conducting polymer/Ti resistive switching cell. *RSC Adv.* **4**, 14822–14828 (2014).
- 18. Uosaki, K. *et al.* Boron nitride nanosheet on gold as an electrocatalyst for oxygen reduction reaction: Theoretical suggestion and experimental proof. *J. Am. Chem. Soc.* **136**, 6542–6545 (2014).

- 19. Marković, N. M., Schmidt, T. J., Stamenković, V. & Ross, P. N. Oxygen Reduction Reaction on Pt and Pt Bimetallic Surfaces: A Selective Review. *Fuel Cells* **1**, 105–116 (2001).
- 20. Lim, B. *et al.* Pd-Pt bimetallic nanodendrites with high activity for oxygen reduction. *Science* (80-.). **324**, 1302–1305 (2009).
- 21. Liu, R., Wu, D., Feng, X. & Müllen, K. Nitrogen-doped ordered mesoporous graphitic arrays with high electrocatalytic activity for oxygen reduction. *Angew. Chemie Int. Ed.* **49**, 2565–2569 (2010).
- 22. Wu, Z., Yang, S., Sun, Y., Parvez, K. & Feng, X. 2004 Journal of the ... 3D Nitrogen-Doped Graphene Aerogel-Supported Fe 3 O 4 Nanoparticles as E ffi cient Electrocatalysts for the O.pdf. 10–13 (2012).
- 23. Chen, Y. *et al.* Hexagonal Boron Nitride as a Multifunctional Support for Engineering Efficient Electrocatalysts toward the Oxygen Reduction Reaction. *Nano Lett.* **20**, 6807–6814 (2020).
- 24. Lyalin, A., Nakayama, A., Uosaki, K. & Taketsugu, T. Functionalization of monolayer h-BN by a metal support for the oxygen reduction reaction. *J. Phys. Chem. C* **117**, 21359–21370 (2013).
- 25. Lyalin, A., Nakayama, A., Uosaki, K. & Taketsugu, T. Theoretical predictions for hexagonal BN based nanomaterials as electrocatalysts for the oxygen reduction reaction. *Phys. Chem. Chem. Phys.* **15**, 2809–2820 (2013).
- 26. Elgrishi, N. *et al.* A Practical Beginner's Guide to Cyclic Voltammetry. *J. Chem. Educ.* **95**, 197–206 (2018).
- 27. Khan, A. F. *et al.* 2D Hexagonal Boron Nitride (2D-hBN) Explored as a Potential Electrocatalyst for the Oxygen Reduction Reaction. *Electroanalysis* **29**, 622–634 (2017).
- 28. Langer, J. *et al.* Present and future of surface-enhanced Raman scattering. *ACS Nano* **14**, 28–117 (2020).
- 29. Naqvi, T. K. *et al.* Ultra-sensitive reusable SERS sensor for multiple hazardous materials detection on single platform. *J. Hazard. Mater.* 124353 (2020) doi:10.1016/j.jhazmat.2020.124353.
- 30. Pilot, R. et al. A review on surface-enhanced Raman scattering. Biosensors 9, (2019).
- 31. Alessandri, I. & Lombardi, J. R. Enhanced Raman Scattering with Dielectrics. *Chem. Rev.* **116**, 14921–14981 (2016).
- 32. Mosier-Boss, P. A. Review of SERS substrates for chemical sensing. *Nanomaterials* **7**, (2017).
- 33. Cai, Q. *et al.* Boron Nitride Nanosheet-Veiled Gold Nanoparticles for Surface-Enhanced Raman Scattering. *ACS Appl. Mater. Interfaces* **8**, 15630–15636 (2016).
- 34. Ling, X. *et al.* Raman enhancement effect on two-dimensional layered materials: Graphene, h-BN and MoS2. *Nano Lett.* **14**, 3033–3040 (2014).
- 35. Zhao, Y., Newton, J. N., Liu, J. & Wei, A. Dithiocarbamate-coated SERS substrates: Sensitivity gain by partial surface passivation. *Langmuir* **25**, 13833–13839 (2009).
- 36. Ma, L., Huang, Y., Hou, M., Xie, Z. & Zhang, Z. Silver nanorods wrapped with ultrathin Al2O3layers exhibiting excellent sers sensitivity and outstanding sers stability. *Sci. Rep.* **5**, 1–9 (2015).

- 37. Li, Y. *et al.* Probing Local Potentials inside Metallic Nanopores with SERS and Bipolar Electrochemistry. *Adv. Opt. Mater.* **5**, 6–11 (2017).
- 38. Lin, X. *et al.* Solid-phase synthesis of atomically thin two-dimensional non-layered MoO2 nanosheets for surface enhanced Raman spectroscopy. *J. Mater. Chem. C* **7**, 7196–7200 (2019).
- 39. Xia, M. A Review on Applications of Two-Dimensional Materials in Surface-Enhanced Raman Spectroscopy. *Int. J. Spectrosc.* **2018**, 1–9 (2018).
- 40. Chen, M. *et al.* 2D materials: Excellent substrates for surface-enhanced Raman scattering (SERS) in chemical sensing and biosensing. *TrAC Trends Anal. Chem.* **130**, 115983 (2020).
- 41. Zhang, H. *et al.* Boron nitride/gold nanocomposites for crystal violet and creatinine detection by surface-enhanced Raman spectroscopy. *Appl. Surf. Sci.* **457**, 684–694 (2018).
- 42. Ling, X. *et al.* Lighting Up the Raman Signal of Molecules in the Vicinity of Graphene Related Materials. *Acc. Chem. Res.* **48**, 1862–1870 (2015).
- 43. Ling, X., Wu, J., Xu, W. & Zhang, J. Probing the effect of molecular orientation on the intensity of chemical enhancement using graphene-enhanced Raman spectroscopy. *Small* **8**, 1365–1372 (2012).
- 44. Stehle, Y. *et al.* Synthesis of Hexagonal Boron Nitride Monolayer: Control of Nucleation and Crystal Morphology. (2015) doi:10.1021/acs.chemmater.5b03607.
- 45. Wang, H. *et al.* Controlled Growth of Few-Layer Hexagonal Boron Nitride on Copper Foils Using Ion Beam Sputtering Deposition. 1–6 (2014) doi:10.1002/smll.201402468.
- 46. Elbadawi, C. *et al.* Electron beam directed etching of hexagonal boron nitride. *Nanoscale* **8**, 16182–16186 (2016).
- 47. Cai, Q. *et al.* Boron nitride nanosheets as improved and reusable substrates for gold nanoparticles enabled surface enhanced Raman spectroscopy. *Phys. Chem. Chem. Phys.* **17**, 7761–7766 (2015).
- 48. Kim, N. Y., Leem, Y. C., Hong, S. H., Park, J. H. & Yim, S. Y. Ultrasensitive and Stable Plasmonic Surface-Enhanced Raman Scattering Substrates Covered with Atomically Thin Monolayers: Effect of the Insulating Property. *ACS Appl. Mater. Interfaces* (2019) doi:10.1021/acsami.8b17847.
- 49. Chugh, D., Jagadish, C. & Tan, H. Large-Area Hexagonal Boron Nitride for Surface Enhanced Raman Spectroscopy. *Adv. Mater. Technol.* **4**, 1–7 (2019).
- 50. Li, L. H. & Chen, Y. Atomically Thin Boron Nitride: Unique Properties and Applications. *Adv. Funct. Mater.* **26**, 2594–2608 (2016).
- 51. Chi, T. T. K., Le, N. T., Hien, B. T. T., Trung, D. Q. & Liem, N. Q. Preparation of SERS Substrates for the Detection of Organic Molecules at Low Concentration. *Commun. Phys.* **26**, 261–268 (2017).
- 52. Xiao, G. N. & Man, S. Q. Surface-enhanced Raman scattering of methylene blue adsorbed on cap-shaped silver nanoparticles. *Chem. Phys. Lett.* **447**, 305–309 (2007).
- 53. Chatterjee, A., Gale, D. J. G., Grebennikov, D., Whelan, L. D. & Merschrod, E. F. Surface potential and morphology mapping to investigate analyte adsorption effects on surface enhanced Raman scattering (SERS). *Chem. Commun.* **53**, 12024–12027 (2017).

- 54. Boginskaya, I. *et al.* SERS-Active substrates nanoengineering based on e-beam evaporated self-assembled silver films. *Appl. Sci.* **9**, (2019).
- 55. Meng, X. *et al.* A Graphene-Silver Nanoparticle-Silicon Sandwich SERS Chip for Quantitative Detection of Molecules and Capture, Discrimination, and Inactivation of Bacteria. *Anal. Chem.* **90**, 5646–5653 (2018).
- 56. Muehlethaler, C. *et al.* Ultrahigh Raman Enhancement on Monolayer MoS2. *ACS Photonics* **3**, 1164–1169 (2016).

#### Chapter 7

#### **Conclusion and Outlook**

#### 7.1 Conclusion.

This thesis work explored the synthesis and application of a two-dimensional material namely hexagonal boron nitride. Which is a wide band gap (5.9 eV) meta-material also known as white graphene. As it is structurally similar to graphene. The synthesis work has been carried out into two disciplines 1) radio frequency magnetron sputtering 2) chemical vapour deposition. This thesis work is categorized into three major sections which are -synthesis of hBN via radio frequency magnetron sputtering, hBN synthesis via CVD and application of CVD grown hBN film.

The deposition of hBN via r.f magnetron sputtering was carried out in a single step and double step configuration as discussed in chapter 4. Single step deposition tends to generate growth in the Z axis rather than a layered growth. Whereas multiple step/two-step deposition leads to a more layered growth. This is due to less nucleation density in multiple step deposition than a single step. The two/multiple step growth process creates a larger grain size by reducing the nucleation density in the second step of the deposition. In the second step the already nucleated islands grow in size creating larger grains. On the other hand single step growth creates high nucleation density and the the grain sized are smaller in dimension. Our study about radio frequency sputter deposition of hBN over 25 µm thick copper foil shows that the surface roughness of the copper surface also plays a crucial role in formation of the film. High surface roughness (96 nm) tends to create isolated island with very poor wettability. It generally encourages three dimensional growth. Surface roughness of 4 nm or less creates a uniform and homogeneous films. The decrease in surface roughness of the as-received copper foil can be achieved by electropolishing of the copper foil. This study also finds that copper annealing at 900 °C in Ar/H<sub>2</sub> atmosphere generates Cu (001) surface termination whereas annealing at 1040 °C generates Cu (111) termination. The surface orientation of the copper surface plays a decisive role in determining the crystal phase of the synthesized BN. For Cu (111) surface termination the synthesized phase is hBN and for Cu (001) it is cBN. This phase selection happens due to the similarities between the lattice constants of cBN- Cu (001) and hBN -Cu (111). The lattice mismatch between Cu (111) and hBN is less than 1.8 %. We found that two step deposition over electropolished Cu (111) achieves hBN film, which is continuous and uniform. And for Cu (001) deposition under same condition achieves cBN phase.

Chemical vapour deposition of hBN- This study is about the growth of hBN via atmospheric pressure CVD. It has been successfully demonstrated that the thickness of the deposited film can be tuned by just regulating the amount of precursor material. Ammonia borane was used as a precursor material and it was sublimated at 130° C by using a heating tape kept at 120 V. It has also been demonstrated that by increasing the gas flow rate from 50 sccm to 200 sccm Ar/H<sub>2</sub> during the cooling phase thermally induced wrinkles can be generated. Electropolishing of the copper substrate achieves more uniform and continuous films. We also noticed silica contaminants from the quartz tube can be minimized by cleaning the quartz tube regularly after each deposition.

Applications of CVD grown hBN- The CVD grown hBN films has been used for four different types of applications, the major conclusion of these four areas are as follows:

SERS – The synthesized hBN film has been used to enhance the Raman signal of three different organic molecules, Methylene blue, malachite green and Rhodamine 6G.In all three probe molecules, hBN films have shown similar enhancement factors. Films of three different thickness 1.5 nm, 6 nm and 7 nm has been used for SERS study with conjugation of a 36 nm thick hBN flake. hBN of all thickness behaved similarly in terms of enhancement factor. This shows that the Raman enhancement produced by the hBN film is independent of the thickness of the film. We have also demonstrated the durability, repeatability and reproducibility of hBN film. hBN films are extremely durable when compared to metal nanoparticles. hBN films tested after 7 months of their growth showed similar enhancement with respect to the freshly synthesized films.

Resistive switching – 6 nm thick film has been used to investigate the resistive switching properties of hBN/Cu. A conductive atomic force microscope has been used for this purpose. The film showed considerable stability, ran through 100 I-V cycles. The 100 cycles have consistent SET and RESET voltage. Neuromorphic learning studies like potentiation has been carried on with this film and promising results were achieved.

Oxygen reduction reaction- Oxygen reduction reaction is an important reaction in a fuel cell. Catalysts like platinum plays role in enhancing the cathode current. Hexagonal boron nitride is emerging as a potential competitor in this field. We have investigated the efficacy of hBN as an electrocatalyst in Cu electrodes. Our results show that hBN in nitrogen saturated condition has been able to produce  $20~\mu\text{A}$  current.

hBN heterostructure- Hexagonal boron nitride heterostructure has been fabricated by using the wet transfer method. The encapsulation of MoS<sub>2</sub> by multilayer hBN exhibited a considerable rise in photocurrent when compared to bare MoS<sub>2</sub>.

#### 7.2 Outlook or perspective.

The thesis work has potential for further propagation in many ways. The following are the major future scope for the research carried out in this thesis:

Defects in CVD grown hBN films can be tuned to in particular  $V_NC_B$  defects. These defects are the bedrock for single photon study in hBN. Single-photon emission is sought after in quantum computing as a source of one photon qbit. Controlled synthesis of hBN films with specific and quantifiable  $V_NC_B$  defects can be a game changer for defects related application of hBN. The difficult part here is to control the defect percentage in the film and also the distribution of defects throughout the film.  $V_NC_B$  defects in hBN film can also be generated by means of ion irradiation. Nevertheless, the process of defect generation via ion irradiation is less scalable for practical applications than a controlled synthesis of hBN film with defects.

Roughness tuning of the hBN film can be carried out in conjugation with the deposition of gold. As high roughness creates multifold of different surfaces, covering them with gold shall increase the plasmonics enhancement regarding the Raman enhancement. Controlled growth of wrinkles over hBN films can also be used for controlling the roughness of the hBN film. The wrinkle dimension can be controlled by controlling the cooling rate after the growth of the film. As wrinkles in hBN are thermally induced wrinkle formation has explicit dependence

over the cooling rate.

Hexagonal boron nitride thin films have been explored for resistive application. It is emerging as a potential candidate for resistive random access memory devices (RRAM) alongside conventional materials like  $TiO_2$  and  $HfO_2$ . Stable I-V loops in hBN/Cu systems serve as the bedrock for studying neuromorphic computing. Potentiation and depression studies can be done with hBN system.

Heterostructure synthesis of hBN and 2D materials can be initiated in a CVD. Insitu heterostructures have a lot of advantages, they do no suffer from the contaminations that arise from the transfer process. Novel photon-induced excitonic behaviour at the interface of two materials can be studied.

## Synthesis and applications of hexagonal boron nitride ultrathin films

by Nilanjan Basu

**Submission date:** 26-May-2021 02:35PM (UTC+0530)

**Submission ID:** 1594470784

File name: For\_Plagarism\_check\_full\_thesis..pdf (5.89M)

**Word count:** 39759

Character count: 197830

# Synthesis and applications of hexagonal boron nitride ultrathin films

ORIGIN	ALITY REPORT			
	8% ARITY INDEX INTERNET SOURCES	10% PUBLICATIONS	7% STUDENT	PAPERS
PRIMAR	RY SOURCES			
	Nilanjan Basu, Moram S Manju Sharma, Kanchar Parmar, Venugopal Rao "Large Area Few-Layer I Nitride as a Raman Enha Nanomaterials, 2021 Publication	n Yadav, Avan Soma, Jayeet Hexagonal Bo	ish Singh a Lahiri. ron	6%
2	arxiv.org Internet Source	JAYEETA PROFESSION ASSISTANCE PROPERTY ASSISTANCE PROOF OF HYDER		5%
3	Submitted to Banaras H Student Paper	indu Universit	ty	2%
4	www.mdpi.com Internet Source			<1%
5	"Conductive Atomic Ford 2017 Publication	e Microscopy	", Wiley,	< 1 %
	Ren-Jie Chang, Xiaochen Wang, Yuewen Sheng, Be Bhaskaran, Jamie H. War 3 on Shidmis our	ner. "Growth	of Large	4

### Single-Crystalline Monolayer Hexagonal Boron Nitride by Oxide-Assisted Chemical Vapor Deposition", Chemistry of Materials, 2017

Publication

7	worldwidescience.org Internet Source	<1%
8	www.azonano.com Internet Source	<1%
9	purehost.bath.ac.uk Internet Source	<1%
10	Submitted to The University of Manchester Student Paper	<1%
11	iopscience.iop.org Internet Source	<1%
12	Submitted to Alfaisal University Student Paper	<1%
13	silo.pub Internet Source	<1%
14	en.wikipedia.org Internet Source	<1%
15	Nicholas D. Kay. "Nanomechanical and Nanoelectromechanical Phenomena in 2D Atomic Crystals", Springer Science and Business Media LLC, 2018 Publication	<1%

16	mrs.org Internet Source	<1%
17	Janocha, Eike. "Electronic Properties of ALD Zinc Oxide Interfaces and its Implication for Chalcopyrite Absorber Materials", Technische Universität Berlin, 2012.	<1 %
18	baadalsg.inflibnet.ac.in Internet Source	<1%
19	epdf.pub Internet Source	<1%
20	dspace.lboro.ac.uk Internet Source	<1%
21	Submitted to University of Ulster Student Paper	<1%
22	Pakdel, Amir, Yoshio Bando, and Dmitri Golberg. "Nano boron nitride flatland", Chemical Society Reviews, 2014. Publication	<1%
23	amsdottorato.unibo.it Internet Source	<1%
24	pubs.rsc.org Internet Source	<1%
25	Bijay Kumar Sharma. "Graphene: an exotic condensed matter and its impact on	<1%

## technology", Emerging Materials Research, 2020

Publication

26	Sro.sussex.ac.uk Internet Source	<1%
27	"Spectroscopic Methods in Mineralogy and Geology", Walter de Gruyter GmbH, 1988	<1%
28	Submitted to Monash University Student Paper	<1%
29	e-space.mmu.ac.uk Internet Source	<1%
30	Christine Kranz, Maria Wächtler. "Characterizing photocatalysts for water splitting: from atoms to bulk and from slow to ultrafast processes", Chemical Society Reviews, 2021 Publication	<1%
31	Merad, A.E "Ab initio study of electronic properties of zincblende AlN and deformation potentials under hydrostatic stress", Materials Chemistry & Physics, 20031115 Publication	<1%
32	Submitted to Queensland University of Technology  Student Paper	<1%

33	M. Terrones, JC. Charlier, A. Gloter, E. Cruz- Silva et al. "Experimental and Theoretical Studies Suggesting the Possibility of Metallic Boron Nitride Edges in Porous Nanourchins", Nano Letters, 2008 Publication	<1%
34	Submitted to University of Durham Student Paper	<1%
35	Campbell, Stephen A "Fabrication Engineering at the Micro- and Nanoscale", Oxford University Press	<1%
36	Fendler, Janos. "Biomimetic Nanoparticle Synthesis", Surfactant Science, 2003. Publication	<1%
37	www.beilstein-journals.org Internet Source	<1%
38	"Fundamentals of Nanoscale Film Analysis", Springer Science and Business Media LLC, 2007 Publication	<1%
39	"Green Tribology", Springer Science and Business Media LLC, 2012 Publication	<1%
40	Submitted to Higher Education Commission Pakistan Student Paper	<1%

41	M Albertí, A Castro, A Laganà, F Pirani, M Porrini, D Cappelletti. "Properties of an atom- bond additive representation of the interaction for benzene-argon clusters", Chemical Physics Letters, 2004 Publication	<1%
42	Michael S. Bresnehan, Matthew J. Hollander, Maxwell Wetherington, Michael LaBella et al. "Integration of Hexagonal Boron Nitride with Quasi-freestanding Epitaxial Graphene: Toward Wafer-Scale, High-Performance Devices", ACS Nano, 2012 Publication	<1%
43	Oleshko, V.P "Aperiodic core structures of Pd and Pt giant clusters chemically stabilized with diphenyl phosphide ligands", Journal of Molecular Catalysis. A, Chemical, 20060418 Publication	<1%
44	isindexing.com Internet Source	<1%
45	www.science.gov Internet Source	<1%
46	Baalousha, M., and J.R. Lead. "Characterization of natural and manufactured nanoparticles by atomic force microscopy: Effect of analysis mode, environment and sample preparation",	<1%

## Colloids and Surfaces A Physicochemical and Engineering Aspects, 2013.

Publication

47	Submitted to University of Surrey Student Paper	<1%
48	Submitted to West Thames College London Student Paper	<1%
49	www.freepatentsonline.com Internet Source	<1%
50	www.ir.nctu.edu.tw Internet Source	<1%
51	www.slideshare.net Internet Source	<1%
52	Submitted to University of St Andrews Student Paper	<1%

Exclude quotes

On

Exclude matches

< 14 words

Exclude bibliography On

"Where there is evidence, no one speaks of faith" **Bertrand Russell**